**The Dissertation Committee for Yashar Mehmani Certifies that this is the approved version of the following dissertation:**

# Modeling Single-Phase Flow and Solute Transport across Scales

**Committee:**

Matthew Balhoff, Supervisor

Todd Arbogast

Steven Bryant

Maša Prodanović

Mary Wheeler

# Modeling Single-Phase Flow and Solute Transport across Scales

**by**

**Yashar Mehmani, B.S.; M.S.E**

**Dissertation**

Presented to the Faculty of the Graduate School of

The University of Texas at Austin

in Partial Fulfillment

of the Requirements

for the Degree of

**Doctor of Philosophy**

**The University of Texas at Austin**

**December 2014**

# Dedication

To my mother Soraya

# Acknowledgements

My sincerest gratitude is due foremost to my graduate advisor Matthew Balhoff for his guidance and feedback throughout this research. I am particularly indebted to him for giving me the freedom and opportunity to pursue some of my own ideas and showing consistent support and confidence in them, even in the face of my own self-skepticism. Without him none of this work would have been possible.

My appreciation goes to my committee members, Todd Arbogast, Steven Bryant, Maša Prodanović, and Mary Wheeler, with whom I have had countless stimulating discussions over various topics inside and outside their classrooms. I would additionally like to thank Todd Arbogast, Clint Dawson, Hans Koch, and Serge Prudhomme for allowing me to take part in their classes and indulge my curiosity with abstract/applied mathematics (a pleasure unfortunately engineering students rarely get to experience), and my advisor Matthew Balhoff for giving me the uncommon permission to do so.

I would like to acknowledge the Center for Subsurface Modeling and Mary Wheeler for allowing me to use the computational resources essential to the modeling work herein. My special thanks go to the faculty and staff of the department of Petroleum and Geosystems Engineering especially Kamy Sepehrnoori, Frankie Hart, Heather Felauer, and Barbara Messmore for their help and support throughout my graduate studies. I would also like to extend my gratitude to Steven Bryant and Peter Eichhubl for their valuable inputs on the geological as well as geochemistry aspects of this work. I must credit Mart Oostrom for providing the excellent and invaluable (micromodel) experimental data set used for validating one of the models developed in this work. I have

very much enjoyed our collaborative work and hope for many more alike to come in the future.

I am thankful to a number of colleagues and friends over the years including (but certainly not limited to) Pengpeng Qi, Hongtao Yang, Shaina Kelly, Amirreza Rahmani, Greg Jackson, Daniel Ehrenfried, Daniel Sanchez-Rivera, Tie Sun, Ben Ganis, Gergina Pencheva, Reza Tavakoli, Pexi Zhu, Zhuang Sun, Ke Xu, Joe Tansey, Ali Afsharpoor, for their camaraderie and thought-provoking discussions.

The implicit contribution of my family towards this work cannot be overstated. The constant love and support of my parents Soraya and Ali is the crucial prerequisite for all current/future success in my career. I am also grateful to my brother Ayaz with whom I constantly exchanged research ideas and constructive criticism during our simultaneous studies here at UT. Finally, I want to thank Kara for rendering my graduate life fun and full of adventure while making certain that I sustained a social life outside of school.

The financial support for this work was sponsored by the U.S. Department of Energy, Office of Science, and Office of Basic Energy Sciences under Award Number DE-SC0001114 as part of the Center for Frontiers of Subsurface Energy Security, and Energy Frontier Research Center. The micromodel experiments were performed using EMSL, a national scientific user facility sponsored by the Department of Energy's Office of Biological and Environmental Research and located at Pacific Northwest National Laboratory.

# Modeling Single-Phase Flow and Solute Transport across Scales

Yashar Mehmani, Ph.D.

The University of Texas at Austin, 2014

Supervisor: Matthew Balhoff

Flow and transport phenomena in the subsurface often span a wide range of length (nanometers to kilometers) and time (nanoseconds to years) scales, and frequently arise in applications of $CO_2$ sequestration, pollutant transport, and near-well acid stimulation. Reliable field-scale predictions depend on our predictive capacity at each individual scale as well as our ability to accurately propagate information across scales. Pore-scale modeling (coupled with experiments) has assumed an important role in improving our fundamental understanding at the small scale, and is frequently used to inform/guide modeling efforts at larger scales. Among the various methods, there often exists a trade-off between computational efficiency/simplicity and accuracy. While high-resolution methods are very accurate, they are computationally limited to relatively small domains. Since macroscopic properties of a porous medium are statistically representative only when sample sizes are sufficiently large, simple and efficient pore-scale methods are more attractive.

In this work, two Eulerian pore-network models for simulating single-phase flow and solute transport are developed. The models focus on capturing two key pore-level mechanisms: a) partial mixing within pores (large void volumes), and b) shear dispersion within throats (narrow constrictions connecting the pores), which are shown to have a substantial impact on transverse and longitudinal dispersion coefficients at the macro

scale. The models are verified with high-resolution pore-scale methods and validated against micromodel experiments as well as experimental data from the literature. Studies regarding the significance of different pore-level mixing assumptions (perfect mixing vs. partial mixing) in disordered media, as well as the predictive capacity of network modeling as a whole for ordered media are conducted.

A mortar domain decomposition framework is additionally developed, under which efficient and accurate simulations on even larger and highly heterogeneous pore-scale domains are feasible. The mortar methods are verified and parallel scalability is demonstrated. It is shown that they can be used as "hybrid" methods for coupling localized pore-scale inclusions to a surrounding continuum (when insufficient scale separation exists). The framework further permits multi-model simulations within the same computational domain. An application of the methods studying "emergent" behavior during calcite precipitation in the context of geologic $CO_2$ sequestration is provided.

# Table of Contents

# List of Tables

# List of Figures

# Chapter 1: Introduction

Flow and transport phenomena in the subsurface often span many different length (nanometers to kilometers) and time scales (nanoseconds to years), and reliable predictions relevant to engineering field applications hinges on our predictive capacity at each individual scale as well as our ability to accurately propagate information across scales. For example, with the steady rise in global temperatures largely attributed to anthropogenic greenhouse emissions, $CO_2$ sequestration has become recognized as an increasingly viable mitigating measure. The process involves injecting large volumes of supercritical $CO_2$ into abandoned hydrocarbon reservoirs or deep saline aquifers (fig. 1.1). Upon contact with the resident brine, $CO_2$ dissolves (although at a slow rate) and subsequently undergoes a series of dissolution and precipitation reactions with the rock minerals. The complex interaction/feedback between the fluid mechanics, transport of chemical species, bulk and mineral reactions (interacting via diffusion through boundary layers), and geometric alterations of the rock at the pore scale could potentially give rise to "emergent" macroscopic manifestations. These manifestations are referred to as "emergent" because they cannot be foreseen from the individual behavior of each of the mechanisms involved. Prediction under such circumstances behooves multiscale modeling strategies.

Over the past few decades, pore scale modeling (in conjunction with experiments) has assumed a predominant role in improving our fundamental understanding of various subsurface phenomena at the small scale. Its applications have range from studying multiphase flow and reactive transport (Blunt, 2001) to drying processes (Prat, 2002) in porous media. Several modeling strategies have been developed, each of which possess certain advantages over the rest. Among them, two broad categories can generally be

recognized: a) those that simulate on an "exact" geometric representation of the pore space (obtained from rock imaging), and b) those that do so on a simplification thereof. The first category is typically referred to as *direct* modeling approaches, while the latter is closely related to *pore-network* modeling. While direct modeling is capable of capturing a substantial amount of details of a given phenomenon with very few simplifying assumptions, it comes at a higher computational cost limiting the largest sample size to which they can be applied. This is particularly important if the representative elementary volume (REV), the size at which statistical fluctuations of averaged properties due to small-scale variations asymptote, for a given problem is beyond this computational limit. Pore network models, on the other hand, relax this difficulty by approximating the pore-space geometry with an assemblage of simple geometric elements. This is often accompanied by a secondary approximation in describing the problem physics, which further reduces the predictive capacity of network models. Nevertheless, the substantial flexibility offered by pore networks in reformulating the governing equations, provides the modeler with the opportunity to rethink/modify the problem description.

Throughout this dissertation, we develop modeling strategies for single-phase flow and (reactive/passive) solute transport at the pore scale as well as across scales. At the pore scale, we focus on two important pore-level mechanisms controlling macroscopic longitudinal and transverse dispersion: a) partial mixing within pores (i.e. larger void volumes), and b) shear dispersion within throats (i.e. narrow constrictions connecting the pores). At low Peclet numbers (defined as the ratio of advection to diffusion), diffusion is the dominant mechanism and homogenizes solute concentrations within pores. This is referred to as the "perfect mixing" or "complete mixing" scenario. At moderate to high Peclet numbers, an inflowing stream of solute tends to exit the pore

through only a subset of its outflowing throats, while undergoing a small amount of Brownian mixing. This is the "partial mixing" scenario, and is the first pore-level mechanism we attempt to capture. It is shown in chapter 3, that failure to properly account for this mechanism leads to large errors in predicting macroscopic transverse dispersion (depending on the pore-space structure). By "shear dispersion" we refer to the stretching of the solute due to non-uniform velocity profiles at the pore scale. This is the second mechanism we attempt to capture in chapter 4, and is shown to play an important role in predicting macroscopic longitudinal dispersion.

Pore network models of solute transport can be divided into Eulerian and Lagrangian methods. All Eulerian methods in the literature (to our knowledge) fail to account for either mechanism, while Lagrangian methods fail at describing pore-level partial mixing (but elegantly incorporate shear dispersion). In developing our network models, we have placed special emphasis on simplicity and computational efficiency. For this reason, an Eulerian framework was chosen as they generally provide better computational performance. We then verify the models with *direct* approaches (e.g. computational fluid dynamics, CFD) and validate them by comparison against experiments.

In order to propagate pore-scale information to larger scales, one common approach involves deriving macroscopic properties (e.g. permeability) from either experiments or pore-scale simulations on statistically representative samples, followed by their direct substitution into continuum-scale simulators. While such an approach is appropriate for situations in which a separation between scales exists, it may lead to errors otherwise. Recent theoretical and computational work (Kechagia et al., 2002; Li et al., 2006; Battiato and Tartakovsky, 2011; Molins et al., 2012) provides evidence that under certain flow and (reactive) transport regimes, a coupling between the scales exists.

This means that pore-scale details can no longer be ignored (or interpreted in an average sense alone), and predictive modeling must rely to some extent on pore-scale simulations. This has given rise to the development of a vast variety of "hybrid multiscale methods" in the recent literature, whose essence is to dynamically combine pore-scale and continuum-scale models over the same computational domain. The hybrid methods differ from each other on the particular circumstance to which they are most suitable. The proper choice of one hybrid method over another depends primarily on the degree of separation between the length and time scales present in the problem, as well as on the fraction of the domain to be represented at the pore scale (Sheibe et al., 2014).

On the other hand, while accurate and efficient pore-scale methods are essential for predictive modeling, our ability to simulate on sufficiently large (i.e. statistically representative) domains may still remain quite limited. Common limitations are either computational (i.e. simulations are time consuming), or due to difficulties in characterizing the pore-space geometry/heterogeneity. As an example of the latter, it is very difficult to obtain high resolution voxilized images of large samples, since size and resolution are inversely correlated (Beckingham et al., 2013). In addition, sudden large-scale discontinuities in the pore structure may be difficult to characterize within a single domain (and impart to further computational problems e.g. ill-conditioned systems).

In this work, we present a mortar domain decomposition framework to address the foregoing issues. Within this framework, we develop methods that allow the coupling of pore-scale and continuum-scale models. Therefore, they can be regarded as hybrid methods and used to perform "concurrent" simulations (i.e. when insufficient scale separation exists; Sheibe et al, 2014) of localized pore-scale inclusions in an otherwise continuum domain (e.g. a pore-scale "skin" around wellbores). The domain decomposition methods further lend themselves to parallel computing, which renders

efficient simulations on large pore-scale samples feasible. Additionally, characterization of the pore-space geometry/heterogeneity is easier when abrupt changes in pore structure are viewed as subdomain interfaces, and voxilized images of these domains are obtained piece by piece each interpreted as subdomains. Finally, various pore-scale modeling strategies (each most suitable to the local flow/transport physics at work) can be incorporated into the same computational domain under the current framework.

The dissertation is outlined as follows: in chapter 2 we provide sufficient background information and review relevant literature. In chapter 3, we detail the development of the streamline splitting method (SSM) for capturing partial mixing within pores. Comparison of the model predictions to CFD simulations and micromodel experiments is provided. A discussion on the impact and importance of pore-level mixing assumptions in disordered granular media is given. In chapter 4, we detail the development of the superposing transport method (STM) for capturing shear dispersion within throats. The model is compared against CFD simulations as well as experimental data from the literature. A discussion on the origins of the supra-linear scaling of longitudinal dispersion vs. Peclet number with reference to modeling results from the literature, as well as on the predictive capacity of Eulerian network models for ordered media is presented. In chapter 5, we develop domain decomposition methods for advection-dominated transport on large pore-scale domains. A simplified reactive transport model is additionally developed in order to investigate "emergent" behavior due to calcite precipitation in the context of geologic $CO_2$ sequestration. In chapter 6, the domain decomposition methods are formalized and extended to include diffusive transport, and coupling of pore-scale and continuum-scale subdomains. A thorough study of the computational efficiency and parallel scalability of the methods is presented. Chapter 7 concludes by drawing general conclusions (specific conclusions are limited to

each chapter) and implications regarding the presented material. The appendices provide substantial detail and supplementary information for the interested reader.

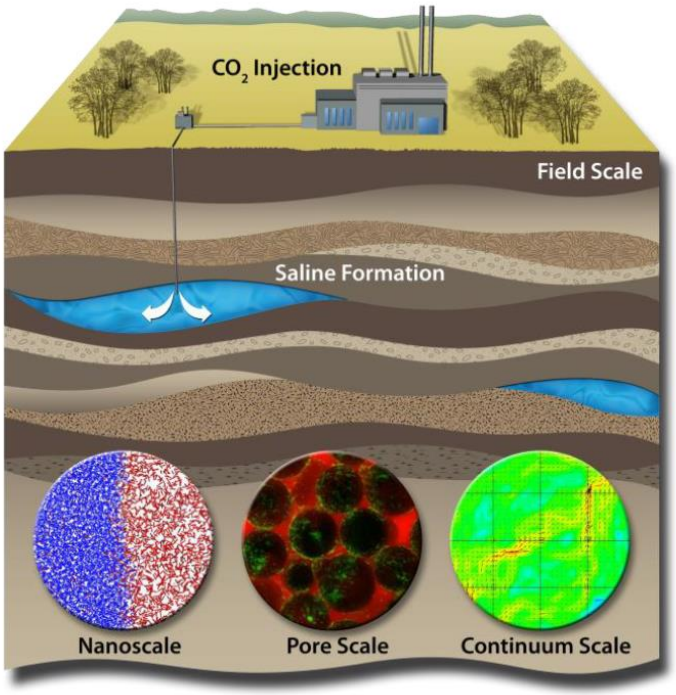


Figure 1.1: Schematic of the injection of anthropogenic $CO_2$ into deep saline aquifers. The insets communicate the fact that relevant *in situ* flow and reactive transport processes span scales starting from the nanometer to several kilometers.

# Chapter 2: Background and Literature Review

In this chapter, we provide sufficient background and cover literature in relevance to the following chapters. Since the dissertation concerns itself with single-phase solute transport, the bulk of what follows revolves around this topic with occasional references to extraneous physics/applications. It is to be noted that the literature in some instances is quite rich and well developed, and the following is by no means a fair representation of the whole. Therefore, our strategy is to focus on the most relevant pieces while providing useful references for the interested reader.

## 2.1 Modeling at the pore scale

Over the past few decades modeling flow and transport at the pore scale has seen the adoption and development of various computational methods. The first and perhaps the most critical step prior to modeling is the accurate characterization of the pore-space geometry/topology. Imaging techniques such as X-ray microtomography (XMT) (Wildenschild and Sheppard, 2013) have made it possible to obtain accurate 3D characterizations of the complex pore-space geometry of rock samples. For granular media, Monte Carlo (Maier et al., 2003), cooperative rearrangement (Thane, 2006), and sequential sedimentation (Coelho et al., 1997; Øren and Bakke, 2002) are among algorithms that have been developed to digitally reconstruct various grain packs, in which the pore space geometry is exactly defined. Such reconstructions, although approximate in representing real porous media, provide valuable insights into the link between depositional processes (e.g. cementation and compaction) and hydraulic/transport properties (e.g. permeability) of granular media (Bryant et al., 1993a, 1993b; Bakke and Øren, 1997). Modeling can then proceed either by simulating directly on the complex

void geometry, or on a simplification thereof. The former approach is typically referred to as *direct modeling*, while the latter is closely associated with *pore-network modeling* (discussed in the following section). In the following, we review a handful of direct modeling approaches recently used at the pore scale.

Direct modeling approaches include computational fluid dynamics (CFD) (Anderson, 1995), Lattice-Boltzmann (LB) (Chen and Doolen, 1998), and smoothed particle hydrodynamics (SPH) (Monaghan, 1992). While both flow and transport can be solved via either of these approaches, Eulerian methods are typically preferred for computing flow and Lagrangian methods for transport as they are devoid of numerical dispersion. The former requires a spatially discretized mesh, while the latter does not. A popular Lagrangian method used for simulating transport at the pore scale is particle tracking (PT). In this method, particles (or random walkers) are propagated through the void space via a deterministic advection step (following the streamlines) followed by a stochastic diffusion step (obeying Einstein's equation). Maier et al. (2000, 2003) studied dispersion on digitally generated sphere packs using LB and PT to solve flow and transport, respectively; and reported good agreement with measurements from nuclear magnetic resonance (NMR) spectroscopy experiments. Molins et al. (2012) used an adaptive meshing CFD method to study the "lab-field discrepancy" of geochemical reaction rates. Their study provides invaluable insight into the vital role of pore-scale modeling as a crucial guide towards predictive macro-scale modeling. Yang et al. (2013) used CFD to solve the Navier-Stokes flow equations on a bead pack and successfully compared the velocity field to that obtained from magnetic resonance velocimetry measurements. Zaretskiy et al. (2010) used a finite-element-finite-volume method to study longitudinal dispersion on a digitized sample of Fontainebleau sandstone. They highlighted the sensitivity of the pore-scale modeling results to the computational mesh

employed. Mostaghimi et al. (2012) used a combination of finite difference and PT for flow and transport, respectively, on micro-CT images of Berea sandstone and produced longitudinal dispersion coefficients in quantitative agreement with experimental data. Ovaysi and Piri (2011) used a Lagrangian approach referred to as the modified moving particle semi-implicit (MMPS) method to solve flow and transport on sandstone samples. They obtained longitudinal dispersion coefficients in favorable agreement with experimental data, and included non-inertial effects in their simulations.

Despite the high fidelity of direct modeling predictions and the fundamental insights they provide about the underlying physical mechanisms of a given phenomenon, they often demand high performance computational resources and massive parallelism (Oostrom et al., 2014). This poses a computational limit on the size and scale of the problems to which they can be applied. Such limitations have made pore-network modeling very popular over the past few decades, which overcome this limitation by simplifying the void space geometry while preserving essential features thereof. However, the predictive capacity of network models has been somewhat elusive in the literature with a few important exceptions discussed in section 2.2. Even so, it is the aim and contention of the author that modeling efforts shall be directed towards reducing complexity, while preserving only the most essential features of a given phenomenon. The first step in this effort is identification of these features for which direct modeling serves as an invaluable guide.

## 2.2 PORE NETWORKS

The popularity of pore networks arose out of the pioneering works of Fatt (1956a, b, c), who studied two-phase drainage on a 2D lattice network of randomly assigned

throat radii. This was a radical shift from the hitherto bundle-of-tubes representation of porous media for computation of various macroscopic properties. Pore networks are simplified representations of the complex pore-space geometry and consist of an interconnected network of pores (or nodes) and throats (or bonds). These elements are typically assigned relatively simple shapes amenable to analytical treatment (e.g. spheres for pores and cylinders for throats). Scenarios in which either pores or throats are assigned zero volumes have also been considered. A summary of various pore/throat shapes used in the literature can be found in Joekar-Niasar (2010). The manner in which pores are connected to their nearest neighbors constitutes the network *topology* (coordination number is a parameter closely related to the network topology and is defined as the number of connected neighbors to a given pore) while the specific geometric idealizations used to represent pores/throats comprise the network *geometry*. Proper characterization of both the topological and geometric aspects of porous samples is the first necessary step, if pore networks are to be predictive. Early works on pore-network characterization typically involved statistical mappings of pore/throat properties (e.g. radii, coordination number, etc.) onto a lattice structure (e.g. Mohanty et al., 1987), or adjusting pore/throat properties to match one set of measurements (e.g. capillary pressure) followed by predictions of more difficult-to-measure properties (e.g. relative permeability) (e.g. Fischer and Celia, 1999). However, statistically mapped networks often ignore spatial correlations present in real rocks (due to the random assignment of pore/throat properties), and adjusted networks (to match one set of measurements) suffered from non-uniqueness in their representation. For these reasons, statistically generated networks are typically not considered to be predictive. Bryant and coworkers (Bryant et al., 1993a, 1993b and Bryant and Blunt, 1992) introduced the concept of physically representative networks, which marked the beginning of truly predictive

network modeling. In their work, permeability, relative permeability, capillary pressure, and permeability-porosity relationships, were all accurately and directly predicted (with no adjustable parameters) from shear knowledge of grain positions in a disordered sphere pack (measured by Finney, 1968). The network was extracted via Delaunay Tessellation of the sphere centers, and its main attraction was that spatial correlations of the pore space were elegantly imbedded into the extracted network. Recent advances in computer and imaging facilities has given rise to various image analysis techniques whereby physically representative networks can be obtained from digitized images of real samples. These include medial-axis (Thovert et al, 1993; Lindquist et al, 1996; Lindquist and Venkatarangan, 1999; Prodanovic et al., 2006), water-shed (Sheppard et al., 2006; Thompson et al., 2008), and maximal-ball (Silin and Patzek, 2006; Dong and Blunt, 2009) algorithms. These techniques have resulted in further quantitative predictions of single-phase and multi-phase flow properties in water-wet and mixed-wet media (e.g. Bakke and Øren, 1997; Øren et al., 1998; Patzek 2001). In this dissertation we employ a modified Delaunay tessellation algorithm (Al-Raoush, 2003) to extract networks from digitally created sphere packs as well as imaged sandstone samples.

Since Fatt (1950a, b, c), pore networks have been used in many other applications including: non-Newtonian flow (Lopez et al., 2003; Balhoff, 2005), non-Darcy flow (Thauvin and Mohanty, 1998; Balhoff and Wheeler, 2009), solute dispersion (Sahimi 1986; Sorbie and Clifford, 1991; Bijeljic et al., 2004, Bijeljic and Blunt, 2007; Acharya et al., 2007b), reactive transport (Hoefner and Fogler, 1988; Li et al., 2006; Algive et al., 2010; Kim et al., 2011), multi-phase flow (Koplik and Lasseter, 1985; Al-Gharbi and Blunt, 2005; Piri and Blunt, 2005; Joekar-Niasar et al., 2010), biofilm growth (Suchomel et al., 1998a, 1998b), etc. A larger portion of this literature is devoted to two-phase flow (drainage and imbibition), due to its significance in petroleum engineering (oil recovery)

and soil sciences. As this is not the focus of our work, the reader is referred to comprehensive reviews by Celia et al., (1995) and Blunt (2001) for more information. An excellent review by Berkowitz and Ewing (1998) further provides insights into the close connection between (quasi-static) two-phase flow and (invasion) percolation theory. In this dissertation, a portion of the effort is directed towards developing simple, efficient, and accurate pore-scale modeling methods for simulating single-phase flow and solute transport, for which pore networks appeared to be an appropriate starting point. The following section reviews various network modeling approaches developed/applied in the literature.

### 2.3 NETWORK MODELING OF SOLUTE TRANSPORT

Pore-network modeling of solute transport has received special interest amongst many authors in the past few decades and several methodologies have been proposed. A prerequisite to simulating transport is the computation of the velocity field within throats. The procedure is quite standard and involves: imposing pressure boundary conditions on the network, describing flow rates within throats via a constitutive equation (e.g. Hagen-Poiseuille for Newtonian fluid in a cylindrical throat), writing mass balance at each pore, solving the resultant system of (linear or nonlinear depending on the fluid rheology and/or flow regime) equations for pore pressures, and computing throat flow rates/velocities from said constitutive equation (mathematics detailed in chapter 3). The simulation of transport then resumes using computed throat flow rates/velocities.

Bryntesson (2002), Acharya et al. (2005, 2007b), Li et al. (2006), Kim et al. (2011) and Nogues et al. (2013) are among those who have adopted the popular mixed cell method (MCM), in which solute balance equations are written for each pore. In this

method, throats are assumed to be volumeless and the solute within pores perfectly mixed. Solute flow rates within throats are formulated as the algebraic sum of an upwinded advection term and a linearly varying diffusion term. Essentially, MCM can be regarded as a low-order finite volume method on an unstructured pore network (mathematics detailed in chapter 3). The advantage of MCM is that it is very computationally efficient and highly adaptable to various transport scenarios. For example, Acharya et al. (2005) used MCM to study non-linearly adsorbing solute transport, and determined that more than a million pores were required for their results to be statistically representative. Li et al. (2006) and Kim et al. (2011) studied complex geochemical reaction kinetics of anorthite and kaolinite precipitation/dissolution relevant to $CO_2$ sequestration. Nogues et al. (2013) studied porosity/permeability evolutions in carbonates due to carbonic-acid driven precipitation/dissolution reactions. They considered 18 aqueous species and 5 mineral species undergoing 14 independent reactions. The flexibility and computational efficiency of MCM is why such complex systems acting on sufficiently large pore-scale domains can even be considered.

A number of variants and/or modifications of MCM have also been developed in the literature. For instance, Raoof et al. (2013) assign volume to both pores and throats (solute still perfectly mixed in both) and sub-discretize the wetting filaments in the corners of partially drained pores to account for the partial mixing of solute within them. Milligen and Bons (2014) propose a modification to the throat rate expressions used in MCM (i.e. algebraic sum of an upwinded advection term and a linearly varying diffusion term) by deriving analytical expressions based on a steady-state plug-flow assumption within throats (a generalization of this method for non-uniform velocity profiles is given in chapter 4). They occasionally sub-discretized throats into smaller “pores” for increased modeling resolution. Algive et al. (2009, 2012) and Varloteaux et al. (2013) similarly

modified throat rate expressions in the context of reactive transport. They employed moment theory to derive corrected macroscopic parameters (i.e. solute mean velocity, dispersion coefficient, reaction source term) for each pore/throat element in the long-time asymptotic regime. The model was used to study the effects of dissolution/precipitation reactions on macroscopic single- and two-phase flow properties in the contexts of $CO_2$ sequestration and diagenetic alterations in carbonate rocks. Suchomel et al. (1998b) developed a model in which pores were assumed volumeless and throats were sub-discretized into finite difference grids. Interpore diffusion was implicitly incorporated by adjusting numerical diffusion via grid size and time step (although this does not account for diffusion countercurrent to the flow direction), and perfect mixing was assumed within pores. The model was used to study permeability/porosity alterations during bacterial biofilm growth in porous media. A simple but interesting model was developed by Martins et al. (2009), in which the solute balance equations at the pores were formulated as a system of delay-differential equations. In essence, the model took into account pore concentrations from previous time steps for computing solute flow rates in/out of pores in the current time step. This was implemented by sub-discretizing throats and marching pore concentrations forward within the sub-discretized segments (akin to a traveling wave). However, several limiting assumptions were made including the neglect of diffusion, plug-flow within throats, and perfect mixing within pores. Despite these limitations, their model shares similar spirit with the more accurate and general superposing transport method (STM) developed in chapter 4 (i.e. pore concentrations from previous time steps are used in evolving the concentration field).

A different set of models formulate transport equations in the Laplace domain (with respect to time). There is a certain extent of elegance and convenience associated with working in the Laplace domain, mainly due to the fact that convolutions of transit-

time probabilities are converted to simple multiplications. Another advantage is that computation of temporal moments becomes rather straightforward. De Arcangelis et al. (1986) developed first-passage-time probabilities for tracer particles in moving from one pore to the next. They assumed perfect mixing at the (volumeless) pores, and plug flow with simultaneous diffusion at the throats. Under these conditions, they derived exact probabilities (in the Laplace domain) for particle motions in a network. They then used a "probability propagation" algorithm to determine the first-passage-time distribution of a 10×10 diamond lattice network and computed longitudinal dispersion coefficients for various Peclet numbers. At no point was the time-domain concentration field computed. Using the same set of equations, Koplik et al. (1988) diverged in their analysis by writing species balance equations for each pore in the Laplace domain. The linear system of equations was then solved and numerically inverted into the time domain using the Stehfest (1970) algorithm. A strategy for computing higher order moments of the first-passage-time distribution of the network was further outlined. This method was later extended by Alvarado et al. (1997) to reversible adsorption/reaction scenarios, where they arrived at the interesting conclusion that dispersion coefficients depend on the degree of spatial heterogeneity of reactive sites in a porous sample and scale non-linearly with Peclet number. However, they noted that the numerical Laplace inversion step was prohibitive for networks larger than 20×20 pores and inaccurate for large Peclet numbers (>10). Indeed numerical inversion of the Laplace transform is known to be notoriously difficult (often unstable) and ill-posed in computational and applied mathematics. For this reason, (although valuable for performing moment analyses) time-domain predictions via these methods on representative sample sizes seems impractical and unlikely.

All network models discussed so far describe solute transport from an Eulerian perspective. A more natural description is provided by Lagrangian models, among which

particle tracking (PT) is almost exclusively employed. In this method, the steady-state flow equation is solved on the network (as described in the beginning of the section) to obtain mean fluid velocities within each throat. Depending on the specific throat geometry, a (rectilinear) velocity profile is assumed and used to track particles from pore to pore subject to simultaneous convection and molecular diffusion. PT methods on pore networks can be divided into two categories: a) those that trace particle motions in detail within throats following a discrete-time random walk process (Bruderer and Bernabe, 2001; Bijeljic et al., 2004; Acharya et al., 2007a; Jha et al., 2011), and b) those that perform continuous-time random hops from one pore to the next (without explicit throat-level simulations) using throat transit-time distributions (Sahimi et al., 1986; Sorbie and Clifford, 1991; Rhodes and Blunt, 2005; Bijeljic and Blunt, 2006; Picard and Frey, 2007). We refer to the first class as DPT (discrete-time particle tracking) and to the second as CPT (continuous-time particle tracking). Compared to CPT, DPT simulations are more time consuming since computational performance is limited by the time step size (controlled by the minimum throat transit time within the network). However, it can be quite accurate and has been successfully used to predict dispersion coefficients in unconsolidated granular media (e.g. Bijeljic et al., 2004; Jha et al., 2011). It is also very flexible in the sense that throats can assume various velocity profiles (e.g. parabolic or plug-flow) and substantial control is granted over particle reassignments to new throats upon their arrival at the pores (i.e. particles can be reassigned to any desired throat connected to the arrival pore, and even any desired location on the cross-section of that throat). In contrast, CPT is computationally more efficient but comparatively less flexible and less accurate (depending on the problem). The efficiency is due to the fact that particle motions within throats are not explicitly simulated, but are imbedded in the throat transit-time statistics instead. The reduced flexibility/accuracy is due to the loss of control

in reassigning particles to arbitrary cross-sectional locations of outlet throats in the arrival pores. This is particularly important in simulating dispersion in ordered media, for which CPT will not yield the expected (e.g. Edwards et al., 1991) $D_L \sim Pe_d^2$ scaling ($D_L$ is the longitudinal dispersion coefficient, and $Pe_d$ is the Peclet number defined as the ratio of advection to diffusion) (discussed further in chapter 4).

CPT methods can be further subdivided into those that use deterministic transit-time distributions in passing particles from pore to pore (e.g. Sorbie and Clifford, 1991; Picard and Frey, 2007), and those that use ensemble-averaged transit probabilities (e.g. Bijeljic and Blunt, 2006; Rhodes et al., 2009). Bijeljic and Blunt (2006) derived such an ensemble-averaged probability distribution for Berea sandstone by fitting a truncated power-law distribution to their simulation results. They provided physically meaningful interpretation of the distribution variables and fitted the data with a single adjustable parameter. Deterministic transit probabilities are often derived based on similar mathematics and assumptions (i.e. perfectly mixed (volumeless) pores and plug flow within throats; non-uniform velocity profiles are not amenable to closed-form analytical treatments) as those already discussed in the context of Laplace domain Eulerian network models (e.g. Rhodes and Blunt, 2005; Picard and Frey, 2007). An exception to this is Sorbie and Clifford (1991) who derived transit probabilities based on rigorous single throat simulations (assuming non-uniform velocity profiles).

The most common ambiguity and source of error in both Eulerian and Lagrangian network models is in describing mixing conditions within pores, and shear dispersion (i.e. spreading due to non-uniform velocity profiles) within throats. Accurate description of these fundamental transport physics could have a significant impact on quantitative macroscopic predictions of solute dispersion. All Eulerian network models developed in the literature (to our knowledge) assume perfect mixing within pores and neglect shear

dispersion within throats. While the incorporation of shear dispersion in Lagrangian networks is quite straightforward, ambiguity in describing pore-level mixing conditions still persists. The ambiguity is sourced in the difficulty in approximating flow streamlines within pores, as well as the extent of diffusive mixing taking place therein. Sahimi et al. (1986) and Bruderer and Bernabe (2001) developed simple intuitive rules for the redistribution of streamlines from the inlet to the outlet throats of a 2D cross-shaped volumeless pore. Both ignored any extent of diffusive mixing within pores, in the sense that particles could not "hop" from one outlet throat to the next (although Sahimi et al. (1986) did include some element of randomness in assigning particles to cross-sectional locations of the non-randomly chosen outlet throat). Sorbie and Clifford (1991) introduced general heuristic (and admittedly approximate) rules for the redistribution of particles (upon their arrival at the pores) among outlet throats. These rules (and variants thereof) were subsequently applied and analyzed in later publications (e.g. Acharya et al., 2004, 2007a, 2007b; Bijeljic et al., 2004; Bijeljic and Blunt, 2007). At high Peclet numbers the rules reduce to redistribution based on flow rate-averaged probabilities, while at low Peclet numbers they reduce to redistribution based on (throat) cross-sectional area-averaged (multiplied by other corrective parameters) probabilities. The biggest problem with these rules is that the "memory" of a particle is effectively erased upon its arrival to the pore (i.e. Markovian), whereas in reality particles retain their memory over a given distance (depending on the local Peclet number) before diffusion has had enough time to scramble it. At moderate to high Peclet numbers, particle memories extend beyond the distance of a single throat, which behooves a modeling strategy that preserves this behavior (although inherent limitations apply to Eulerian models as discussed in chapter 4). To our knowledge, Jha et al. (2011) seem to have come closest to proposing a general rule for mapping incoming particles to outlet throats

in a pore. Their rules were developed as an attempt to generalize those of Bruderer and Bernabe (2001) and are limited to pores with a coordination number of four or less. However, their rules do not take into account important interactions between inflowing streams, which causes them to produce erroneous predictions as discussed in chapter 3. They also ignored the possibility of diffusive mixing within pores.

Perhaps the most comprehensive analysis of pore-level mixing has been conducted in the field of fracture-network modeling (e.g. Berkowitz et al., 1994, Park and Lee, 1999; Park et al., 2001a, 2001b). In particular, Park and Lee (1999) derived physically sound, efficient, and accurate transition probabilities for incoming particles at fracture junctions. Park et al. (2001a, 2001b) later studied the effect of various mixing assumptions (perfect mixing vs. no mixing) at fracture junctions on overall macroscopic transport behavior in ordered and disordered fracture networks. They found that mixing assumptions have a larger impact in ordered media compared to random media (i.e. less than 5% of fracture junctions showed sensitivity in random media), and they attributed it to the lower effective coordination number and higher inlet flux ratios (at fracture intersections) in random networks. This conclusion is shown to corroborate very well with our results in chapter 3 for 3D disordered granular media. However, since fracture intersections are essentially 2D cross-shaped pores, the mixing equations of Park and Lee (1999) are not applicable in 3D networks of porous media, where non-planar throat geometries are connected at various orientations to the pores. Lastly, Park and Lee (1999) did not take into account the influence of pore walls in their mixing criterion.

The foregoing discussion forms the motivation for the studies presented in chapters 3 and 4. Therein, we develop efficient Eulerian network models capable of predicting (partial) mixing conditions within pores and shear dispersion within throats. These transport physics are separately captured in two different modeling approaches, but

the approaches are shown to be additive (i.e. combination of the two is straightforward). The models compare favorably against direct modeling results as well as experiments. Special emphasis was placed on simplicity and computational efficiency, which is why development under an Eulerian framework was pursued (generally known to be more efficient than Lagrangian methods). Interpretations, considerations, and implications of the results as well as the predictive capacity of the models are discussed.

## 2.3 HYBRID MODELING

Flow and transport occurs over a wide range of spatial scales (nanometer to kilometer) rendering the developments of predictive models capable of bridging all these scales a formidable task. One common approach has been to extract macroscopic parameters (e.g. permeability) or closure relations (e.g. capillary pressure) from smaller scale samples followed by their direct substitution into larger field-scale simulators. These data can either be obtained through experiments or modeling on microscale (or pore-scale) samples representative of the real medium. However, such an approach may not always be applicable when scales are not separable (Kechagia et al., 2002; Battiato and Tartakovsky, 2011), in which case modeling at the pore scale becomes imperative.

Li et al. (2006, 2007a, 2007b) used pore networks to study reaction kinetics of kaolinite and anorthite in the context of geologic carbon sequestration. They demonstrated that reaction rates obtained from continuum-scale representations of transport and/or using volume/flux-averaged concentrations in reaction rate expressions leads to large errors, sometimes even wrongly predicting the direction of the reactions (i.e. precipitation vs. dissolution). Although their study was qualitative in nature (using 3D regular lattice networks), it provided an explanation to the commonly reported

discrepancy between reaction rates observed at the field scale and those obtained from well-mixed batch experiments on crushed samples. Namely, transport limitations at the pore scale control overall reaction rates, which are non-existent under well-mixed conditions in batch experiments. Effects of flow rate and reactive cluster size/abundance were also studied, and it was concluded that the higher the degree of incomplete mixing (i.e. spatial variability of concentration) the higher the scaling error. Incomplete mixing was found to be the strongest at medium flow rates (i.e. Peclet numbers). Kim et al. (2011) and Kim and Lindquist (2012) extended the work of Li and coworkers using networks extracted from X-ray computed microtomography (XCMT) images of real sandstones. They were able to determine surface mineral distributions from XCMT images allowing for better quantitative analysis. Similar conclusions were drawn regarding the "lab-field-discrepancy", and an approximately power-law scaling of reaction rates vs. flow rate was reported for anorthite, while a more complex scaling emerged for kaolinite. In the context of filtration combustion in porous media, Lu and Yortsos (2005) similarly observed that spatially averaged macroscopic reaction rates were very different (discrepancies of a factor of two or higher) than those determined from using averaged variables in microscopic reaction rate expressions. They attributed this to the strong influence of microscopic heterogeneities on macro scale behavior. Recently, Molins et al. (2012) conducted sophisticated direct pore-scale simulations of calcite dissolution, and showed that pore-scale heterogeneities can result in an underestimation of reaction rates (due to mass transport limitations) even when total reactive surface area and porosity are held constant between samples.

Kechagia et al. (2002) demonstrated that for reactive transport with fast/finite kinetics, homogenization of microscopic equations via volume averaging does not hold except at the limit of macroscopic equilibrium. They further showed that even under

these circumstances an eigenvalue problem maintains a coupling between the micro and the macro scales. Battiato and Tartakovsky (2011) performed a systematic study to identify transport regimes (characterized by Damköhler (*Da*) and Peclet (*Pe*) numbers), under which the continuum representation of pore-scale advection-diffusion (with nonlinear surface reactions) breaks down. They used multiple-scale expansions to upscale pore-scale equations, and presented their results in the form of a Pe-Da phase diagram. This was concordant with an earlier work (Battiato et al., 2009) that used volume-averaging, substantiating the independence of their conclusions from the specific upscaling method employed. A recent work by Boso and Battiato (2013) extended this analysis to three-component systems undergoing two homogeneous and one heterogeneous reactions (all reversible). It is interesting to note that Molins et al. (2012) located their simulations on the aforementioned Pe-Da phase diagram and determined their correspondence to a case in which spatial scales were coupled.

The implications of the foregoing studies have given rise to a new class of modeling approaches referred to as "hybrid multiscale methods" (Sheibe et al., 2007), in which micro- and macro-scale simulations are simultaneously performed on the same computational domain. Balhoff et al. (2007) were one of the first to couple a pore scale model to the continuum. However the iterative coupling strategy had strong limitations in terms of flexibility and efficiency. These limitations were lifted in a later work (Balhoff et al., 2008) through the introduction of mortars (discussed in section 2.4). The work only focused on coupling linear, single-phase Newtonian flow. Tartakovsky et al. (2008a) used an SPH formulation for both the pore and continuum scales in a diffusion-reaction system and were able to non-iteratively couple the two scales together. Despite the non-iterative nature of the method, which makes it very attractive, both domains need to be formulated using SPH. Furthermore, advection was ignored in their work. Battiato et al. (2011)

developed an overlapping method for coupling pore-scale inclusions to the surrounding continua and successfully verified their method for Taylor dispersion through a fracture with reactive walls. Despite the increased generality of this approach compared to the previous work (inclusion of advection and lifting the restriction to SPH), the method appears to be limited to small pore-scale inclusions and is dependent upon the underlying macro-grid structure of the domain. The presented interface algorithm is also very expensive, because it is far more efficient to solve differential-algebraic systems as a whole rather than iteratively switching between the differential and algebraic parts. Such effects might not have appeared significant since the number of interface unknowns was limited to two. Chu et al. (2012) proposed a different approach in which macroscopic conservation equations were written assuming constitutive relations for flow were unavailable at the macro scale. Instead, the unavailable data were supplied from network simulations sampled locally across the domain. The method was also extended to two-phase flow (Chu et al., 2013) and provides a superior alternative compared to upscaled continuum models in cases where local effects are dominant. However, since pore-scale models were used as providers of accurate in/out-fluxes at the boundaries of macroscopic control volumes, the extension of this method to heterogeneous reaction scenarios in which the macroscopic source/sink term is unknown (and highly coupled to transport itself) does not seem straightforward.

The essence of all foregoing hybrid methods is a two-way "communication" between the pore scale and the continuum. Hybrid methods are a relatively recent development compared to single-scale modeling strategies such as molecular dynamics (MD), pore-scale modeling, and reservoir simulation. Naturally, they have been building upon the vast diversity of single-scale methods and various combinations thereof. Therefore, they themselves exhibit a vast diversity of strategies, which might raise the

natural question as to which hybrid method is most appropriate for any given problem. An excellent recent paper by Sheibe et al. (2014) has attempted to provide a general road map for choosing an appropriate hybrid strategy (referred to as the Multiscale Analysis Platform), depending on the degree of complexity of the hydrological problem at hand (i.e. degree of separability of temporal/spatial scales). The reader might find it beneficial to view the hybrid modeling methods developed in chapter 6 in the context of this road map (i.e. "motif F: concurrent hybrid methods"). Finally, we note that there are other physical scenarios in which pore-scale details bear important impact on macroscopic manifestations of a given phenomenon. These include wormhole formation and growth during reactive dissolution (Hoefner and Fogler, 1988; Fredd and Fogler, 1998), viscous instabilities, and viscous-dominated multi-phase flow (Kechagia et al., 2002).

## 2.4 MORTAR DOMAIN DECOMPOSITION

Mortar coupling is a domain decomposition method in which sub-domains are non-overlapping. It uses an intermediate function space (called the mortar space) to represent the state variables (e.g. pressures/concentrations) at the interface between two subdomains. These functions are represented by a linear combination of finite element basis-functions whose coefficients (referred to as Lagrange multipliers) are unknown. The "interface problem" involves solving for these unknowns (Bernardi et al., 1994; Arbogast et al., 2000; Peszynska et al., 2002). The accuracy of the mortar solution can be improved by using higher order mortars and/or finer mortar mesh (Arbogast et al., 2007). The advantages of mortars are that they (a) allow for different physics, scales, and models in various parts of the domain, (b) are easily parallelizable, and (c) even in serial computing are potentially faster because of (commonly encountered) nonlinear scaling of

computational costs with domain size. The basic idea of mortars is to: decompose the domain into subdomains; guess the Lagrange multipliers that determine the interface conditions (e.g. pressures); solve subdomains independently and compute fluxes at their shared interfaces; iterate until fluxes match on both sides of the interface. The described algorithm (known as the forward difference (FD) scheme) has been used by various authors in the past e.g. Wheeler et al. (1999), Peszyńska et al. (2002), Sun et al. (2012a), Sun et al. (2012b). Recently, Ganis et al. (2012) demonstrated that this algorithm can become quite inefficient especially in the case of nonlinear problems, and developed alternative schemes that resulted in significant computational speed-up. In chapter 6, similarly efficient schemes are developed that bear similarities with those of Ganis et al. (2012). These similarities as well as differences are highlighted therein.

Mortars have primarily been used purely at the continuum, but were recently extended by Balhoff et al. (2008) to couple flow at multiple spatial scales (i.e. hybrid modeling). Their work demonstrated that mortars can provide accurate pressure boundary conditions to the pore scale that depend on surrounding media. Subsequently, Sun et al. (2012a) showed that mortars can be used as accurate upscaling tools for pore-scale models in obtaining macroscopic properties (e.g. permeability). They showed that a large heterogeneous pore-scale domain could be decomposed along structural discontinuities and coupled via mortars to closely approximate the true permeability. Sun et al. (2012b) developed a near-well single-phase reservoir simulator where Darcy grids in the near-well region were substituted for pore-scale models. The study focused on upscaling strategies for the permeability field of the near-well region. In all foregoing literature, mortar application was limited to (linear) single-phase Newtonian flow and computational aspects were left unexamined. This, in part, forms the motivation for the

extension of these methods to solute transport as well as the computational studies presented in chapters 5 and 6.

# Chapter 3: Pore-Scale Modeling of Transverse Dispersion[1]

In this chapter, we focus on pore-scale modeling of transverse dispersion. Specifically, our goal is to develop a computationally inexpensive and accurate network model that is capable of capturing partial mixing within pores. It is shown that the streamline splitting method (SSM) developed herein, produces predictions that are in excellent agreement with micromodel experiments and direct modeling results. Implications of pore-level mixing assumptions in disordered granular media are further studied and discussed.

## 3.1 MOTIVATION

Solute transport on pore networks is commonly solved using the mixed cell method (MCM) (e.g. Bryntesson, 2002; Acharya et al., 2005) due to its simplicity and computational efficiency. The mathematical details of this method are outlined later in section 3.2.2. The modeling proceeds by first solving a flow equation, which yields the velocity field inside the pore space. Then the MCM transport equation is solved, which yields the evolution of the concentration field within the pore space in time. Although the simplistic MCM transport equation is an adequate description of (non-) reactive transport in many situations, it has an important deficiency that comes at the cost of its simplicity. The model assumes, by default, that concentrations are perfectly mixed within each pore regardless of the flow regime. At low Peclet numbers (= $vR/D_m$ where $v$, $R$ and $D_m$ are the throat fluid velocity, throat radius and molecular diffusion coefficient respectively), this

[1] The material in this chapter was published under the following reference, which was completed under the supervision of Matthew Balhoff. The experimental data in this chapter was provided by Mart Oostrom.

Mehmani, Y., M. Oostrom, and M. Balhoff. "A Streamline Splitting Pore-Network Approach for Computationally Inexpensive and Accurate Simulation of Species Transport in Porous Media." In AGU Fall Meeting Abstracts, vol. 1, p. 1514. 2013.

assumption is reasonable because the solute particles diffuse much faster than they convect. However, at moderate to high Peclet numbers, such an assumption is no longer valid and large concentration gradients may exist within individual pores.

Figure 3.1 shows the steady state concentration fields and streamlines obtained for a typical pore from direct COMSOL simulations. Boundary conditions consist of constant concentrations at the inlets and zero concentration gradients at the outlets. The figures clearly demonstrate that at low Peclet numbers (<1) the contents within the pore are perfectly mixed. However, at moderate to high Peclet numbers (>1), large concentration gradients within the pore exist. Under such transport regimes MCM could yield large errors in predicting transverse dispersion (as shown in section 3.3.2). This work presents a novel alternative approach for formulating the transport equation in a pore network, devoid of such restrictions to low Peclet regimes. The new s*treamline splitting method* (SSM) circumvents the perfect-mixing assumption by taking into account the distribution of streamlines within the pores (fig. 3.1d).

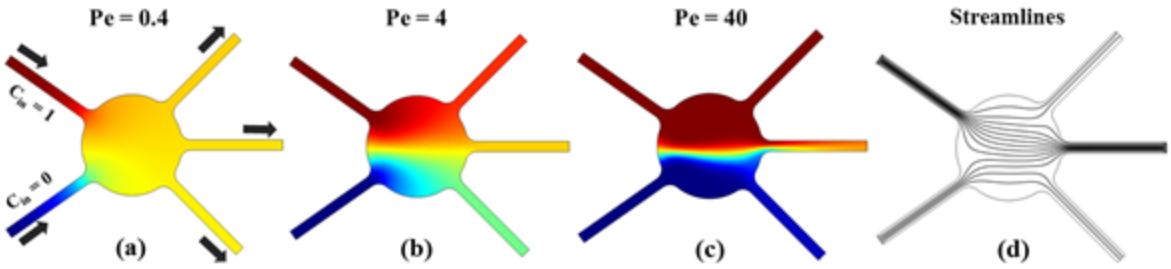


Figure 3.1: (a), (b), (c) Schematic of steady state concentration fields for a typical pore at three different Peclet numbers. Inlet/outlet flow directions as well as inlet concentrations are annotated. (d) Streamline field obtained from flow equation.

One of the more common direct modeling approaches for simulating transport in pore networks (or voxelized media) is particle tracking (PT) (e.g. Bruderer et al., 2001; Bijeljic et al., 2004, 2007). In this method, (given the velocity field) transport is simulated by tracking individual solute particles, which consists of a deterministic advection step followed by a stochastic diffusion step. Within the throats the particles have a well-defined advection path, as velocity profiles are straightforward to compute (especially for simple geometries). However, difficulties arise when particles arrive at the pores. One typical approach (e.g. Bijeljic et al., 2004) is that depending on the arrival mechanism (advection/diffusion), either a "complete mixing" or a "stream-tube routing" method is employed. If particles arrive via diffusion, they are assigned to a new throat based on an area-weighted probability (i.e. "complete mixing"). And if they arrive via advection, they are assigned (only to outflowing throats) based on a flow rate-weighted probability (i.e. "stream-tube routing"). This means that the probability of assignment to an outflowing throat $o$ is given by eq. 3.1. It is shown, in section 3.2.3.2, that "stream-tube routing" in PT is equivalent to "perfect mixing" in MCM and, therefore, limited. Another approach is taken by Bruderer et al. (2001) and Jha et al. (2011) who recognized the importance of determinism of advection in pores. Bruderer et al. (2001) proposed simple rules for mapping streamlines from the inflowing to the outflowing throats of the pores in a 2D regular lattice network. Jha et al. (2011) generalized these rules for a 3D disordered pack of equal spheres, where each pore is connected to exactly 4 neighbors. However, both authors eliminated any mechanism responsible for randomness (characteristic of diffusion) within pores. Considering that fluid residence times are longer in pores than in throats, this assumption leads to the absence of a critical mechanism responsible for transverse dispersion i.e. pore-level mixing (this is discussed further in section 3.3.2). Finally, the rule-based mapping of Jha et al. (2011) are shown to

neglect important physics rendering them incorrect even for simple 2D pores. The only proper characterization of partial mixing (to our knowledge) has been that of Park and Lee (1999), who derived transit probabilities for incoming particles at fracture junctions (in a fracture network). However, since fracture intersections are essentially two-dimensional cross-shaped "pores", the equations developed by them are not applicable in 3D networks of porous media (where throats are non-planar and assume arbitrary orientations). Moreover, Park and Lee (1999) did not take into account the influence of pore walls in their mixing criterion (considered herein). It is proposed that the *streamline splitting algorithm* presented in this work could serve as a more realistic alternative to "stream tube routing" in the methodology employed by Bijeljic et al. (2004) (i.e. described above) for capturing pore-level mixing in PT.

$$P_o = \frac{|q_o|}{\sum_{k}^{outflowing} |q_k|} \tag{3.1}$$

The rest of the chapter is organized as follows: in section 3.2 we present the mathematical formulation of SSM for flow and transport and a brief account on the MCM formulation. In sections 3.31 and 3.3.2, we present verification of SSM against direct CFD simulations and validations against micromodel experiments. Finally, section 3.3.3 discusses effects of pore-level mixing on transverse dispersion in 3-D disordered granular media.

## 3.2 MODEL DEVELOPMENT

Pore-network models are comprised of an assembly of pore bodies and interconnecting pore throats. Thus the domain is naturally discretized into nodes (pores)

and bonds (throats). Such simplification of the pore-space geometry significantly reduces the computational complexity of the flow and transport equations to be solved. In the following sections we discuss the details of our pore-network model and compare to existing approaches in the literature.

### 3.2.1 The flow equation

Solving flow and transport in a network involves two steps: a) solving the flow equation to obtain the velocity field, and b) solving the transport equation using the computed velocity field. The flow equation is formulated by assuming a single pressure value per node and writing mass balance for each node (eq. 3.1). The bulk fluid is assumed to be Newtonian with creeping flow ($Re<<1$), hence the constitutive relation describing flow inside a throat is given by $q = (g/\mu)\Delta p$; where $g$ and $\mu$ are throat conductivity and viscosity, respectively. Thus, the resultant system arising from the balance equations is linear. At the pore-scale, the flow equation is typically formulated in elliptic form for typical liquids present in the subsurface, since pressure pulses generally have negligible effects at small domain sizes. Therefore, we have assumed that the fluid of interest is incompressible. In the following mass balance, $p_i$ is pressure at pore $i$, $\mu$ is fluid viscosity, $g_{ij}$ is the conductivity of the throat connecting pore $i$ to $j$ and $N_i^{th}$ is the number of throats connected to pore $i$ (i.e. coordination number):

$$\sum_{j=1}^{N_i^{th}} \frac{g_{ij}}{\mu} \Delta p_{ij} = 0 \quad on \ \ \Omega_p \tag{3.2}$$

The resulting linear system of equations (i.e. eq. 3.1) is solved using the `mldivide` routine in MATLAB which attempts Cholesky factorization for the resultant symmetric positive definite system.

### 3.2.2 The traditional mixed cell method (MCM)

The transport equation (also known as the advection-diffusion-reaction (ADR) equation) for a pore network is traditionally written by imposing a species mass balance per node. Such formulation assumes a single concentration value per node, which is equivalent to assuming perfect mixing at the pores. However, this may not hold at moderate to high Peclet numbers which could give rise to high concentration gradients within a node. In the following MCM formulation of species balance for node $i$ (eq. 3.3), $V_p$ is the pore volume, $c_i$ the pore concentration, $D_m$ the molecular diffusivity, $R(c_i)$ the reaction term and $q_{ij}$ , $l_{ij}$ and $a_{ij}$ are the flow rate, length and cross-sectional area of the throat connecting pore $i$ to $j$, respectively. The throat flow rates come from solving the flow equation (eq. 3.2) and the throat cross-sectional areas are calculated by assuming cylindrical tubes with equivalent throat conductivities.

$$V_{p_i}\frac{dc_i}{dt} = \sum_{j=1}^{N_i^{th},q<0} c_i q_{ij} + \sum_{j=1}^{N_i^{th},q>0} c_j q_{ij} + \sum_{j=1}^{N_i^{th}} D_m a_{ij}\frac{\Delta c_{ij}}{l_{ij}} + R(c_i) \tag{3.3}$$

The reaction term is ignored here since, in this chapter, we are merely interested in the pore-level competition between diffusion and advection. In eq. 3.3, we have deterred from discretizing the time derivative for the benefit of using an adaptive time-stepping ODE solver. The transport equation (eq. 3.3) is solved using the adaptive time

stepping `ode23tb` solver in MATLAB which is an implementation of TR-BDF2, an Implicit Runge-Kutta formula.

### 3.2.3 The streamline splitting method (SSM)

The *streamline splitting method* (SSM) is based on an *a priori* estimate of how the streamlines of an inflowing throat distribute among the outflowing throats of a pore. In particular, the inflowing stream is split into several portions, each of which enters one of the outflowing throats. Subsequent to "splitting" the streamlines, a species balance is written on each inflowing stream. Each stream is assumed to occupy a separate compartment within the pore, which we refer to as a "pocket". Pockets consist of only one inlet (the inflowing throat) and several outlets (equal to the number of outflowing throats). Pockets within a pore are allowed to exchange mass between one another (which accounts for pore-level mixing). For this reason, SSM can be viewed as dividing the network into several interconnected sub-networks. Figure 3.2 shows an abstract schematic of the configuration of these pockets within a pore, and their connection to other neighboring pockets. Such a construct allows one to circumvent the perfect-mixing assumption in the formulation of the transport equation, which results in more accurate prediction of transverse dispersion at moderate to high Peclet numbers. In the following, we present the details of each step in the *streamline splitting method* (SSM).

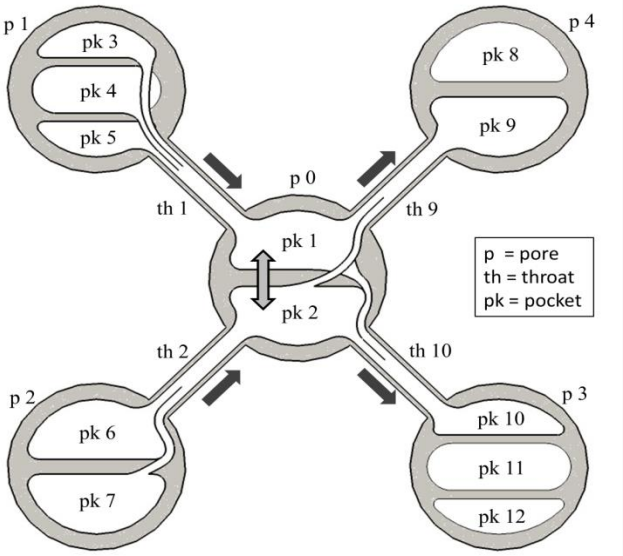


Figure 3.2: Schematic of the pockets within pore 0 in connection with the pockets inside the neighboring pores (1, 2, 3 and 4). Here, each pocket is an abstract representation of an inflowing stream (it does not represent the actual stream nor its configuration). Dark arrows indicate flow directions within throats. Note that throats have the same indices as the pockets they flow into.

#### *3.2.3.1 Streamline splitting algorithm*

The algorithm developed in this section is based on two physical principles regarding the flow field: 1) inflowing streams are conserved (sum of the split sub-streams equals the original stream), and 2) streamlines cannot intersect. It also relies on an important observation made from numerous CFD simulations on single pore geometries: the splitting of streamlines is generally independent of throat radii, velocities, pore shape and size. The splitting depends primarily on *throat orientations* and their *flow rates*. This is plausible since regardless of the origin of the inflowing streams (throat size, velocity) they all expand into a common larger space (i.e. the pore). Pore shapes also have a negligible effect in the splitting of inflowing streams. That said, the authors have

observed rare cases in which concave structures (protruding inward from the pore wall) cause the creation of vortices which promote mixing. Such occurrences are deemed rare in the typical porous media encountered in hydrology/biology/petroleum and chemical engineering (e.g. sandstones, carbonates, micro-fluidic devices, etc.). Pores are typically convex as they are larger openings connected by narrower paths.

Consider pore $p_0$ with $N$ throats connecting it to its neighboring pores; denoted by $p_k$ ($k = 1,..,N$). We assume that the flow system given by eq. 3.2 is already solved. Therefore, the total inflowing flow rate into pore $p_0$ equals the total outflowing flow rate. We identify the inflowing throats by indexing them with $i = 1$ to $N_i$ and the outflowing throats by indexing them with $o = 1$ to $N_o$ (note that $N = N_i + N_o$). Note the difference in the indexing convention compared to that used for MCM (section 3.2.2). The objective is to determine how the inflowing *stream* (or flow rate) from a throat is to be distributed among the outflowing throats. We denote the fraction of the outflowing flow rate of throat $o$, originated from the inflowing flow rate of throat $i$ by $x_{io}$ (eq. 3.4a). Let $q_i$ and $q_o$ denote the flow rates of the inflowing and outflowing throats respectively. Equations 3.4b and 3.4c must be satisfied for pore $p_0$. Equation 3.4b simply states mass balance for an inflowing stream.

$$x_{io} := \frac{|q_{i\to o}|}{|q_o|} \tag{3.4a}$$

$$|q_i| = \sum_{o=1}^{N_o} x_{io}\,|q_o| \qquad i = 1,\ldots,N_i \tag{3.4b}$$

$$\sum_{i=1}^{N_i} x_{io} = 1 \qquad o = 1,\ldots,N_o \tag{3.4c}$$

The system (i.e. eq. 3.4b and 3.4c written for all throats) consists of $N_i + N_o$ ($= N$) equations in $N_i \times N_o$ unknowns (i.e. $x_{io}$). One of these equations is redundant because

summing up eq. 3.4b over $i = 1$ to $N_i$, and combining with eq. 3.4c yields the overall mass balance equation in the pore which was assumed to hold in the first place. Therefore, the number of independent equations is $N - 1$. Depending on the total number of inflowing and outflowing throats there may exist more than one solution to this system. If $(N - 1) = (N_i \times N_o)$, the system has only one solution (in the case of one inflowing or one outflowing throat). However, if $(N - 1) < (N_i \times N_o)$, the system has more than one solution and is under-determined (the other direction for the strict inequality is not possible for a flowing pore). In this case, an optimization problem must be solved, the details of which are outlined in the following.

The optimization problem must take into account the preference of an inflowing stream towards a select subset of the outflowing throats. This is because the inflowing stream is assumed to be deflected as a result of the influence of other inflowing streams. Therefore, any inflowing stream is inclined to exit the pore through a few select throats while avoiding others. To this end, the orientation of the opposing inflowing streams needs to be taken into account (which was neglected by Jha et al., 2011). The interaction of the opposing influx on any given inflowing stream results in an imaginary *barrier* which the streamlines cannot intersect. Such a *barrier surface* (denoted by $S_{bar}$ hereafter) exists whenever two (or more) laminar streams merge or coincide. A schematic of the *barrier surface* is presented in figure 3.3a. One can certainly envision such a barrier in the streamline field given in figure 3.1d as well. In pores with large numbers of inflowing throats, the complexity of the *barrier surface* increases. However, one can account for most of the complexities using the approach outlined later in the section.

For now assume that the preferred outlets for inlet $i$ have been identified (denote them by the set $Pr_i$). Subsequently, the $x_{io}$ values corresponding to these outlets must be maximized and the $x_{io}$ values for the outlets in $Pr_i^c$ (i.e. complement of $Pr_i$) must be

minimized (for all *i*); all while satisfying eq. 3.4b and 3.4c. However, since some of the $x_{io}$ values are to be maximized and others minimized, it is difficult to define an objective function for optimization. Therefore, the $x_{io}$ values that correspond to the throats in $Pr_i$ are replaced by $(1-y_{io})$ in eq. 3.4b and 3.4c, and those for the throats in $Pr_i^c$ are simply renamed to $y_{io}$ (eq. 3.7). Now, all $y_{io}$ values can be minimized by minimizing the objective function given by eq. 3.5 constrained by the conditions given by eq. 3.6a and 3.6b. The right-hand-side constants $C_i$ and $C_i$ in eq. 3.6a and 3.6b are determined by substituting eq. 3.7 into eq. 3.4b and eq. 3.4c.

$$F(\vec{y}_{io}) := \sum_{i=1}^{N_i}\sum_{o=1}^{N_o} \omega_{io} y_{io}^2 \tag{3.5}$$

Constrained by,

$$\sum_{o=1}^{N_o} (-1)^{\beta_{io}} y_{io} \mid q_o \mid = C_i \qquad i = 1,...,N_i \tag{3.6a}$$

$$\sum_{i=1}^{N_i} (-1)^{\beta_{io}} y_{io} = C_o \qquad o = 1,...,N_o \tag{3.6b}$$

Where,

$$y_{io}(\in[0,1]) = \begin{cases} x_{io} & if \quad o \in Pr_i^c \\ 1-x_{io} & if \quad o \in Pr_i \end{cases} \qquad \beta_{io} = \begin{cases} 1 & o \in Pr_i \\ 0 & o \in Pr_i^c \end{cases} \tag{3.7}$$

The $\omega_{io}$ coefficients in eq. 3.5 are weighting factors and their significance is described at the end of the section. In this work, we use $\omega_{io} = |q_o|$ for all values of *i* and *o*. Thus, the *streamline splitting algorithm* (referred to as such hereafter) for pore $p_0$ involves solving a bounded (i.e. $0 \leq y_{io} \leq 1$) and constrained (i.e. eq. 3.6a and 3.6b) optimization problem. Here we use the `quadprog` routine in MATLAB, to perform the

optimization. Once the $y_{io}$ (and hence $x_{io}$) values are determined, an estimate of how each of the inflowing streams distributes among the outflowing throats is obtained. In the following, the process for selecting outlet throats that an inflowing stream has preferred access to (i.e. members of the set $Pr_i$), is explained.

We first differentiate between the three ways an inlet may access an outlet: a) the inlet stream is the only stream that flows into an outlet (referred to as *full access*), b) the inlet stream is not the only stream flowing into an outlet (referred to as *partial access*), and c) *limited access* which is discussed later in the section. If an inflowing stream *i* has *full access* to an outflowing throat *o*, then its corresponding $x_{io}$ value is equal to one. Consequently, the $x_{jo}$ values for any other inflowing stream *j* are equal to zero. Note that this reduces the number of unknowns in the system represented by eq. 3.6a and 3.6b and, thus, greatly simplifies the optimization problem to be solved. Considering the inflowing stream *i*, the *barrier surface* ($S_{bar}$) determines which outlets are accessible to the inlet (i.e. $\epsilon$ $Pr_i$). Namely, these are the outlets that fall on the same side of the *barrier surface* as the inlet itself. A schematic of the *barrier surface* is shown in figure 3.3a, and it can be seen that the surface can bend and twist depending on the orientation and magnitude of the outflowing streams and the opposing inflowing stream. The following procedure attempts to capture the approximate orientation of the *barrier surface*, and thus allowing us to determine the members within each $Pr_i$ set (for all *i*).

Let $u_i$ be the unit vector in the direction of inlet *i*, and $u_{op}^{\ i}$ the unit vector in the direction of its opposing inlet which is calculated using eq. 3.8a. Note that if there are more than one opposing inlets, an effective (flow rate weighted) opposing direction is computed.

$$\vec{u}_{op}^{\,i} = \frac{\sum_{\substack{k=1 \\ k\neq i}}^{N_i} |q_i| \vec{u}_k}{\| \sum_{\substack{k=1 \\ k\neq i}}^{N_i} |q_i| \vec{u}_k \|_2} \tag{3.8a}$$

$$\vec{u}_{op}^{\,i} = \frac{\sum_{\substack{k=1 \\ k\neq i}}^{N_i} \frac{q_i^2}{a_i} \vec{u}_k}{\| \sum_{\substack{k=1 \\ k\neq i}}^{N_i} \frac{q_i^2}{a_i} \vec{u}_k \|_2} \tag{3.8b}$$

Note that an alternative (and perhaps more physical) way of calculating $u_{op}{}^{i}$ is using eq. 3.8b, which corresponds to the vectorial sum of the inflowing momentum of the opposing inflowing streams ($a_i$ denotes the cross-sectional area of the inflowing throat). Throughout this chapter we have used eq. 3.8a. It was verified that the streamline splitting algorithm is quite insensitive to this choice for all cases considered herein. Thus, our results and conclusions remain unaffected.

First we introduce a few frequently-used definitions and figure 3.3 can be used as a schematic reference: we denote the centroid of pore $p_0$ with $O$ and draw $u_i$ and $u_{op}{}^{i}$ from this point. We refer to the plane that goes through the two vectors (and $O$) as the *flowing plane* and denote it by $P_{fl}$. The rays (or half-lines) that contain $O$ and are in the *opposite* directions of $u_i$ and $u_{op}{}^{i}$ are denoted by $L_i$ and $L_{op}$ respectively. The ray bisecting the angle between $L_i$ and $L_{op}$ is referred to by $L_{bi}$ (which lies also on $P_{fl}$). On the *flowing plane* $P_{fl}$, we refer to the region between $L_i$ and $L_{op}$ (where the rays build an angle less than 180°) as the *interior region* and to the region outside as the *exterior region*. We also consider two imaginary rays $L_{bar}{}^{ex}$ and $L_{bar}{}^{in}$ drawn from the center of the pore $O$ towards the *exterior* and *interior regions* respectively (also on $P_{fl}$). $L_{bar}{}^{ex}$ and $L_{bar}{}^{in}$ are used to mimic the behavior of the *barrier surface* in the *exterior* and *interior* regions respectively (for now the *barrier surface* is assumed to be perpendicular to the *flowing plane* i.e. $S_{bar}$ in fig.

3.3a). We also refer to the region between $L_{bar}^{ex}$ and $L_{bar}^{in}$ (on $P_{fl}$ and containing $L_i$) as the *territory* of inlet $i$. Finally, let the angles that $L_{bar}^{ex}$ and $L_{bar}^{in}$ make with $L_i$ be denoted by $\theta_{bar}^{ex}$ and $\theta_{bar}^{in}$ in order; and initialized to zero.

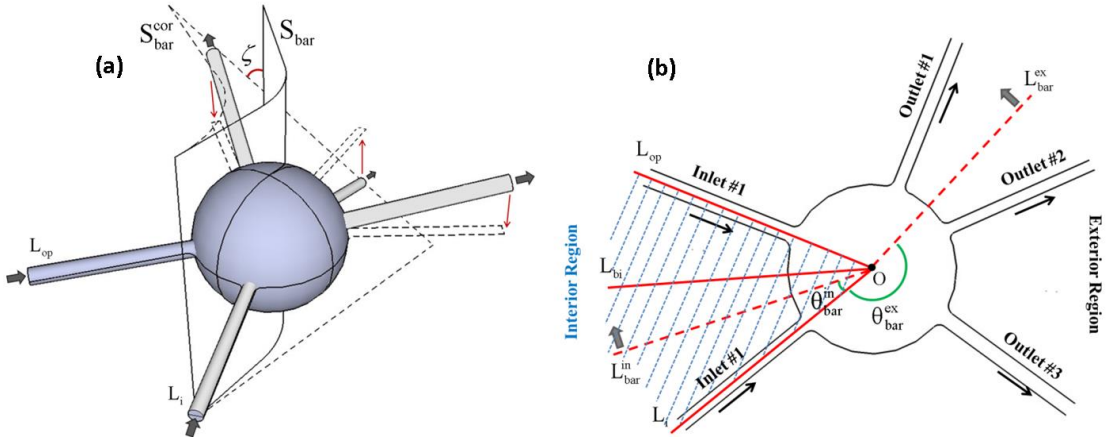


Figure 3.3: Schematic of a pore with two inflowing and three outflowing throats. (a) 3D schematic of the pore, projection of the outflowing throats onto the *flowing plane*, the *barrier surface*, and the *transverse angle* corresponding to the twisting of the *barrier surface*. (b) 2D projection of all throats on the *flowing plane* (on $P_{fl}$) with annotations of the *interior region, exterior region,* $L_i$, $L_{op}$, $L_{bi}$, $L_{bar}^{ex}$, $L_{bar}^{in}$, $\theta_{bar}^{ex}$ and $\theta_{bar}^{in}$.

The following main steps are taken to identify preferred outlets (i.e. $\epsilon\ Pr_i$) and their accessibility (*full* or *partial*) for inlet $i$ of pore $p_0$:

i) Project all outlet throats onto the *flowing plane* $P_{fl}$ (see figure 3.3a).

ii) Keep increasing both $\theta_{bar}^{ex}$ and $\theta_{bar}^{in}$ from zero (by rotating $L_{bar}^{ex}$ and $L_{bar}^{in}$) until the sum of the outlet flow rates in the *territory* of inlet $i$ exceeds (or becomes equal to) its own inflowing rate. Hereafter, we refer to this condition as *reaching overflow*.

iii) In the process of expanding the inlet's *territory* by increasing $\theta_{bar}^{ex}$ and $\theta_{bar}^{in}$, label the outlets prior to *overflow* as *full-access* outlets, and at the moment of *overflow*, as *partial-access* outlets.

The details of the algorithm used for achieving these three steps are summarized in the flowchart presented in figure A.1 (in appendix A). As mentioned earlier, once the *full-access* outlets of any inlet $i$ are identified, the optimization problem given by eq. 3.5-3.6 can be greatly simplified and reduced in unknowns. This is because if inlet $i$ has *full access* to outlet $o$, then $x_{ko}$ will be equal to one for $k = i$ and zero for all $k \neq i$. The reduced optimization problem can then be solved for (the $x_{io}$ values corresponding to) the remaining *partial-access* outlets. In short, the *streamline splitting algorithm* expands the *territory* of any given inlet $i$ until the inlet can access enough outlets that have the capacity to accommodate its inflowing rate. In the process, generally, outlets well within the inlet's *territory* are accessed *fully* and outlets that verge on the boundaries of the *barrier surface* are accessed *partially* (refer to figure A.1 for a more detailed description). The above procedure is performed for all inlets, and special notes need to be made which are discussed at the end of this section.

Finally, an inlet may additionally have *limited access* to an outlet outside its *territory*. This is only possible for 3D pores and is due to the twisting of the *barrier surface*, as shown with the dotted surface $S_{bar}^{cor}$ in figure 3.3a. In the foregoing, we had implicitly assumed that the *barrier surface* is perpendicular to the *flowing plane* and thus we were able to represent it with its projection onto $P_{fl}$; namely the half-lines $L_{bar}^{in}$ and $L_{bar}^{ex}$. However, the *barrier surface* may twist as shown in figure 3.3a by $S_{bar}^{cor}$, in which case we may need to grant *limited access* to one more outlet (along with imposing an inequality condition on the optimization as discussed next). We proceed by example:

consider the pore schematized in figure 3.3, its inlet *i* and its three outlets. Let $S_{bar}$, in this figure, be the *barrier surface* obtained from following the aforementioned three steps. From figure 3.3b, it is seen that outlets #3 and #2 are within the inlet's *territory*. However, it is possible for inlet *i* to have *limited access* to outlet #1 as well. This depends on the *transverse angle* ($\zeta$), which is the complement of the angle the plane going through outlets #1 and #2 (and *O*) makes with the *flowing plane* $P_{fl}$ (indicated in figure 3.3a). The following expresses the condition under which inlet *i* is granted *limited access* to outlet #1:

If $\zeta < 45^{\circ}$,

$$\frac{|q_1^{out}|x_{i1}}{|q_1^{out}|x_{i1}+|q_2^{out}|x_{i2}} \le M \qquad \Rightarrow \qquad (1-M)|q_1^{out}|x_{i1} \le M|q_2^{out}|x_{i2} \tag{3.9}$$

Where,

$$M = 0.5\frac{(45^o-\zeta)}{45^o} \tag{3.10}$$

Equation 3.9 states: if we consider the total amount of fluid entering outlets #2 and #1 combined, the fraction that enters outlet #1 is bounded above by $M \in [0, 0.5]$. This upper bound, *M*, depends on how far deviated the plane going through outlet #1 and #2 (and *O*) is from vertical (i.e. magnitude of $\zeta$). If $\zeta \ge 45°$, *limited access* to outlet #1 is not granted and we need not concern ourselves with this condition. However, if $\zeta < 45°$, outlet #1 will "steal" some of the fluid (originating from inlet *i*) that enters outlet #2 (i.e. due to the twisting of the *barrier surface*). The stealing is maximized when $\zeta = 0°$ (i.e. outlets #1 and #2 are on top of one another when projected onto the *flowing plane*),

where outlet #2 may lose up to half of its flow rate to outlet #1. This dependence on *transverse angle* was investigated via numerous CFD simulations and it was observed that beyond a *transverse angle* of 45° the "stealing effect" is negligible; and it is maximal at 90° (more discussion along with comparison against CFD data is provided in appendix E). One important remark is that, in this work, we only consider the stealing effect in the *exterior* and not in the *interior region*. This is because generally pores with more than one outlet in the *interior region* are rare (since flow is unidirectional in most cases). Additionally, CFD simulations showed that the stealing effect was much more pronounced in the *exterior* compared to the *interior region*.

Equations 3.9-3.10 in the example given above can be adapted to any other pore with the correct choice of outlets (instead of #1 and #2 above). See the flowchart in figure A.1 for a detailed depiction of where in the algorithm *limited accesses* are granted. Note, that once inlet $i$ is granted *limited access* to an outlet $o$, outlet $o$ belongs to the $Pr_i$ set. Thus the change of variable, given by eq. 3.7, from $x_{io}$ to $y_{io}$ is needed (both in the optimization problem and in the condition given i.e. eq. 3.5-3.6 and 3.9). Furthermore, if *limited access* is granted to any outlet the condition given by eq. 3.9 needs to be included as yet another restriction in the optimization (here we use the `quadprog` routine in MATLAB which accommodates inequality restrictions as well). Lastly, note that for a 2D pore (or pores with *transverse angles* larger than $45^o$) the condition given by eq. 3.9 is not required and the optimization problem is simpler.

We conclude this section with a few important remarks: a) *full access* to an outlet cannot be granted if another inlet has *any* kind of access to that outlet. In this case, *partial access* is granted instead. b) In the process of granting *full*, *partial* or *limited access* to an outlet, any inlets having *full access* on that outlet need to be changed to *partial access*. c) One of the additional advantages of formulating the problem as an optimization is that the

coefficients of the objective function, $\omega_{io}$, can be chosen in such a way to yield desired effects. In this work, we have chosen $\omega_{io} = |q_o|$ for all $i$ and $o$, and we demonstrate in appendix B that this leads to a flow rate-weighted distribution of the remaining influx (after subtracting the portion dedicated to *full-access* outlets, and in the absence of *limited access* outlets) among the remaining *partial-access* outlets. Other choices include $\omega_{io} = 1$ and $\omega_{io} = |q_o|^2$ (for all $i$ and $o$) in which low-flow-rate inlets have a tendency towards low-flow-rate and high-flow-rate outlets respectively. However, our choice in this work produced the best results and seemed to be the most reasonable. A verification of the methodology presented in this section against direct CFD simulations (both in 2D and 3D) is presented in section 3.3.1.

#### *3.2.3.2 Streamline splitting and particle tracking*

The foregoing streamline splitting algorithm is also very useful in a more direct (but more computationally expensive) method for solving transport in pore networks (or voxelized media) referred to as particle tracking (PT). As mentioned in section 3.1, "stream-tube routing" is what is commonly used for redistributing incoming solute particles (via the advection step) to pores. Particles are assigned to new (outflowing) throats by flow rate-weighted probabilities given by eq. 3.1. This entails that an inflowing stream distributes among outflowing throats in proportions given by eq. 3.1. Therefore, $x_{io}$ values for "stream-tube routing" are obtained as follows:

$$x_{io} = \frac{P_o |q_i|}{|q_o|} = \frac{\frac{|q_o|}{\sum_{outflowing} |q_k|} |q_i|}{|q_o|} = \frac{|q_i|}{\sum_{outflowing} |q_k|} = \frac{|q_i|}{\sum_{inflowing} |q_{k'}|} \tag{3.11}$$

The last equality in eq. 3.11 comes from the continuity of the total in/out flow rates in a pore. Note that, in "stream-tube routing", $x_{io}$ is equal to the fraction of the total inflowing rate comprised by stream *i*. This is precisely what "perfect mixing" entails: all inflowing streams are mixed within the pore in proportion to their flow rates. Furthermore, although the flow rate-weighted rule assigns more particles to outflowing throats with larger flow rates, the number of particles *per outflowing volume* remains constant. Hence, a "perfectly mixed" concentration is what exits the pore through every outflowing throat. Therefore, it is proposed that particles arriving at a pore via the advection step in PT be redistributed using the streamline splitting algorithm discussed in section 3.2.3.1, which would increase the modeling accuracy of PT in pore networks.

Bruderer et al. (2001) and Jha et al. (2011) also proposed simple streamline splitting rules. Jha et al. (2011) attempted to generalize those of Bruderer et al. (2001) for 3D pores connected to a maximum of four neighbors. However, they neglected throat orientations in developing their rules. In appendix C, we provide counter examples to these rules and demonstrate the importance of throat orientations in splitting streamlines. A comparison of the predictions made by their method and our streamline splitting algorithm vs. CFD is provided. The results show that their method is limited even for simple 2D pore geometries, while the algorithm developed herein performs considerably better.

#### *3.2.3.3 Formulation of the SSM transport equation*

Once the distribution of inflowing streams among outflowing throats (in every pore) is calculated, species balance can be written on each inflowing stream. We assume that each inflowing stream occupies a separate space within the pore, which we refer to as a "pocket". The number of pockets for a given pore is, thus, equal to the number of

inflowing streams (or throats). Therefore, each pocket has only one inlet but multiple outlets (equal to the number of outflowing throats). For this reason, we enumerate throats with the same index as the pockets they flow into (fig. 3.2). Figure 3.2 is an abstract schematic of the pockets within pore *0* connected to the pockets in the neighboring pores (i.e. pores *1, 2, 3, 4*). In this section, we proceed by example and form the species balance equation for pocket *1* of pore *0* in figure 3.2. We then provide a general species balance expression for the streamline splitting method.

In figure 3.2, pocket *1* is connected from its inlet to pockets *3*, *4* and *5* (in pore *1*), each of which has a different concentration value. However, the concentration in pocket *1* is assumed to be homogeneous. This is a sound assumption, since streamlines from the three pockets (i.e. 3, 4 and 5) must converge to pass through throat *1*. The large reduction in flow area causes an even larger reduction in the diffusion time scale. According to Einstein's equation for Brownian motion (i.e. $x^2 \propto Dt$), diffusion time reduces quadratically with reduction in diffusion distance. Therefore, it is quite reasonable to assume that contents of different pockets mix almost completely in passing through the throats (this can also be seen in the concentration fields of fig. 3.1). Using the streamline splitting algorithm of section 3.2.3.1 we know the proportion in which pocket *1* distributes among throats *9* and *10*. Moreover, note that there is mass transfer between pockets *1* and *2* as a result of concentration differences. This mass transfer is strictly diffusive, since streamlines from two pockets do not intersect. The mass transfer is taken into account as a source terms in the species balance equation. Species balance for pocket *1* can, thus, be written as follows:

$$V_1 \frac{dc_1}{dt} = (q_1 x_{3,1} c_3 + q_1 x_{4,1} c_4 + q_1 x_{5,1} c_5) - (q_9 x_{1,9} c_1 + q_{10} x_{1,10} c_1)$$
$$+ D_m (a_1 x_{3,1} \frac{c_3 - c_1}{l_1} + a_1 x_{4,1} \frac{c_4 - c_1}{l_1} + a_1 x_{5,1} \frac{c_5 - c_1}{l_1} + a_9 x_{1,9} \frac{c_9 - c_1}{l_9} + a_{10} x_{1,10} \frac{c_{10} - c_1}{l_{10}})$$
$$+ \Psi_{21}(c_2, c_1) + R(c_1) \tag{3.12}$$

$$V_1 = \frac{|q_1|}{|q_1| + |q_2|} V_p \tag{3.13}$$

In eq. 3.12-3.13, $q_k$, $a_k$ and $l_k$ are the flow rate, cross-sectional area and length of throat $k$, respectively. Concentration and volume of pocket $k$ are denoted by $c_k$ and $V_k$, respectively. $D_m$ is the molecular diffusion coefficient and $x_{io}$ (ref. section 3.2.3.1) is the fraction of the flow rate of throat $o$ that flows out of pocket $i$ (or throat $i$). $\Psi_{21}$ is the inter-pocket mass transfer rate from pocket *2* to *1*, which is a function of their concentrations. Finally, $R$ represents the (homogeneous or heterogeneous) reaction rate in pocket *1*. Throughout this chapter, $R$ is assumed to be zero.

The general form of the SSM transport equation can now be written as follows. Consider pore $p_k$ with its connecting throat indices inside the set $S_k$. We refer to its neighboring pores by $p_l$. We denote the throat connecting pores $p_k$ and $p_l$ by $t_{kl}$. To distinguish inflowing from outflowing throats we define $S_k^i$ and $S_k^o$ as the sets of inflowing and outflowing throats of pore $p_k$, respectively (note $S_k = S_k^i \cup S_k^o$). Once again, pockets are labeled with the same index as their corresponding inflowing throats i.e. $pk_{kl} = t_{kl}$ and $t_{kl} \in S_k^i$. The following (eq. 3.14) is the species balance equation for pocket $pk_{kn}$ ( $= t_{kn} \in S_k^i$) within pore $p_k$:

$$V_{pk_{kn}} \frac{dc_{pk_{kn}}}{dt} = \sum_{pk_{nm}=t_{nm}\in S_n^i} q_{t_{kn}} x_{t_{nm}t_{kn}} c_{pk_{nm}} - \sum_{pk_{kl}=t_{kl}\in S_k^o} q_{t_{kl}} x_{t_{kn}t_{kl}} c_{pk_{kn}} +$$

$$D_m \sum_{pk_{nm}=t_{nm}\in S_n^i} a_{t_{kn}} x_{t_{nm}t_{kn}} \frac{c_{pk_{nm}} - c_{pk_{kn}}}{l_{t_{kn}}} + \sum_{pk_{kl}=t_{kl}\in S_k^o} a_{t_{kl}} x_{t_{kn}t_{kl}} \frac{c_{pk_{kl}} - c_{pk_{kn}}}{l_{t_{kl}}} + \tag{3.14}$$

$$\sum_{pk_{kl}\in S_k^i \setminus pk_{kn}} \Psi_{pk_{kl}pk_{kn}}(c_{pk_{kl}}, c_{pk_{kn}}) +$$

$$R(c_{pk_{kn}}) \quad =: \quad F(\vec{c}_{pk})$$

$$V_{pk_{kn}} = \frac{|q_{t_{kn}}|}{\sum_{t_{kl}\in S_k^i} |q_{t_{kl}}|} V_{p_k} \tag{3.15}$$

Eq. 3.14 is solved using the adaptive time stepping ode23tb solver in MATLAB which is an implementation of TR-BDF2, an Implicit Runge-Kutta formula. Usually pocket sizes vary widely in a pore network, thus an explicit formulation becomes rather expensive and severely limited by time step size (i.e. the CFL condition). Therefore, an implicit formulation is of great advantage in solving the above transport problem. Finally, for no-flow throats, two pockets are assigned, one in each of the connecting pores (called *stagnant* pockets versus *flowing* pockets). If a pore contains only stagnant pockets then the volume of the pore is evenly divided among the pockets. However, if the pore contains flowing pockets as well, then an imaginary volume equal to 10% of the pore volume is assigned to the stagnant pocket, and the volume of the flowing pockets are kept unaltered. This volume is assigned so that the system resulting from eq. 3.14 is solvable. Finally, the SSM formulation typically increases the number of transport unknowns by a factor of ~2 in comparison with MCM. This is because each pore typically contains two pockets on average (this is true for both the micromodels and 3D granular media studied in section 3.3). The increase in the number of unknowns is minimal compared to the significant gain in predictive accuracy (section 3.3.2). Finally, in section 3.2.3.4 we present a condition for checking the validity of the perfect mixing assumption within

each pore. If the condition holds, no splitting of streamlines is required and a single transport unknown is sufficient for the pore. This leads to a further decrease in the number of transport unknowns and hence computational cost.

The formulation of the SSM transport equation (i.e. eq. 3.14) takes into account both the splitting of streamlines as well as the amount of pore-level mixing within the pore (via the inter-pocket mass transfer term). However, pore-level mixing is typically treated at its extremes in the literature. For instance, Bijeljic et al. (2004) use "stream-tube routing" (shown to be equivalent to perfect mixing), which is only valid at very low Peclet numbers. Whereas Bruderer et al. (2001) and Jha et al. (2011) apply rules that eliminate any mechanism responsible for randomness (characteristic of diffusion) within the pores which is valid only at very high Peclet numbers. Considering that fluid residence time is longer in pores than in throats, this assumption leads to the absence of a critical mechanism responsible for transverse dispersion i.e. pore-level mixing (discussed further in section 3.3.2). Therefore, solute particles must be allowed to switch streamlines within pores (in addition to within throats); an exact point-to-point mapping of streamlines from one throat to another (as was done by Jha et al., 2011) may not be necessary. The next section focuses on computing the mass transfer term in eq. 3.14.

#### *3.2.3.4 Inter-pocket mass transfer*

The mass transfer term $\Psi$ in eq. 3.14 can be calculated by solving something analogous to a Riemann problem for the inter-diffusion of two bounded bodies (i.e. pockets *1* and *2* in eq. 3.12). Assuming an idealized geometry (a cuboid) for the pore and the containing pockets, this term can be quantitatively approximated. The details of the

derivation can be found in appendix D. Here, we only present the final expression for $\Psi$. The average mass transfer rate from pocket 2 to 1 (i.e. $\Psi_{21}$) can, therefore, be obtained as:

$$\Psi_{21}(c_2, c_1) = -\frac{\Delta N(T)|_{x=a}}{T} \tag{3.16}$$

Where,

$$\Delta \mathrm{N(T)}|_{x=a} = [-HW\sum_{n=1}^{\infty}\frac{2L}{(n\pi)^2}\sin^2(\frac{n\pi a}{L})(e^{-(\frac{n\pi}{L})^2 D_m T} - 1)](\mathrm{c}_1 - c_2) \tag{3.17}$$

Eq. 3.16 is the rate of mass transfer between pockets 1 and 2 (within the same pore), and eq. 3.17 is the cumulative mass transferred between the two pockets in a given time (i.e. T). Eq. 3.17 is obtained from solving a bounded Riemann problem in the idealized cuboid geometry (see appendix D). In eq. 3.16 and 3.17, dimensions of the idealized pockets (i.e. $L$, $W$, $H$ and $a$) are required (see figure D.1). If an *a priori* knowledge of these parameters is known from the network and flow geometry (as is the case in section 3.3.2), then they can be used in the computations. Otherwise, one can use the following approximations:

$$\gamma = (V_p)^{1/3} \qquad W = H = \gamma \qquad L = \frac{V_1 + V_2}{\gamma^2} \qquad a = \frac{V_1}{\gamma^2} \tag{3.18}$$

In eq. 3.18, $V_1$ and $V_2$ are the pocket volumes obtained from eq. 3.13 and $V_p$ is the pore volume. It is noteworthy that simply assuming $L = \gamma$ and $a = 0.5$ (instead of eq. 3.18) did not cause a significant difference in the final results of the cases studied in this work. In eq. 3.16, $T$ is the *transport time scale* and is very important in calculating $\Psi_{21}$. Here, we only present the final expression for computing $T$, however a detailed analysis can be found in the appendix D:

$$T = \begin{cases} t_a & if \quad r \geq X \\ -\dfrac{n_1 t_a + n_2 t_d}{n_3} & if \quad X > r > Y \\ \alpha t_d & if \quad r \leq Y \end{cases} \tag{3.19}$$

Where,

$$t_a = \frac{V_p}{|Q_p|} \qquad t_d = \frac{[\min(a, L-a)]^2}{2D_m} \qquad r = \frac{t_d}{t_a}$$
$$\vec{n} = \vec{b}_1 \times \vec{b}_2 \qquad \vec{b}_1 = (1, Y, \alpha Y) \qquad \vec{b}_2 = (1, X, 1) \tag{3.20}$$

In eq. 3.19-3.20, $Q_p$ is the total flow rate through the pore, and $n_i$ is the $i^{th}$ components of the $\vec{n}$ vector. The values for $X$, $Y$, and $\alpha$ are determined through comparisons against direct pore-level simulations and were found to be 6, 0.5 and 0.1, respectively (see appendix D for details). $t_a$ is fluid residence time in the pore and $t_d$ is the time required for a Brownian particle, starting from the inter-pocket interface, to traverse the shortest of the two lateral dimensions of the pockets. Therefore, the transport time scale, $T$, varies from an advection-dominated value (i.e. $t_a$) to a diffusion-dominated one (i.e. $\alpha t_d$), and $r$ represents the competition of the two transport mechanisms within the pore. If $r \leq Y$ the pore can be safely assumed to be perfectly mixed, which could further reduce the number of transport unknown in SSM.

A remark should be made about the applicability of the current inter-pocket mass transfer term in the presence of reactions. There are two kinds of reactions that may occur within the pore space: homogeneous and heterogeneous. Homogeneous reactions occur within the bulk of the fluid and are typically instantaneous and in equilibrium at all times, whereas heterogeneous reactions occur at the mineral-fluid interface and are kinetically controlled (i.e. time dependent). Homogeneous reactions occurring within the fluid bulk

(e.g. radioactive decay) are not expected to cause large concentration gradients within the pockets and can simply be accounted for by a source term in eq. 3.14 (i.e. *R(c)*) . Homogeneous reactions that occur due to mixing of two separate species between two neighboring pockets may affect the applicability of the currently derived mass transfer term in eq. 3.16-3.17. Moreover, fast heterogeneous reactions at mineral-fluid interfaces may cause concentration gradients within individual pockets, rendering the applicability of eq. 3.16-3.17 questionable. In these cases, one can solve the appropriate local problem, similar to the Riemann problem in appendix D, and derive a modified inter-pocket mass transfer term. For heterogeneous reactions appropriate boundary conditions, as opposed to the currently used no-flux boundary conditions, at the pore walls needs to be imposed (see appendix D). Naturally approximations are inevitable in such analyses and they are currently under investigation by the authors.

## 3.3 RESULTS AND DISCUSSION

### 3.3.1 Verification of streamline splitting algorithm against direct simulation

In this section, we present examples (both in 2D and 3D) for the verification of the streamline splitting algorithm discussed in section 3.2.3.1. In particular we attempt to compare the $x_{io}$ values obtained from the streamline splitting algorithm to those obtained from direct simulations; specifically CFD modeling. For this purpose, one 2D-pore (two inlets and three outlets) with different boundary conditions and three distinct 3D-pores are considered (see fig. 3.4). Since there is no direct way of computing $x_{io}$ from direct simulations, a dummy tracer is injected through one of the inlet throats in the absence of diffusion. It should be reemphasized that diffusion must be ignored in the following CFD simulations (by assigning it a very small value) in order to be able to draw a comparison.

This is because the $x_{io}$ values only quantify the splitting of streamlines, and not the amount of intra-pore diffusion (for which $\Psi$ in eq. 3.14 is responsible). The Stokes-flow as well as the purely convective steady-state transport equations, with boundary conditions summarized in table 3.1, were then solved in COMSOL for each case. Since $x_{io}$ is dimensionless, only the relative magnitudes of the flow rates are important; thus, the boundary conditions listed in table 3.1 are presented without units. Figure 3.4 demonstrates the concentration fields obtained. The streamline fields for the 2D pore are also shown for clarity. The concentration fields show a sharp separation between the two injected fluids, that clearly delineates the boundaries of each pocket. In the presence of diffusion, this inter-pocket interface would provide a zone for mass transfer between the two fluids. The concentration fields of the dummy tracer were then used to indirectly compute $x_{io}$ for the direct simulations using the following simple equation. Here, we denote the inlet throats with and without the dummy tracer by *a* and *b*, respectively. Thus we have:

| | Throat #1 | Throat #2 | Throat #3 | Throat #4 | Throat #5 |
|---|---|---|---|---|---|
| **Case I** | $q_i = 2$<br>$c_i = 1$ | $q_i = 1$<br>$c_i = 0$ | $q_o = -1$<br>$\partial c/\partial n\|_o = 0$ | $q_o = -1$<br>$\partial c/\partial n\|_o = 0$ | $q_o = -1$<br>$\partial c/\partial n\|_o = 0$ |
| **Case II** | $q_i = 2$<br>$c_i = 1$ | $q_i = 1$<br>$c_i = 0$ | $q_o = -0.5$<br>$\partial c/\partial n\|_o = 0$ | $q_o = -2$<br>$\partial c/\partial n\|_o = 0$ | $q_o = -0.5$<br>$\partial c/\partial n\|_o = 0$ |
| **Case III** | $q_i = 2$<br>$c_i = 1$ | $q_i = 1$<br>$c_i = 0$ | $q_o = -0.5$<br>$\partial c/\partial n\|_o = 0$ | $q_o = -0.5$<br>$\partial c/\partial n\|_o = 0$ | $q_o = -2$<br>$\partial c/\partial n\|_o = 0$ |
| **Case IV** | $q_i = 1.5$<br>$c_i = 0$ | $q_o = -0.5$<br>$\partial c/\partial n\|_o = 0$ | $q_o = -0.5$<br>$\partial c/\partial n\|_o = 0$ | $q_i = 1.5$<br>$c_i = 1$ | $q_o = -2$<br>$\partial c/\partial n\|_o = 0$ |
| **Case V** | $q_i = 1$<br>$c_i = 0$ | $q_i = 1$<br>$c_i = 1$ | $q_o = -1$<br>$\partial c/\partial n\|_o = 0$ | $q_o = -1$<br>$\partial c/\partial n\|_o = 0$ | - |
| **Case VI** | $q_i = 2$<br>$c_i = 1$ | $q_i = 1$<br>$c_i = 0$ | $q_o = -1$<br>$\partial c/\partial n\|_o = 0$ | $q_o = -2$<br>$\partial c/\partial n\|_o = 0$ | - |
| **Case VII** | $q_i = 2$<br>$c_i = 0$ | $q_i = 1$<br>$c_i = 1$ | $q_o = -1$<br>$\partial c/\partial n\|_o = 0$ | $q_o = -0.5$<br>$\partial c/\partial n\|_o = 0$ | $q_o = -1.5$<br>$\partial c/\partial n\|_o = 0$ |

Table 3.1: Flow and transport boundary conditions for inlet/outlet throats of the pores depicted in figure 3.4.

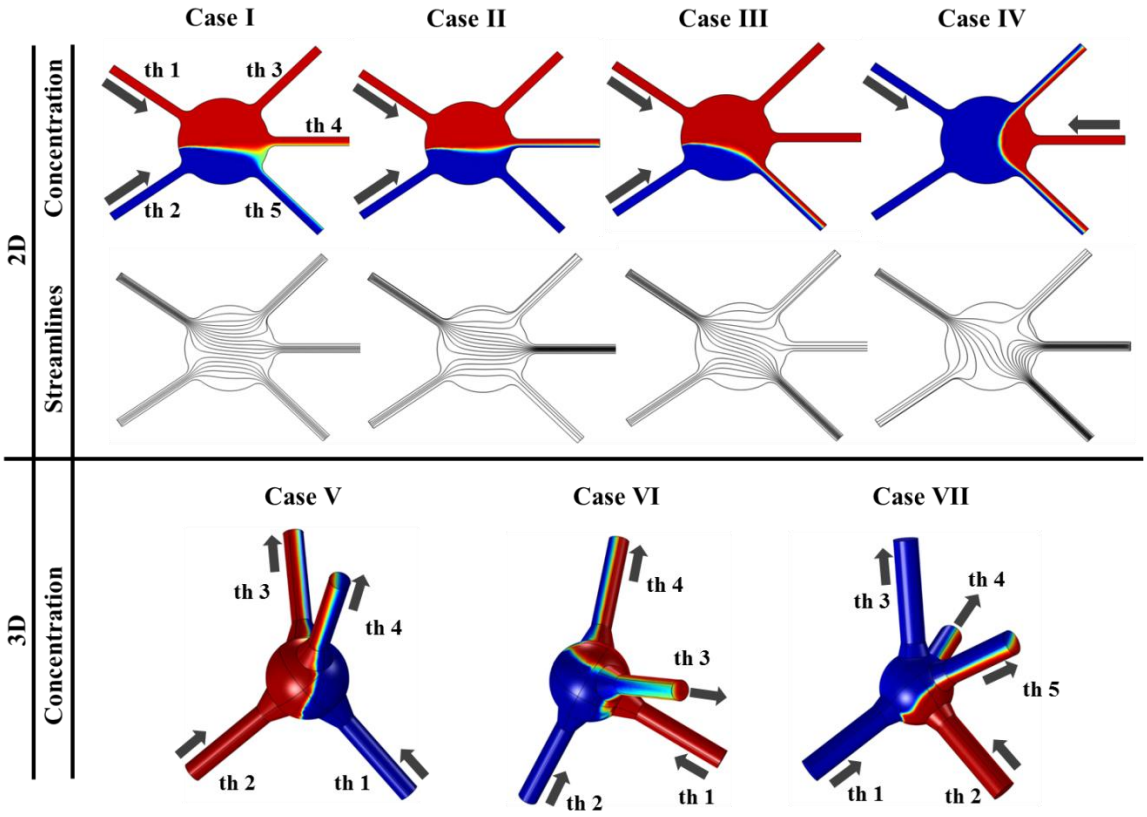


Figure 3.4: Concentration fields of a dummy tracer (injected through one inlet) obtained from COMSOL simulations on one 2D pore (different boundary conditions) and three distinct 3D pores. Inlet and outlet throats are annotated for each case and streamline fields are provided for the 2D pore only (for clarity).

$$c_a x_{ao} q_o \overset{c_a=1}{=} x_{ao} q_o = \iint_{\Gamma_o} \vec{cv} \cdot \vec{ds} \qquad \Rightarrow \qquad x_{ao} = \left| \frac{\iint_{\Gamma_o} \vec{cv} \cdot \vec{ds}}{q_o} \right| \tag{3.21}$$

Table 2 summarizes the $x_{io}$ values obtained from direct simulations (i.e. eq. 3.21), the streamline splitting algorithm (presented in section 3.2.3.1) and the "stream-tube routing" method (discussed in section 3.2.3.2). It is evident from table 2, that the predictions made by the streamline splitting algorithm are in excellent agreement with

direct simulations. Whereas, the "stream-tube routing" predictions are poor in comparison. Thus, we conclude that the streamline splitting algorithm accurately captures the realistic distribution of inflowing streamlines among outflowing throats even for relatively complex pore geometries. Lastly, it should be noted that for cases V, VI and VII the twisting of the *barrier surface* was taken into account via eq. 3.9.

| | **COMSOL simulations** | | | **Streamline Splitting** | | | **Stream-Tube Routing** | | |
|---|---|---|---|---|---|---|---|---|---|
| **Case I** | $x_{13}$ | $x_{14}$ | $x_{15}$ | $x_{13}$ | $x_{14}$ | $x_{15}$ | $x_{13}$ | $x_{14}$ | $x_{15}$ |
| | 0.98 | 0.91 | 0.05 | 1 | 1 | 0 | 0.66 | 0.66 | 0.66 |
| **Case II** | $x_{13}$ | $x_{14}$ | $x_{15}$ | $x_{13}$ | $x_{14}$ | $x_{15}$ | $x_{13}$ | $x_{14}$ | $x_{15}$ |
| | 0.98 | 0.73 | 0 | 1 | 0.75 | 0 | 0.66 | 0.66 | 0.66 |
| **Case III** | $x_{13}$ | $x_{14}$ | $x_{15}$ | $x_{13}$ | $x_{14}$ | $x_{15}$ | $x_{13}$ | $x_{14}$ | $x_{15}$ |
| | 0.98 | 0.98 | 0.48 | 1 | 1 | 0.5 | 0.66 | 0.66 | 0.66 |
| **Case IV** | $x_{42}$ | $x_{43}$ | $x_{45}$ | $x_{42}$ | $x_{43}$ | $x_{45}$ | $x_{42}$ | $x_{43}$ | $x_{45}$ |
| | 0 | 0.52 | 0.59 | 0 | 0.6 | 0.6 | 0.5 | 0.5 | 0.5 |
| **Case V** | $x_{23}$ | $x_{24}$ | - | $x_{23}$ | $x_{24}$ | - | $x_{23}$ | $x_{24}$ | - |
| | 0.67 | 0.33 | - | 0.72 | 0.28 | - | 0.5 | 0.5 | - |
| **Case VI** | $x_{13}$ | $x_{14}$ | - | $x_{13}$ | $x_{14}$ | - | $x_{13}$ | $x_{14}$ | - |
| | 0.92 | 0.54 | - | 0.9 | 0.55 | - | 0.66 | 0.66 | - |
| **Case VII** | $x_{13}$ | $x_{14}$ | $x_{15}$ | $x_{13}$ | $x_{14}$ | $x_{15}$ | $x_{13}$ | $x_{14}$ | $x_{15}$ |
| | 0 | 0.37 | 0.52 | 0 | 0.41 | 0.53 | 0.33 | 0.33 | 0.33 |

Table 3.2: $x_{io}$ values obtained from COMSOL, streamline splitting and "stream-tube routing" for the pores in figure 3.4.

### 3.3.2 Validation against micromodel experiments

In this section, we compare simulation results from SSM and MCM to data obtained from nonreactive tracer micromodel experiments, which were conducted in the Environmental Molecular Sciences Laboratory (EMSL) at the Pacific Northwest National Laboratory. The $2\times1$ $cm^2$ micromodels were manufactured in the EMSL clean room using standard photolithography and plasma dry etching techniques (Willingham et al. (2008) and Chomsurin and Werth (2003)). A general schematic of the micromodels used in the experiments is given in figure 3.5. The micromodels consist of cylindrical posts, comprising the grain space, bound between two transparent glass plates and are equipped with two inlet ports and one outlet port (fig. 3.5). During the experiments, micromodels were placed in a horizontal position and de-ionized water and an Alexa 488 dye solute were co-injected into the first and second inlet ports, respectively (fig. 3.5). After injection, the two fluids come into contact and subsequently mix inside the micromodel. The micromodels were then given enough time to reach steady state. As figure 3.9 shows, the line of contact between the two fluids grows progressively more diffuse as the fluids travel further away from the inlet towards the outlet. Transect concentration profiles of the fluorescent tracer along the 0.25, 0.5, 0.75, 1, 1.25, 1.5 and 1.75 cm lines (shown in fig. 3.5) were measured.

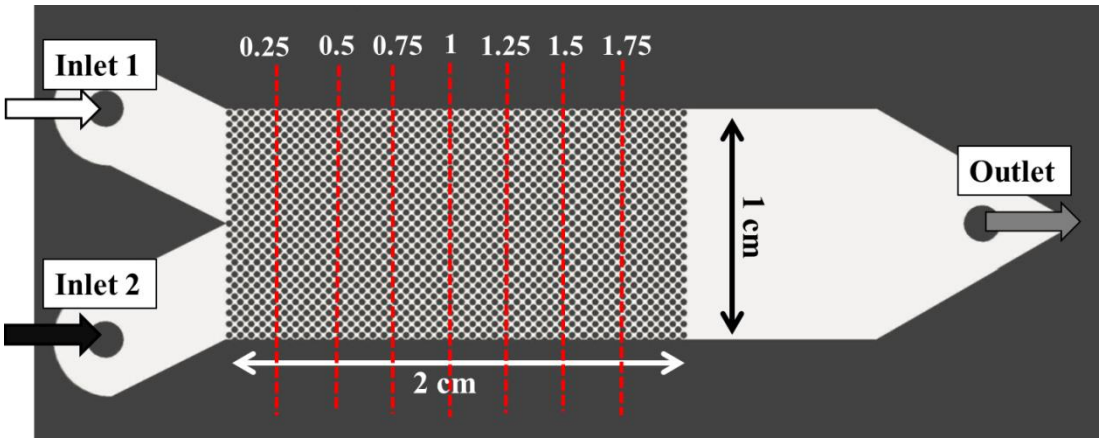


Figure 3.5: General schematic of the micromodels used in the experiments. Inlet and outlet ports are annotated and the transect lines, along which concentration profiles were obtained, are delineated.

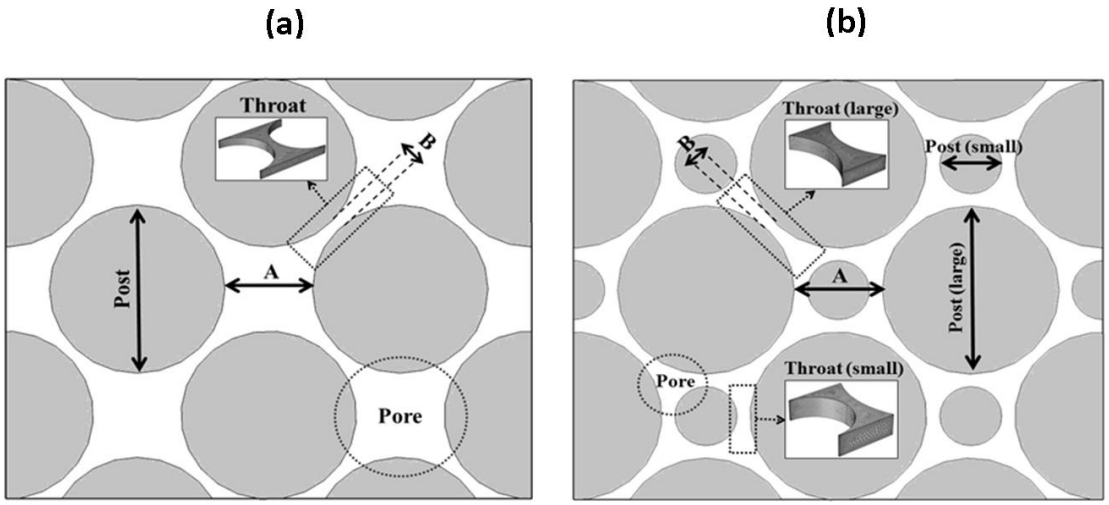


Figure 3.6: Close-up schematic of the single- and double-post micromodel structures. The pore space is divided into pores and throats. Dimensions of the micromodels are annotated.

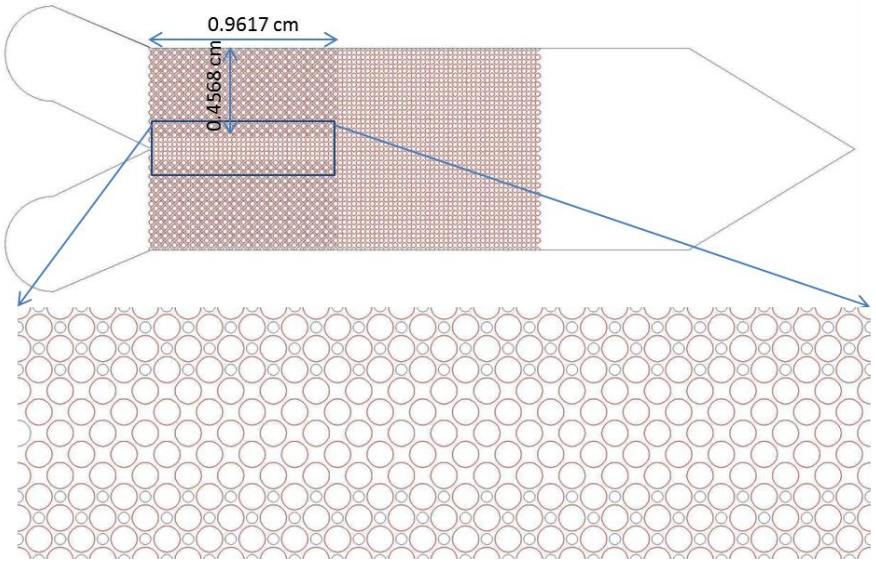


Figure 3.7: Schematic of the non-periodic (heterogeneous) micromodel used in Exp. 5 (Table 3). The single- and dual-post areas of the model are identical to the configuration used in Exp. 1 and 4, respectively.

A total of eight experiments were performed. Table 3 summarizes the details of the parameters used in each experiment. For comparison purposes, the experiments are divided into sets 1-5, based on the physical micromodel used in the experiments. The first three experimental sets are completed in periodic micromodels with a single post size, as illustrated in figure 3.6a. Experiment 4 is conducted in a periodic micromodel with two distinct post sizes (figure 3.6b). A non-periodic model (figure 3.7) is used in experiment 5.These sets were designed to focus on investigating the effects of changing (a) Darcy velocity (sets 1 and 3) , (b) grain diameter (comparison of Exp. 1a and 2), (c) aspect ratio (comparison of Exp. 1a and 3a) , and (d) heterogeneity (comparison of Exp. 1a, 4 and 5) on model predictions. The molecular diffusion coefficient of Alexa 488 in water is $4.3\times10^{-10}$ $m^2/s$ (Nitsche et al., 2004) and the viscosity of water was taken to be

1.002 *mPa.s*. In all experiments, water and Alexa 488 were injected with equal flow rates into the inlet ports 1 and 2 (see fig. 3.5).

The micromodels are divided into pores and throats as indicated in figure 3.6. The throat conductivities (i.e. $g$) were obtained by solving the Stokes equation, in COMSOL, on individual throat geometries and using $q = (g/\mu)\Delta p$. Since the micromodels have regular patterns, only one (or two in the case of Exp. 4 and 5) representative throat had to be considered. Note that the top and bottom plates of the micromodels provide additional no-slip boundary conditions in calculating throat conductivities. Once the conductivities are calculated, the flow system (eq. 3.2) can be solved to obtain the velocity field and the permeabilites of each micromodel (using Darcy's law i.e. $Q = (KA_c/\mu)(\Delta P/L)$). Subsequently, transport was simulated using both SSM and MCM until steady state was reached. Table 3 summarizes the calculated throat conductivities, and the calculated versus measured micromodel permeabilities. Note that there is good agreement between the computed and measured permeabilites. For solving the SSM transport equation, the following parameters (except for pores in the dual-post regions) were used as a result of an *a priori* knowledge of the pore/flow geometries:

$$L = W = A \qquad H = thickness \qquad a = 0.5 \tag{3.22}$$

Figure 3.8 demonstrates the simulated (MCM and SSM) and the experimental concentration profiles along the 0.5, 1 and 1.5 cm transects (concentration profiles along the 0.25, 0.75, 1.25 and 1.75 transect lines are not shown for brevity, however similar results were obtained for these lines as well). It should be noted that the "oscillations" in the experimental data are due to the fact that the concentration values over the grain space (i.e. posts) are measured as zero. On the other hand, the simulation results are

expressed in pore concentrations and the values over the grain space is interpolated. Therefore, the simulated concentration profiles appear smooth and devoid of any such "oscillations". Thus, correct comparison of the simulated results should be made against the "peaks" of the experimental data (i.e. disregarding data points inside the peak envelope).

| Exp. | Post-Diam (μm) | A – B (μm) (ref. fig. 3.6) | Thickness (μm) | Darcy Vel. ($\times 10^{-3}$ cm/s) | Porosity (%) | Cond. Calc. ($\times 10^{-12}$ cm$^3$) | Perm. Calc. ($\times 10^{-7}$ cm$^2$) | Perm. Meas. ($10^{-7}$ cm$^2$) | Peclet Num. |
|---|---|---|---|---|---|---|---|---|---|
| **1a** | 300 | 180.8-40 | 29 | 4.52 | 39.0 | 308.7 | 1.0 | 1.3 | 11.9 |
| **1b** | 300 | 180.8-40 | 29 | 45.24 | 39.0 | 308.7 | 1.0 | 1.3 | 119.0 |
| **2** | 600 | 361.7-80 | 29 | 4.52 | 39.0 | 385.5 | 1.3 | 1.5 | 14.6 |
| **3a** | 300 | 152.5-20 | 39 | 6.56 | 31.2 | 215.5 | 0.52 | 0.48 | 28.0 |
| **3b** | 300 | 152.5-20 | 39 | 0.656 | 31.2 | 215.5 | 0.52 | 0.48 | 2.8 |
| **3c** | 300 | 152.5-20 | 39 | 0.0656 | 31.2 | 215.5 | 0.52 | 0.48 | 0.28 |
| **4** | large: 300<br>small: 135 | 180.8-40 | 39 | 5.76 | 26.7 | large: 723.5<br>small: 378.0 | 0.62 | 0.59 | 13.8 |
| **5** | large: 300<br>small: 135 | 180.8-40 | 39 | 14.56 | 26.7 | large: 723.5<br>small: 378.0 | 1.0 | 0.84 | 34.9 |

Table 3.3: Summary of the experiments including micromodel parameters, calculated throat-conductivities and calculated/measured micromodel permeabilities.

Figure 3.8 shows excellent agreement between SSM simulations and the experimental data. The agreement remains very close in all sets, in which (a) Darcy

velocity (sets 1 and 3), (b) grain diameter (Exp. 1a vs. 2), (c) aspect ratio (Exp. 1a vs. 3a), and (d) heterogeneity (Exp. 1a, 4 and 5) are subject to change. The predictions cover a large range of Peclet numbers (= $vR/D_m$ where $v$, $R$ and $D_m$ are the average throat fluid velocity, average throat radius and molecular diffusion coefficient respectively) from 0.28 to 119.0 as summarized in table 3. On the other hand, predictions made by MCM are generally poor and largely over-predict transverse dispersion. This is to be expected, since the implicit perfect-mixing assumption naturally aids the dispersion of the solute in the transverse direction. MCM predictions are poorer when pore sizes are larger (leading to mixing of more fluid e.g. Exp. 2) and Peclet number is higher (>~1). The only cases in which MCM yields accurate predictions is Exp. 3c and 4. The MCM solution for Exp. 3b appears acceptable, however the two methods deviate further as the distance from the inlet increases; thus for longer domains MCM predictions would become inaccurate. Experiment 3c is in the diffusion-dominated regime (Pe ≈ 0.28), therefore the perfect-mixing assumption in MCM becomes appropriate and the two methods yield similar result. Furthermore, the agreement in Exp. 4 is merely due to the specific symmetric structure of the dual-post micromodel. The pores in this network consist of three throats (thus a maximum of one *flowing pocket*), one of which has a zero flow rate (this is the throat perpendicular to the flow direction). Transverse dispersion in this network is, therefore, solely due to diffusion through the non-flowing throats. Finally, note that in Exp. 5, MCM predictions do not even follow the correct trend of the transect concentration profiles. This is due to the fact that the single-post region of the micromodel (figure 3.6a) consists of fewer but larger pores, thus leading to more lateral mixing; whereas the dual-post region (figure 3.6b) consists of more pores per bulk volume of the micromodel, thus resulting in less lateral dispersion.

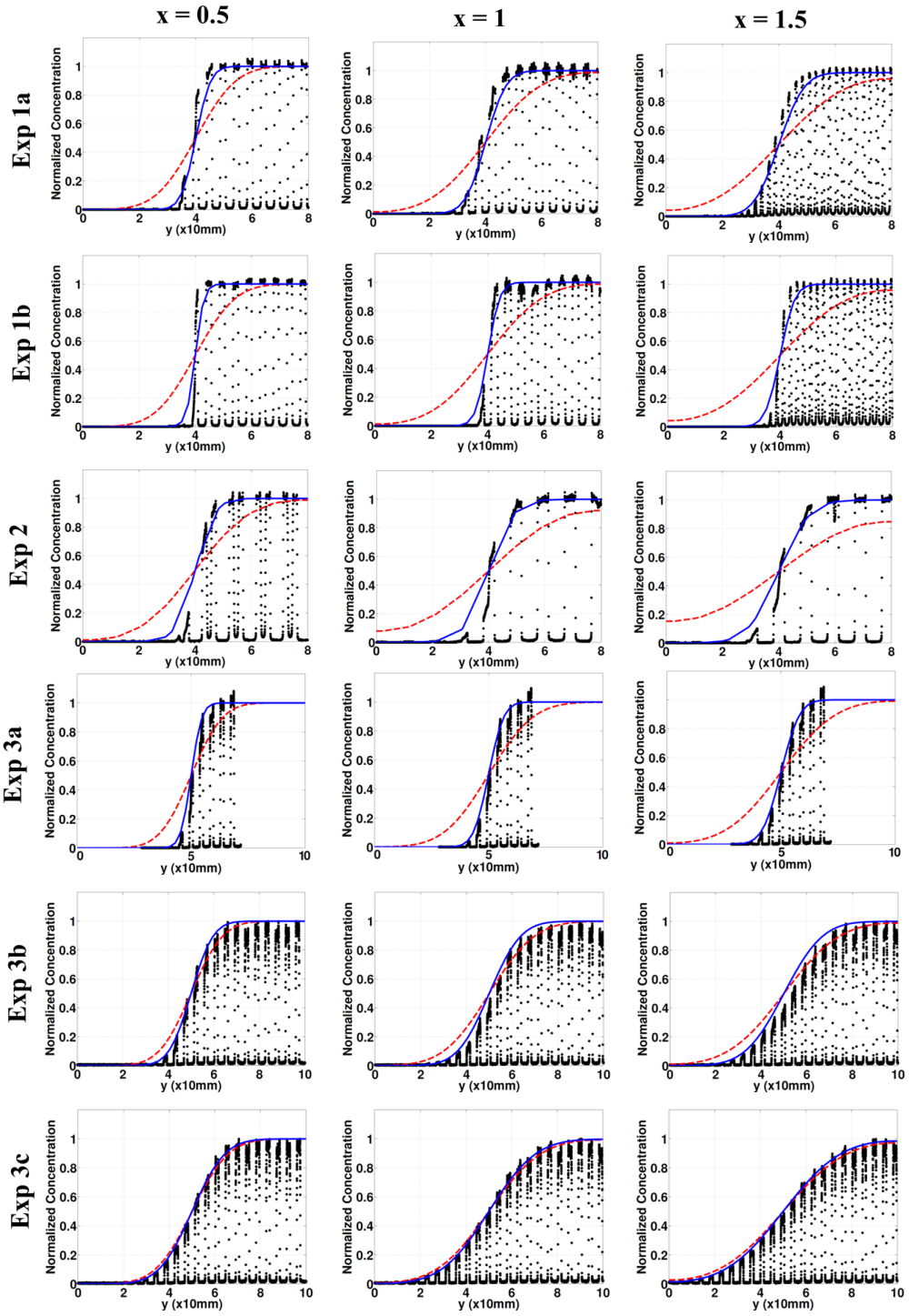


Figure 3.8: Concentration profiles along the 0.5, 1 and 1.5 cm transect lines including experimental data (dots), SSM transects (solid blue line), and MCM transects (dashed red line).

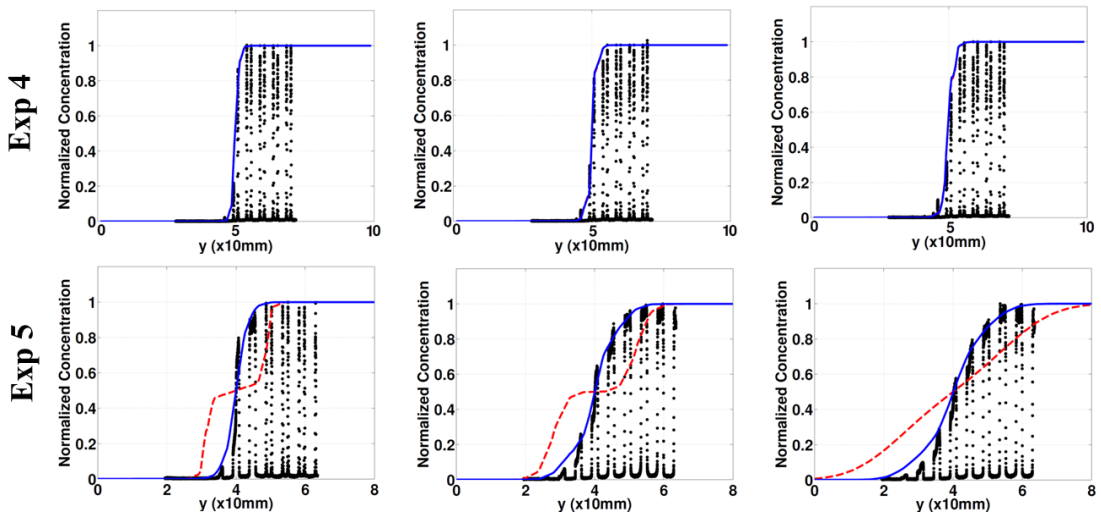


Figure 3.8: Contd.

Figure 3.9 compares 2D concentration field plots obtained from SSM and MCM for the micromodels in experiments 1b, 2, 3a and 5. These field plots also clearly show that MCM largely over-predicts transverse dispersion. Similar behavior was observed for all other experiments (except Exp. 4 and 3c where SSM and MCM results agree). It should be noted that the concentration fields appear smooth because the simulated pore concentrations were interpolated over the grain space. The ripples in the SSM concentration field of experiment 2 in figure 3.9 are not numerical artifacts and are the result of adjacent pore layers with very different concentration values. Therefore, we conclude that SSM provides a much more accurate description of solute transport (in particular transverse dispersion) than MCM which is in excellent agreement with experimental data. Finally, the number of SSM and MCM transport unknowns for each of the experiments is listed in table 4. Note that, on average, the number of SSM unknowns is ~2 times the unknowns of MCM. This is generally also true in realistic 3D granular

media as shown in section 3.3.3. It is also noteworthy that the longest SSM simulation time was ~2 minutes (for Exp. 4) which is less than any direct method known to the authors for the domain sizes considered. In closing, we would like to note that if these problems were solved via PT with pore-level rules as the ones used by Bijeljic et al. (2004) (i.e. "stream-tube routing" for the advection step and "complete mixing" for the diffusion step), the resultant predictions would have been the same as the ones obtained by MCM. Moreover, if the pore-level rules were adopted from Bruderer et al. (2001) and Jha et al. (2011), no transverse dispersion would have been observed in their corresponding predictions. This means that the current pore-level rules used in PT verge on the extremes of the pore-level Peclet spectrum and the propositions made in section 3.2.3.2 could rectify this deficiency.

| **Experiment** | **Number of MCM Unknowns** | **Number of SSM Unknowns** |
|---|---|---|
| **1a** | 1370 | 2824 |
| **1b** | 1370 | 2824 |
| **2** | 349 | 740 |
| **3a,b,c** | 1914 | 3918 |
| **4** | 6888 | 10500 |
| **5** | 4126 | 6798 |

Table 3.4: Number of SSM and MCM transport unknowns for each experiment.

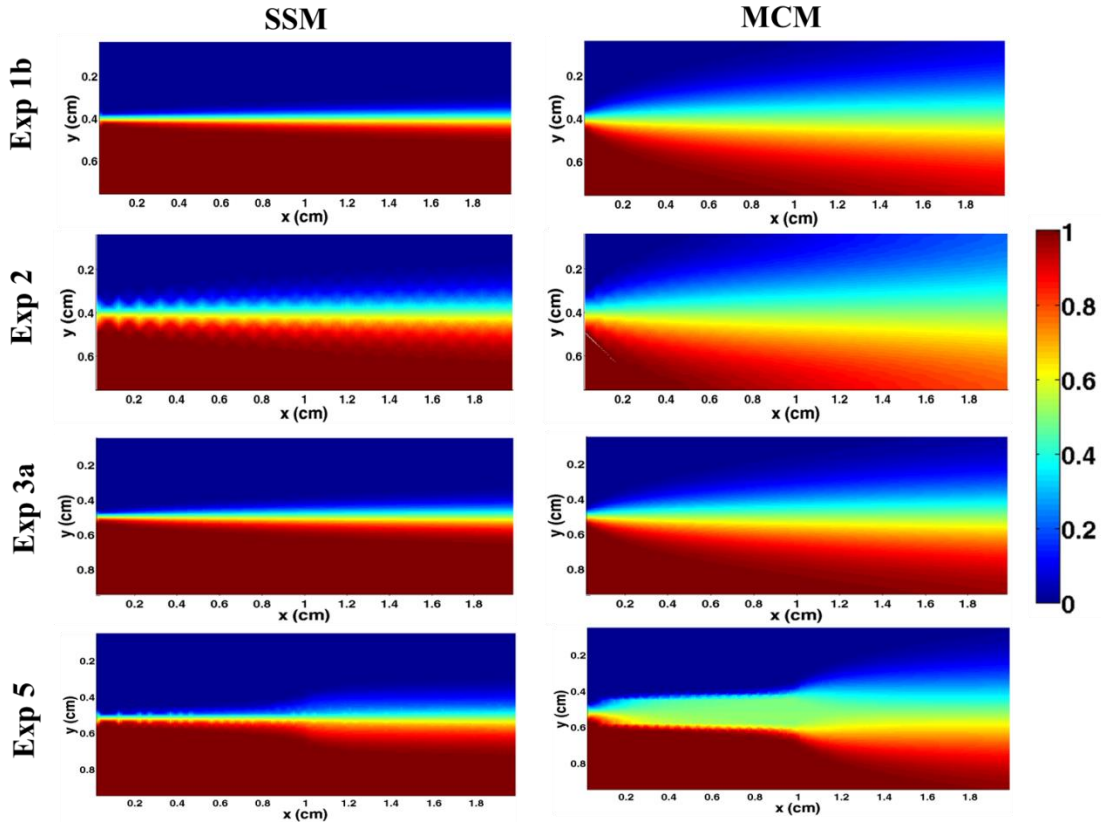


Figure 3.9: Comparison of 2D concentration fields obtained using SSM and MCM for the micromodels in experiments 1b, 2, 3a and 5. The smooth concentration fields were obtained by interpolation over the grain space.

### 3.3.3 Transverse dispersion in 3D disordered media

In this section, we examine transverse dispersion in 3D disordered granular media. Specifically, we attempt to simulate transverse dispersion at high Peclet regimes using SSM and MCM (since this is when the two methods diverge the most) in 3D disordered networks and draw comparisons between them. We utilize pore networks extracted from two different types of porous media: a) a 3D sphere pack obtained from using a collective rearrangement algorithm (Jodrey and Tory, 1985); and b) a real and

naturally occurring sandstone (Gani and Bhattacharya, 2003) imaged using X-ray computed microtomography (Thompson et al. 2008). Both networks were extracted using a modified Delaunay tessellation algorithm (Al-Raoush et al., 2003). The sphere pack consists of 4094 pores and 10184 throats with permeability and porosity of 24D and 0.38 respectively. The sandstone consists of 9463 pores and 15555 throats with permeability and porosity of 0.19D and 0.17 respectively. Both networks have dimensions of $1\times1\times1\text{mm}^3$.

In each network, the flow problem (eq. 3.2) was solved by imposing a constant pressure drop in the $x$-direction and sealing all other boundaries. For transport, the concentration at the inlet was kept at a constant value of one for $y\geq 0.5$mm and at a constant value of zero for $y<0.5$mm. At the outlet a zero-concentration-gradient boundary condition was imposed. The transport problem was then solved both using SSM and MCM until steady-state was reached. Here, we define the characteristic Peclet number by $vR/D_m$ where $v$ is the interstitial fluid velocity ($= U/\varphi$ where $U$ is Darcy velocity and $\varphi$ is porosity), $R$ is the average throat radius, and $D_m$ the molecular diffusion coefficient. The simulations were carried out at a characteristic Peclet number of ~60 for both the sphere pack and sandstone networks (which is advection-dominated). The number of transport unknowns in SSM is ~2 times the number of unknowns in MCM for both networks (i.e. sphere pack: 9949 for SSM versus 4094 for MCM; sandstone: 16486 for SSM versus 9463 for MCM). This is similar to the micromodels studied in section 3.3.2.

Figure 3.10 shows a 2D plane view of the steady state concentration fields obtained using SSM and MCM, and the difference field plots calculated via eq. 3.23. The difference field plots quantify the divergence of the two methods from one another relative to the maximum inlet concentration value (i.e. one). Figure 3.10 shows that the average difference between the two methods is ~5% and ~7% of the maximum

concentration value (i.e. one) in the sphere pack and sandstone networks, respectively (with some pores registering differences close to ~10%). Furthermore, the difference between the two methods is more pronounced in the sandstone in comparison to the sphere pack. Despite the fact that such errors could ultimately become important in obtaining transverse dispersion coefficients via upscaling for these media, the difference is nevertheless *not* substantial. Similar observations were made for different and much (up to ten times) larger sphere packs. This is contrary to the observations made for the micromodels in section 3.3.2, where the difference between the two solutions ranged from 25% to 45%. In order to explain the foregoing observation made for the 3D networks, we distinguish between six types of pores:

i) *Type I:* more than one inlet but only one outlet

ii) *Type II:* more than one outlet but only one inlet

iii) *Type III*: one inlet and one outlet

iv) *Type IV:* more than one inlet and more than one outlet with the $x_{io}$ values differing by *less* than 0.1 from the "stream-tube routing" method values

v) *Type V*: more than one inlet and more than one outlet with the $x_{io}$ values differing by *more* than 0.1 from the "stream-tube routing" method values

vi) *Type VI*: non-flowing pores i.e. flow rate in all connecting throats is equal to zero

$$difference = \frac{|\,c_{SSM} - c_{MCM}\,|}{c_{max}} \overset{c_{max}=1}{=} |\,c_{SSM} - c_{MCM}\,| \tag{3.23}$$

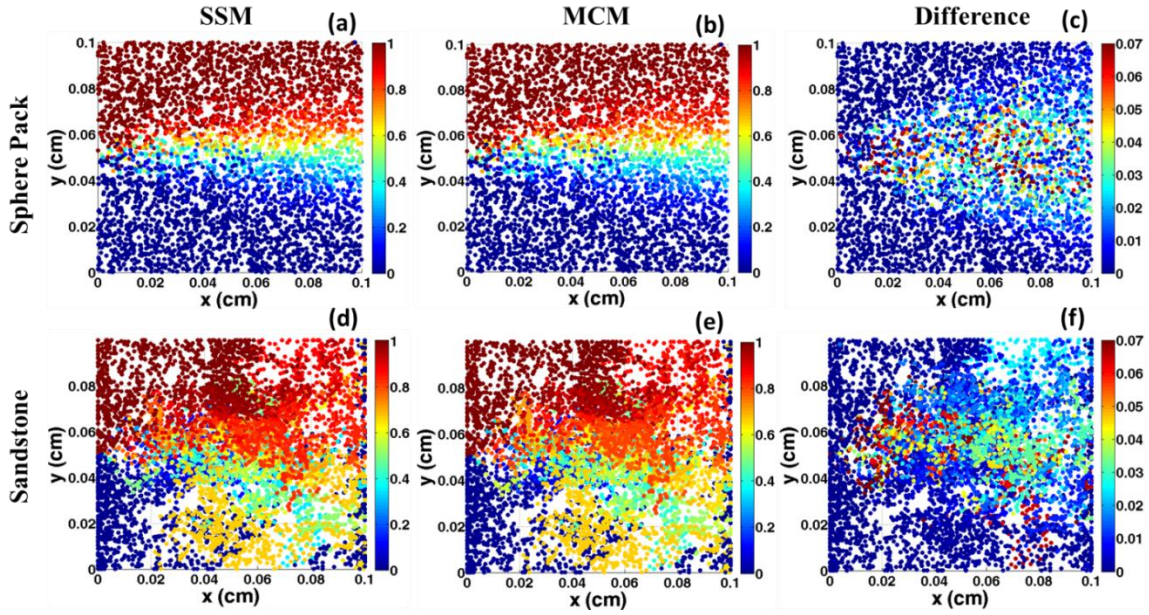


Figure 3.10: (a), (b), (d), (e) Plane view of the steady state concentration fields obtained using SSM and MCM for the sphere pack and sandstone networks. Plots (c) and (f) show the difference field plots between the two methods obtained via eq. 3.23.

Pores of type I act as mixers, in which several inlet streams converge into a single throat. The convergence reduces the diffusion distance which, in turn, causes a quadratic reduction in the diffusion time scale (via Einstein's equation) greatly enhancing diffusive mixing. Type II pores act as distributors; in other words they divide and dispense a single inflowing stream among many other throats. Type III pores simply act as transmitters of a single stream from one throat to another. Type IV pores essentially act as mixers as well because, as shown in section 3.2.3.2, "stream-tube routing" is equivalent to assuming perfect mixing in pores; where the actual mixing occurs in the outflowing throats. The 0.1 deviation of the $x_{io}$ values from the "stream-tube routing" method was chosen arbitrarily, nevertheless was considered sufficiently close for the qualitative arguments presented

next. Only pores of type V keep different inflowing streams sufficiently segregated, therefore allowing for possible differences between the two methods to emerge. Finally, Type VI pores are connected to throats with zero flow rates. Type VI pores are common in tree-type networks where large clusters of pores become off-shoots from a main flowing branch (e.g. the sandstone network is of this type as shown next). Transport in these pores is only through diffusion. Table 5 summarizes the percentage of the pores belonging to each of the aforementioned six categories for both the sphere pack and sandstone networks.

Note from table 5 that 27% of the pores in the sphere pack are of type V and the remaining 73% are mixer, distributor or transmitter pores. Additionally, all type V pores are evenly distributed across the network because the porous medium is disordered and well-connected (percentage of type VI pores is zero). Therefore, any stream flowing into a pore has only a probability of 27% for remaining segregated; which reduces geometrically if a short succession of pores is considered. Additionally, not all the pores within this 27% make equally significant contributions. Some pores have one or more inlets/outlets that carry very low flow rates, thus creating insignificant differences in the final concentration field. In the sandstone network, however, 30% of the pores are of type VI (table 5), indicating that a large number of pores belong to off-shoot clusters from a main flowing branch. To make the percentages comparable to the sphere pack network, we exclude type VI pores (table 5 second column) in our analysis. Having excluded type VI pores, we compare the recalculated sandstone percentages with that of the sphere pack. From table 5 is it evident that the two have similar percentages (except for type III and IV, which have similar combined percentages). Moreover, the percentage of type V pores in the sandstone (i.e. 33%) is only slightly higher (by 6%) than that of the sphere pack (i.e. 27%), which is partially responsible for the slightly larger discrepancy between

SSM and MCM in the sandstone (i.e. figures 3.10c and 3.10f). Another reason for this discrepancy is the special placement of type V pores within the sandstone network. Since 30% of the pores in the sandstone are non-flowing (i.e. type VI), all other pore types are located on the main flowing branch of the tree-type network; thus, influencing larger segments of the domain. Therefore, we conclude that the segregation of inflowing streams by type V pores is not effective in causing substantial differences between the SSM and MCM solutions in 3D granular media (compared to the micromodels studied in section 3.3.2). Nevertheless, these differences could still prove to be important in obtaining transverse dispersion coefficients for these media (via upscaling). We note that our conclusion corroborates very well with the findings of Park et al. (2001b), who conducted a similar study (using PT) on 2D random fractured networks (discussed in chapter 2). Despite the various differences between the two media, the conclusions appear to be the same.

| **pore type** | **sandstone (%pores)** | **sandstone type VI omitted (% pores)** | **sphere pack (% pores)** | **sphere pack flattened (% pores)** |
|---|---|---|---|---|
| **Type I** | 12 | 17 | 18 | 18 |
| **Type II** | 12 | 17 | 18 | 18 |
| **Type III** | 14 | 20 | 4 | 4 |
| **Type IV** | 9 | 13 | 33 | 7 |
| **Type V** | 23 | 33 | 27 | 53 |
| **Type VI** | 30 | - | 0 | 0 |

Table 3.5: Percentage of each pore type in the 3D granular pore networks studied.

From the foregoing observations one can categorize two dominant mixing mechanisms responsible for transverse dispersion: *pore-level mixing* (due to intra-pore mass transfer) and *structural mixing* (due to network tortuosity and structure). *Inter-pore diffusion*/*dispersion* is another mechanism but becomes only dominant at very low Peclet regimes. In the micromodels of section 3.3.2, *pore-level mixing* was the dominant mechanism, whereas in the 3D granular pore networks studied here *structural mixing* appears to be the dominant mechanism. The dominance of one mechanism over the other is a strong function of the network *structure*. In this context, there are three important components to *structure*: *connectivity*, *geometry* and *orientation*. *Connectivity* (i.e. determining the neighbors of each pore) is a graph property and is the most important morphologic parameter influencing the competition between *pore-level* and *structural mixing*. Both c*onnectivity* and *geometry* are the only structural inputs required for solving the flow equation given by eq. 3.2. The result consists of only the magnitude of the in/outflowing rates within each throat. *Orientation* determines, in addition, how the streamlines split within the pores. In order to demonstrate the effect of *orientation* on transverse dispersion, consider the feasibility of squeezing and "flattening" the sphere-pack network along its z-dimension into a two dimensional network (ignoring for now the topological/geometric possibility of doing this). Figure 3.11 compares the difference field plots obtained (via eq. 3.23) for the "flattened" and original sphere-pack networks. It is evident from figure 3.11, that *pore-level mixing* is more dominant in the "flattened" network in comparison to the original network. The average difference between SSM and MCM in the "flattened" network is ~10% versus ~5% in the original network. This is a direct consequence of altering the network *structure* by reducing randomness in its throat *orientations*. Furthermore, the very special throat *orientations* in a single pore of a 3D

granular medium (i.e. the tetrahedron configuration; similar to case V in figure 3.4) allows for the twisting of the *barrier surface* (ref. section 3.2.3.1) ultimately resulting in a reduction in the number and efficiency of type V pores. Therefore, it is the *structure* of a medium (i.e. *connectivity*, *geometry*, *orientation*) that determines the percentage and distribution of its type V pores, ultimately dictating the competition between *pore-level* and *structural mixing* for transverse dispersion. A quantitative description of this competition is currently outside the scope of this work, but a possible parameter candidate may be identified. Imagine a swarm of observer particles released from a single point at the inlet. The trajectories of these particles, in moving from the inlet towards the outlet, would be bound by a cone (particles move away from each other due to tortuosity). The rate of growth of such a cone may be an appropriate parameter for classifying porous media in terms of their dominant mixing mechanisms. The faster the aforementioned cone grows, the more *structural mixing* dominates over *pore level mixing* and vice versa. However, further study regarding this is needed.

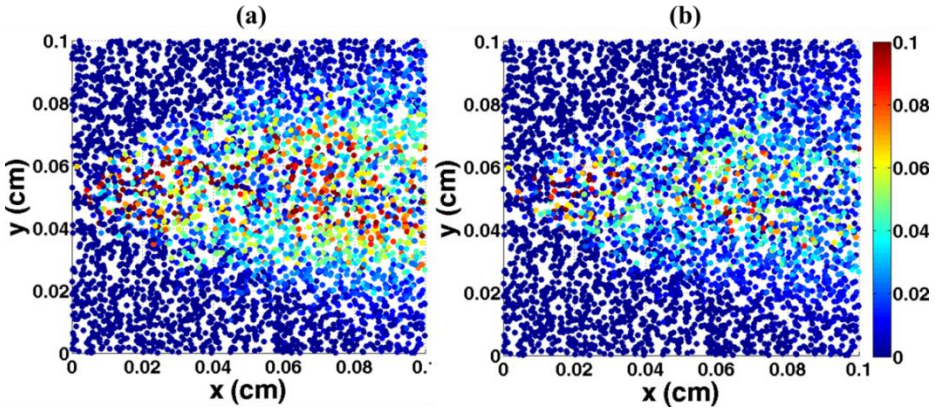


Figure 3.11: Plane view of difference field plots of the (a) "flattened" and (b) original sphere pack.

## 3.4 CONCLUSIONS

In this chapter, a novel Eulerian approach for modeling species transport in pore networks, referred to as the *streamline splitting method* (SSM), was presented. The new method lifts the limitation of the relatively simple and computationally attractive *mixed cell method* (MCM) to diffusion-dominated regimes at a minimal increase in computational cost. The following is a summary of our findings:

- The streamline splitting algorithm developed in section 3.2.3.1 was shown to be in excellent agreement with direct CFD simulations. The method was considerably more accurate than both the "stream-tube routing" method and the method proposed by Jha et al. (2011).
- The commonly used "stream-tube routing" method in PT (for redistributing solute particles at the end of the advection step) was shown to be equivalent to pore-level perfect mixing. On the other hand, the approach taken by Bruderer et al. (2001) and Jha et al. (2011) eliminates any mechanism responsible for pore-level mixing. Thus, both methods are only valid at the extremes of the Peclet spectrum. It was proposed that the streamline splitting algorithm (in section 3.2.3.1) be used instead of "stream-tube routing" in the methodology employed by Bijeljic et al. (2004). This would potentially preserve the determinism of the advection step (i.e. reversibility) while incorporating a mechanism for randomness (characteristic of diffusion).
- The *streamline splitting method* (SSM) was validated against several micromodel experiments designed to focus on investigating the effects of (a) Darcy velocity, (b) grain diameter, (c) aspect ratio, and (d) heterogeneity on model predictions. In all cases, excellent agreement was obtained against experiments. On the contrary,

MCM predictions were shown to be poor and largely over-predicting transverse dispersion except at diffusion-dominated regimes.

- The relative increase in the computational cost of SSM compared to MCM is minimal in regards to the level of accuracy gained. The difference involves a factor of ~2 increase in the number of transport unknowns and a streamline splitting step following the solution of the flow equation. The number of transport unknowns and computational cost of SSM can be further decreased *a priori* by evaluating the perfect mixing condition in each pore (i.e. $r \leq Y$; this was not done in this work) (ref. section 3.2.3.4 and 3.2.3.3). Maximum wall-clock time of all simulations (until steady state) within this work was ~4 minutes for the sandstone (with 16486 unknowns for SSM and 9463 unknowns for MCM).
- The difference between the SSM and MCM solutions was found to be insubstantial in 3D disordered granular media (i.e. sphere pack: ~5%, and sandstone: ~7% deviation relative to maximum concentration value) in comparison to the micromodels studied in section 3.3.2. This was attributed to the relatively small percentage of type V pores and their uniform distribution within these media. Nevertheless, these differences could still prove to be important in obtaining transverse dispersion coefficients for these media (via upscaling).

Two important mechanisms responsible for transverse dispersion were isolated: *pore-level mixing* and *structural mixing*. The dominance of either mechanism was attributed to three facets of the pore-space *structure*: *connectivity*, *geometry* and *orientation*. It was shown that these structural parameters affect the percentage and distribution of type V pores, ultimately dictating the importance of one mechanism over the other in various porous materials.

# Chapter 4: Pore-Scale Modeling of Longitudinal Dispersion

In this chapter, we focus on pore-scale modeling of longitudinal dispersion. Specifically, we explore the feasibility of incorporating "shear dispersion" due to non-uniform velocity profiles within throats, within the framework of an Eulerian network model. The superposing transport method (STM) developed herein, is efficient (although current limitations along with proposed solutions are discussed) and produces predictions in good agreement with experimental data from the literature. Predictive capacity of various pore network idealizations commonly used in the literature, as well as network modeling of solute transport as a whole for *ordered* media, is studied and discussed.

## 4.1 MOTIVATION

Longitudinal dispersion at the pore-scale originates from spatial variations of the velocity field at the scale of many pores as well as within individual pores. The latter is a result of the shearing of the fluid as it flows through the pore space, and we refer to it as "shear dispersion". In the context of a pore network, shear dispersion is typically thought of as the additional spreading of solute due to the non-uniform velocity profile within throats. While Lagrangian network models (e.g. particle tracking) are quite elegant in describing shear dispersion (as well as other intricacies of the transport process), they can be quite expensive computationally depending on the application (e.g. continuous injection of solute, where an increasing number of particles are required). On the other hand, they currently seem to be the only option in the literature for capturing shear dispersion in pore networks. In this chapter, we seek for an efficient alternative from an Eulerian perspective, as this allows for a description in terms of concentrations instead of discrete particle counts.

Proper incorporation of shear dispersion within an Eulerian framework is far from a trivial task. Despite few recent attempts that invoke Taylor-Aris dispersion coefficients for individual throats (Köhne et al., 2011; Li et al., 2014), it is very unlikely for local transport regimes to satisfy the ranges of applicability of the asymptotic theory. In other words, individual throats are typically far too short to accommodate asymptotic behavior (see appendix F). Such attempts are, therefore, unjustified and incorrect (as rightfully pointed out by Sorbie and Clifford, 1991). In a network model, throats must be assigned finite volumes if shear dispersion is to be properly considered, otherwise solute particles experience zero residence times in passing through them. Therefore, the most salient difficulty in formulating a transport equation becomes the determination of the solute flow rates within the throats, as the boundary conditions at their two ends are time-dependent. For *linear* transport problems, the superposing transport method (STM) developed herein, dynamically performs space-time superpositions across the network to evolve pore concentrations in time. This is the essence of STM, and section 4.2.1 details its mathematical development. In addition, we investigate the predictive capacity of various geometric/physical idealizations commonly used in pore networks, by comparison to CFD simulations. Predictive capacity of pore network modeling of solute transport as a whole for *ordered* media is also discussed.

## 4.2 MODEL DEVELOPMENT

The main focus of STM is to capture transport physics within individual throats (specifically shear dispersion) and incorporate them within the construct of a pore network. This is in contrast to SSM, where the main focus was placed on transport physics within pores (see chapter 3). This section is concerned with detailing the

mathematical development of STM. In section 4.2.2, we additionally explore the option of modifying the rather arbitrary rate expressions used in MCM.

### 4.2.1 The superposing transport method (STM)

#### *4.2.1.1 Transport within throats*

In order to perform space-time superpositions in a pore network, STM requires solute flow rates at the two ends of every throat under 0-1 and 1-0 dirichelet boundary conditions. These are the so called "elementary" solutions used in the superposition process. Figure 4.1 provides an axisymmetric depiction of this scenario for the cylindrical throat geometry considered in this work (generalizations to other geometries are discussed later in the section). To avoid confusion, we define the throat *inlet* and *outlet* on the basis of the bulk flow direction (not solute transport). We refer to the case in which the inlet and outlet concentrations are fixed at 1 and 0, respectively, as *forward transport* (i.e. fig. 4.1a), and to the case in which they are fixed at 0 and 1, respectively, as *backward transport* (i.e. fig. 4.1b). *F* and *B* are used as superscripts to denote forward and backward transport, respectively. *O* and *I* are used as superscripts to denote *solute* outflow (i.e. boundary with concentration 0) and inflow (i.e. boundary with concentration 1), respectively. *F*, *B*, *I*, and *O* are additionally used in combination to denote, for example, outflow of solute in forward transport by *FO* (i.e. outlet in fig. 4.1a), and inflow of solute in backward transport by *BI* (i.e. outlet in fig. 4.1a).

A schematic of the typical *FO*, *FI*, *BO*, and *BI* solute flow rates versus time is shown in figure 4.1c (i.e. $q_c^{FO}$, $q_c^{FI}$, $q_c^{BO}$, and $q_c^{BI}$). We note that figure 4.1c is for illustration purposes only, since even though there are gross similarities in the overall shapes of $q_c^{FO}$ vs. $q_c^{BO}$ and $q_c^{FI}$ vs. $q_c^{BI}$, important quantitative and qualitative differences

exist between them as one would naturally expect. The goal of this section is to obtain simple functional forms for $q_c^{FO}$, $q_c^{FI}$, $q_c^{BO}$, and $q_c^{BI}$.

The passive transport of a dilute solute species under laminar flow conditions of a Newtonian fluid within a cylindrical duct is described by eq. 4.1a. Additional assumptions include: isothermal flow, concentration-independent molecular diffusion coefficient, and negligible entrance effects. Eq. 4.1b represents the initial condition and eq. 4.1c-d the relevant boundary conditions for forward/backward transport.

$$\frac{\partial c}{\partial t} + V_0\left(1-\left(\frac{r}{R}\right)^2\right)\frac{\partial c}{\partial x} = D_m\left(\frac{1}{r}\frac{\partial}{\partial r}\left(r\frac{\partial c}{\partial r}\right) + \frac{\partial^2 c}{\partial x^2}\right) \tag{4.1a}$$

$$c(t=0,x,r)=0 \tag{4.1b}$$

$$\frac{\partial c}{\partial r}\Big|_{r=0}=0 \qquad \frac{\partial c}{\partial r}\Big|_{r=R}=0 \tag{4.1c}$$

$$c|_{x=0}=1 \ (or\ 0) \qquad c|_{x=L}=0 \ (or\ 1) \tag{4.1d}$$

In eq. 4.1, $c$ is the solute concentration, $V_0$ is the maximum centerline fluid velocity (a positive number), $D_m$ is the molecular diffusion coefficient, $R$ is the duct radius, and $L$ is the duct length. $x$, $r$, and $t$ denote axial, radial, and time coordinates, respectively. To work with a minimum number of free parameters, eq. 4.1 is non-dimensionalized with the following choice of non-dimensional variables (i.e. eq. 4.2):

$$\xi = \frac{r}{R} \qquad \lambda = \frac{x}{L} \qquad \tau = \frac{tV_0}{L} \qquad Pe_L = \frac{V_0 L}{D_m} \qquad \kappa = \frac{L}{R} \tag{4.2}$$

To obtain eq. 4.3:

$$\frac{\partial c}{\partial \tau} + (1-\xi^2)\frac{\partial c}{\partial \lambda} = \frac{\kappa^2}{Pe_L}\frac{1}{\xi}\frac{\partial}{\partial \xi}\left(\xi\frac{\partial c}{\partial \xi}\right) + \frac{1}{Pe_L}\frac{\partial^2 c}{\partial \lambda^2} \tag{4.3a}$$

$$c(\tau=0,\lambda,\xi)=0 \tag{4.3b}$$

$$\frac{\partial c}{\partial \xi}\Big|_{\xi=0} = 0 \qquad \frac{\partial c}{\partial \xi}\Big|_{\xi=1} = 0 \tag{4.3c}$$

$$c|_{\lambda=0} = 1 \ (or\ \ 0) \qquad c|_{\lambda=1} = 0 \ (or\ \ 1) \tag{4.3d}$$

In eq. 4.3, $Pe_L$ (Peclet number) and $\kappa$ (duct aspect ratio) are the only two parameters controlling the solution. For later convenience, we also define $Pe_R = V_0 R/D_m$. Note that both dimensional and dimensionless concentrations are denoted by $c$. This is because normalizing dimensional concentration by the boundary condition (= 1) would yield itself.

In appendix K, we derive the first (to our knowledge) semi-analytical solution to eq. 4.3, which is further applicable to scenarios with adsorption, decay, arbitrary velocity profiles and time- and radially-dependent inlet/outlet/wall boundary conditions. The unique solution method seemed to be a straightforward extension of the power-series/Frobenius methods (for ODEs) to solve PDEs with variable coefficients. However, there are limitations at early times and high Peclet numbers, due to numerical instabilities resulting from finite precision computer arithmetic. The solution also involves a numerical Laplace inversion step and obtaining the roots of a characteristic polynomial. In a pore network, where rapid computation on thousands of throats over a wide range of Peclet regimes is necessary, the solution seems ill-suited (despite being theoretically and practically useful elsewhere; see appendix K). For this reason, the development of much simpler semi-empirical solute flow rate expressions was pursued.

A total of 163 CFD simulations, using COMSOL©, were performed over a range of $Pe_R \in [0.01\text{-}30000]$ and $\kappa \in [1\text{-}20]$ on the axisymmetric computational domains depicted in figures 4.1a and 4.1b (the results extend even beyond these bounds for $Pe_R$ as discussed later). In forward transport, $q_c^{FI}$ and $q_c^{FO}$ were, respectively, recorded at the *AA'* and *BB'* transects shown in figure 4.1a. Similarly in backward transport, $q_c^{BI}$ and $q_c^{BO}$

were, respectively, recorded at *AA'* and *BB'* (fig. 4.1b). Notice that *BB'* is a distance of (1-$\varepsilon$)*L* ($\varepsilon$ = 0.95) away from the nearest boundary. Since COMSOL© uses a non-flux-conservative implementation of the finite elements method, we found noticeable errors (in violation of global mass balance) when data were recorded at the actual boundary. These errors are of higher significance in forward transport (fig. 4.1a) (where a boundary layer is formed near the outlet at high Peclet numbers) than backward transport (which effectively vanishes at high Peclet numbers). Recording solute flow rates a small distance of (1-$\varepsilon$)*L* away from the boundary seemed to circumvent this issue. Corrections were then made to the recorded $q_c^{FO}$ and $q_c^{BO}$ values to adjust them for the actual boundaries. Here we only present the final forms of the semi-empirical rate expressions and discuss some of their main properties. We defer detailed discussion regarding their derivation, parameterization, and aforementioned boundary corrections to appendix G.

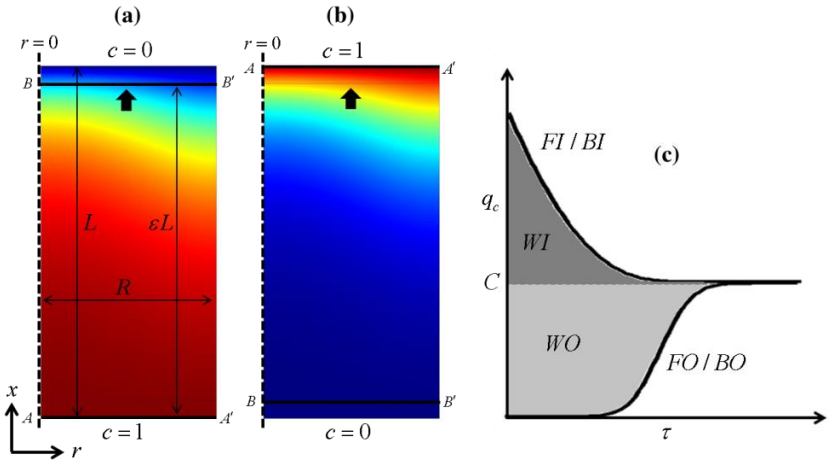


Figure 4.1: Schematic of the axisymmetric computational domain (and boundary conditions) used in the CFD simulations of (a) forward and (b) backward transport. Solute flow rates were computed at *AA'* and *BB'* transects. (a), (b) also depict steady-state concentration fields for the special case of $\kappa = 2$ and $Pe_L = 10$. (c) Schematic of typical $q_c^{FO/BO}$ and $q_c^{FI/BI}$ profiles vs. time. The area sandwiched between the two curves is annotated and is relevant in eq. 4.5 for enforcing mass conservative properties on solute rate expressions.

Solute flow rates were non-dimensionalized according to eq. 4.4 ($v = V_0(1-(r/R)^2)$ and $q_c^{flx}$ is the solute flux).

$$q_{cd} = \frac{q_c}{2\pi R^2 V_0} \qquad q_c = 2\pi \int_0^R q_c^{flx} r dr \qquad q_c^{flx} = vc - D_m \frac{\partial c}{\partial x} \tag{4.4}$$

One of the most important criteria the rate expressions must satisfy is mass conservation. This is expressed in non-dimensional form by eq. 4.5a (which applies for both forward and backward transport).

$$\int_0^\infty (q_{cd}^I - q_{cd}^O) d\tilde{\tau} = \frac{\overline{c}_{ss}}{2} \tag{4.5a}$$

$$\underbrace{\int_0^\infty (q_{cd}^I - C) d\tilde{\tau}}_{WI} + \underbrace{\int_0^\infty (C - q_{cd}^O) d\tilde{\tau}}_{WO} = \frac{\overline{c}_{ss}}{2} \tag{4.5b}$$

In eq. 4.5a, $c_{ss}$ denotes the volume-averaged steady-state concentration of the portion of the duct between the axial positions where $q_{cd}^I$ and $q_{cd}^O$ are measured (this can be either between the inlet and the outlet, or between *AA'* and *BB'*). For eq. 4.5a to hold, the time variable must be non-dimensionalized with the distance between these two axial positions (see appendix G.4). Since the integral on the LHS of eq. 4.5a is finite, we can split it into *WI* and *WO* as shown in eq. 4.5b. In eq. 4.5b, *C* is the dimensionless steady-state solute flow rate. A visual schematic of eq. 4.5b is provided in figure 4.1c, where *WI* and *WO* correspond to the shaded areas and *C* corresponds to the horizontal line separating them. For forward transport, figure 4.1c bears familiar similarities to Danckwerts's (1953) analysis in his classic paper on residence time distributions. Note that if the duct boundaries are closed to diffusion (i.e. Dankwerts boundary conditions), then $WI^F = 0$ and $c_{ss}^F = 1$. This corresponds to the situation studied by Danckwerts. If the boundaries are open to diffusion, then $WI^F \to 0$ and $WO^F \to 0.5$ as $Pe_R \to \infty$ (since $c_{ss}^F \to 1$).

For backwards transport $WI^B$, $WO^B$, and $c_{ss}{}^B$ all approach 0 as $Pe_R \rightarrow \infty$ . Eq. 4.5b is used to enforce mass conservative properties on the semi-empirical rate expressions by constraining their parameters. These expressions are given below by eq. 4.6:

$$q_{cd}^{FO} = C^F \left[ \underbrace{\frac{1}{2}\left(erf\left(a^F \log(\tau) + b^F\right) + 1\right)}_{Pe_R \rightarrow 0} e^{-Pe_R d} + H(\tau - 1) \underbrace{\left(1 - \frac{1}{\tau^2}\right)}_{Pe_R \rightarrow \infty} \left(1 - e^{-Pe_R d}\right) \right] \quad (4.6a)$$

$$q_{cd}^{BO} = \frac{C^B}{2}\left(erf\left(a^B \log(\tau) + b^B\right) + 1\right) \quad (4.6b)$$

$$q_{cd}^{FI} = \frac{A^F e^{-D\tau/\varepsilon}}{\sqrt{Pe_L \tau}} + C^F \quad (4.6c)$$

$$q_{cd}^{BI} = \frac{A^B e^{-D\tau/\varepsilon}}{\sqrt{Pe_L \tau}} + C^B \quad (4.6d)$$

Where,

$$a^F = a_1\left(\log(\varepsilon(\kappa - 1) + 10) - 1\right) e^{-\frac{(\log(Pe_R) - a_2)^2}{a_3 \ln(\varepsilon\kappa) + a_4}} + a_5 \qquad a^B = a_5 \quad (4.7a)$$

$$C^F = \frac{1}{2Pe_L}\left(\frac{1}{1 + C_1 Pe_L^{C_2} + C_3 Pe_L^{C_4}}\right) + \frac{1}{4} \qquad C^B = C^F - \frac{1}{4} \quad (4.7b)$$

$$d = e^{d_1(\varepsilon\kappa - d_2)} + d_3 \qquad D = e^{D_1(\log(\varepsilon Pe_L) - D_2)} + D_3 \quad (4.7c)$$

In eq. 4.6a, $H(x)$ is the Heaviside function. Parameters with numbered subscripts in eq. 4.7a-c are fitting constants and are summarized in table 4.1. The parameters $A^F$, $A^B$, $b^F$, and $b^B$ are obtained indirectly by combining the correlations given in eq. 4.8:

$$WO_p^F = \mu_1 erf\left(\mu_2 \log(\varepsilon Pe_L) + \mu_3\right) + \left(0.5 - \mu_1\right) \qquad \forall Pe_R \quad (4.8a)$$

$$WO_p^B = \frac{\eta_1}{2}\left(erf\left(\eta_2 \log(\varepsilon Pe_L) + \eta_3\right) + 1\right) \qquad \forall Pe_R \quad (4.8b)$$

$$\bar{c}_{ss,p}^F = \Pi_1 erf\left(\alpha_1 \log(\varepsilon Pe_L) + \alpha_2\right) + (1 - \Pi_1) \qquad Pe_R \leq 200 \quad (4.8c)$$

$$(\bar{c}^F_{ss,f} - \varepsilon\bar{c}^F_{ss,p}) = \Pi_2 erf\left(\beta_1 \log(\varepsilon Pe_L) + \beta_2\right) + (\Pi_2 + \Pi_3) \qquad Pe_R \le 200 \qquad (4.8d)$$

$$(\bar{c}^B_{ss,f} - \varepsilon\bar{c}^B_{ss,p}) = \Pi_4 erf\left(\gamma_1 \log(\varepsilon Pe_L) + \gamma_2\right) + (\Pi_4 + \Pi_3) \qquad Pe_R \le 200 \qquad (4.8e)$$

$$\bar{c}^F_{ss,f} = 1 - \frac{\Pi_5}{\kappa Pe_R} \qquad \bar{c}^F_{ss,p} = 1 \qquad \bar{c}^B_{ss,p} = \frac{\Pi_5}{\varepsilon\kappa Pe_R} \qquad Pe_R > 200 \qquad (4.8f)$$

$$\bar{c}^B_{ss,f} = 1 - \bar{c}^F_{ss,f} \qquad \forall Pe_R \qquad (4.8g)$$

With the mass balance constraint of eq. 4.5b, to obtain eq. 4.9:

$$A^F = \frac{\sqrt{\varepsilon Pe_L D}}{\Gamma(0.5)} WI^F_p \qquad A^B = \frac{\sqrt{\varepsilon Pe_L D}}{\Gamma(0.5)} WI^B_p \qquad (4.9a)$$

$$b^F = (-\varsigma a^F)\left( Pe_R d + \ln\left( \frac{WO^F_f}{C^F} - 2(1 - e^{-Pe_R d}) \right) - \frac{1}{(2\varsigma a^F)^2} \right) \qquad (4.9b)$$

$$b^B = (-\varsigma a^B)\left( \ln\left( \frac{WO^B_f}{C^B} \right) - \frac{1}{(2\varsigma a^B)^2} \right) \qquad (4.9c)$$

Where,

$$\begin{aligned} WI^F_p &= \max\left\{ \frac{\bar{c}^F_{ss,p}}{2} - WO^F_p, 0 \right\} \qquad & WO^F_f &= \frac{\bar{c}^F_{ss,f}}{2} - \varepsilon WI^F_p \\ WI^B_p &= \max\left\{ \frac{\bar{c}^B_{ss,p}}{2} - WO^B_p, 0 \right\} \qquad & WO^B_f &= \frac{\bar{c}^B_{ss,f}}{2} - \varepsilon WI^B_p \end{aligned} \qquad (4.10)$$

Lower case Greek letters with numbered subscripts in eq. 4.8 are fitting constants, whereas $\Pi_i$ $\forall i \in$ [1-6] are theoretical constants; both summarized in table 4.1. In eq. 4.9, $\varsigma$ = log (e) (i.e. the logarithm of the Euler number). For $Pe_R \le 200$, $c_{ss,f}{}^F$ and $c_{ss,p}{}^B$ can be calculated using eq. 4.8c-e in combination. The interested reader is referred to appendix G for a detailed discussion on the formulation of the above equations.

The expression for $q_{cd}{}^{FO}$ (i.e. eq. 4.6a) consists of a diffusion-dominated part and an advection-dominated part, which are weighted by an exponential factor. The first is

merely a proposed correlation, whereas the latter is the exact traveling-wave solution for the pure-advection transport problem in a cylindrical duct i.e. $(1\text{-}1/\tau^2)$.

| $WO^F_p$ | | | $WO^B_p$ | | |
|---|---|---|---|---|---|
| $\mu_1$ | $\mu_2$ | $\mu_3$ | $\eta_1$ | $\eta_2$ | $\eta_3$ |
| 2.04e-1 | 1.33 | -1.21 | 8.49e-2 | -1.59 | 5.04e-1 |
| $c^F_{ss,p}$ | | $c^F_{ss,f} - \varepsilon c^F_{ss,p}$ | | $c^B_{ss,f} - \varepsilon c^B_{ss,p}$ | |
| $\alpha_1$ | $\alpha_2$ | $\beta_1$ | $\beta_2$ | $\gamma_1$ | $\gamma_2$ |
| 1.32 | -1.01 | 1.02 | -1.90 | 1.42 | -0.54 |

| $\Pi_1$ | $\Pi_2$ | $\Pi_3$ | $\Pi_4$ | $\Pi_5$ |
|---|---|---|---|---|
| 2.375e-1 | 2.44e-2 | 1.25e-3 | -6.25e-4 | 1.98 |

| $a^F / a^B$ | | | | |
|---|---|---|---|---|
| $a_1$ | $a_2$ | $a_3$ | $a_4$ | $a_5$ |
| 15.51 | 1.18 | 2.29e-1 | 1.06e-1 | 2.75 |

| $C^F$ | | | |
|---|---|---|---|
| $C_1$ | $C_2$ | $C_3$ | $C_4$ |
| 3.58e-1 | 1.40 | 2.63e-9 | 9.83 |

| $d$ | | | $D$ | | |
|---|---|---|---|---|---|
| $d_1$ | $d_2$ | $d_3$ | $D_1$ | $D_2$ | $D_3$ |
| -3.44e-1 | -12.39 | 5.16e-4 | -2.44 | 0.70 | 2.56 |

Table 4.1: Summary of fitting parameters and theoretical constants in eq. 4.7-8.

At low Peclet numbers, $q_{cd}^{FO}$ and $q_{cd}^{BO}$ correlate extremely well with the error function on a semi-logarithmic (surprisingly not linear) time axis. At high Peclet numbers, $q_{cd}^{FO}$

transitions towards the traveling-wave solution, while $q_{cd}^{BO}$ vanishes towards zero. The expressions for $q_{cd}^{FI}$ and $q_{cd}^{BI}$ are based on the early- and late-time asymptotic analysis of appendix G.1. At high Peclet numbers, $q_{cd}^{FI}$ and $q_{cd}^{BI}$ converge to ¼ and 0, respectively. All rate expressions in eq. 4.6 additionally satisfy the mass balance constraint of eq. 4.5b.

The transitioning of $q_{cd}^{FO}$ from moderate to high Peclet regimes is shown in figure 4.2a (which also compares eq. 4.6a, the global fit, to CFD). The slope of the S-shaped profile changes from low at $Pe_R < 10$ (not shown because out of scope), to high at $Pe_R = 10$, and low again at $Pe_R = 250$ until it smoothly converges to the pure-advection solution at $Pe_R = 5000$. First, note that at $Pe_R = 250$, eq. 4.6a does not produce a sharp breakthrough as seen in the CFD data. Instead, it starts increasing rather smoothly, which is due to the exponential weighting in eq. 4.6a. Since this region is small (notice the logarithmic time axis) and, more importantly, finite in time, we expect negligible errors. Second, notice the triple inflection in the $Pe_R = 250$ profile. This corresponds to the well understood double peek (i.e. triple extrema) behavior of a traveling slug within a cylindrical duct, and is a direct result of the tight interaction between convection and radial/axial diffusion (ref. Gill and Ananthakrishnan, 1967; Yu 1979; Korenaga et al., 1989). Third, figure 4.2b shows that a mismatch, between eq. 4.6c and CFD for $q_{cd}^{FI}$, becomes apparent at $Pe_R \geq 10$. Since the early-time behavior of the CFD data does not corroborate with the exact asymptotic analysis of appendix G.1, we ascribe this to numerical errors in the CFD simulations (finer mesh sizes, than the highest setting of the software, may have been necessary near the inlet at high $Pe_R$). Finally, eq. 4.6 provides only absolute values of the solute flow rates (and not their sign).

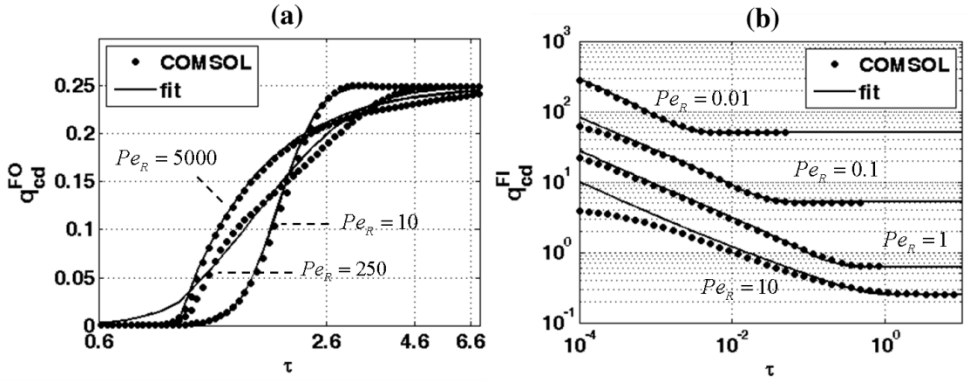


Figure 4.2: Typical (a) $q_c^{FO}$ ($\kappa = 15$), and (b) $q_c^{FI}$ ($\kappa = 1$) profiles obtained from CFD simulations and eq. 4.6 (the global fit) for various $Pe_R$.

We conclude this section with a few important remarks: a) even though the rate expressions in eq. 4.6 assume parabolic velocity profiles within throats, similar equations for plug-flow can be developed. In appendix H, we provide such expressions that treat throats as semi-infinite acting ducts. This means that, for forward transport, the zero-concentration outlet boundary is effectively moved to infinity (while $q_{cd}^{FO}$ still corresponds to a distance $L$ from the inlet). Therefore, backward transport vanishes and only forward transport needs to be considered. However, using these rate expressions in STM ignores backward diffusion from one inlet throat to the next within the same pore, which is valid only for $Pe_L > 10$ (see appendix H). To properly account for backward transport in plug-flow, one may derive semi-empirical expressions similar to eq. 4.6 (analytical solutions exist but involve series expansions that may prove to be computationally ill-suited for pore networks). b) Even though eq. 4.6-10 are based on CFD simulations for $Pe_R \in [0.01\text{-}30000]$, they can be applied for the entire range of $Pe_R$. This is because the parameters in eq. 4.7-8 satisfy appropriate asymptotes (see appendix G). The only exception is $D$, in eq. 4.7c, whose inaccuracies are, to some extent,

mitigated by eq. 4.9a for $A^F$ and $A^B$ (from the mass balance constraint of eq. 4.5b). More accurate CFD simulations could extend and improve this and other parameters in the future. While applicable in the entire range for $Pe_R$, the usage of eq. 4.6 should be strictly limited to $\kappa \in$ [1-20]. Specifically, eq. 4.6 shall *not* be used for $\kappa <1$ (due to eq. 4.7 for $a$ and $d$). c) If throats are not cylindrical, a first-level approximation would be to replace them with a cylindrical throat of the same length, cross-sectional area, and bulk flow rate (the cylinder is not hydraulically equivalent, but this is unimportant for transport). CFD simulations on square prisms for different Peclet numbers showed surprisingly negligible differences. Keeping cross-sectional area and flow rate the same ensures that steady-state solute flow rates converge to correct values at high and low Peclet limits. Such an approximation should work well for throats that are not too different from cylindrical (regular $n$-polygons with $n\geq$ 4 are thought suitable). A second-level approximation would be to replace the $(1-1/\tau^2)$ term in eq. 4.6a with the particular travelling wave solution of the non-cylindrical throat (and replacing the normalizing factor $2\pi R^2 V_0$ by $4q$ in eq. 4.4; where $q$ is the bulk flow rate through the throat). A similar approximation can be made for non-Newtonian fluids as well, as long as the corresponding traveling wave solution is known. The chemical engineering literature is replete with such "F-diagrams" (as referred to by Danckwerts, 1953) and a few practical choices can be found in Nigam and Saxena (1986), Wörner (2010), Pegoraro et al. (2012). If the fluid is too different from being Newtonian, or the duct is too different from being cylindrical, one may fit eq. 4.6 directly to CFD simulations, having replaced the $(1-1/\tau^2)$ term in eq. 4.6a with the appropriate traveling-wave solution, resulting in different values for the parameters listed in table 4.1.

#### *4.2.1.2 Formulation of the STM transport equation*

The central idea in STM is: given any, possibly time-dependent, dirichelet boundary conditions at the two ends of a throat, one may express the solute flow rate through that throat in terms of the elementary rate expressions developed in section 4.2.1.1 (i.e. a linear combination thereof), *if* the transport problem is *linear*. This is important because in a pore network, pore concentrations at the two ends of every throat change with time and can be regarded as dirichelet type boundary conditions on the throat (this seems to be the simplest and most realistic boundary condition compared to others, which typically inhibit diffusion). Once solute flow rates within throats are determined, species balance can be written for every pore. These balance equations then comprise a linear system of equations, which allow computation of pore concentrations at the next time step.

We make clear, at once, that pore-level perfect mixing is assumed in the current formulation of STM, even though methods for circumventing this assumption were developed in chapter 3. In this context, the assumption is made for two reasons: 1) pore-level mixing assumptions have little impact in disordered granular media (studied here) as demonstrated in chapter 3, and 2) it makes the problem mathematically, algorithmically, and physically more tractable and allows for the study of the macroscopic effects of shear dispersion in isolation. We note that there are no theoretical limitations against combining STM (developed here) and SSM (from chapter 3) into a single model, as the physics addressed by either do not interfere with the other and are, therefore, additive.

Assuming the flow equation is solved as discussed in section 3.2.1, the species balance equation for pore $p_i$, with volume $V_{pi}$ can be written as eq. 4.11a. $N_{pi}^t$ is the number of throats connected to $p_i$, $t_{ij}$ denotes the throat connecting pores $p_i$ and $p_j$, and $q_{c,tij}$

is the species flow rate within $t_{ij}$. Integrating eq. 4.11a from $t^l$ to $t^{l+1}$ yields eq. 4.11b ($l$ is the time step index), where $c_{pi}^{\ l}$ and $c_{pi}^{\ l+1}$ denote concentrations of pore $p_i$ at the current and next time steps, respectively.

$$V_{p_i} \frac{dc_{p_i}}{dt} = \sum_{j=1}^{N_{p_i}^t} q_{c,t_{ij}} \tag{4.11a}$$

$$V_{p_i} (c_{p_i}^{l+1} - c_{p_i}^{l}) = \sum_{j=1}^{N_{p_i}^t} \int_{t^l}^{t^{l+1}} q_{c,t_{ij}} dt \tag{4.11b}$$

In MCM, $q_{c,tij}$ is expressed based on analogy with the finite difference method at the continuum (see eq. 3.3). It assumes zero residence time within throats, thereby excluding shear dispersion as a result of non-uniform velocity profiles at the pore scale. In STM, throats do assume finite volumes (while pores are free to assume either zero or finite volumes), which complicates a closed-form expression for $q_{c,tij}$. This is because pore concentrations at the two ends of each throat change with time, and there exists a time-lag for this change to travel from one pore to the next. For *linear* problems, STM takes advantage of the superposition principle to account for the time-dependent throat boundary conditions. The main idea consists of: 1) recording pore concentrations vs. time at predefined intervals, 2) approximating these profiles with piecewise-constant staircase functions, 3) performing superposition in time (i.e. of recorded history) and space (i.e. forward and backward transport) to approximate net solute throughput for each throat from $t^l$ to $t^{l+1}$ (i.e. integral terms on the RHS of eq. 4.11b), and 4) updating pore concentrations at the next time step via eq. 4.11b.

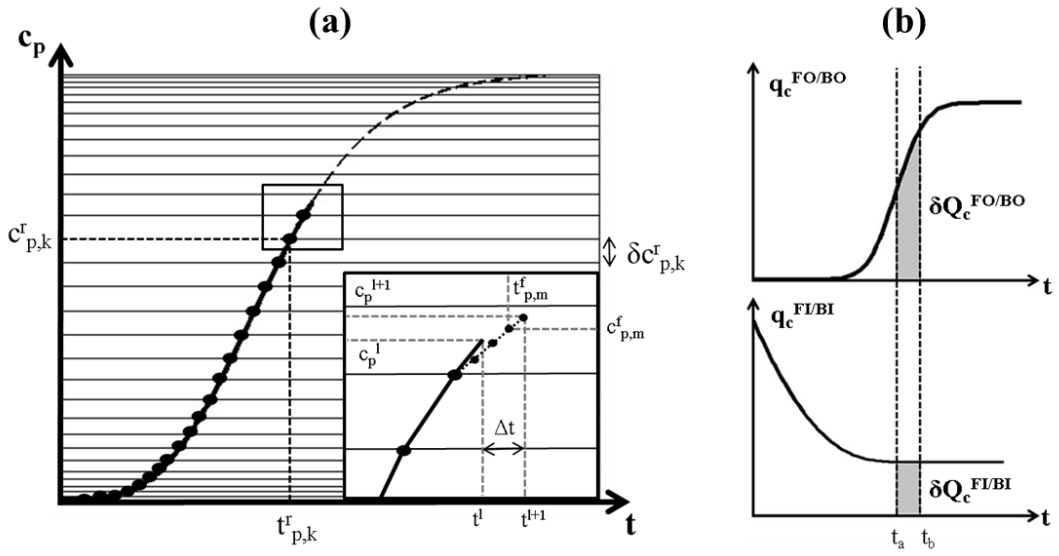


Figure 4.3: (a) Schematic of an evolving pore concentration. Annotations denote variables used in STM. Horizontal lines represent predefined values at which pore concentrations are recorded (i.e. solid dots are the recorded values). In this work, they are spaced apart according to a normal distribution. The insert depicts components used in STM for advancing pore concentrations to the next time step (via eq. 4.11b). (b) Schematic of typical $q_c^{FO}$, $q_c^{BO}$, $q_c^{FI}$, and $q_c^{BI}$ profiles, used to compute $\delta Q_c$ in eq. 4.12. $t_a$ and $t_b$ represent lower and upper integration limits in eq. 4.13d-e, respectively.

Figure 4.3a shows a schematic of a typical pore concentration profile, $c_p$, vs. time. Horizontal lines represent predefined values at which pore concentrations are recorded. The recorded points (i.e. time-concentration pairs) are depicted by black dots in figure 4.3a, which are used to update concentrations at the next time step. We denote the $k^{th}$ recorded pore concentration by $c_{p,k}^r$ and the time at which it is recorded by $t_{p,k}^r$. The total solute throughput for each throat from $t^l$ to $t^{l+1}$ can be approximated by eq. 4.12:

$$
\begin{aligned}
\int_{t^l}^{t^{l+1}} q_{c,t_{ij}}\,dt \simeq\; & H(\Delta p_{ij})\left(\sum_{k=0}^{N_{p_j}^r}\delta c_{p_j,k}^r\,\delta Q_{ct_{ij},k}^{r,FO}-\sum_{k=0}^{N_{p_i}^r}\delta c_{p_i,k}^r\,\delta Q_{ct_{ij},k}^{r,BI}\right)+ && (=RU)\\
& H(-\Delta p_{ij})\left(\sum_{k=0}^{N_{p_j}^r}\delta c_{p_j,k}^r\,\delta Q_{ct_{ij},k}^{r,BO}-\sum_{k=0}^{N_{p_i}^r}\delta c_{p_i,k}^r\,\delta Q_{ct_{ij},k}^{r,FI}\right)+ && (=RD)\\
& H(\Delta p_{ij})\left(\delta c_{p_j}^f\sum_{m=0}^{M-1}\delta Q_{ct_{ij},m}^{f,FO}-\delta c_{p_i}^f\sum_{m=0}^{M-1}\delta Q_{ct_{ij},m}^{f,BI}\right)+ && (=FU)\\
& H(-\Delta p_{ij})\left(\delta c_{p_j}^f\sum_{m=0}^{M-1}\delta Q_{ct_{ij},m}^{f,BO}-\delta c_{p_i}^f\sum_{m=0}^{M-1}\delta Q_{ct_{ij},m}^{f,FI}\right) && (=FD)
\end{aligned}
\tag{4.12}
$$

Where,

$$\Delta p_{ij} = p_j - p_i \tag{4.13a}$$

$$\delta c_{p,0}^r = c_p^{l=0} \qquad \delta c_{p,k}^r = c_{p,k}^r - c_{p,k-1}^r \qquad \forall k \in [1, N_p^r] \tag{4.13b}$$

$$\delta c_p^f = \frac{c_p^{l+1} - c_{p,N_p^r}^r}{M} \tag{4.13c}$$

$$\delta Q_{ct_{ij},k}^{r,XI} = \int_{t^l - t_{p_i,k}^r}^{t^{l+1}-t_{p_i,k}^r} q_{ct_{ij}}^{XI}\,d\tilde{t} \qquad \delta Q_{ct_{ij},k}^{r,XO} = \int_{t^l - t_{p_j,k}^r}^{t^{l+1}-t_{p_j,k}^r} q_{ct_{ij}}^{XO}\,d\tilde{t} \tag{4.13d}$$

$$\delta Q_{ct_{ij},m}^{f,XI} = \int_{\max\{t^l - t_{p_i,m}^f,0\}}^{t^{l+1}-t_{p_i,m}^f} q_{ct_{ij}}^{XI}\,d\tilde{t} \qquad \delta Q_{ct_{ij},m}^{f,XO} = \int_{\max\{t^l - t_{p_j,m}^f,0\}}^{t^{l+1}-t_{p_j,m}^f} q_{ct_{ij}}^{XO}\,d\tilde{t} \tag{4.13e}$$

In eq. 4.12, $H(x)$ is the Heaviside function, and $N_{pi}{}^r$ is the total number of recorded points for pore $p_i$ (i.e. black dots in fig. 4.3a). In eq. 4.13d-e, $X$ is a placeholder for either $F$ (i.e. forward transport) or $B$ (i.e. backward transport). The $\delta Q_c$ quantities (i.e. eq. 4.13d-e) correspond to the shaded areas depicted in figure 4.3b, and are computed by integrating the rate expressions presented in section 4.2.1.1 (i.e. eq. 4.6). Closed-form equations for these time-integrated solute flow rates are provided in appendix G.3 (by eq. G.9).

The four terms on the RHS of eq. 4.12 are denoted by *RU*, *RD*, *FU*, and *FD*, which abbreviate *recorded-upstream*, *recorded-downstream*, *forecasted-upstream*, and *forecasted-downstream*, respectively. *RU* and *RD* are contributions from the *recorded* points to the net solute throughput of throat $t_{ij}$ (i.e. black dots in fig. 4.3a). Each of the two summations in *RU* and *RD* denote superposition in time (of previously recorded points), and together they denote superposition in space (of forward and backward transport). Since the formulation of STM is fully-implicit, contributions from *forecasted* points, into the next time step, are also required (i.e. black dots in the insert of fig. 4.3a); these are the *FU* and *FD* terms in eq. 4.12. The summations in *FU* and *FD* bear similar interpretations as in *RU* and *RD*. We use superscripts *r* and *f* along with indices *k* and *m* to denote recorded and forecasted points, respectively.

The insert in figure 4.3a illustrates the procedure used for updating pore concentrations at the next time step (i.e. the forecast step). The interval between $t_{pi}^{Nr}$ and $t^{l+1}$ is subdivided into *M* forecast points (including the end points), and the concentration is assumed to vary linearly from $c_{pi}^{Nr}$ to $c_{pi}^{l+1}$. Denoting the concentration and time of each forecast point by $c_{p,m}^{f}$ and $t_{p,m}^{f}$, respectively, eq. 4.14a follows. From eq. 4.14a and 4.14b, eq. 4.13c is then readily verified.

$$c_{p,m}^{f} = \frac{c_p^{l+1} - c_{p,N_p^r}^{r}}{t^{l+1} - t_{p,N_p^r}^{r}} \left( m \frac{t^{l+1} - t_{p,N_p^r}^{r}}{M} \right) + c_{p,N_p^r}^{r} \qquad \forall m \in [1, M] \tag{4.14a}$$

$$\delta c_p^f = c_{p,m}^f - c_{p,m-1}^f \tag{4.14b}$$

In the forecast step, pore concentrations were assumed to vary linearly between $c_{pi}^{Nr}$ and $c^{l+1}$, instead of between $c^l$ and $c^{l+1}$ (see insert in fig. 4.3a). Despite the fact that $c^l$ provides a more recent point to launch the forecast step from (compared to $c_{pi}^{Nr}$), it was

found that $c^l$ had to be accounted for as a (permanently) recorded point to avoid numerical artifacts from appearing (this essentially entails the recording of every single time step, which is impractical). If time step size and recording frequency (i.e. spacing between horizontal lines in fig. 4.3a) are sufficiently refined, however, the two converge to the same solution regardless. Throughout this work, the values given in eq. 4.15a-b were used for time step size (i.e. $\Delta t$), number of forecast points (i.e. $M$), and recording frequency (i.e. $N_{max}^r$; defined as the number of horizontal lines in figure 4.3a between concentration extrema i.e. 0 and 1) unless stated otherwise. In eq. 4.15a, $V_{tij}$, $q_{tij}$, and $L_{tij}$ denote volume, flow rate, and length of throat $t_{ij}$, respectively. Eq. 4.15a is essentially one quarter of the harmonic sum of the advection and diffusion characteristic times.

$$\Delta t = t^{l+1} - t^l = \frac{1}{4}\left( \frac{1}{\min\limits_{\forall t_{ij}}\{V_{t_{ij}} / q_{t_{ij}}\}} + \frac{1}{\min\limits_{\forall t_{ij}}\{L_{t_{ij}}^2 / 2D_m\}} \right)^{-1} \tag{4.15a}$$

$$M = 20 \qquad N_{\max}^r = 1000 \tag{4.15b}$$

In this work, plug-flow within throats is modeled using the rate expressions provided in appendix H (i.e. eq. H.1). As mentioned in section 4.2.1.1, using them in STM ignores backward diffusion from one inlet to the next within the same pore. Since this is only valid when $Pe_L > 10$ within the throats, all plug-flow simulations herein are presented for sufficiently high Peclet numbers (with the exception of the 1D geometries in section 4.3.2; discussed further therein). When eq. H.1 is used, all terms in eq. 4.12 regarding backward transport (i.e. $BI$ and $BO$) shall be set to zero (everything else remains unaltered). In addition, the $\delta Q_c$ quantities (in eq. 4.13d-e) are computed via numerically integrating eq. H.1 using composite Simpson's rule (analytical integration seems not possible).

Lastly, applications of STM extend far beyond passive tracer transport at the pore scale. Examples include passive/reactive/adsorptive and/or Fickian/non-Fickian transport at the pore/core/field scale, and transmission of voltage/heat/etc. signals through interconnected electrical/conductor/etc. networks. In essence, regardless of the underlying physics, if "response functions" to elemental inputs (e.g. unit step or Dirac delta) are known for a set of bonds (e.g. eq. 4.6), the response of any network assembled thereof to any input can be computed via STM. This is what makes the method so useful and worthy of further pursuit.

#### *4.2.1.3 Current limitations and proposed solutions*

In its current formulation, STM dynamically records pore concentrations at fixed and predetermined intervals with sufficient frequency $N_{max}{}^{r}$. The intervals correspond to the horizontal lines in figure 4.3a, and the recording frequency corresponds to the spacing between them. In this work, the spacing follows a normal distribution (mean = 0.5, standard deviation = 2.8) as shown in figure 4.3a. Since the recorded concentration profiles are approximated by piecewise-constant staircase functions for time-superposition, recordings have to be more frequent near concentration extrema (i.e. 0 and 1) where profiles evolve more slowly. If not, the time-lag between two consecutively recorded points would become too large and cause noticeable numerical inaccuracies. These inaccuracies compound with the number of pores traveled by a concentration front. A similar situation arises at highly diffusion-dominated regimes, in which pore concentrations evolve very slowly altogether (i.e. not just at the extrema). We propose that a better approach might be to approximate said profiles by continuous-piecewise-linear (instead of piecewise-constant) functions. This would potentially require far fewer

recording points (i.e. less computer memory), no time-lag between consecutive recordings (i.e. higher accuracy), no need for sub-discretization of the forecast step (i.e. no need for $M$), and, thus, improve overall performance. This seems possible, as one can derive elementary rate expressions (such as eq. 4.6) for forward and backward transport under linearly varying dirichelet boundary conditions, by simply convolving eq. 4.6 with the derivative of said boundary conditions (closed-form expressions seem possible). Because no time-lag between consecutive recordings exists under such a scheme, one could additionally attempt to dynamically adapt the recording frequency to the specific shape of the evolving concentration profile (which varies with local Peclet number). For example, a new point may be recorded only if it is sufficiently divergent from the trajectory of the last linear piece of the approximated profile (otherwise the linear piece can simply be extended). Current memory requirements of STM have hindered our ability, in section 4.3.3, to simulate on very large pore networks. The above reformulation could dramatically relax this requirement, and shall be the object of future investigation.

In the displacement simulations of section 4.3.3, concentrations behind the front increase and gradually approach steady state. In the current implementation of STM, if a sufficiently long time after the last recorded point has elapsed, throats are considered to be at steady state and recorded histories are discarded. This practice essentially concentrates the recording process right at the displacement front, and has the potential of lifting the remaining burden on computer memory. While we have observed that this works well at diffusion-dominated regimes, at high Peclet numbers, $q_{cd}^{FO}$ (i.e. eq. 4.6a) possesses strong tailing (see fig. 4.2a; due to the parabolic velocity profile) which substantially delay the time necessary to reach steady state. In fact, naively discarding recorded histories based on a seemingly reasonable tolerance results in large errors. This is because the tails carry substantial weight, and discarding them is tantamount to

discarding solute mass. This posed another memory limitation in the simulations of section 4.3.3. A practical solution would be to approximate infinite tails with truncated (most preferably after a characteristic diffusion time scale) ones *a priori* (in the advection-dominated portion of eq. 4.6a). This is permissible as long as all the mass is taken into account i.e. *WO* (the shaded area in figure 4.1c) is kept constant.

Finally, the constant time step size used herein (i.e. eq. 4.15a) is quite stringent, which adversely affects computational performance. This conservative value was determined through a series of sensitivity studies on long 1D strings of concatenated pores and throats (e.g. fig. 4.5). In transport simulations, typically smaller time steps are required initially, when temporal concentration gradients are steep, but can be increased over time as the solute disperses over the domain. Hence, an adaptive time stepping scheme is very desirable. Current computational performance for each of the simulations in section 4.3.3 is in the order of ~7hrs. An adaptive scheme could reduce the number of time steps by more than an order of magnitude, reducing computation costs to a few minutes. Tests on MCM, which is implemented under both schemes, confirm this.

The current work provides the first blueprint for STM, where much effort was spent on demonstrating its algorithmic feasibility and accuracy. The above propositions pave potential pathways towards futures improvements of the method. In doing so, it may also be worthwhile to audit the literature in other fields such as signal processing and transmission, in electrical engineering, to seek commonalities and borrow useful ideas. It is important to note that, even in its current form, STM is computationally more efficient than particle-tracking methods (i.e. commonly used in the literature for network modeling of solute transport) for certain boundary conditions and moderate domain sizes (few thousand pores). Typical in particle tracking simulations is the dispersal of a finite collection of random walkers. The continuous injection of a well-mixed solution which

reacts, adsorbs, or mixes with another, is a scenario that would require an increasingly large number of random walkers and would be computationally expensive. However, such problems are easily handled by STM, producing solutions equivalent to those of particle tracking methods at the limit of infinite number of particles. On the other hand, particle tracking provides considerable flexibility for modeling truly infinite (i.e. periodic) domains, whereas STM requires domains to be finite (and moderate in size under the current implementation). In this regard, the two methods appear to complement each other quite well in tackling a large array of problems, where either would be limited by itself. We should note, however, that there are scenarios for which the most elegant (i.e. simple while accurate) solution appears to be provided by particle tracking alone, i.e. *ordered* media as discussed in section 4.3.4.

### 4.2.2 The rate-modified mixed cell method (rmMCM)

Here the rather arbitrary rate expressions of MCM are modified and the resulting model is referred to as rmMCM. In rmMCM, throats are assumed to have zero volumes and pore concentrations are assumed to be perfectly mixed (as in MCM). Since throat residence times are zero, concentrations within them reach steady state immediately. Therefore, the steady-state rate expressions in eq. 4.7b seem to be an appropriate choice for $q_{c,tij}$ (i.e. solute flow rate in throat $t_{ij}$) in eq. 4.11a. The species balance equation for pore $p_i$, thus, follows (i.e. eq. 4.16):

$$V_{p_i}\frac{dc_{p_i}}{dt}=\sum_{j=1}^{N_{p_i}^t}H(\Delta p_{ij})\left(c_{p_j}q_{c_{ij}}^{ss,FO}-c_{p_i}q_{c_{ij}}^{ss,BI}\right)+\sum_{j=1}^{N_{p_i}^t}H(-\Delta p_{ij})\left(c_{p_j}q_{c_{ij}}^{ss,BO}-c_{p_i}q_{c_{ij}}^{ss,FI}\right) \qquad (4.16)$$

Where,

$$q_{c,ss}^{F} = (2\pi R^2 V_0) C^F \qquad q_{c,ss}^{B} = (2\pi R^2 V_0) C^B \tag{4.17}$$

In eq. 4.16-17, $q_{c,ss}{}^{F}$ and $q_{c,ss}{}^{B}$ denote the dimensional steady state solute flow rates for forward and backward transport, respectively. The RHS of eq. 4.16 is essentially the superposition of forward and backward transport in space. It is, therefore, a special case of STM, with no superposition in time. rmMCM can also be regarded as a generalization to the transport model proposed by Milligen and Bons (2014), which assumes steady-state plug flow within throats. Nevertheless, shear dispersive effects of the parabolic velocity profile are practically non-existent under steady-state conditions, save for the existence of a non-uniform boundary layer; see fig. 4.1a-b. For this reason, the model by Milligen and Bons (2014) and rmMCM are considered, for all practical purposes, equivalent.

## 4.3 RESULTS AND DISCUSSION

### 4.3.1 Verification of STM against convolution

Consider a sequence of identical cylindrical throats joined together in series. We verify STM against two cases: the juncture between two consecutive throats 1) is volumeless, and 2) is occupied by identical pores with non-zero volumes (and pore-to-throat mean residence time ratios of 0.76). The junctures are referred to as "pores" if they have volume and "joints" otherwise. We assume joint/pore concentrations to be perfectly homogenized at all times. Additionally diffusion is assumed absent, which means that transport within throats can be described by a simple traveling-wave solution. With these simple ingredients, the flux-averaged outlet concentration profiles of a string of *n* throats

in case 1, and $n$ throat-pore pairs in case 2, in response to a unit step injection profile (i.e. $U$) can be expressed by eq. 4.18a and 4.18b, respectively:

$$R_t^n(t) = U * E_p^{*n} \tag{4.18a}$$

$$R_{tp}^n(t) = U * (E_t * E_p)^{*n} \tag{4.18b}$$

Where,

$$x^{*n} = \underbrace{(x * x * x * \cdots * x * x)}_{n} \tag{4.19}$$

$$E_t(t) = \frac{t_0^2}{2}\frac{1}{t^3} \qquad E_p(t) = \frac{e^{-\frac{t}{t_0}}}{t_0} \tag{4.20}$$

In eq. 4.18, $R_t^n$ and $R_{tp}^n$ are the outlet profiles (or response functions) for cases 1 and 2, respectively. $E_t$ is the impulse response function (commonly referred to as the "E-function") for purely-advective transport in a cylindrical duct with mean residence time $t_0$ (used for throats in cases 1 and 2). $E_p$ is the E-function for a continuously-stirred tank reactor (CSTR) with mean residence time $t_0$ (used for pores in case 2). $E_t$ and $E_p$ are standard in process and reactor design in chemical engineering (more information can be found in Nauman, 2008). Thus, $R_t^n$ and $R_{tp}^n$ consist of an $n$-fold convolution of the injected unit step profile, $U$, with the impulse response functions of the throats (in case 1) and the throat-pore pairs (in case 2), respectively. Since closed-form expressions for eq. 4.18a and 4.18b are not available, they are evaluated by numerically calculating the convolution integrals. These are then compared to outlet concentration profiles obtained from STM for different values of $n$.

Figure 4.4a shows that the agreement between STM and eq. 4.18a for $n = 1$, 5, and 15 is excellent. Similarly close agreements are seen in figure 4.4b between STM and eq. 4.18b for $n = 1$, 3, and 10. Since numerical evaluation of the convolutions is rather

computationally expensive, $n$ had to be limited to 15 for case 1, and 10 for case 2. This verifies that STM is doing what is expected from it: computing response functions for an entire network by convolving response functions of the elements that comprise it (i.e. pores and throats). Figure 4.4a additionally contains the *true* response function for a string of cylindrical throats with zero joint volumes (i.e. the $(1\text{-}1/\tau^2)$ term in eq. 4.6a). Note that this is the traveling wave solution, which does *not* assume any homogenization of concentrations at the joints. For this reason, only the STM response function for $n = 1$ matches the true solution, while deviations become manifest for $n > 1$. These deviations are precisely due to the cross-sectional smearing of concentrations, and are discussed in detail in section 4.3.4.

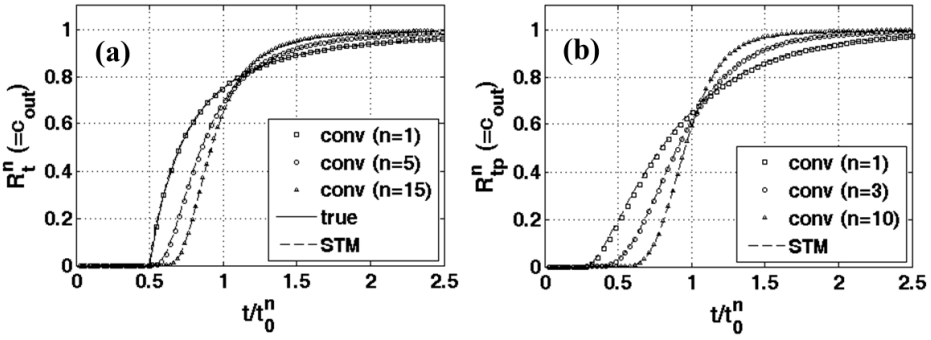


Figure 4.4: Comparison of STM against convolutions given by eq. 4.18, for a string of throats in series with (a) zero and (b) finite pore volumes. Plots represent outlet concentration profiles vs. normalized time ($t_0^n$ is the mean residence time of the string) for $n = 1$, 5, and 15 (a) and $n = 1$, 3 and 10 (b). Pore-to-throat mean residence time ratios in (b) are 0.76. *True* outlet concentration profile for a string of throats with zero joint volume is included in (a).

### 4.3.2 Comparison against CFD

Consider the short string of identical spherical pores and cylindrical throats shown in figures 4.5a and 4.5b. Figures 4.5a and 4.5b depict, respectively, strings with pore-to-throat aspect ratios (defined as the ratio of pore to throat diameters) of 2 and 7.5, and pore-to-throat mean residence time ratios of 0.76 and 42. For convenience we refer to the strings in figures 4.5a and 4.5b as SA and SB, respectively. Geometric dimensions of SA and SB (normalized by the string length) are annotated in figures 4.5a and 4.5b. Stokes flow and species transport was simulated in these geometries via COMSOL© under the boundary conditions shown in figure 4.5a. Initially at zero concentration, solute was injected at a constant concentration of 1 through the inlet. Zero concentration gradient was maintained at the outlet. The flux-averaged outlet concentrations (or response functions) were then recorded. The goal of this section is to compare these response functions to those obtained from simplified conceptualizations of the transport physics and geometries of SA and SB. We consider three conceptualizations:

- **MCM:** all the string volume is concentrated at the pores, with throats having zero volumes. Solute is perfectly mixed within pores. A schematic is depicted in figure 4.5c. The conceptualization is solved via MCM and throat lengths and radii needed in the transport equation (i.e. eq. 3.3) are the same as those annotated in figures 4.5a and 4.5b.
- **STM1:** throats and pores have the same dimensions as in the original domains (i.e. figures 4.5a and 4.5b). Solute is perfectly mixed within pores. A schematic is depicted in figure 4.5d. The conceptualization is solved via STM with either plug-flow or parabolic velocity profiles within throats.

- **STM2:** all the string volume is concentrated at the throats, with pores (or joints) having zero volume. Solute is homogenized across the cross-section at every joint. A schematic is depicted in figure 4.5e. The conceptualization is solved via STM with either plug-flow or parabolic velocity profiles within throats. Inlet/outlet throats have the same radii and lengths as in the original domains (i.e. figures 4.5a and 4.5b), which also ensures the same available area for diffusion in both.

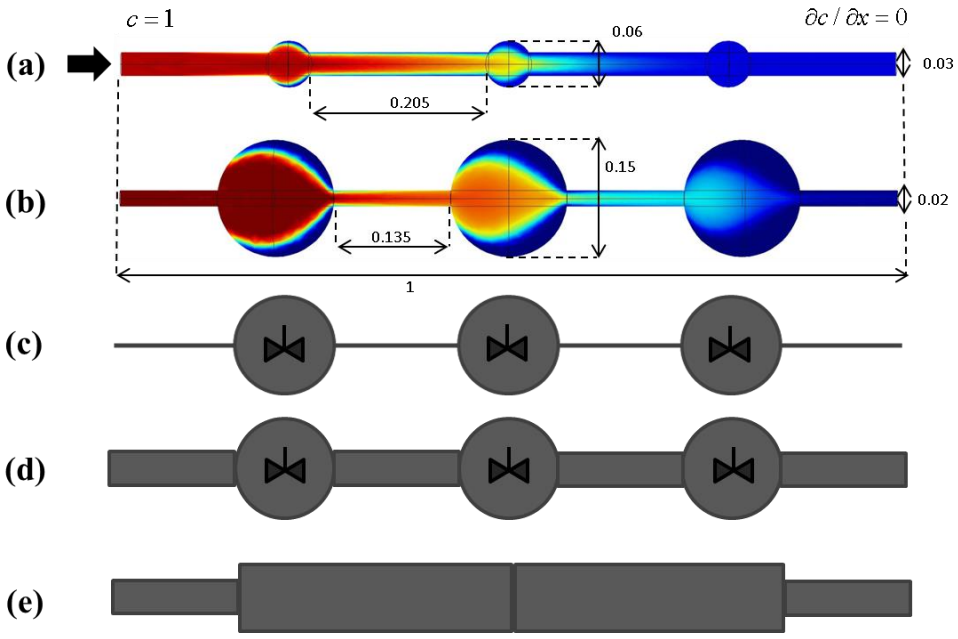


Figure 4.5: (a) Low aspect ratio (SA), and (b) high aspect ratio (SB) strings used for comparison against CFD. Boundary conditions and dimensions (normalized by the total domain length) are annotated. Figures (a) and (b) also depict concentration fields obtained from CFD for $Pe_R$ = 4000 and 3700 (defined with respect to throat properties), respectively. (c) MCM, (d) STM1, and (e) STM2 conceptualizations.

Figures 4.6-9 compare outlet concentration profiles obtained from CFD against the MCM, STM1, and STM2 conceptualizations for SA and SB. Comparisons are made for a wide range of Peclet numbers, $Pe_R$ (defined with respect to throat properties). We additionally use the subscripts *par* and *plug* with STM1 and STM2 to denote whether parabolic or plug-flow velocity profiles were assumed within the throats. We remark that for cases with plug-flow profiles, backward transport is implicitly taken into account because of the 1D geometries of SA and SB (see appendix H). However, since the outlet boundary conditions in SA and SB preclude diffusion (see fig. 4.5a), deviations at low Peclet numbers are to be expected for $STM1_{plug}$ and $STM2_{plug}$.

Consider the SA geometry in figure 4.5a: Figure 4.6 shows that the agreement between $STM1_{par}$ and CFD is quite good, whereas MCM incurs gross deviations especially at moderate to high Peclet numbers. $STM1_{plug}$ also deviates at large Peclet numbers towards underestimating longitudinal spreading, but agrees well at low and moderate Peclet regimes. Slight deviations of $STM1_{par}$ at high Peclet numbers may be attributed to the perfect-mixing assumption at the pores. Figure 4.7 confirms this, as the predictions of $STM2_{par}$ (with zero pore volumes) are further improved compared to $STM1_{par}$. In contrast, $STM2_{plug}$ does very poorly across the Peclet spectrum (the deviation at $Pe_R = 0.04$ is expected as previously noted). At high Peclet numbers $STM2_{plug}$ clearly converges to piston-like displacement with zero longitudinal spreading.

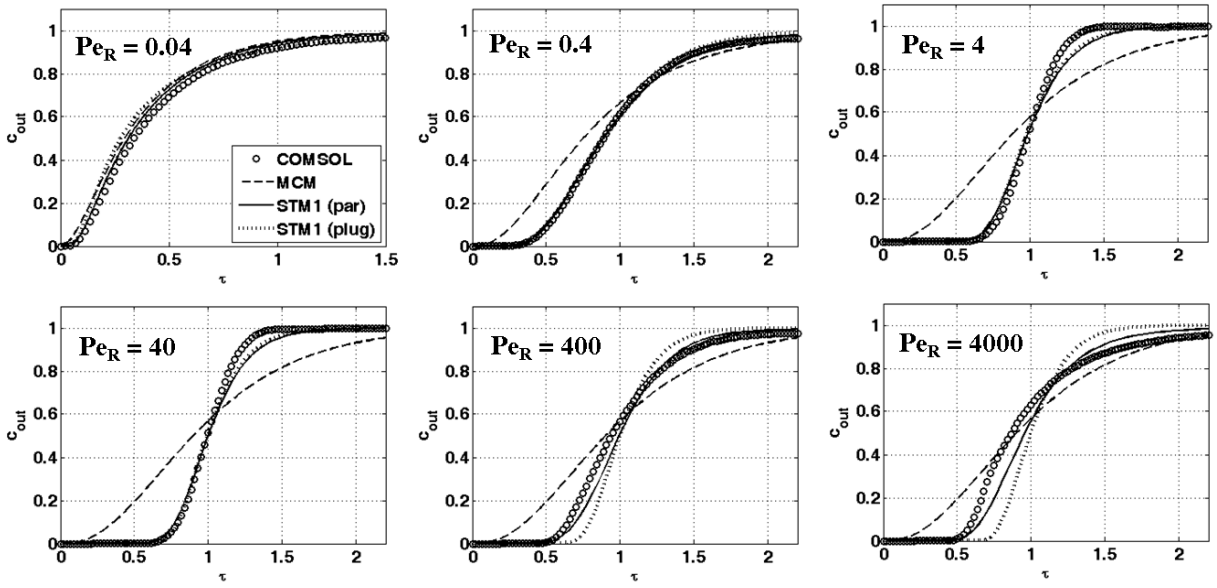


Figure 4.6: Comparison of outlet concentration profiles of $STM1_{par}$, $STM1_{plug}$ and MCM, against CFD for SA.

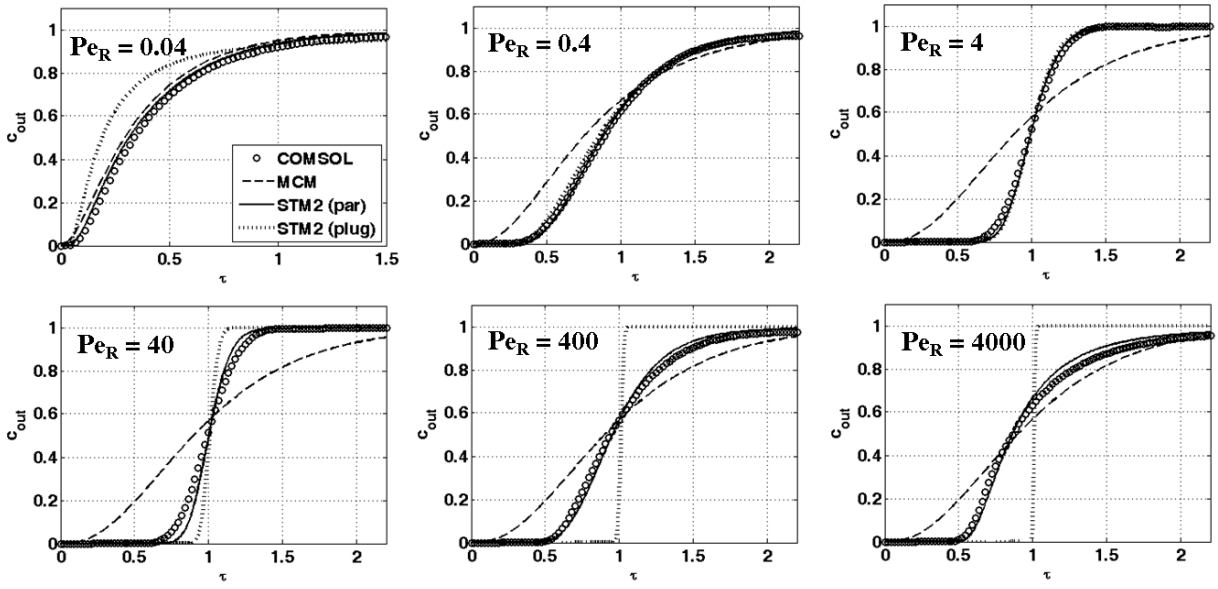


Figure 4.7: Comparison of outlet concentration profiles of $STM2_{par}$, $STM2_{plug}$, and MCM, against CFD for SA.

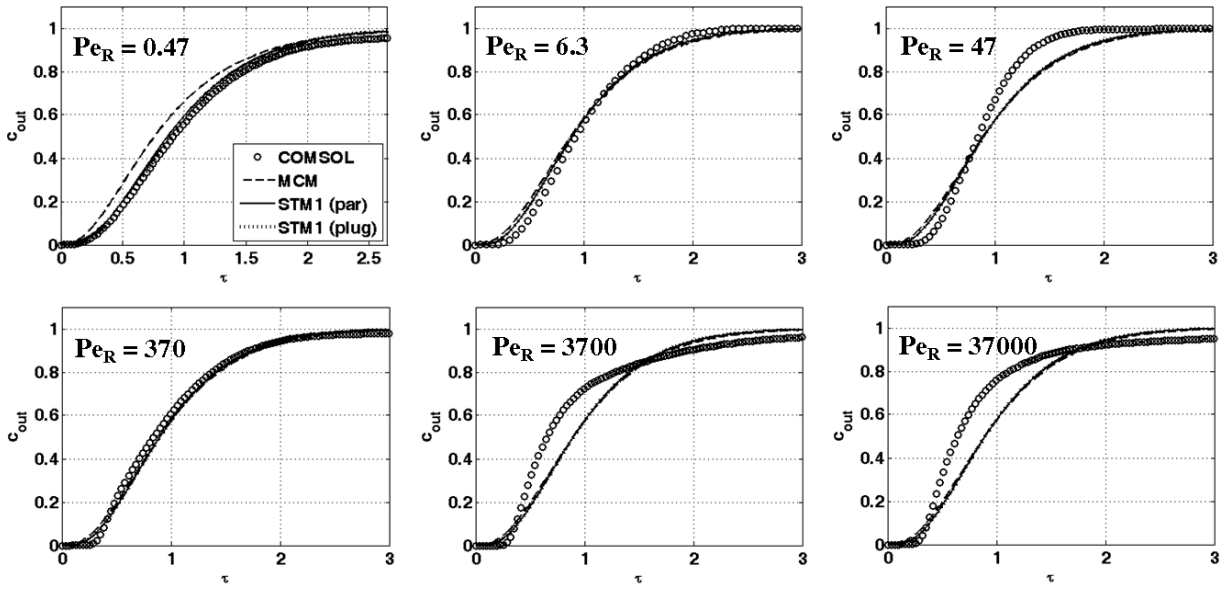


Figure 4.8: Comparison of outlet concentration profiles of $STM1_{par}$, $STM1_{plug}$, and MCM, against CFD for SB.

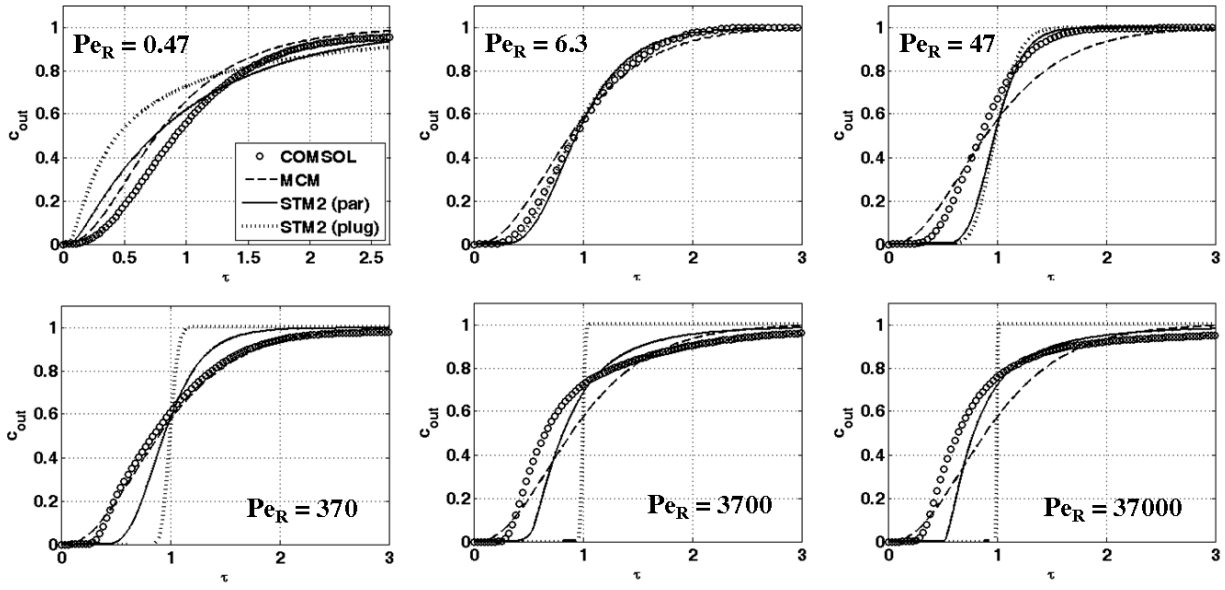


Figure 4.9: Comparison of outlet concentration profiles of $STM2_{par}$, $STM2_{plug}$, and MCM, against CFD for SB.

Consider the SB geometry in figure 4.5b: Figure 4.8 shows that practically no difference exists among the MCM, $STM1_{par}$, and $STM1_{plug}$ predictions for all Peclet numbers. Overall, all predictions are satisfactory except for very high $Pe_R$ (= 3700 and 37000). It should also be noted that in going from low to high $Pe_R$, predictions temporarily deteriorate at $Pe_R = 47$. It is quite curious as to why they recover above this value at $Pe_R = 370$. The reason may be that the "coning" of the solute in the pores (as seen in fig. 4.5b) causes early breakthroughs from the pores similar to a CSTR (or continuously mixed pore). A perfect match was obtained when volume-averaged pore concentrations were compared to those of, for example, MCM (not shown here). This means that two completely different physical mechanisms can lead to the same overall transport outcome. Further increase in $Pe_R$ (=3700 and 37000) results in the emergence of unswept regions within the pores (fig. 4.5b; which are the cause for the deviations). While one may attempt to include unswept regions into the conceptualizations, correct identification and characterization of such regions in realistic pore networks remains a challenge. Figure 4.9 shows that for the SB geometry, $STM2_{par}$ and $STM2_{plug}$ are not good conceptualizations altogether. Extremely high Peclet numbers might seem to be the exception in $STM2_{par}$, but it is very likely that non-inertial effects become more important in these regimes.

In general, a one-to-one mapping of the actual pore-space geometry (without concentrating volumes at either the pores or the throats alone), approximating pores (or "pockets") by CSTRs, and including shear dispersion within throats, seems to be a satisfactory and minimalistic idealization of the actual transport process. It is very important to note that if a pore is met by more than one inlet, it is necessary to conceptualize each "pocket" (not the entire pore) by a CSTR (ref. chapter 3 for definition of pocket). For reasons already given in section 4.2.1.2, the latter was pursued in this

chapter for simplicity. Simplifying further, in porous media where pores have much longer mean residence times compared to throats, MCM is the method of choice (i.e. simpler). This is because transport physics within throats would have no impact on the macroscopic transport behavior (see fig. 4.8). Longer residence time within pores additionally justifies the appropriateness of their idealization by CSTRs (i.e. more time available for diffusion to homogenize concentrations). On the other hand, in porous media where throats have longer or equal mean residence times compared to pores, STM2 is the method/conceptualization of choice. If pore-level mixing is to be accounted for accurately, one shall use SSM (instead of MCM) or a combination of STM and SSM (instead of STM alone) depending the method of choice selected based on the aforementioned.

We conclude this section by noting, that even though SA and SB are homogeneous and short (longer domains were computationally difficult with CFD), they have provided a direct means of evaluating the predictive capacity of the different conceptualizations considered. While the homogeneity of the domains have provided a sufficiently strict case for comparison (see discussion in section 4.3.4), care must be exercised in extending the conclusions drawn herein to longer domains, i.e. throats connected by more pores in the longitudinal direction. For instance, despite the excellent predictions made by $STM2_{par}$ for SA, at high Peclet numbers large inaccuracies may arise as domain lengths increase (see section 4.3.4).

### 4.3.3 Longitudinal dispersion in disordered granular media

#### *4.3.3.1 Comparison against experiments*

In this section, we compare longitudinal dispersion coefficients from STM (with parabolic and plug-flow velocity profiles within throats; denoted by $STM_{par}$ and $STM_{plug}$ hereafter), MCM, and rmMCM against available experimental data in the literature for unconsolidated bead/sand packs. In $STM_{par}$ and $STM_{plug}$, it was assumed that pores are volumeless and throats are cylindrical, to maximize shear-dispersive effects and to follow common practice in the literature for comparison. In appendix I, we describe the procedure whereby pore volumes obtained from Delaunay tessellation (Al-Raoush et al., 2003) were assigned to the throats, followed by computing throat lengths and radii. We note that the same throat lengths and radii were used in MCM and rmMCM. Here we consider the $1\times1\times1mm^3$ monodisperse sphere pack described in section 3.3.3, whose corresponding physically-representative pore network consists of 4094 pores and 10184 throats with permeability and porosity of 24D and 0.38, respectively. We define the characteristic Peclet number as $Pe_d = v_{int}d_p/D_m$, where $v_{int}$ and $d_p$ denote interstitial fluid velocity and grain diameter, respectively.

For $Pe_d<1$, the original sphere pack is used to compute dispersion coefficients, while for $Pe_d>1$, the network is lengthened in the $x$-direction by physically attaching another replica of it to itself (this is possible because the sphere pack is periodic). Therefore, in the latter case, the domain has dimensions $2\times1\times1mm^3$ and is 20 grains and 32 pores across in the $x$-direction. This is a relatively small domain when compared to typical sizes used in the literature for dispersion calculations. Acharya et al. (2007b) determined that a 33×23×23 cubic lattice network is necessary for MCM to produce asymptotic longitudinal dispersion coefficients. Although comparable in the $x$-dimension to our domain, one must be careful in drawing a parallel as their network was generated

statistically. Jha et al. (2011) used a physically representative network of a sphere pack (i.e. their results provide a more appropriate comparison case herein) that was 34 grains long and 17 grains wide. The reason for the selected domain sizes herein was strictly out of computer memory requirements for STM. Ample discussion and proposed solutions for alleviating these requirements were provided in section 4.2.1.3. While MCM and rmMCM do not incur this limitation, the above domain sizes are used regardless, to ensure comparisons on equal ground.

Longitudinal dispersion coefficients were computed by fitting the *flux-averaged* concentration (i.e. eq. 4.23), corresponding to the following macroscopic convection-dispersion equation (CDE) (i.e. eq. 4.21), to the breakthrough profiles obtained from the network simulations.

$$\frac{\partial C_v}{\partial t} + v_{int}\frac{\partial C_v}{\partial x} = D_L\frac{\partial^2 C_v}{\partial x^2} \tag{4.21a}$$

$$C_v(t=0) = 0 \tag{4.21b}$$

$$v_{int}C_v - D_L\left.\frac{\partial C_v}{\partial x}\right|_{x=0} = v_{int}C_{in} \qquad \left.\frac{\partial C_v}{\partial x}\right|_{x\to\infty} = 0 \tag{4.21c}$$

The *volume-averaged* solution to eq. 4.21 can be found in Van Genuchten and Alves (1982), and is given by eq. 4.22:

$$C_v(x,t) = C_{in}\left\{\frac{1}{2}erfc\left[\frac{x-v_{int}t}{2\sqrt{D_L t}}\right] + \left(\frac{v_{int}^2 t}{\pi D_L}\right)^{1/2}\exp\left[-\frac{(x-v_{int}t)^2}{4D_L t}\right] - \frac{1}{2}\left(1+\frac{v_{int}x}{D_L}+\frac{v_{int}^2 t}{D_L}\right)\exp\left(\frac{v_{int}x}{D_L}\right)erfc\left[\frac{x+v_{int}t}{2\sqrt{D_L t}}\right]\right\} \tag{4.22}$$

$$C_f(x,t) = C_{in}\left\{\frac{1}{2}erfc\left(\frac{x-v_{int}t}{2\sqrt{D_L t}}\right)+\frac{1}{2}\exp\left(\frac{v_{int}x}{D_L}\right)erf\left(\frac{x+v_{int}t}{2\sqrt{D_L t}}\right)\right\} \quad (4.23)$$

In eq. 4.21-23, $D_L$ denotes the longitudinal dispersion coefficient, and $C_v$ and $C_f$ denote macroscopic volume-averaged and flux-averaged concentrations, respectively. Parker and Van Genuchten (1984) showed (by transformation of eq. 4.21) that eq. 4.23 is the corresponding flux-averaged concentration of eq. 4.22. Furthermore, they correctly argued that eq. 4.23 is preferred for fitting experimental breakthrough profiles, as opposed to finite-domain solutions with dispersion-free outlet conditions (e.g. Brenner, 1962). This is because postulating a dispersion-free outlet is tantamount to assuming no outflow of solute due to pore-scale variations of fluid velocity. Similarly, dispersion-free outlet conditions are inappropriate for fitting breakthrough profiles from pore-scale simulations. The only exception is when dispersion is diffusion-dominated and a corresponding diffusion-free outlet condition is imposed on the pore scale model (e.g. Jourak et al., 2014).

For the network simulations herein, flux-averaged effluent concentrations are computed according to eq. 4.24 ($t_{ib}$ denotes the throat connecting pore $p_i$ to the boundary). In eq. 4.24, $x = L_N$ is where effluent concentrations are computed, which is 1mm for $Pe_d$ <1 and 2mm for $Pe_d$ >1 in this work. This, of course, is equivalent to the definition by Parker and Van Genuchten (1984) at the macro scale. Note that if eq. 4.23 is to be fitted to flux-averaged effluent concentrations from pore-scale simulations (e.g. eq. 4.24), then the pore-scale inlet condition must translate to $C_f(x=0) = C_{in}$ (i.e. after transforming 4.21c). This means that the commonly used (e.g. Acharya et al., 2007b; Zaretskiy et al., 2010; Jourak et al., 2014) pore-scale dirichelet inlet condition $c(x=0) = 1$ is, strictly speaking, incorrect. The situation is similar when macroscopic solutions for finite

domains are used. In other words, since macroscopic concentrations of the fitting equation are to be interpreted as flux-averaged, the inlet condition $C_f(x=0) = C_{in}$ corresponds to a constant solute injection rate at the inlet, not a dirichelet boundary condition, where rates may vary with time. Surprisingly, such a distinction is rarely drawn in the literature. At sufficiently high Peclet numbers, however, the difference between the two inlet conditions becomes negligible (e.g. Acharya et al., 2007b where $Pe_d > 10$). In this light, we use eq. 4.25 as the inlet condition for the pore networks ($A_N$ is the network cross-sectional area available to flow), which is diffusion-free and assumes zero-residence time within inlet throats (appropriate modifications to STM balance equation, i.e. eq. 4.11-12, for the boundary pores are straightforward).

$$C_{f,e} = \left. \frac{\sum_{\substack{\forall outlet \\ throats}} q_{c,t_{ib}}}{\sum_{\substack{\forall outlet \\ throats}} q_{t_{ib}}} \right|_{x=L_N} \tag{4.24}$$

$$\sum_{\substack{\forall inlet \\ throats}} C_{in} q_{t_{ij}} \Big|_{x=0} = C_{in} A_N v_{int} \qquad \left. \frac{\partial c}{\partial x} \right|_{x \to \infty} = 0 \tag{4.25}$$

The proper pore-scale outlet condition, in connection with the semi-infinite condition of eq. 4.21c at the macro scale, is given by eq. 4.25. In order to satisfy it, one of two approaches is taken. For MCM and rmMCM, we sufficiently augment the domain size in the $x$-direction by physically attaching replicas of the periodic network to itself (effluent concentrations are still recorded at $x = L_N$ via eq. 4.24). This reduces the effects of the actual diffusion-free, Neumann boundary imposed at the outlet of the augmented network. This approach suits MCM and rmMCM quite well, as they are highly efficient computationally. For $STM_{par}$ and $STM_{plug}$, the outlet throats are assumed to be semi-

infinite acting ducts with plug-flow velocity profiles. The actual velocity profile is immaterial, as the solute spends a negligible fraction of its total network residence time within these throats. However, the plug-flow assumption allows us to use the semi-infinite acting rate expressions in appendix H (i.e. eq. H.1). The STM outlet condition is, therefore, given by eq. 4.26 (where $\Delta p_{ib} = p_b - p_i$ and $p_b$ is the outlet pressure, and $q_c{}^{r,FO/BO}{}_{tib,k}(t-t^r{}_{pi,k})$ denotes time-shifted forward/backward solute flow rates).

$$C_{f,e} = \left. \frac{\sum\limits_{\substack{\forall outlet \\ throats}} \left( U(-\Delta p_{ib}) \sum\limits_{k=0}^{N^r_{p_i}} \delta c^r_{p_i,k}\, q^{r,FO}_{ct_{ib},k}(t - t^r_{p_i,k}) + U(\Delta p_{ib}) \sum\limits_{k=0}^{N^r_{p_i}} \delta c^r_{p_i,k}\, q^{r,BO}_{ct_{ib},k}(t - t^r_{p_i,k}) \right)}{\sum\limits_{\substack{\forall outlet \\ throats}} q_{t_{ib}}} \right|_{x=L_N} \tag{4.26}$$

By fitting eq. 4.23 to effluent profiles obtained via eq. 4.24 (or eq. 4.26) under boundary conditions discussed above, with flow in $x$-direction and lateral boundaries sealed, longitudinal dispersion coefficients for $STM_{par}$, $STM_{plug}$, MCM, and rmMCM were computed. Figure 4.10a compares network model predictions to available experimental data in the literature. This is a standard way of presenting dispersion data, where the vertical axis represents normalized dispersion coefficient, $D_L$, (against molecular diffusion, $D_m$) and the horizontal axis represents characteristic Peclet number, $Pe_d$. All experimental data correspond to unconsolidated bead/sand packs, and were extracted from Jha et al. (2011) (and references therein). These include: breakthrough results of Pfannkuch (1963); NMR imaging measurements of Seymour and Callaghan (1997), Kandhai et al. (2002), Khrapitchev and Callaghan (2003); planar laser-induced florescence imaging results of Stöhr (2003), and sand pack data of Perkins and Johnston (1963) (and references therein), Jha (2005).

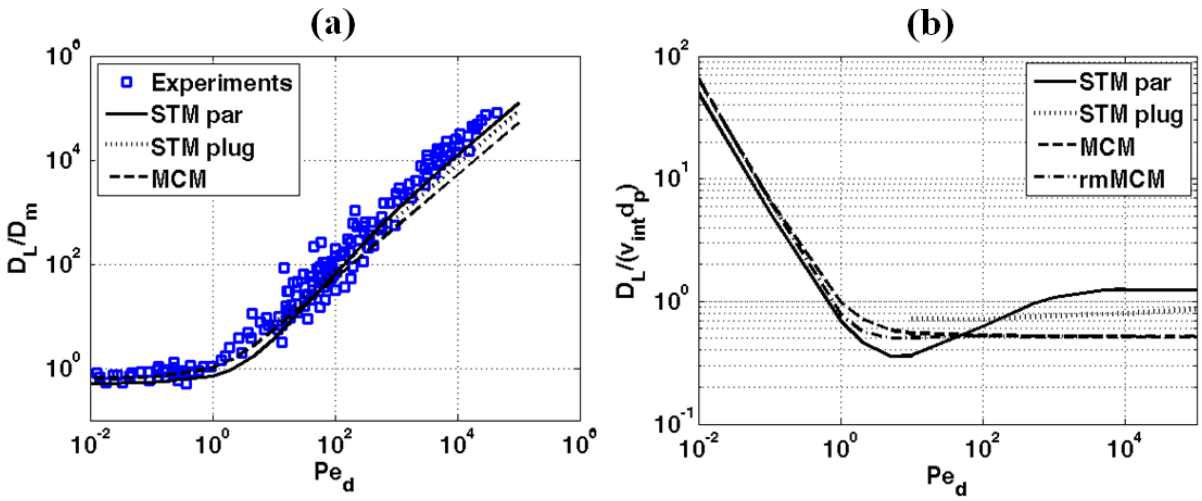


Figure 4.10: (a) Normalized longitudinal dispersion vs. Peclet number ($=v_{int}d_p/D_m$) for STM (with parabolic/plug-flow velocity profiles) and MCM against experimental data in the literature (extracted from Jha et al., 2011 and references therein). Predictions for STM with plug-flow span $Pe_d$ >10, as the rate expression used (eq. H.1) are valid only in this range (i.e. backward transport in negligible). (b) $D_L/(v_{int}d_p)$ vs. Peclet number ($=v_{int}d_p/D_m$) for STM (with parabolic and plug-flow velocity profiles), MCM, and rmMCM for the sphere pack network. Note that only STM with the parabolic velocity profile produces the signature power-law regime characteristic of intermediate Peclet numbers.

Figure 4.10a shows very good agreement between $STM_{par}$ and the experimental data over the entire Peclet spectrum. In comparison, MCM under-predicts dispersion at $Pe_d$ >100 up to a factor of ~2.5, whereas predictions at $Pe_d$ <1 are very good. Since MCM and rmMCM were almost indistinguishable in figure 4.10a, the corresponding plot for rmMCM is not shown. Note that $STM_{plug}$ simulations were conducted only for $Pe_d$ >10 (see figure 4.10a). This is because the corresponding rate expressions used (i.e. eq. H.1) do not account for backward diffusion from one inlet to the next within the same pore

(see discussion in section 4.2.1.1). Although not very obvious from figure 4.10a, $STM_{plug}$ is smaller by a factor of ~1.5 compared to $STM_{par}$ (differences at high $Pe_d$ are more apparent in figure 4.10b as discussed later).

The dependence of longitudinal dispersion on Peclet number is typically divided into discrete regimes in which the scaling of $D_L$ with $Pe_d$ is influenced by different mechanisms (Fried and Combarnous, 1971; Sahimi, 2012). These roughly follow: i) dispersion dominated by restricted diffusion ($Pe_d$ <0.3), ii) *transition* regime where advection and diffusion are comparable in magnitude (0.3< $Pe_d$ <5), iii) *power-law* regime where coupled interaction between diffusion and advection gives rise to the supra-linear dependence $D_L \sim Pe_d^{\delta}$ where $1<\delta<2$ (5< $Pe_d$ <200-4000), and iv) pure *mechanical* dispersion which is characterized by the linear dependence $D_L \sim Pe_d$ ($Pe_d$ >200-4000). Non-inertial effects typically become apparent beyond this limit. The regime boundaries (especially between power-law and mechanical) are known to vary throughout the literature and are typically ascribed to pore-scale heterogeneities from one sample to the next (Wood 2007). The theoretical studies of Saffman (1959) and Koch and Brady (1985) identified the underlying physical mechanisms of dispersion; from which the expression given by eq. 4.27 is typically written (and used to fit experimental data):

$$\frac{D_L}{D_m} = D_r + c_1 Pe_d + c_2 Pe_d^{\delta} + c_3 Pe_d^2 \tag{4.27}$$

In eq. 4.27, $D_r$ is the restricted diffusion coefficient and $c_1$, $c_2$, $c_3$ are constants dependent on the porous medium. The RHS terms in eq. 4.27, from left to right, correspond to: restricted diffusion, mechanical dispersion, boundary-layer dispersion (also expressed as $Pe_d \log Pe_d$ and due to diffusion in and out of boundary layers near the solid surface), and hold-up dispersion (due to diffusion in and out of stagnant zones in the pore space). In the highly connected sphere-pack studied herein, hold-up dispersion is

practically non-existent. In order to highlight the emergence of the foregoing dispersive regimes from our network simulations, we plot $D_L/(v_{int}d_p)$ vs. $Pe_d$ (which is yet another common way of depicting dispersion data) in figure 4.10b.

Figure 4.10b clearly shows that $STM_{par}$ successfully reproduces all the regimes described above. From this figure the regime boundaries are: i) restricted diffusion at $Pe_d$ <0.3, ii) transition regime at 0.3< $Pe_d$ <6, iii) power-law regime at 6<$Pe_d$<1000, and iv) mechanical regime at $Pe_d$ >1000. The first non-linearities become apparent at $Pe_d$ >0.3. A minimum is reach around $Pe_d \simeq 6$, which marks the beginning of the power-law regime. A power-law exponent $\delta = 1.19$ is obtained in this regime (6<$Pe_d$<1000), which is in good agreement with values obtained from both experiments and modeling in the literature. These include for modeling: $\delta = 1.2$ Mostaghimi et al. (2012) (micro-CT image of Berea sandstone), $\delta = 1.19$ Bijeljic et al. (2004) (2D diamond lattice network of mapped Berea statistics), $\delta = 1.23$ Jha et al. (2011) (sphere-pack pore network), $\delta = 1.19$ Saffman (1959) (fitted) (theoretical value for a network of disordered capillaries). Experimental values lie within the range $\delta \in$ [1.05-1.33] (see Bijeljic et al., 2004 for a thorough compilation), with average values of all data approximately $\delta = 1.2$ (Sahimi, 2012). The scatter in the experimental values is due to inclusion of various types of sandstones, mostly consolidated. For unconsolidated sand/bead packs $\delta = 1.18$ Stöhr (2003) and $\delta = 1.19$ Pfannkuch (1963) agree well with this work (see Bijeljic et al., 2004). For $Pe_d$ >1000 dispersion is purely mechanical.

In figure 4.10b, $STM_{plug}$ shows that $\delta = 1$ for plug flow in a sphere pack (no power-law regime), which is in agreement with Jha et al. (2011). The same conclusion was drawn by Sahimi et al. (1986), who used a 2D square lattice network with perfect mixing at the pores and plug flow at the throats (note that diffusion was neglected). Plug-flow results of Acharya et al. (2007a) demonstrate $\delta > 1$ (their figure 6.b). This apparent

discrepancy is resolved in light of arguments provided in section 4.3.3.2, and is attributed to contributions from hold-up dispersion in the cubic lattice network used.

MCM and rmMCM show very close agreement in figure 4.10b, except at the transition regime. The small deviations appear because advection and molecular diffusion are assumed additive processes in the formulation of solute flow rates in MCM. Both models agree with the theoretical result of Aris and Amundson (1957) for a 1D string of CSTRs: $D_L/(v_{int}d_p) \simeq 0.5$ at high $Pe_d$. Furthermore, the MCM plot in figure 4.10b is *exactly* described by the simple addition of mechanical dispersion and restricted diffusion given by eq. 4.28 (see Delgado, 2006) (although not plotted in figure 4.10b to avoid cluttering). This should come as no surprise, since advection and diffusion are assumed to be additive processes at the pore scale in MCM.

$$\frac{D_L}{D_m} = D_r + \frac{Pe_d}{2} \qquad or \qquad \frac{D_L}{v_{int}d_p} = \frac{D_r}{Pe_d} + \frac{1}{2} \tag{4.28}$$

MCM and rmMCMC predict $D_r = 0.65$, which is within [0.6-0.7] as noted by Perkins and Johnston (1963). A slightly lower value of $D_r = 0.53$ was obtained by $STM_{par}$. For reasons discussed in section 4.2.1.3, at $Pe_d << 1$, STM simulations are quite sensitive to the recording frequency and the time step size (i.e. eq. 4.15). Larger time steps were, therefore, taken to avoid a very high recording frequency (we recognize this as the source of the error). The reformulation proposed in section 4.2.1.3 is expected to grossly alleviate this problem. Nevertheless, MCM is clearly the method of choice for $Pe_d <<1$, whose computational performance lies within a few seconds.

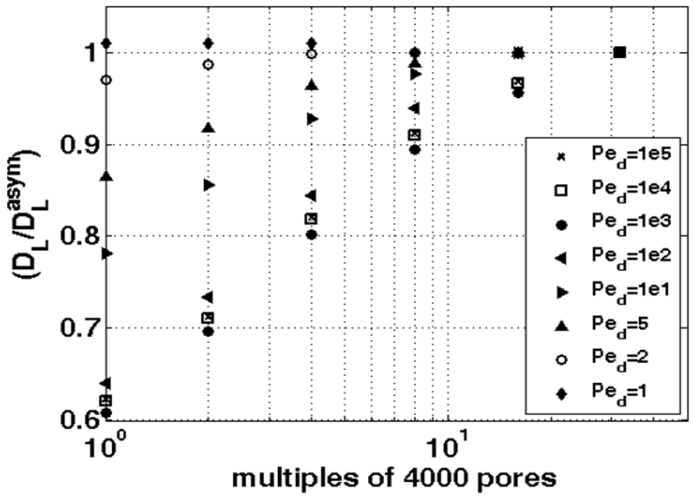


Figure 4.11: MCM dispersion coefficients normalized by their asymptotic value (for very long domains) vs. domain size for different $Pe_d$. Larger domains are required for higher $Pe_d$ to asymptote.

Finally, figure 4.11 shows the dependence of the MCM dispersion coefficient on domain size (increased in the *x*-direction by physically attaching replicas of the periodic network to itself). Dispersion coefficients were normalized by their asymptotic (or near asymptotic) values at the largest simulated domain size. As expected, higher $Pe_d$ regimes necessitate larger domain sizes. Moroni and Cushman (2001) conducted 3D particle tracking velocimetry experiments of dispersion in a sphere pack. They used air bubbles as particles (which do not sample velocities near boundary layers; similar to MCM) and very large grains (= 1.9cm in diameter; hence very high $Pe_d$). They found that dispersion varied linearly (as expected in the absence of boundary-layer dispersion in a sphere pack; see section 4.3.3.2) and asymptoted after 5 to 6 pore diameters. This is certainly not the case in figure 4.11, where much larger travel distances seem to be required.

In an interesting paper, Maier et al. (2003) showed that velocity variations due to imposed lateral no-flow boundary conditions (even if sphere packs are periodic) enhance longitudinal dispersion and prolong the time required for it to asymptote. Furthermore, the larger the lateral dimension, the longer it takes to reach asymptotic behavior. The increase in dispersion coefficient with domain size in figure 4.11 is, therefore, attributed to the no-flow lateral boundaries imposed. In this regard, the relatively small domain length chosen seems to be appropriate for its lateral dimensions. In other words, increasing the domain length while keeping the lateral dimensions constant, allows more time for the solute to sample velocity variations near the no-flow boundaries (which pollutes the actual variations we intend to sample). For a few cases, where increasing domain size was computationally possible, $STM_{par}$ and $STM_{plug}$ demonstrated the same behavior as in figure 4.11. It is noteworthy that if the largest domain size was chosen (i.e. 120,000 pores) for MCM, then we would obtain $D_L/(v_{int}d_p) \simeq 0.7$ at high $Pe_d$, which is in disagreement with the theoretical value by Aris and Amundson, 1957 i.e. 0.5).

#### *4.3.3.2 On the origin of supra-linear dispersion*

In section 4.3.3.1, a power-law exponent of $\delta = 1.19$ was obtained for a monodisperse disordered sphere pack using $STM_{par}$. This value was shown to be in good agreement with experiments and modeling results in the literature with an average $\delta \simeq 1.2$. Slightly larger values have also been reported in the simulations of: $\delta = 1.19$-$1.25$ Sorbie and Clifford (1991) (2D square lattice network), $\delta = 1.29$ Acharya et al. (2007a) (3D cubic lattice), $\delta = 1.27$ (2D square lattice) and $\delta = 1.24$ (3D cubic lattice) Sahimi et al. (1986). We contend that hold-up dispersion ($D_L \sim Pe_d^2$) is the additional contributor to

the observed supra-linearity in these simulations, due to the lattice network structures used.

Recent studies by Milligen and Bons (2012), Bons et al. (2013), and Milligen and Bons (2014), have called into question the necessity of a Taylor type dispersion mechanism (or boundary-layer dispersion) to explain the emergence of a supra-linear power-law regime. An analytical model based on heuristic statistical arguments was developed by Milligen and Bons (2012), that conceptualized dispersion as successive diffusive motions of particles governed by mechanical dispersion ($D_L \sim Pe_d$) and microscopic diffusion. Milligen and Bons (2014) then conducted network simulations, with a model equivalent to rmMCM herein, and demonstrated the emergence of a supra-linear power-law regime in their 2D networks. We contend that the observed supra-linearity in their work is due to contributions from hold-up dispersion as well.

In Milligen and Bons (2014), the networks for which a power-law regime was observed were those with "Elle", hexagonal and square grid structures. Supra-linearity was strongest in the square and hexagonal networks (where lateral throats have substantially smaller flow rates than those in the flow direction), and very weak in the foam-like "Elle" network. It was altogether absent in the "tile" grid network, where lateral throats contained appreciable flow rates. It seems, therefore, that even in the absence of boundary-layer dispersion, networks with a sufficient fraction of near-stagnant throats manifest a power-law regime. In addition, the square and hexagonal networks seem to fit perfectly into the assumptions of the analytical model of Millegen and Bons (2012) (which coincidentally produces an intermediate $D_L \sim Pe_d^2$ dependence similar to hold-up dispersion), i.e. some fraction of the particles experience mechanical dispersion while the rest molecular diffusion at any given $Pe_d$. Such a decoupling of particle motions by diffusion and mechanical dispersion is generally not realistic. Figure 4.10b confirms

this for the sphere-pack network studied, which is devoid of near-stagnant zones, as rmMCM does *not* produce a supra-linear regime.

The following factual statement is readily verifiable: a supra-linear regime exists *if and only if* a plot of $D_L/(v_{int}d_p)$ vs. $Pe_d$ exhibits a minimum. Such a minimum is seen in figure 4.10b for $STM_{par}$, while it is absent for MCM, rmMCM, and $STM_{plug}$. The theoretical works of Saffman (1959) and Koch and Brady (1985) (among others) identified boundary-layer dispersion and hold-up dispersion as mechanisms capable of producing supra-linearity (and thus a minimum in figure 4.10b). In both mechanisms, pore-scale diffusion acts as a regulator in transporting solutes in and out of stagnant zones within the pore space. Therefore, a minimum in the plot of $D_L/(v_{int}d_p)$ vs. $Pe_d$ is reached if pore-scale diffusion can temporarily hinder the linear growth of longitudinal dispersion (in response to an increasing $Pe_d$) by stretching the solute laterally, thus shortening its length, over a certain range of the Peclet spectrum (i.e. by diffusing in/out of boundary-layers/stagnant zones). This, of course, is well known to occur for Taylor-Aris dispersion in a tube. To see this for the sphere pack network modeled via $STM_{par}$, we point to the intuitive pictures figures 4.2a and G.2a provide.

As discussed in section 4.2.1.1, the slope of the S-shaped $q_{cd}^{FO}$ profile (for each throat) in figure 4.2a experiences a maximum at moderate Peclet numbers. Alternatively, figure G.2a shows that $a^F$ (i.e. the parameter controlling the slope) exhibits a maximum and follows approximately a Gaussian, with an amplitude and variance dependent on $\kappa$, in a semi-logarithmic plot. Therefore, the "slump" (or minimum) seen in figure 4.10b for $STM_{par}$, seems to be precisely a result of the "humps" (or maxima) in figure G.2a. In other words, the minimum in figure 4.10b is a direct result of diffusion in and out of boundary-layers. However, if such a pore-scale mechanism is excluded from a computer model, a plot of $D_L/(v_{int}d_p)$ vs. $Pe_d$ does not experience a minimum, *unless* the pore-space

topology provides other opportunities for lateral diffusion to temporarily curb the linear growth of longitudinal dispersion in response to an increasing $Pe_d$. Dead-end zones provide such opportunities, giving rise to hold-up dispersion in the lattice type networks discussed from the literature (e.g. Milligen and Bons, 2014). If the computer model additionally includes boundary-layer dispersion, i.e. parabolic profiles within throats, supra-linearity is expected to amplify (e.g. $\delta = 1.29$ Acharya et al., 2007a).

One may be further tempted to define a parameter such as $\Delta\delta = (\delta\text{-}1.2)$ to quantify specific contributions from hold-up dispersion, which is known to be difficult in experiments, to the overall dispersion process in *disordered* granular media (i.e. sandstones). Further research is required to demonstrate the feasibility of such a metric. An alternative, however, is to simulate a given sample using $STM_{plug}$, for which any supra-linearity would be purely topological (e.g. plug-flow results of Acharya et al., 2007a). The difference between $STM_{par}$ and $STM_{plug}$ further isolates the contribution from boundary-layers. Knowledge of these contributions allows better rock classification and helps in correlating experimental data.

We conclude this section with the following remark: Saffman's (1959) theory predicts that the supra-linearity of dispersion does not disappear at very high Peclet numbers, as long as diffusion is non-zero. Yet mechanical dispersion (i.e. $D_L \sim Pe_d$) is the classification very often invoked at high $Pe_d$. Although this classification is supported by an overwhelming body of experimental data (see Delgado, 2006) and modeling results, there appears to be little mention of this discrepancy in the literature. One possibility is that all modeling and experimental data are, in some form or shape, limited by the large domain sizes requisite for supra-linear behavior at very high $Pe_d$. To show this, however, one is faced with the task of reconciling any discrepancies, of which there are many,

observed in the literature. This we shall not attempt herein, instead we simply pose the issue as a matter in need of addressing.

### 4.3.4 Predictive capacity of network models of solute transport for ordered media

Consider the very long cylindrical tube shown in figure 4.12a, in which solute is continuously injected from left to right in the absence of diffusion ($Pe_R \to \infty$ ). The cross-sectional average ($c_A$) and flux-averaged ($c_F$) concentrations at an axial position $x$ obey eq. 4.29 (easily verifiable from the parabolic velocity profile).

$$\bar{c}_A = \begin{cases} 1 - \dfrac{x}{V_0 t} & \forall x \le V_0 t \\ 0 & else \end{cases} \qquad \bar{c}_F = \begin{cases} 1 - \left(\dfrac{x}{V_0 t}\right)^2 & \forall x \le V_0 t \\ 0 & else \end{cases} \tag{4.29}$$

We then divide the tube into smaller segments, along the dashed lines shown in figure 4.12a. We refer to the dashed lines as "joints" and enumerate them by the variable $N_J$ (from left to right). The cross-sectional average and flux-averaged concentration profiles at these joints (computed via eq. 4.29), are plotted in figure 4.12b for different times. The horizontal axis $\lambda$ is obtained by normalizing $x$ by the length of 50 segments. Now, if we treat each segment as a throat, and each joint as a volumeless pore, STM yields the joint concentration profiles depicted by the thick solid lines in figure 4.12b. It is seen that STM profiles represents neither the cross-sectional average nor the flux-averaged concentrations. It is only at very early times, that STM approaches flux-averaged concentrations.

In section 4.3.1, we showed that STM essentially computes successive convolutions of the impulse response function of each segment with the input signal to the system. Since successive convolutions represent aggregating random variables drawn

from the same distribution (of segment residence times with a uniform inlet concentration), STM is effectively smearing the solute uniformly across the tube cross-section at every joint. Therefore, it is not surprising that it systematically deviates from the flux-averaged concentrations at later times. For comparison, the MCM conceptualization (see section 4.3.2) was additionally applied to the tube shown in figure 4.12a, and its concentration profiles are depicted in figure 4.12b (thin solid lines). Note that STM and MCM are similarly inadequate in describing the transport process for this case.

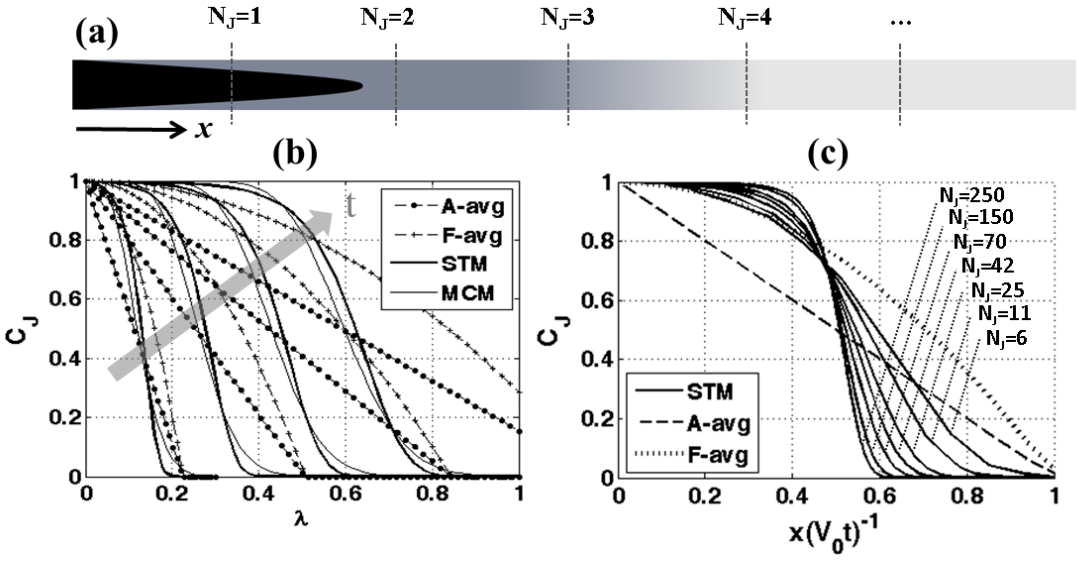


Figure 4.12: (a) Schematic of a circular tube under pure advection (constant inlet concentration), divided into segments with joint locations annotated (dashed lines). (b) Joint concentration profiles at different times along the duct, including: cross-sectional average (dashed-dotted line), flux-averaged (dashed-plus line), STM (thick solid line), and MCM (thin solid line). Arrow of time is annotated. $\lambda$ is obtained by normalizing $x$ against the length of 50 segments. (c) STM, cross-sectional average, and flux-averaged concentration profiles. $x$ normalized against distance travelled by centerline velocity (= $V_0 t$). Number of joints travelled by the centerline velocity (= $N_J$) are annotated (note the gradual convergence towards normality).

It is even more interesting to investigate the STM profile as $t \to \infty$ . Equivalently, we would like to know $E_t^{*n}$ as $n \to \infty$ (where $E_t$ is the impulse response function of a pipe segment given by eq. 4.20). Upon examining eq. 4.20, we notice that $E_t$ is a Pareto distribution of the form given by eq. 4.30, with $x_m = t_0/2$ and a tail index of $\alpha = 2$ ($t_0$ is the mean residence time of the pipe segment).

$$f(x) = \begin{cases} \dfrac{\alpha x_m^{\alpha}}{x^{\alpha+1}} & x \geq x_m \\ 0 & x < x_m \end{cases} \tag{4.30}$$

Since this distribution has an infinite variance, the classical Central Limit Theorem (CLT) does not apply and we have to invoke the generalized CLT. The reader is referred to Furrer (2012) for a full treatment on the infinite aggregates of Pareto distributions, where it is shown that $E_t$ lies in the domain of attraction of the normal distribution. This means that the concentration profile of STM, for pure advection, converges to a Gaussian (although very slowly; see Furrer, 2012) as the solute passes through an increasing number of joints where it is homogenized across the tube cross-section. The implication is that even though Fickian dispersion may never be reached within a pore network in the absence of diffusion, sufficient smearing of the concentrations at the pores would eventually lead to a Gaussian profile. Figure 4.12c clearly shows this limiting behavior for various numbers of segments ($N_J$) traveled by the centerline velocity ($V_0$) (the $x$-axis is normalized by $V_0 t$). Notice the gradual divergence from the flux-averaged concentration profile as $N_J$ increases. If diffusion is present, the smearing will affect the time required to reach asymptotic behavior (and possibly the magnitude of the dispersion coefficient), unless throats are long enough for their outlet

concentrations to be fairly uniform. As an aside, it is very interesting that for $\alpha \geq 2$, eq. 4.30 lies in the domain of attraction of the normal distribution, whereas for $\alpha < 2$ it lies in the domain of attraction of a non-normal stable distribution, and a Newtonian fluid flowing in a cylindrical tube corresponds to the case verging right at the boundary between the two (i.e. $\alpha = 2$).

We note that *all* Eulerian pore network models of solute transport developed in the literature inherently suffer from some sort of smearing performed at the pores/joints. Lagrangian network models that use particle tracking and draw throat transit times from the *same* distribution (i.e. independent of their spatial position) in order to perform random hops from one pore to the next, are similarly limited (e.g. Sorbie and Clifford, 1991; whose model is conceptually equivalent to STM). The smearing effectively discards the memory a random walker has accumulated upon encountering a pore. The problem is circumvented, if inflowing solute is mapped onto appropriate radial positions of the outlet throats. Eulerian network models are inherently incapable of performing such a delicate task, unless pores are sub-discretized into much smaller control volumes, which defeats the intent for a network representation in the first place. It is noteworthy, while SSM (developed in chapter 3) does discriminate between the different outlets of a pore through a coarse sub-discretization of the pore volume, concentrations within each outlet are still assumed to be perfectly mixed (thus it would yield similar predictions as MCM for the case in figure 4.12a). Lagrangian network models (e.g. Jha et al., 2011), on the other hand, can elegantly preserve solute memory in passing from one radial position of a throat to the next, through appropriate mappings at the pores/joints (and, thus, seem to be the next simplest method of choice).

It is possible that the smearing problem is not particularly pronounced for the disordered media often considered in the literature (and section 4.3.3.1); in which case

STM can be used. This may also justify the use of ensemble average pore-to-pore transition probabilities for performing random hops form one pore to the next, e.g. Bijeljic and Blunt (2006). In ordered media, however, discarding particle memories will almost certainly lead to gross errors (e.g. figure 4.12b), unless Peclet numbers are sufficiently low. Memory preserving pore-to-pore transition probabilities are, thus, required for efficient and accurate simulations of transport in ordered media and will be the subject of a future investigation.

### 4.3.5 Applications to field-scale modeling

We provide a brief account on how STM can additionally be applied at the field scale without further modifications. Consider the two-dimensional macroscopic domain in figure 4.13 for simplicity (3D case follows identically). The domain is discretized into Cartesian grids, which are delineated by bold solid lines. Now, one can always define a dual grid such as the one depicted by the dashed lines. We refer to this dual grid as the macroscopic "network". This network consists of smaller (than the original Cartesian mesh) control volumes (or "pores") denoted by $\Omega_P$, connected to each other by the space in between them (or "throats") denoted by $\Omega_T$. In figure 4.13, the two macroscopic pores $\Omega_P^i$ and $\Omega_P^j$ are connected to each other by the macroscopic throat $\Omega_T^{ij}$. Note that both the pores and the throats have volumes. Through the foregoing analogy with network modeling, the applicability of STM becomes immediately apparent. The only difference is that the required elementary forward/backward transport rate expressions (such as those given by eq. 4.6) for the throats (i.e. $\Omega_T$), must be obtained from pore-scale simulations, or even experiments, on representative samples. The procedure is identical to that described in section 4.2.1.1 for microscopic cylindrical throats. Namely, 1 and 0

dirichelet boundary conditions are imposed interchangeably at the inlet and outlet of the pore-scale domain and solute inflow/outflow rates are computed (see figure 4.1). Admittedly, the foregoing proposed approach is not without ambiguity. For instance, it is not clear precisely what dimensions shall be chosen for $\Omega_P^i$. Nevertheless, the approach can be used to perform efficient field-scale simulations of non-Fickian and anomalous transport (as long as the problem is linear), for which the macroscopic advection-dispersion equation (CDE) breaks down.

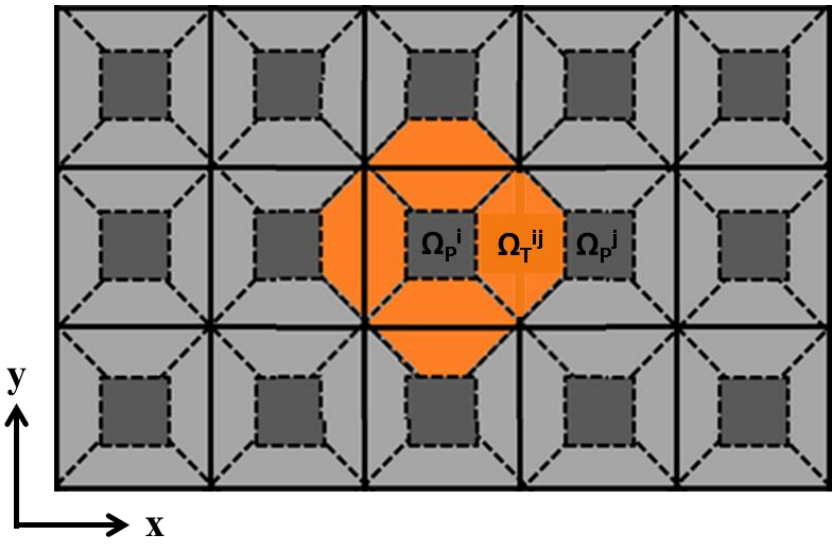


Figure 4.13: Schematic of a two-dimensional field-scale domain, discretized into Cartesian grids delineated by the bold solid lines. The dual "network" grid is shown with dashed lines, where $\Omega_P$ and $\Omega_T$ represent macroscopic "pores" and "throats", respectively. STM is applicable on this dual grid.

## 4.4 CONCLUSIONS

The following summarizes our main conclusions:

- Semi-empirical expressions for solute flow rates at the inlet/outlet of a cylindrical duct under forward/backward transport were developed. These expressions are mass conservative and are valid for all Peclet numbers and $\kappa \in [1\text{-}20]$ (they shall not be used for $\kappa < 1$). They can be easily extended to non-circular cross-sections (as described in section 4.2.1.1), and are thought to be useful in their own right (e.g. as transit time distributions in particle tracking, outflow/inflow solute flow rates of arbitrary input signals when appropriate convolutions are preformed, useful tools in analyzing experimental data for short tubes, etc.).
- A novel Eulerian model (i.e. STM) for simulating *linear* solute transport on pore networks was developed. Its unique feature is the proper incorporation of shear dispersion within throats, and is the first Eulerian network model, to our knowledge, with this capability. STM can simulate on networks with either zero or finite pore volumes. The model was verified against numerically integrated convolution expressions for one-dimensional strings of pores and throats (see section 4.3.1).
- We replaced the rather arbitrary rate expressions of MCM with steady state solute flow rates obtained from CFD simulations (referring to the resultant model as rmMCM). rmMCM appears to be a generalization of the plug-flow model of Milligen and Bons (2014), and is shown (in section 4.3.3.1) to differ only marginally from MCM (and only in the transition regime i.e. $0.3 < Pe_d < 6$) for a sphere pack.
- Three different conceptualizations of (two) one-dimensional three-pore geometries (solved with MCM and STM) were compared to CFD simulations (see figure 4.5). In general, a one-to-one mapping of the pore/throat geometries, or dimensions, approximating pores (or pockets in SSM) with CSTRs, and including

parabolic velocity profiles within throats, seems to be the minimum requirements for satisfactory predictions. More specifically, if the pore-to-throat residence time ratio is $\leq$ 1, $STM2_{par}$ is the most accurate conceptualization. If >>1, details of the transport physics within throats is immaterial and MCM is the simplest method to use.

- Longitudinal dispersion coefficients for a sphere pack were computed via $STM_{par}$ (= parabolic velocity profiles within throats), and shown to agree quite well with experimental data from the literature. $STM_{par}$ produced all known dispersion regimes in agreement with previous theoretical and experimental works. MCM and rmMCM predictions were very good for $Pe_d$ <1, but with under-predictions of up to a factor of ~2.5 compared to $STM_{par}$ for $Pe_d$ >100. Similarly, $STM_{plug}$ values were lower by a factor of ~1.5 compared to $STM_{par}$. None of MCM, rmMCM, and $STM_{plug}$ could reproduce the power-law regime for a disordered sphere pack. MCM dispersion coefficients were accurately described by the algebraic addition of molecular and mechanical dispersion coefficients, and agreed very well with the theoretical results of Aris and Amundson (1957) at high $Pe_d$.
- A discussion on the origin of supra-linear dispersion was provided, in conjunction with an analysis of past numerical results from the literature. It was argued that the supra-linearity observed in models neglecting shear dispersion (e.g. Milligen and Bons, 2014) is purely topological and due to contributions from hold-up dispersion. The higher than typical power-law exponents (i.e. $\delta$) obtained in the literature (e.g. Acharya et al., 2007a) are similarly thought to be the result of additive effects of hold-up dispersion and boundary-layer dispersion. An intuitive explanation for the origin of the power-law regime in figure 4.10b (for a sphere

pack) was provided by linking it to figure G.2a (for a single throat) (see section 4.3.3.2).

- It was shown that *all* Eulerian network models are inherently limited for describing longitudinal dispersion in *ordered* porous media (including SSM from chapter 3). Specifically, sufficient smearing of the solute at the pores eventually results in a Gaussian distribution even in the absence of diffusion, which is unrealistic. Particle tracking models that consist of a series of Markovian hops from one pore to the next, are similarly limited. What is necessary is an accurate mapping of solute concentrations from the radial positions of one throat to the next, which is elegantly handled under a Lagrangian framework.
- STM is currently limited by computer memory requirements, which prevents simulation on very large domains. This is because STM dynamically records pore concentration histories with a set frequency given in eq. 4.15, which is quite conservative. In section 4.2.1.3, we proposed practical solutions that could dramatically reduce said requirements as well as improve overall computational performance and accuracy. We note that, even in its current form, STM is computationally more efficient than particle-tracking methods for certain boundary conditions and domain sizes (few thousand pores). The continuous injection of solute is one such scenario. On the other hand, particle tracking provides considerable flexibility for modeling truly infinite (i.e. periodic) domains, whereas STM is limited to only finite domains. In this regard, the two can be considered complementary to each other.
- Applicability of STM extends far beyond passive tracer transport at the pore scale. In essence, regardless of the underlying physics, if "response functions" to elemental inputs (e.g. unit step/Dirac delta) are known for a set of bonds (e.g. eq.

4.6), the response of any network assembled thereof to any input can be computed via STM (e.g. transmission of voltage signals through interconnected electrical networks, non-Fickian transport at the field scale, etc.). This is what makes the method so useful and worthy of further pursuit.

# Chapter 5: Reactive Transport with Applications to $CO_2$ Sequestration[2]

In this chapter, we focus on a slightly larger scale compared to the previous two chapters, namely one that consists of a conglomeration of multiple (millimeter-scale) pore-scale domains. Such scales allow one to directly observe macroscopic manifestations of various pore-scale physics (without passing through an upscaling filter), and therefore offer access to the responsible fundamental mechanisms. Here, we test whether unexpected emergent behavior can arise from the coupled interaction between various components of a simplified flow and reactive transport model on a domain with large-scale heterogeneities. We develop tools and methods to test this hypothesis. The developed model as well as the emergent behavior of interest (observed at the field scale) fit into the context of $CO_2$ sequestration and storage.

## 5.1 MOTIVATION

Safe and economic storage of $CO_2$ emitted from fossil fuel combustion in depleted hydrocarbon reservoirs and saline aquifers requires an accurate assessment of leakage risk from the reservoir into freshwater aquifers and to the surface. Natural seeps of $CO_2$ illustrate that $CO_2$ is prone to migrate to the surface either as a dissolved phase in moving groundwater or as a buoyant-free gas phase given suitable flow pathways such as connected fault and fracture systems (Pearce et al., 2004; Shipton et al., 2004; Dockrill and Shipton, 2010). Under common thermobaric gradients, upward moving groundwater

[2] The material in this chapter was published under the following reference, which was completed under the supervision of Matthew Balhoff, and co-supervisions of Steven Bryant and Peter Eichhubl. Assistance with some preliminary modeling was received from Tie Sun during the early stages of the project.

Mehmani, Yashar, Tie Sun, M. T. Balhoff, P. Eichhubl, and S. Bryant. "Multiblock pore-scale modeling and upscaling of reactive transport: application to carbon sequestration." Transport in porous media 95, no. 2 (2012): 305-326.

containing dissolved $CO_2$ will approach saturation relative to $CO_2$, favoring $CO_2$ exsolution and the precipitation of carbonate as pore- and fracture-filling cements and as travertine at the earth's surface (Eichhubl and Boles, 2000; Moore et al., 2005). Carbonate cement may occlude pore space reducing further $CO_2$ leakage and potentially leading to self-sealing of $CO_2$ leakage pathways. Carbonate precipitation reactions, their effect on permeability reduction in porous sediment, and their spatial distribution relative to flow conduits are thus of interest in the context of geologic carbon sequestration.

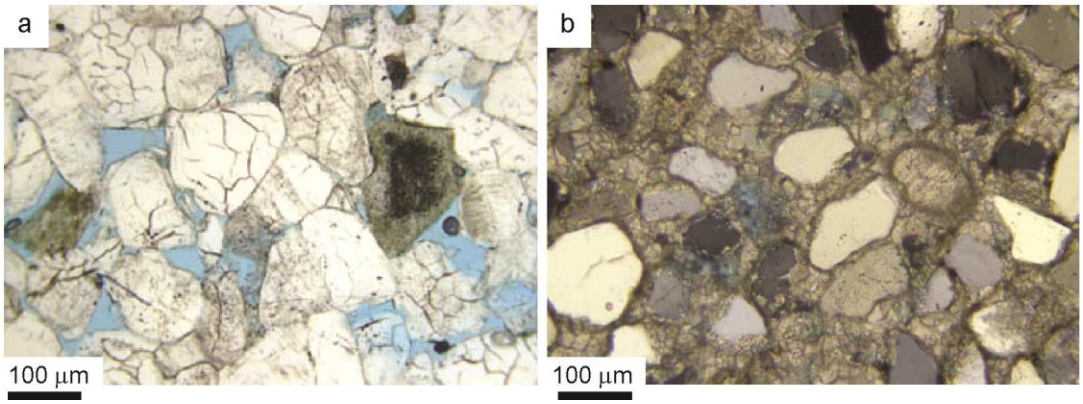


Figure 5.1: (a) Sandstone of the Salt Wash Member of the Morrison Formation sampled ~100 m away from the Little Grand Wash fault, Utah; blue indicates porosity filled with epoxy. (b) Same sandstone with porosity occluded by calcite cement ~1 m from of a natural $CO_2$ flow conduit along the Little Grand Wash fault.

Carbonate pore cement completely occludes sandstone porosity in the vicinity of fossil and active natural $CO_2$ seeps along the Little Grand Wash fault near Green River, Utah (fig. 5.1). Uranium series dating of travertine deposits capping these fossil seeps suggest that, over timescales of $10^5$ years, the seepage sites at the surface have shifted

along fault strike (Burnside et al., 2009). These shifts in seepage may imply that preferential pathways can be diverted as a result of reactive transport with $CO_2$. The formation of these preferential pathways would likely initiate at the pore scale and, therefore, pore-scale modeling is one approach for gaining insight into the controlling fundamental processes. Here, we use pore-network modeling due to its simplicity and flexibility.

The need for large pore networks in studying reactive transport processes is often cited in the literature (e.g. Fredd and Fogler, 1998; Kim et al., 2011). However, this poses several technical and computational problems. First, large pore networks are computationally difficult to solve because of their correspondingly large systems of equations. Second, if there are heterogeneities in the form of abrupt changes in pore structure, it may be difficult to characterize them within a single network. Third, it is difficult to obtain high-resolution images of relatively large samples (from which pore networks are extracted). For example, if X-ray microtomography (XMT) is used, large domains mean less resolution at the pore scale. One solution to these problems is domain decomposition. It may be more feasible to image a larger sample if broken up into smaller subdomains and then imaged one at a time. Computational benefits also arise from the decomposition, because computational cost often scales non-linearly with problem size. In addition, parallel computing follows naturally. Finally, if abrupt changes in pore structure do exist (which is the case in this chapter), network generation and solution is more manageable as subdomains. In this chapter, we draw on mortar domain decomposition methods developed by previous authors in the literature (see chapter 2).

In this study, we model single-phase advection-dominated flow and reactive transport at the pore scale, with application to precipitation during carbon sequestration. New mortar basis functions are introduced that are specifically designed for pore-scale

subdomains, along with a new approach for coupling species transport at the pore scale. Although the assumptions regarding the geochemistry and reactions are relatively simple, our goal is to investigate the effects of calcite precipitation on large-scale preferential flow paths as well as the possibility for the emergence of new ones. Specifically, our aim is to determine if the macroscopic observations of redirected flow paths at field sites, such as Little Grand Wash fault, can be qualitatively predicted from the coupled effects of simplified pore-scale physics.

## 5.2 MODEL DEVELOPMENT

### 5.2.1 Physical and mathematical description of the problem

Our goal is to model the generation and precipitation of calcite during carbon sequestration which results in reduced permeability and possibly the redirection of preferential flow paths. We assume that $HCO_3^-$ is formed first by a dissociation reaction. The $HCO_3^-$ then reacts with calcium to form $CaCO_3$ which then precipitates onto pore walls. For the application to upward migration of brine saturated with $CO_2$ at deep storage conditions, we assume that bicarbonate anion concentration is in equilibrium with dissolved $CO_2$ at depth, and that the brine is also equilibrated with respect to calcite dissolution. As the brine rises, fluid pressure decreases and at some point dissolved $CO_2$ comes out of solution to form a gas phase. The exsolution perturbs the equilibrium composition in the aqueous phase and causes calcite mineral to precipitate. Our modeling focuses on the rock at this $CO_2$ exsolution depth. Although a $CO_2$ gas begins to come out of solution at this depth, we assume that the gas phase is small and does not have a significant effect on the flow field and is not involved in the reactive transport; therefore, flow is modeled as single phase. The effective reactions studied here are summarized as:

$$CO_{2(g)} \rightleftharpoons CO_{2(aq)}$$
$$CO_{2(aq)} + H_2O \xrightarrow{k_1'} HCO_3^-{}_{(aq)} + H^+_{(aq)}$$
$$Ca^{2+}_{(aq)} + 2\left(HCO_3^-\right)_{(aq)} \xrightarrow{k_2} CaCO_{3(s)} + H_2O + CO_{2(aq)} \qquad (5.1)$$

Equation 1 is a simple description of precipitation reactions that occur during carbon sequestration. In reality, there are several complex chemical reactions present but since the focus of this work is on emergent behavior across length scales, we have chosen to investigate a simpler approximation of precipitation.

The perturbation of the bicarbonate concentration is represented as a first-order rate process (with rate constant $k_1'$). In the vicinity of the exsolution depth, this rate is approximately constant. The rate of mineral precipitation is assumed to be first order in the distance-from-equilibrium of the bicarbonate concentration (with rate constant $k_2$). Calcium ion ($Ca^{2+}$) is assumed to be present initially in abundance which implies that the reaction rate is independent of $Ca^{2+}$ and that its (relatively constant) concentration can be lumped in with the rate constant. It also means the reaction is always a forward reaction because $Ca^{2+}$ is also available at large concentrations, or at least until the porous medium cements up completely. Using these assumptions, the rate laws for the two components ($HCO_3^-$ and $CaCO_3$) are written as follows:

$$r_{HCO_3} = k_1'\left(p_{CO_2} - p_{CO_2}^{eq}\right) - k_2\left(c_{HCO_3^-} - c^{eq}_{HCO_3^-}\right) \approx k_1 - k_2\left(c_{HCO_3^-} - c^{eq}_{HCO_3^-}\right)$$
$$r_{CaCO_3} = \frac{1}{2}k_2\left(c_{HCO_3^-} - c^{eq}_{HCO_3^-}\right) \qquad (5.2)$$

The equilibrium partial pressures and concentrations are taken as constants in eq. 5.2. Concentration of bicarbonate (i.e. $c_{HCO3}$) is initialized to its equilibrium value (i.e. $c_{HCO3}^{eq}$) in the system. The medium is then flooded while maintaining a constant boundary condition at the inlet (due to gas exsolution), which is higher than the equilibrium concentration, thereby insuring that the calcite precipitation reaction proceeds only in the forward direction.

In this study, changes in pore concentrations occur as a result of both advection and reaction. The Damköhler number ($Da = k_2 L/v_{int}$; where $L$ is the length of the pore-scale domain and $v_{int}$ is the mean interstitial velocity*)* is the dimensionless group that describes the relative rate of reaction to advection. The numerical formulation presented here is limited to relatively low Damköhler numbers ( $Da << 2\rho_{caco3} / \left( c_{in,HCO_3^-} - c_{HCO_3^-}^{eq} \right)$ ) because of the quasi steady-state assumption of the flow equation. The assumption of low $Da$ is consistent with the physical problem since calcite precipitation is a very slow process compared to advection. Diffusion is assumed negligible, meaning that the Peclet number ($Pe_d$ defined in chapter 4) is large (> 10). This assumption is reasonable for typical ion diffusion coefficients and velocities observed in carbon sequestration. Near faults and abandoned wells (where one might be most concerned with transport in carbon sequestration), advection would be more dominant (i.e. higher $Pe_d$). There are, however, many situations (including carbon sequestration) in which diffusion is significant and may dominate over advection (low $Pe_d$). Since our goal is to determine if preferential pathways are redirected, we focus on advection-dominated transport.

### 5.2.2 Numerical solution in a single network

Modeling is performed using pore-scale network models. The networks are mapped directly from computer-generated, periodic grain packings. Several grain packings are created with porosity 12–41% in a domain that is $1\times1\times1 mm^3$. The number of grains varies from 100 to 10,000 (number of pores vary from ~400 to ~40,000), which results in large permeability variations. All networks are mapped from the grain packs using a modified Delaunay tessellation (Al-Raoush et al. 2003). During creation of the network model, we extract pore-level information including pore positions, volumes, interconnectivity, throat conductivities, and lengths.

In order to solve the transport and precipitation process, we employ an implicit pressure, explicit concentration (IMPEC) approach in which we first solve for pore pressures and flow rates and then solve for species concentration in each pore at a given time step. The specific steps in the time-dependent scheme are summarized as follows:

1. Compute the pressure field and the flow field in the network
2. Compute the concentration field (under advection and reaction) in the network
3. Update pore volumes and throat conductivities due to mineral precipitation
4. Calculate reduced porosity and permeability in the network
5. Advance to next time step and repeat

The first step requires the solution of the flow equation given by eq. 3.2 (section 3.2.1), which yields the pore pressures and throat flow rates throughout the network. Approximating throats with cylinders, the flow equation can be written as eq. (5.3); which assumes single phase and creeping flow ($Re << 1$).

$$\sum_j q_{ij} = \sum_j \frac{\pi R_{ij}^4}{8\mu L_{ij}} \left( p_i - p_j \right) = 0 \tag{5.3}$$

In eq. 5.3, $R_{ij}$ and $L_{ij}$ represent throat radius and length, respectively. All other variables have the same definition as in section 3.2.1. For a single network model, a pressure gradient is imposed in one direction and either no-flow or periodic boundary conditions are implemented on the remaining two. More rigorous boundary conditions are imposed on the network in the context of multi-block modeling as discussed in section 5.2.3. For the second step in the IMPEC approach, an advection-reaction transport equation needs to be solved. Here, we use the MCM formulation from section 3.2.2 due to its simplicity. With regard to all the other assumptions made herein, using the relatively more complicated formulations of SSM or STM (developed in chapters 3 and 4) seems unjustified. The species balance equation for pore *i*, thus, follows:

$$\begin{aligned} V_{p,i} \frac{dc_{HCO_3^-,i}}{dt} &= \sum_{j=1}^{N_i^{th,q<0}} q_{ij} c_{HCO_3^-,i} + \sum_{j=1}^{N_i^{th,q>0}} q_{ij} c_{HCO_3^-,j} + V_{p,i} \left( k_1 - k_2 \left( c_{HCO^-{}_3,i} - c^{eq}{}_{HCO_3^-,i} \right) \right) \\ V_{p,i} \frac{dc_{CaCO_3,i}}{dt} &= \frac{V_{p,i} k_2}{2} \left( c_{HCO^-{}_3,i} - c^{eq}{}_{HCO_3^-,i} \right) \end{aligned} \tag{5.4}$$

In eq. 5.4, $c_{CaCO3,i}$ and $c_{HCO3,i}$ represent the concentration of calcite and bicarbonate in pore *i*, respectively. All other variable definitions are the same as in section 3.2.2. We implement an operator-splitting approach in which we decouple advection and reaction in eq. 5.4. The reactive part of the equations is amendable to an analytical solution, which is summarized in appendix J. Since we have assumed that calcite precipitates on the pore walls, it is not transported to the next pore. Furthermore, since calcite concentration is a function of pore volume, we can effectively solve the transport equation for bicarbonate only, and update the pore volume (see appendix J). The advective part of the transport

equation is solved explicitly using eq. 5.5a. The intermediate concentrations obtained from eq. 5.5a are then used as initial conditions in the reaction step (i.e. eq. 5.5b). In eq. 5.5.b, $\Delta c_{HCO3}|_{reaction}$ denotes the change in concentration due to reaction and is computed using the analytical expressions in appendix J.

$$c^{l+1/2}{}_{HCO_3^-,i} = c^{l}{}_{HCO_3^-,i} + \frac{\Delta t}{V_i}\left[\sum_{j=1} q_j c^{l}{}_{HCO_3^-,j} - \sum_{k=1} q_k c^{l}{}_{HCO_3^-,i}\right] \tag{5.5a}$$

$$c^{l+1}{}_{HCO_3^-,i} = c^{l+1/2}{}_{HCO_3^-,i} + \Delta c_{HCO_3^-}\Big|_{reaction} \tag{5.5b}$$

In the third step, pore volumes are updated using the analytical expressions in appendix J. In network modeling, we typically envision the pores containing all the void volume and throats providing resistance to flow. Therefore, the reduction in pore volume should correspond to a reduced conductivity in the connecting throats. Allocation of reduced volume to adjacent throats is accomplished by distributing the precipitated cement amongst out-flowing throats and proportional to the magnitude of their flow rate. The following equations account for the change in throat volumes (i.e. $V_{tij}$) and radii (from which their hydraulic conductivities are recalculated):

$$\Delta V_{t_{ij}} = \Delta V_{p_i} \frac{q_{ij,out}}{\sum_j q_{ij,out}} \qquad R_{ij}^{l+1} = \sqrt{\frac{V_{t_{ij}}^{l} - \Delta V_{t_{ij}}}{\pi L_{ij}}} \tag{5.6}$$

Once pore volumes and throat conductivities are updated, porosity and permeability (step 4) can be computed. Porosity is calculated as the sum of pore volumes divided by the bulk volume of the network. By imposing a pressure gradient in one dimension, computing bulk flow rates within throats (eq. 5.3), and obtaining the Darcy velocity, permeability can be back-calculated using Darcy's law. Finally, the above procedure is repeated for subsequent time steps leading to an evolution of pressure,

concentration, and pore space geometry/topology in time. Time steps are restrained and adaptively calculated using the Courant–Friedrichs–Lewy (CFL) condition to ensure stability, and are taken as the minimum of all pore residence times.

### 5.2.3 Numerical solution in coupled, multi-block networks

In order to examine potential emerging patterns, we simulate flow and transport at scales larger than a single pore network. This is accomplished by coupling several heterogeneous network models in a multi-block framework to form a much larger domain. For this approach to produce accurate results, we must impose boundary conditions at subdomain interfaces in such a way that ensures continuity (mass conservation) from one block to the next. In the current approach, each subdomain (i.e. pore network) is solved independently at a given time step with guessed interface conditions and the approach described in section 5.2.2. Correct interface conditions are found iteratively by coupling flow and then species transport. Coupling flow involves finding the pressure field at all network interfaces using finite-element mortars to ensure that fluxes match (in weak finite-element sense). The mathematics and successful implementation of the mortar technique on pore-scale models can be found in several works (Balhoff et al., 2008; Sun et al., 2012a), but are summarized here:

1. Guess Lagrange multipliers (= $\beta$) of FEM basis functions. Basis functions along with their Lagrange multipliers describe the pressure field at network interfaces. The bases can be chosen from a number options typically bilinear or biquadratic polynomials (in this study, we develop new piecewise constant mortars on specially designed grids).

2. Project these boundary conditions on each network model and solve the individual networks for pore pressures and throat flow rates
3. Calculate the jump in fluxes (F) across network boundaries and calculate the Jacobian (J) of partial derivatives of the interface problem
4. Update Lagrange multipliers by solving $J\, d\beta = -F$

The procedure is repeated until continuity of flux at all interfaces is reached. For problems linear in flow (such as this one), the solution converges in only one iteration. After the pressure field is determined, ensuring continuity of the convecting bulk phase (in this case water), we attempt to ensure continuity for each component. In this study, we implement a technique we refer to as *transport coupling* (iterative mortar coupling for transport is not required since diffusion is not included).

Transport coupling involves: (1) grouping the interface throats (or points) into bundles that are allowed to communicate, which is labeled here as interface pore partitioning (IPP), and (2) projecting averaged concentration values to the downstream throats of each bundle. We have developed a raw-grid-based IPP (RGBIPP) method that has the capability to control bundle size. The method groups throat-clusters from one side of the interface with clusters from the other side, based on the proximity of their centroids. A raw Cartesian mesh is initially created at the interface; grids containing throats from both sides are then identified and grouped. Bundles containing only throats from one side are merged with previously grouped bundles (based on proximity of clusters measured by the distance between their centroids). Empty grids are ignored. The result is bundles with at least one throat from either side (fig. 5.2). Peterson et al. (2012) used a much simpler approach for matching regularly spaced boundary throats on a 1D

interface, in capillary-dominated flow. The method offered here is more rigorous and general.

The IPP serves two purposes: (1) defining a new mortar space for flow, uniquely designed for pore-scale models; (2) providing a mesh for transport coupling. The mortar space is defined by considering piecewise discontinuous basis functions over each bundle. This will provide localized flux continuity over each bundle which is essential for transport coupling. The bundles are also used to calculate an averaged concentration to be projected onto the downstream side of the interface. Several approaches could be used to project concentrations to ensure continuity of species fluxes; the following is used in this study because of its simplicity:

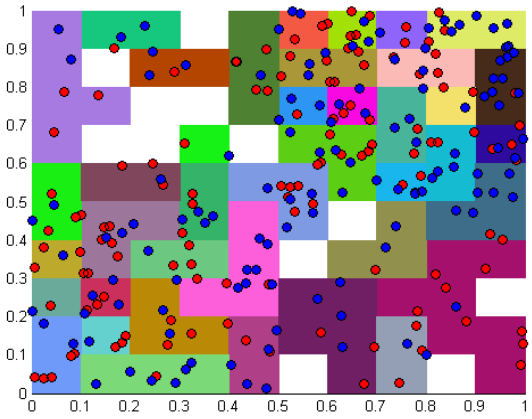


Figure 5.2: Schematic of RGBIPP mesh. Each bundle is represented by a uniform color, and the blue and red dots are boundary throats of sub-domains on either side. Note the more densely populated regions in the top-right and bottom-left corners and the appropriately refined mesh sizes in these regions.

$$\bar{c}_{ds} = \frac{\sum_j c_{i,us} q_{ij,us}}{\sum_j q_{ij,ds}} \tag{5.7}$$

In eq. 5.7, *us* and *ds* refer to upstream and downstream, respectively. $c_{ds}$ is the bundle concentration, $c_{i,us}$ is the concentration of pore *i* connected to the bundle from the upstream side. $q_{ij,us}$ and $q_{ij,ds}$ represent throat flow rates directed in and out of the bundle from the upstream and downstream sides, respectively. Note that the localized flux continuity ensured by the IPP mortars automatically ensures continuity in concentration from the upstream to the downstream side of each bundle via eq. 5.7 (which would not have been achievable through typical Lagrangian mortars e.g. bilinear or biquadratic). Another advantage that IPP mortars offer is that, finer meshing is used in more densely populated sections of the interface, thereby reducing the number of degrees of freedom required to solve the interface problem.

The mortar/transport method, as described above, has the benefit of solving the problem in parallel since each subdomain becomes independent of the other. However, there are some limitations as to when this method would actually be computationally efficient. Eq. 5.8 serves as a rough criterion to determine when this is true for a problem that follows a *p*-order scaling of computational cost with problem size. In eq. 5.8, $\rho_{dof}$ is the number of mortar degrees of freedom per subdomain, $N_{cpu}$ is the number of available processors, and $N_{blk}$ is the total number of subdomains. This computational limit is imposed from the mortar coupling step. Transport coupling through IPP, however, is very efficient and no parallelism is required. Nevertheless, marching the advection-diffusion-reaction equation through time subsequent to transport coupling is block-independent and is performed in parallel.

$$\frac{\rho_{dof}}{N_{cpu} \times N_{blk}^{(p-2)}} < 1 \tag{5.8}$$

In chapter 6, we shall provide a detailed exposition on the computational analysis as well as extensions of the coupling methods discussed herein to cases where diffusion and pore-to-continuum interfaces are present.

## 5.3 RESULTS AND DISCUSSION

### 5.3.1 Regimes

A single network model was created using the approach outlined in the section 5.2.2. The periodic network has 8184 pores, 18770 throats, and a domain size of $2\times1\times1\text{mm}^3$. Boundary conditions were implemented by imposing a constant flow rate in the *x*-direction and no-flow boundary conditions on the four other faces. The inlet condition of component $HCO_3^-$ is equal to the initial condition, i.e. $c^*_{HCO3} = 20$ ( $c^*_{HCO_3^-} = c_{HCO_3^-} \big/ c^{eq}_{HCO_3^-}$ ), as in all simulations presented in this chapter. We solve the network as a single domain to obtain pore pressures, concentrations, and cement distributions. Macroscopic properties (such as permeability, connected porosity, percent cement, and outflow concentration as a function of time) are back-calculated from the model. In doing so, we attempt to qualitatively identify the dependency of the precipitation process with respect to the two controlling dimensionless numbers in this problem: *Da* and $\alpha$ (i.e. eq. 5.9).

$$\alpha = \frac{k_2 (c_{in,HCO_3^-} - c^{eq}_{HCO_3^-})}{k_1} \tag{5.9}$$

In eq. 5.9, $\alpha$ describes the relative rate of the third ($CaCO_3$ precipitation) reaction in eq. 5.1 to the second ($CO_2$ dissociation). Figure 5.3 shows spatial maps of cement for different transport regimes, taken at the same throughput (0.6 pore volumes), corresponding to different values of *Da* and $\alpha$. For high values of $\alpha$, the rate of precipitation is faster compared to the rate at which $CO_2$ dissociates; thus, causing rapid cementation at locations with higher concentrations of bicarbonate. Here, these locations are naturally at the inlet region where a constant concentration front is injected into the medium. This effect can be seen in figure 5.3a. Keeping *Da* constant and decreasing $\alpha$ caused dissociation to occur at a much faster rate throughout the domain thus providing large amounts of bicarbonate to be converted to cement everywhere, yielding a rapid but uniform cementation pattern (fig. 5.3c). The transition between these two figures can be seen in figure 5.3b. The rapid precipitation is due to the dependence of the rate on the "distance" of bicarbonate concentration from equilibrium.

When *Da* was lowered for high and medium values of $\alpha$ i.e. $\epsilon$ [1-100], rate of convection dominated over the rate of precipitation and, thus, created a semi-uniform concentration field prior to significant cementation. This yielded a more uniform cementation pattern as shown in figure 5.3d-e. However, when $\alpha$ was also low, $CO_2$ dissociated at a faster rate, which combined with fast convection created a shock front near the outlet, thus shifting the cementation pattern towards the outlet (or in larger domains further away from the inlet). Figure 5.3f clearly demonstrates this situation.

Figures of macroscopic properties (normalized permeability, connected porosity, percent cement, and dimensionless outlet concentration) as a function of (initial) pore volumes of fluid injected for the six cases are shown in figure 5.4. Permeability was normalized against its initial value. Decreasing $\alpha$ or increasing *Da* causes permeability and connected porosity to decrease, and cementation percentage to increase at a much

faster rate with pore volumes injected. On the other hand, increasing $\alpha$ or deceasing *Da* has the opposite effect. Figure 5.4d depicts that concentration front sharpens as *Da* is decreased (especially for $\alpha \in$ [1-100]), and that outflow concentration increases as $\alpha$ is decreased. It should be noted that when α is small, concentration shocks may form away from the inlet that cause peaks in outflow concentration profiles (prior to breakthrough) that are also responsible for more cementation towards the outlet (fig. 5.3f).

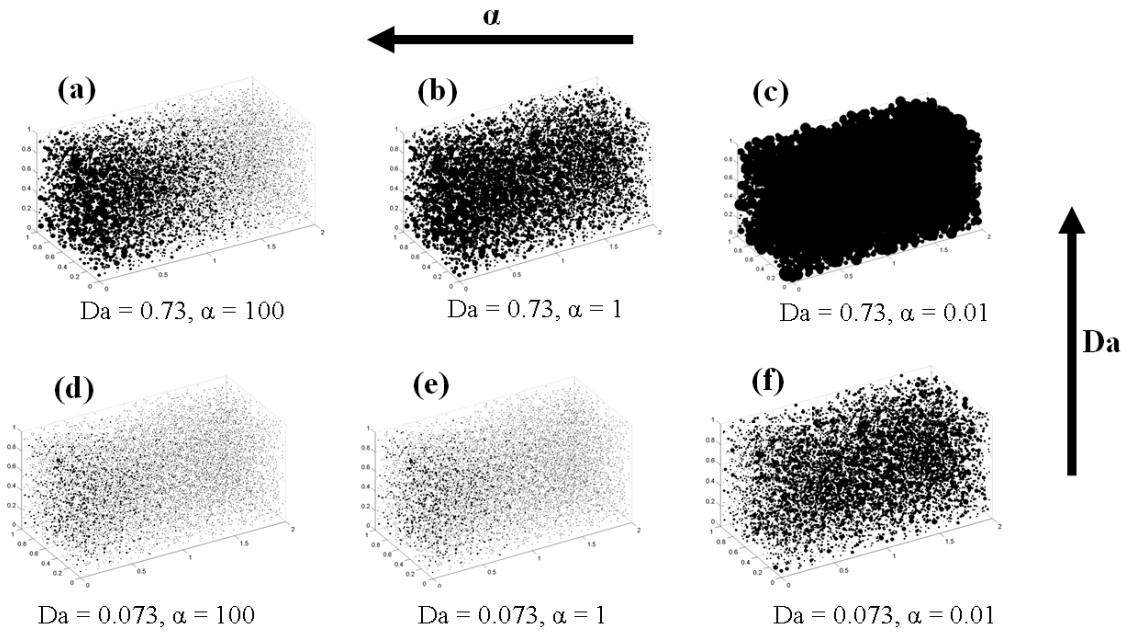


Figure 5.3: Spatial maps of cementation patterns for different values of *Da* and $\alpha$.

### 5.3.2 Verification of coupling method

We verify the accuracy of the mortar and transport coupling approach by slicing the network from the previous section (i.e. fig. 5.3) at the centerline ($x$ = 1.0 mm) and comparing the coupled networks to the unsliced single-network solution. We couple

pressures and overall flux with the specially designed mortars, using the RGBIPP method (with a raw grid of 10×10). Concentrations of $HCO_3^-$ are then matched at the interface using transport coupling. The solutions obtained via coupling are compared to the "whole" (i.e. unsliced) network solution at early and late times in figures 5.5-7 (0.4 and 1.0 pore-volume throughputs, PVTP, respectively). In these figures, $\alpha = 100$ and $Da = 0.73$ which corresponds to the top-left regime shown in figure 5.3. This regime was chosen because it had the most variation in the spatial distribution of cement thus providing the most sensitive case (compared to the others shown) to couple.

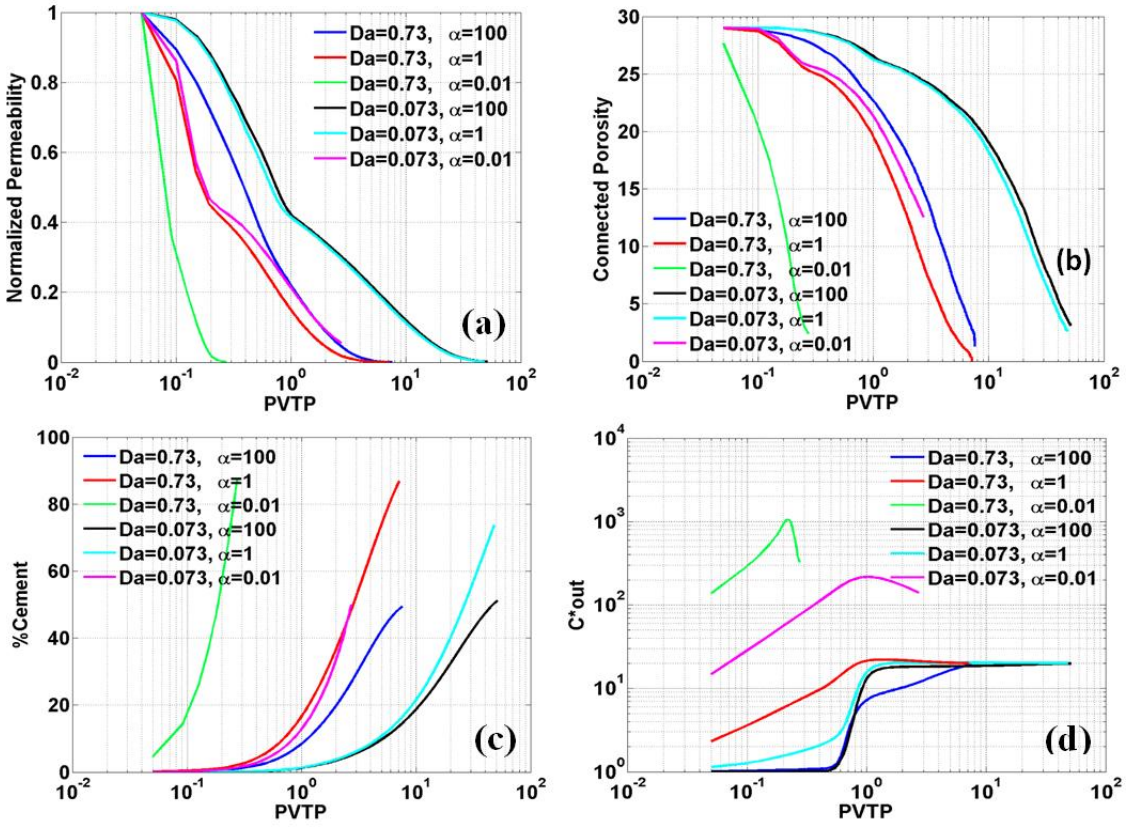


Figure 5.4: (a) Normalized permeability (b) connected porosity (c) percent cement (d) outlet concentration for the six regimes studied.

Figure 5.5 shows the flow rate and concentration fields at the centerline ($x = 1.0$) for both the whole solutions (top row) and the mortar solution (bottom row) at early (left column) and late (right column) times. Figure 5.6 shows similar information about the pressure and concentration fields of the entire domain. The color bars represent dimensionless concentration values, normalized flow rates (against injection flow rate), and normalized pressure (against inlet pressure at each time). The whole, single-network solution and the mortar, multi-block solution match very well and are nearly indistinguishable (at least qualitatively).

Figure 5.7 demonstrates that the mortar/transport coupling method yields very close approximations to the macroscopic properties of the whole solution. The plots are semi-logarithmic in the $x$-axis (and in terms of pore-volume throughput). The plots depict how normalized permeability (against initial permeability), connected porosity, cementation percentage, and dimensionless outflow concentration match between the single-domain solution and the mortar/transport multi-block solution. The permeability plot has about ~10% error at initial times, but decreases at later times. This error can be reduced by using a finer mesh for the mortar space (Sun et al. 2012a). Here, this can be achieved by refining the RGBIPP. These results verify the mortar/transport coupling algorithm as an accurate upscaling tool for advection-dominated reactive transport problems.

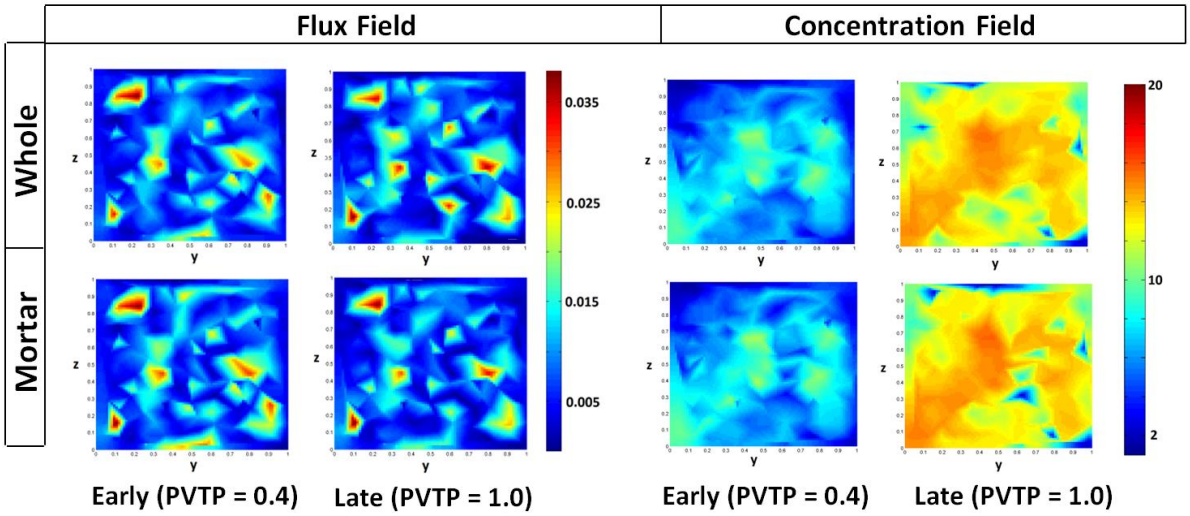


Figure 5.5: Comparison of flux and concentration fields at the centerline plane ($x$ = 1.0mm) of the whole solution and mortar solution at early (left column) and late (right column) times. Color bars represent dimensionless concentration and normalized flow rates (against injection flow rate).

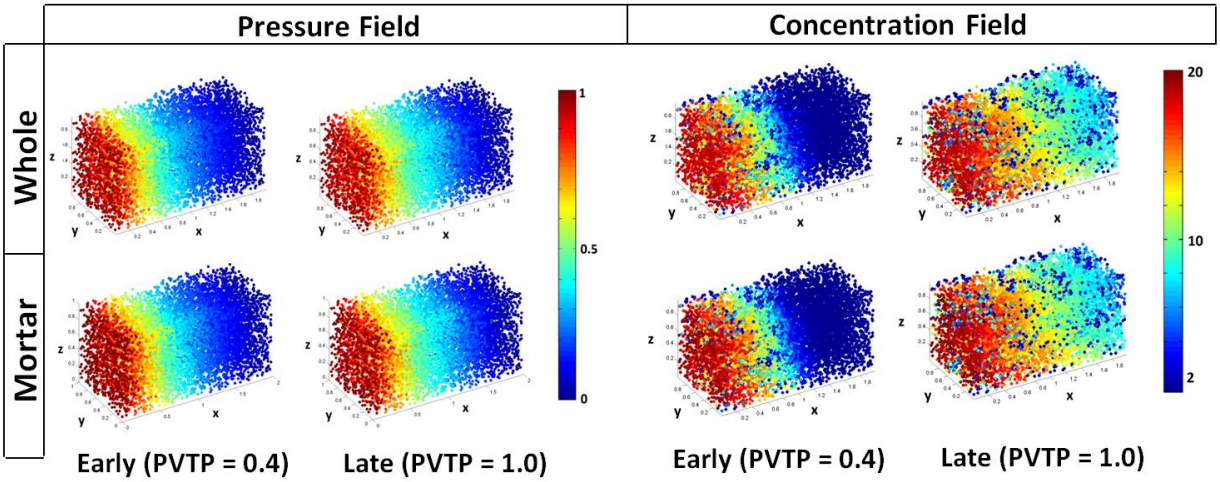


Figure 5.6: Comparison of pressure and concentration fields of the whole solution and the mortar solution at early (left column) and late (right column) times. Color bars represent dimensionless concentration and normalized pressure values (against inlet pressure at each time).

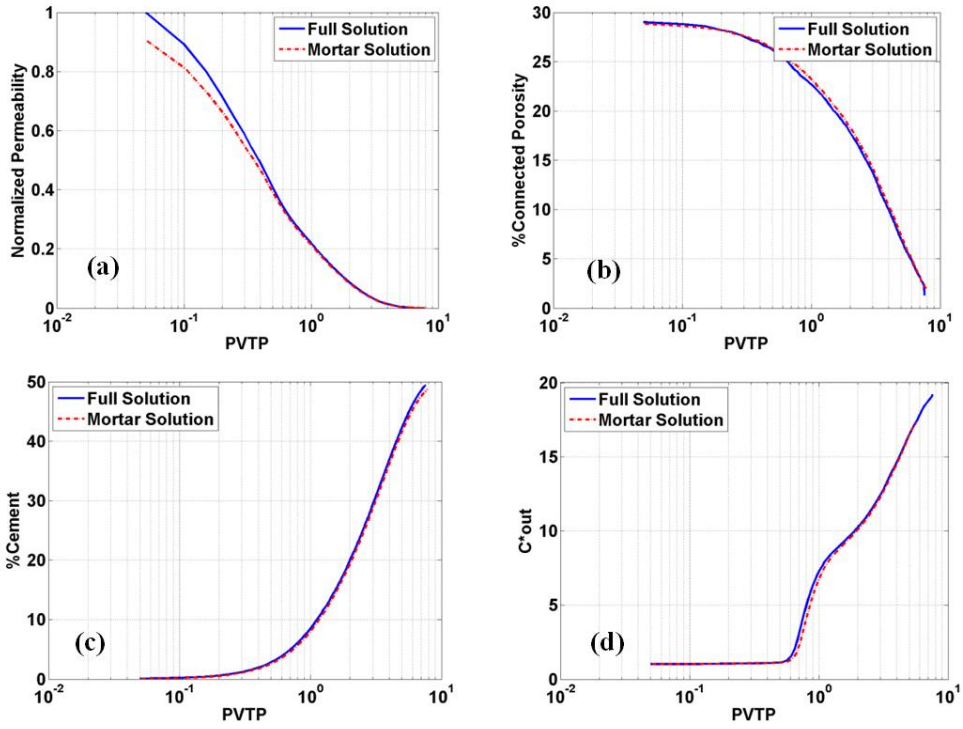


Figure 5.7: (a) Normalized permeability, (b) connected porosity, (c) percent cement, and (d) concentration at the exit, as a function of (initial) pore-volume throughput (PVTP) of fluid injected, for the full and the mortar solutions.

### 5.3.3 Model application

Our goal is to use the mortar/transport coupling approach to model behavior at scales not feasible with a single network, and to capture emergent patterns and heterogeneity that would otherwise be difficult. Here, 64 network models are coupled together on an 8×8×1 grid. The network models are 3D, so the entire domain is 3D but only one network-length in thickness. Each network model is $1\times1\times1 mm^3$ in size and most have a unique pore structure and macroscopic permeability. Figure 5.8 summarizes the initial permeability and porosity of all 64 coupled network models.

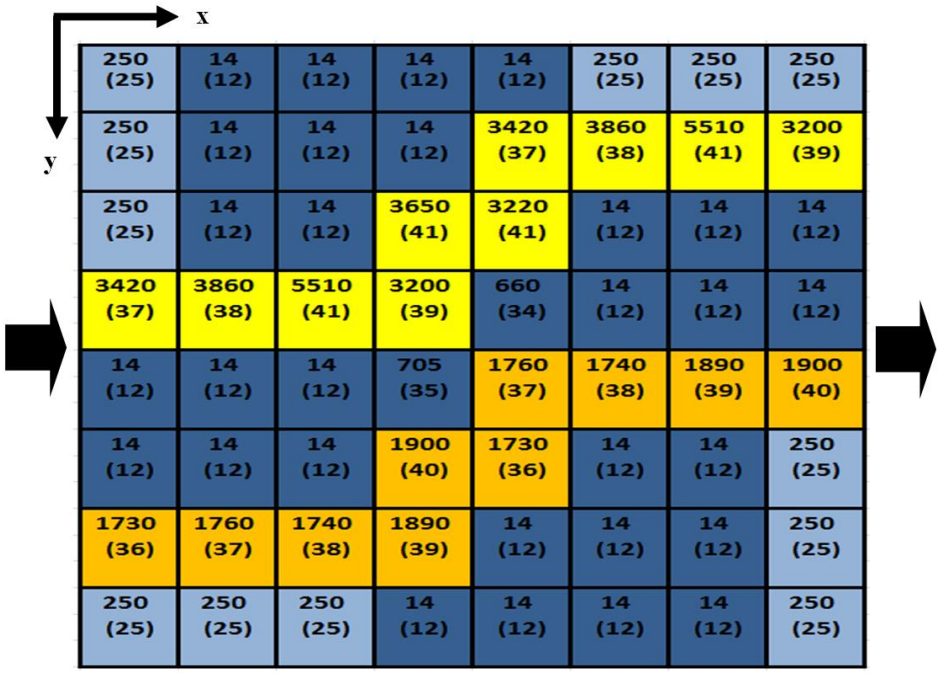


Figure 5.8: Schematic of 64 coupled pore networks denoted by their *x*-permeability (in mD) and porosity (in %) in parentheses. Yellow path is twice as permeable as orange path.

The network models are arranged in such a way that two high-conductivity pathways in the *x*-direction connect the inlet to the outlet of the domain. They are demarcated in figure 5.8 as yellow and orange. The bottom pathway is, on average, half as permeable as the top pathway. The entire domain has 299,129 pores and an average (total) porosity of 23.4%. The simulation was conducted by imposing a constant flow rate across the *x*-direction of the domain. This was achieved by iterating on a uniform pressure value imposed on the inlet boundary, rather than injecting one-eighth of the flux to each boundary block separately. This boundary condition is deemed to be more natural, allowing more flux to go through the high-perm paths. Subdomains were coupled in parallel on a 64-bit quad-core local machine with Intel(R) Xeon(R) 3.6GHz CPU and

12GB RAM. Figures 5.9-12 show pressure, concentration, cementation, and flux fields for $Da = 0.73$ and $\alpha = 100$ at early, intermediate, and late times (0.1, 0.5, and 1.5 PVTP, respectively).

Figures 5.9-12 demonstrate the role of macroscopic heterogeneities in the evolution of the state variables (pressure, concentration) and the pore space through time. Expectedly, the mortar/transport mesh has seamlessly coupled the subdomains together. As before, the plots represent dimensionless concentrations, normalized pressure (against inlet pressure at each time) and normalized flow rate (against injection flow rate). In figure 5.11, spatial maps of cement are shown at various times (darker points correspond to more cement in a pore). The high-permeability paths appear with a lighter contrast at early times because there are fewer pores per unit volume. Figure 5.12 suggests that high-permeability paths persist to be the dominant conduit throughout the reactive process. This is also observed for the other five regimes.

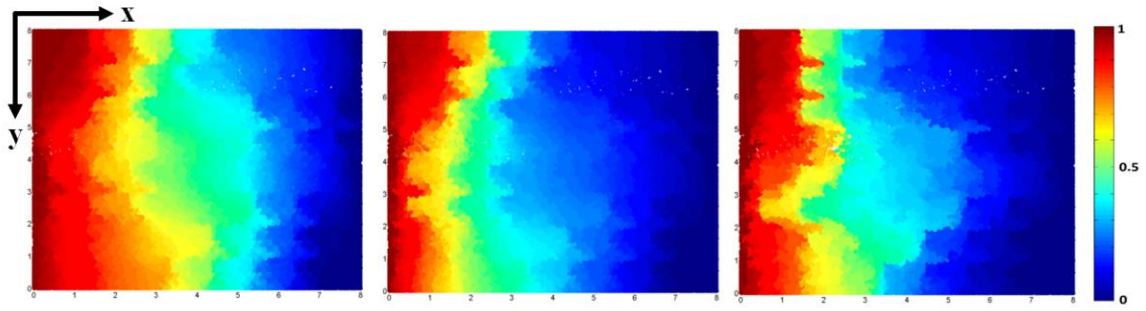


Figure 5.9: Spatial map of normalized pressure field (against inlet pressure at each time) in the domain at various times. All simulations are in 3D but the results are collapsed into 2D for clarity. Here $\alpha = 100$, $Da = 0.73$.

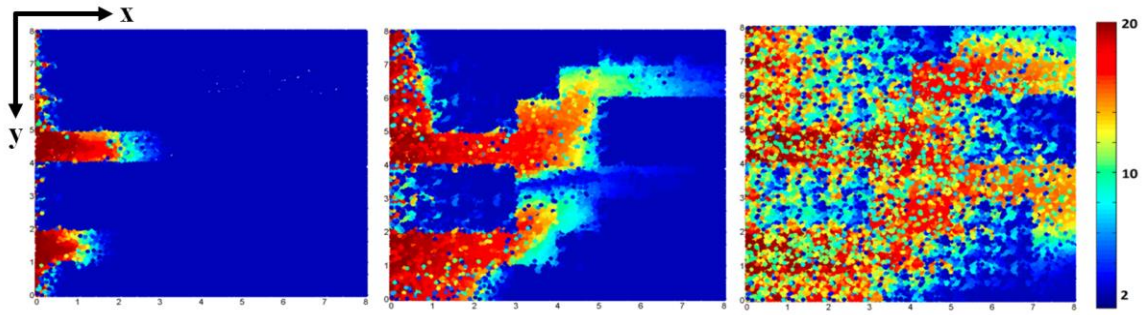


Figure 5.10: Spatial map of (dimensionless) concentration field at various times. All simulations are in 3D but the results are collapsed into 2D for clarity. Here $\alpha = 100$, $Da = 0.73$.

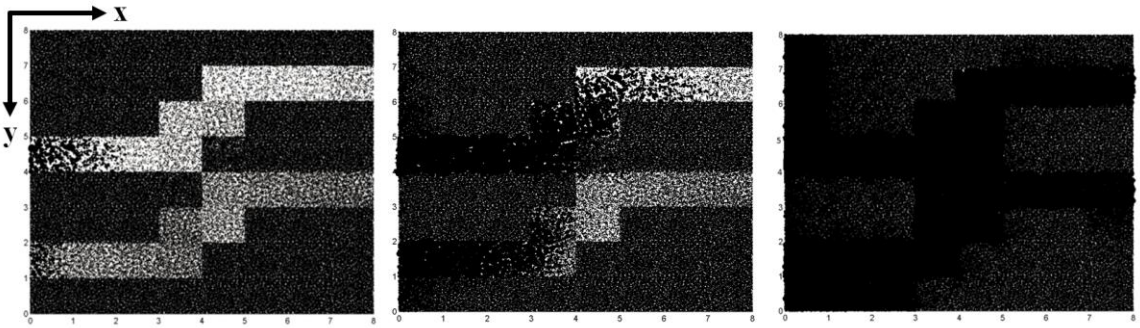


Figure 5.11: Spatial map of cementation field at various times. Darker points correspond to more cement in pores. High-permeability paths appear light at early times because fewer pores per unit volume are present. All simulations are in 3D but the results are collapsed into 2D for clarity. Here $Da = 0.73$, $\alpha = 100$.

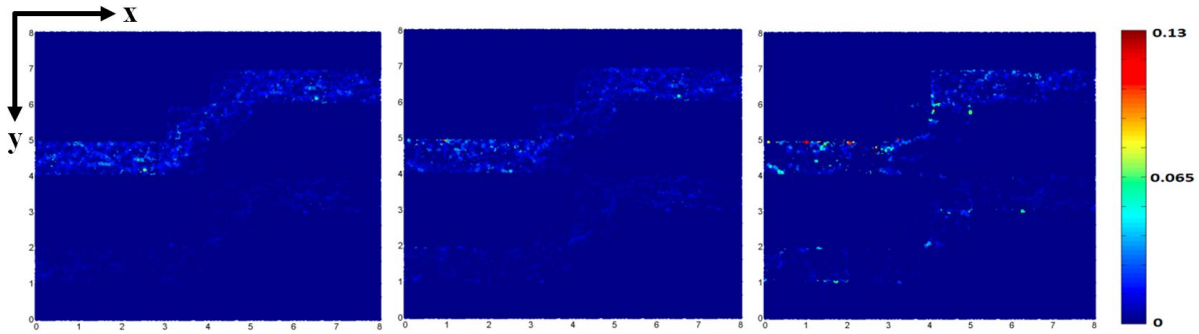


Figure 5.12: Spatial map of normalized flow rate field (against inlet flow rate) at various times. All simulations are in 3D but the results are collapsed into 2D for clarity. Here $\alpha = 100$, $Da = 0.73$.

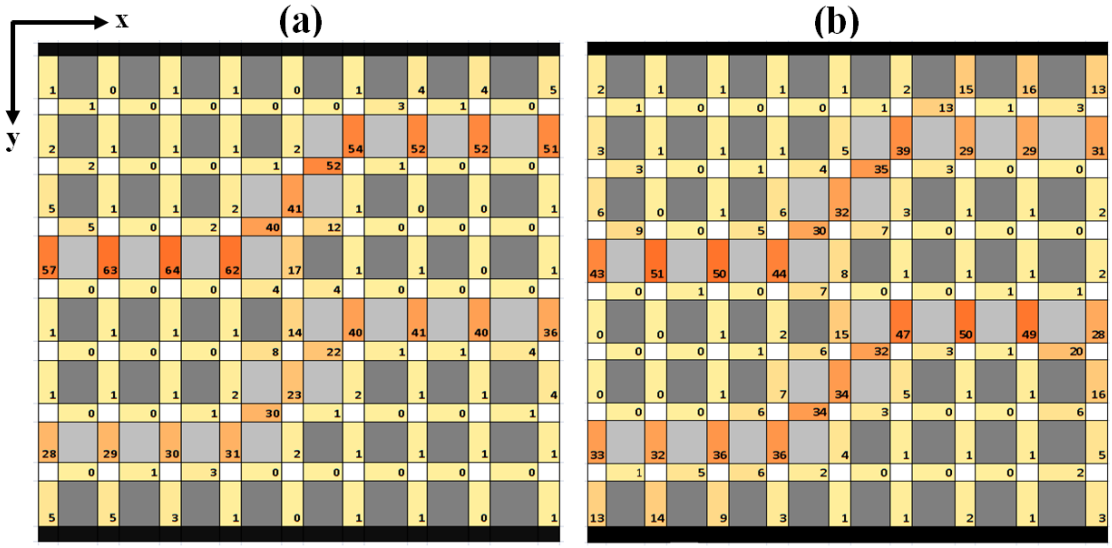


Figure 5.13: Spatial distribution of total flow rates at the interface between any two subdomains (depicted by gray squares) at (a) early and (b) late times for $Da = 0.73$ and $\alpha = 100$. Flow rates are represented as percentages of the injection value (zero suggests flow rate is below 1%).

Figure 5.13 shows the distribution of total fluxes at the interface between any two subdomains for $Da = 0.73$ and $\alpha = 100$. The values of the fluxes are represented as percentages of the total injection rate. At early times (fig. 5.13a), the red color clearly highlights the location of the high-flow paths. At late times (fig. 5.13b), the high-permeability paths have persisted, however, some diversion of flux at the inlet and the outlet are observable. This diversion has occurred into medium permeability networks at the inlet and the outlet.

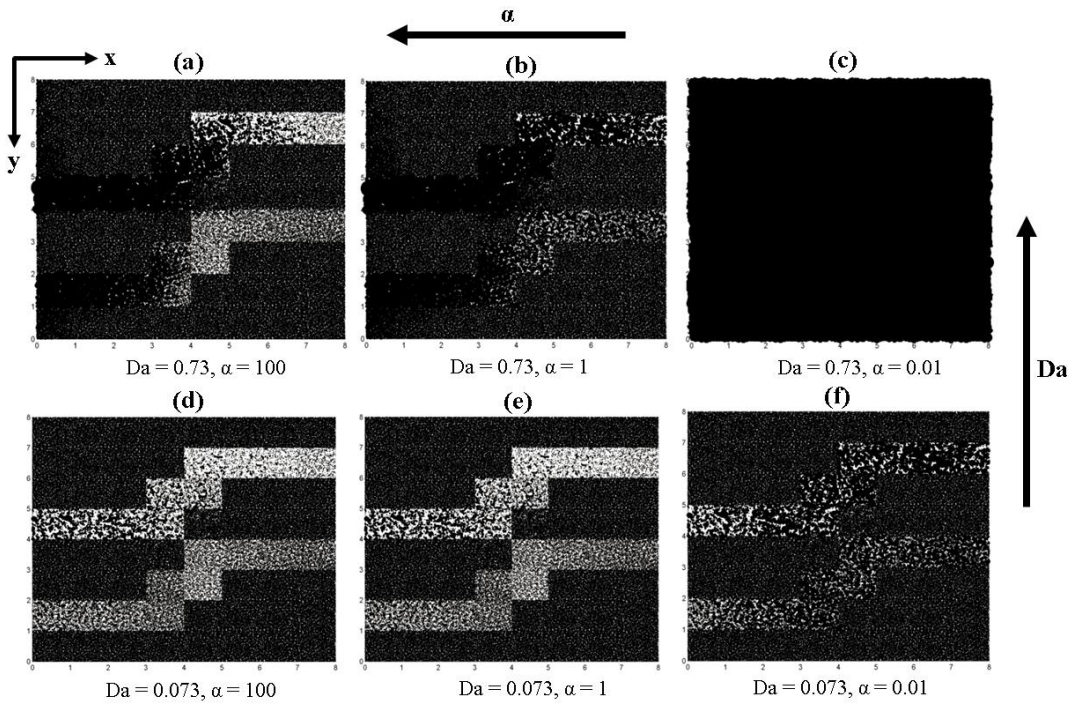


Figure 5.14: Cementation patterns for different values of *Da* and *α*. High-permeability paths appear light at early times because fewer pores per unit volume are present.

Figure 5.14 demonstrates the same qualitative behavior we observed in the case of the smaller domain (in section 5.3.1). However, here, the characteristic quality of the cement distribution is more pronounced inside the high-permeability channels. This is because bicarbonate is transported faster along the high-permeability paths. As before, high *α* and low *Da* shifts the cement more towards the inlet, whereas low *α* and high *Da* shifts the cement more towards the outlet. Any regime in between these two limits is an average of the two. All plots in figure 5.14 are taken at 0.5 pore volumes injected.

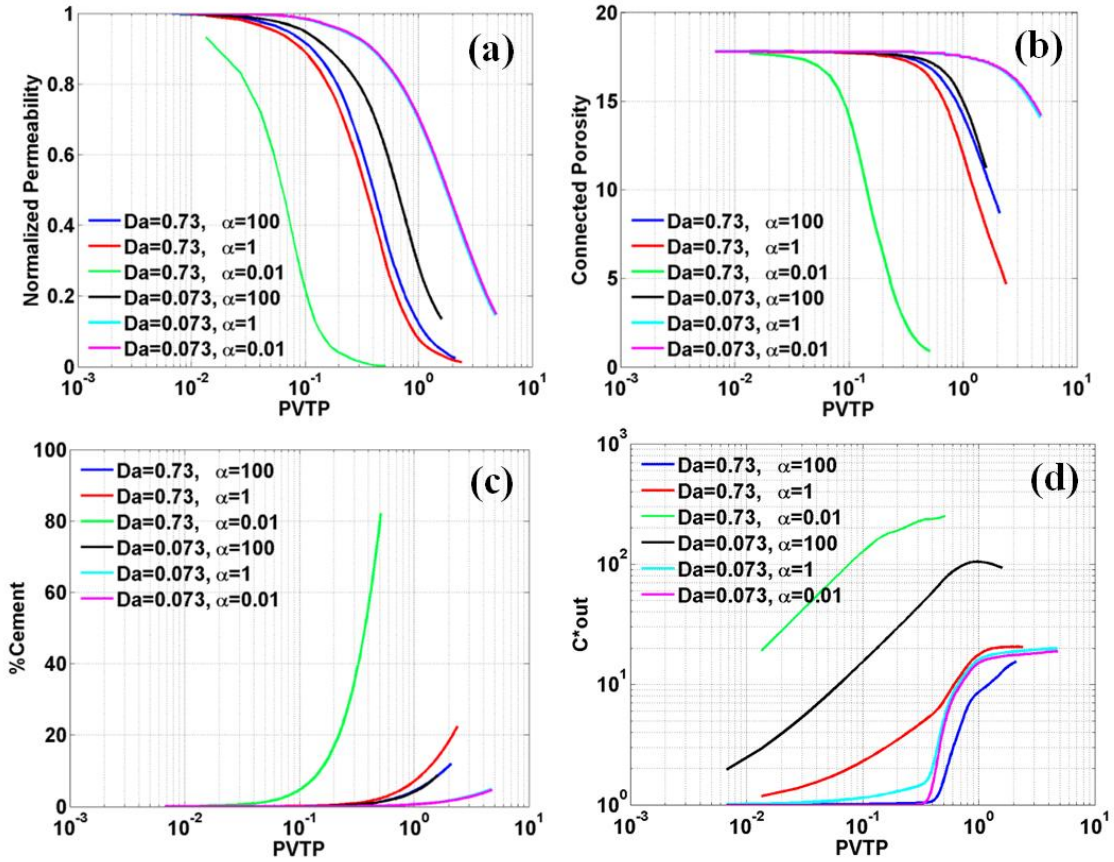


Figure 5.15: (a) Normalized permeability (against initial value), (b) connected porosity, (c) percent cement, and (d) (dimensionless) outflow concentration, as a function of (initial-) pore-volume throughput (PVTP) of fluid injected.

Figure 5.15 also depicts similar behavior to the single-network simulations with respect to variations in the values of $\alpha$ and *Da*. Decreasing $\alpha$ or increasing *Da* results in a faster reduction of permeability and connected porosity and a faster increase in cementation percentage with pore volumes injected. Lower *Da* sharpens the concentration front and lower $\alpha$ increases outflow concentration due to more rapid $CO_2$ dissociation into bicarbonate. The qualitative shapes of these plots are also strikingly similar to the single network case. However, one might notice that the plots for the large,

multi-block domain are over a smaller range of PVTP, as opposed to the small domain. The reason for this is that the 64-block domain has a considerably larger pore volume. Since a large percentage of the injected flux goes through the high-perm path, a few pore volumes of throughput in a high-permeability block in the big domain amounts to roughly the same amount of throughput in the small domain.

#### *5.3.3.1 Upscaling of pore networks for use in continuum-scale models*

The goal of pore networks is often to extract macroscopic properties (e.g., porosity, permeability) for use in a continuum-scale simulator. For example, Kechagia et al. (2002) used volume averaging to upscale reactive transport processes in various flow regimes. In some cases (e.g., fast kinetics), they found volume averaging was not applicable. Here, we argue that these macroscopic properties may be emergent and depend on scales larger than a single network. Coupling models, such as those proposed herein, would allow for modeling wormholes and fingered fronts (Yortsos and Sharma, 1986; Fredd and Fogler, 1998; Lu and Yortsos, 2005) that extend beyond a single domain. Using a single pore network for the upscaling of these and other heterogeneous phenomena may not be sufficient, but modeling an entire reservoir at the pore scale is also out of the question.

A "hybrid" approach (Scheibe et al., 2007; Balhoff et al., 2008; Sun et al., 2012b) might involve coupling pore-scale models to continuum-scale grids, perhaps using mortars. A real-time macroscopic reservoir simulator could be developed that allowed for substitution of pore-scale models in specific regions of strong nonlinearities and dynamics (e.g., near wells and faults). In these regions, hundreds or thousands of pore-scale models could be coupled together and to the continuum simulator. If necessary,

global upscaling could be done *a posteriori*; this would incorporate emergent, coupled behavior that occurs at multiple spatial scales. This approach was used in Sun et al. (2012b) for steady-state flow but could be extended to reactive transport.

#### *5.3.3.2 Application to $CO_2$ flow conduits*

Field observations along the Little Grand Wash fault suggest that pore-filling calcite cement within flow conduits nearly or completely occludes the pore space of the initially porous sandstone (fig. 5.1) potentially resulting in the observed shift of $CO_2$ leakage along fault strike over time. According to the results obtained from the simplified physics in this study, preexisting preferential pathways tend to persist, however. Therefore, in order to account for flow-path shifts, one either has to incorporate more detailed physics (full set of reaction, inclusion of dissolution as well as precipitation, multiphase flow effects, diffusion, etc.) or include more accurate initial conditions for the preexistence of calcite.

In this study, it was assumed that all pores in the domain were seeded and calcite had the potential to precipitate in every pore. However, in reality, only certain portions of the rock may be seeded, thereby allowing localized cementation and growth to occur. The macroscopic implications of such growths could result in structures such as poikilotopes. This has the potential of locally obstructing flow and diverting the streamlines around them. The implementation of non-uniform seeding and their growth in network models, along with more detailed physics will be the subject of future work. The hope is that with minimum complexity in the models, qualitative shifts in pathways could be captured and explained. Nevertheless, the multiscale tools developed in this study are of paramount importance and may be a necessity in studying “emergent” phenomena such as that of

calcite precipitation. The verified multiscale method introduced in this study can be implemented on networks with more detailed physics (although extensions to multi-phase flow are non-trivial) and topology following the same methodology.

## 5.4 CONCLUSIONS

In this study, a simplified, single-phase reactive transport model was developed and studied that allows for precipitation and permeability reduction. Furthermore, a new domain decomposition method was introduced for advection-dominated reactive transport problems across pore-scale models. The following summarize our key findings:

- A reactive transport model for calcite precipitation was created and various precipitation regimes studied by changing $Da$ and $\alpha$. Low $Da$ and $\alpha$ resulted in more precipitate at the inlet and high $Da$ and $\alpha$ meant more precipitate towards the outlet (or away from the inlet).
- A novel coupling approach for pore-scale models, i.e. the mortar/transport method, that uses uniquely designed mortar grids, was developed. The method was verified for coupling reactive transport across pore-scale models. Pressure, concentration, and flux fields at the coupling interface matched with the single-domain "true" solution. Similarly close agreements were obtained for macroscopic properties evolving through time.
- A large domain containing high-permeability streaks was constructed and decomposed into 64 subdomains and solved with the mortar/transport method. This allowed for solving the problem in parallel (on a quad-core machine) and captured heterogeneity features not feasible on a single-domain pore network.

- The model predicts cementation and eventual occlusion of preferential flow paths as observed for natural $CO_2$ seeps along the Little Grand Wash fault. However, the model does not predict the reported shifts in these pathways. In the model, high-permeability paths persisted for all regimes. Possible reasons for the discrepancy were proposed and discussed.

# Chapter 6: (Hybrid) Mortar Domain Decomposition[3]

In this chapter, we develop a framework that allows for modeling flow and solute transport on multiple spatial scales as well as on large heterogeneous pore-scale domains. This study builds on the domain decomposition tools developed in chapter 5 and extends them to scenarios in which diffusive transport is present (ignored in chapter 5) and the computational domain consists of both pore-scale and continuum-scale subdomains. The latter is relevant in the context of "hybrid modeling", which has been receiving increasing attention in the literature over the past few years.

## 6.1 MOTIVATION

Flow and transport phenomena occur over a wide range of spatial scales (nanometer to kilometer) rendering the developments of predictive models capable of bridging all these scales a formidable task. One common approach has been to extract macroscopic parameters (e.g. permeability) or closure relations (e.g. capillary pressure) from smaller scales followed by their direct substitution into larger field-scale simulators. These macroscopic data can be obtained either through experiments or modeling on microscale (or pore-scale) samples representative of the real medium. As discussed in chapter 2, such an approach is not always applicable (when scales are not separable), in which case a "hybrid" modeling strategy is required (see section 2.3).

On the other hand, with regard to the multitude of pore-scale methods developed in the literature (see chapter 2), each possessing specific advantages over the others

[3] The material in this chapter was published under the following reference, which was completed under the supervision of Matthew Balhoff.

Mehmani, Yashar, and Matthew T. Balhoff. "Bridging from pore to continuum: A hybrid mortar domain decomposition framework for subsurface flow and transport." Multiscale Modeling & Simulation 12, no. 2 (2014): 667-693.

(predictive or computational), it would be advantageous if a common framework were developed under which all such methods could be integrated within the same computational domain. In other words, it would be of great value if different parts of the domain could be modeled through different methods appropriate to the local flow and transport conditions in place and the local level of accuracy sought. Furthermore, the need for modeling on larger domains seems to be pervasive in the literature, whether the study includes ascertaining REV sizes for a given process or simply simulating on bigger and more representative samples (e.g. Fredd and Fogler, 1998; Kim et al., 2011).

One solution to the above issues (i.e. hybrid modeling, multi-model domain simulation, and modeling on larger domain sizes) is domain decomposition. In this chapter, we present mortar domain decomposition methods for single-phase flow and solute transport. The methods are capable of bridging the pore scale and the continuum scale (i.e. hybrid modeling), incorporating multiple modeling strategies within the same computational domain, and easily lend themselves to parallel computing allowing the investigation of larger samples. Other advantages include: a) it is typically not feasible to obtain high resolution images of large samples, since sample size and resolution are inversely correlated (Beckingham et al., 2013). However, it is feasible to obtain high resolution images of a large sample if broken up into smaller pieces. Domain decomposition would then view the pieces as subdomains and glue them together, whereby modeling would resume. b) If there are large heterogeneities in the form of abrupt changes in pore structure, they may be easily characterized when considered as subdomain interfaces (Sun et al., 2012a). Among the various pore-scale methods developed in the literature (see chapter 2), we use (but are in no way limited to) pore-network modeling throughout this chapter.

As discussed in chapter 2 and outlined in chapter 5, the basic idea of mortars is to: decompose the domain into subdomains; guess the Lagrange multipliers that determine the interface conditions (e.g. pressures); solve subdomains independently and compute fluxes at their shared interfaces; iterate until fluxes match on both sides of the interface. The described algorithm (known as the forward difference, FD, scheme) has been used by various authors (see chapter 2) in the past (including in chapter 5, section 5.2.3). Recently, Ganis et al. (2012) showed that this algorithm can become quite inefficient especially in the case of nonlinear problems, and they developed alternative schemes that resulted in significant computational speed-up. We similarly develop alternative and more efficient schemes that bear similarities with those of Ganis et al. (2012). The similarities as well as differences are highlighted in section 6.3.

The goals of this chapter include: a) adapt and develop efficient mortar methods for solving single-phase flow and transport on pore-scale and hybrid domains in a parallel environment; b) include diffusive transport in the mortar methods that was ignored in chapter 5; c) verify the methods and demonstrate their accuracy; d) describe in detail the IPP mortars introduced in chapter 5, extend them to pore-to-continuum interfaces, and compare them to Lagrangian mortars; e) demonstrate computational efficiency and parallel scalability on a single dual CPU (hexa-core per CPU) machine; f) demonstrate applicability, scalability and convergence for nonlinear flow problems.

The chapter is outlined as follows: In section 6.2, the mathematical models of the pore scale and the continuum are presented. In section 6.3, the domain decomposition methods for solving flow and solute transport are described. In section 6.4, we present results obtained from these methods accompanied by an ad-hoc discussion of their implications. These consist of verification of the domain decomposition methods, verification and application to hybrid domains, parallel scalability and computational

efficiency, and computational study of the nonlinear flow of a power-law fluid. Section 6.5 provides a summary of important conclusions.

## 6.2 MATHEMATICAL MODELS

### 6.2.1 Pore-network model

In this work, pore networks were extracted from a digitally-generated sphere pack using a modified Delaunay tessellation algorithm (Al-Raoush et al., 2003). As discussed in chapter 3, the flow equation is formulated by assuming a single pressure value per pore and writing mass balance at the pores (eq. 6.1). The constitutive relation used to describe flow of a Newtonian fluid in a throat is $q = g\Delta p$; where $g$ is the throat conductivity. The resultant system arising from the balance equations is linear. At the pore-scale, the flow equation is usually formulated in elliptic form for typical liquids present in the subsurface, since pressure pulses generally have negligible effects at small domain sizes. Therefore, we assume that the fluid of interest is incompressible.

$$\sum_{j=1}^{N_i^{th}} g_{ij}\Delta p_{ij} = 0 \quad on \ \ \Omega_p \tag{6.1}$$

Eq. 6.1 is the flow equation for a pore-scale subdomain $\Omega_p$ where: $p_i$ is pressure at pore $i$, $g_{ij}$ is the conductivity of the throat connecting pore $i$ to $j$, and $N_i^{th}$ is the number of throats connected to pore $i$. In this chapter, we aim to study some computational aspects of the mortar methods for nonlinear problems arising from flow of non-Newtonian fluids.

$$\sum_{j=1}^{N_i^{th}} \tilde{g}_{ij}\Delta p_{ij}^{\ 1/n} = 0 \quad on \ \ \Omega_p \tag{6.2}$$

We have chosen the power-law fluid which has a flow equation of the form given by eq. 6.2. In eq. 6.2, $n$ is the power-law index and $\tilde{g}$ is a function of fluid and throat

properties (Balhoff et al., 2012). In this chapter, the MCM formulation (introduced in chapter 3) is adopted in writing the transport equation (given by eq. 6.3), which implicitly assumes "perfect mixing" at the pores (i.e. a single concentration value assigned per pore). We acknowledge that this assumption may not hold at advection-dominated and/or reaction-dominated regimes. While hybrid modeling is necessary when large concentration gradients exist at the pore scale, the focus of this work does not seek to apply our hybrid methods to such scenarios (although nothing prevents them from it). The validity of our methods stands independently of whether such conditions are met. The choice of the pore-level "perfect mixing" assumption simply allows us to verify our hybrid methods later in section 6.4.2.

$$V_{p_i}\frac{dc_i}{dt} = \sum_{j=1}^{N_i^{th,q<0}} c_i q_{ij} + \sum_{j=1}^{N_i^{th,q>0}} c_j q_{ij} + \sum_{j=1}^{N_i^{th}} D_m a_{ij}\frac{\Delta c_{ij}}{l_{ij}} + R(c_i) \qquad on\ \ \Omega_p \tag{6.3}$$

Eq. 6.3 is the transport equation for subdomain $\Omega_p$ where: $V_p$ is the pore volume, $c_i$ the concentration of pore $i$, $D_m$ the molecular diffusion coefficient, $R(c_i)$ the reaction term and $q_{ij}$ , $l_{ij}$ and $a_{ij}$ are the flow rate, length and cross-sectional area of the throat connecting pore $i$ to $j$, respectively. The throat cross-sectional areas are calculated by assuming cylindrical tubes with equivalent conductivities. The reaction term is ignored throughout this work since it is a local phenomenon, as opposed to a transport mechanism such as diffusion or advection. Therefore, it poses no restrictions on the coupling methods discussed later, and is not considered for simplicity. Solving the flow and transport systems for a single stand-alone network involves two steps: a) solving the flow system and calculating throat flow rates, $q_{ij}$, and b) using the flow rates to solve the

transport system for a given time interval. In eq. 6.3, we have postponed discretizing the time derivative for the benefit of using an adaptive time-stepping ODE solver.

The linear flow equation (eq. 6.1) is solved using the `mldivide` routine in MATLAB which performs Cholesky factorization for the resultant symmetric positive definite system. The nonlinear flow equation (eq. 6.2) is solved using a standard Newton-Raphson method in which the linearized system is solved similar to eq. 6.1. The transport equation (eq. 6.3) is solved using either the adaptive time stepping `ode23tb` solver in MATLAB which is an implementation of TR-BDF2, an Implicit Runge-Kutta formula, or a simple backward Euler method with constant time stepping. The usage depends on the context and is explicitly stated wherever necessary.

### 6.2.2 Continuum model

The single-phase continuum flow equation is similarly derived from mass balance and is known as the "diffusivity equation" (defined on the continuum domain $\Omega_c$).

$$\nabla \cdot (\frac{k}{\mu} \nabla p) = 0 \qquad on \ \ \Omega_c \tag{6.4}$$

In eq. 6.4, $k$ is permeability (a scalar in this work) and $\mu$ is viscosity. The balance equation (eq. 6.4) is elliptic because we assume fluid incompressibility, consistent with section 6.2.1. Compressible (or slightly-compressible) fluids can also be used without loss of generality of the hybrid methods developed. Continuum subdomains are discretized into Cartesian grids, and eq. 6.4 is solved using the finite difference method (FDM). The continuum formulation of the transport equation is similar to that of the pore scale and assumes the following form:

$$\frac{\partial c}{\partial t} = -\nabla \cdot (vc) + \nabla \cdot (D \nabla c) + R(c) \tag{6.5}$$

In eq. 6.5, $v$ is the interstitial velocity determined from the flow equation, $D$ the dispersion coefficient and $R(c)$ the reaction term. For similar reasons discussed in section 6.2.1, the reaction term is neglected. To solve eq. 6.4 and eq. 6.5, we use second order central difference for the space derivatives, first order upwind for the advection term, and backward difference for the time derivative in the FDM discretization (note that any other method such as the finite elements method (FEM) or the finite volume method (FVM) could have been used for the continuum equations without loss of generality).

### 6.2.3 Dimensionless groups

All results in this work are presented in dimensionless form. The transport system consists of the advection, diffusion/dispersion and the reaction components. Ignoring reaction, the dimensionless transport equation at the pore-scale can be written as (eq. 6.6):

$$\bar{V}_{p_i} \frac{\Delta \bar{c}_i}{\Delta \bar{t}} = \sum_{j=1}^{N_i^{th}, \bar{q}<0} \bar{c}_i \bar{q}_{ij} + \sum_{j=1}^{N_i^{th}, \bar{q}>0} \bar{c}_j \bar{q}_{ij} + \sum_{j=1}^{N_i^{th}} \frac{1}{Pe} \bar{a}_{ij} \frac{\Delta \bar{c}_{ij}}{\bar{l}_{ij}} \tag{6.6}$$

Where,

$$\bar{c} = \frac{c}{c_0}, \quad \bar{l} = \frac{l}{l_0}, \quad \bar{a} = \frac{a}{l_0^2}, \quad \bar{V}_p = \frac{V_p}{l_0^3}, \quad \bar{t} = \frac{t v_0}{l_0}, \quad \bar{v} = \frac{v}{v_0}, \quad Pe = \frac{v_0 l_0}{D_m}, \quad \bar{q} = \bar{v}\bar{a} \tag{6.7}$$

In eq. 6.7, $l_0$, $c_0$ and $v_0$ are the characteristic parameters for length, concentration and velocity, respectively. $l_0$ is taken to be the arithmetic average of throat radii in the network, $c_0$ the inlet concentration value, and $v_0$ the arithmetic average of throat fluxes in the network. The dimensionless form allows us to present the results in a more general

setting, which would be valuable for future comparative work. The continuum transport equation can be non-dimensionalized in a similar fashion. However, this is not necessary in the analyses performed in section 6.4.2, because the results are reported in terms of the pore-scale dimensionless parameters (using the equivalence between the upscaled continuum subdomains and their pore-scale counterparts).

## 6.3 MORTAR DOMAIN DECOMPOSITION METHODS

We develop a mortar method called the *Global Jacobian Schur* (GJS) scheme for solving the flow problem, a name that we have adopted due to its similarity to the method presented by Ganis et al. (2012). For the transport problem, two novel schemes are developed: a) The *Implicit Coupling* (IMPC) method which is based on the GJS scheme, and b) The *Explicit Coupling* (EXPC) method which is an extension of the non-iterative scheme presented in chapter 5. Ganis et al. (2012) presented the *Global Jacobian* (GJ) and the *Global Jacobain Schur* (GJS) methods in an attempt to simplify the previously used *Forward Difference* (FD) scheme for nonlinear problems. The resultant algorithms were used and tested for the case of slightly compressible flow at the continuum, and provided significant computational speed-up against the FD scheme due to reductions in their nested structure. Ganis et al. (2012) implemented the methods in a mixed mortar finite element framework (MMFEM) and denoted the method associated with the 1$^{st}$ Schur complement system (after elimination of velocities) the GJ scheme and the one associated with the 2$^{nd}$ Schur complement system (after further elimination of subdomain pressures) the GJS scheme.

Despite structural similarities of the GJS method in this work and that presented by Ganis et al. (2012), there are some important differences: a) In our pore- and

continuum-scale formulations, the subdomain unknowns consist of only pressures as opposed to pressures and velocities (velocity is a dependent variable). What we refer to as the GJS method, is associated with the 1st Schur complement system similar to the GJ method (not GJS) of Ganis et al. (2012). b) Our methods are for modeling on pore-scale and hybrid domains whereas their work focused on domains entirely at the continuum. c) We investigate flow and transport whereas they studied slightly compressible (including incompressible) flow. d) We perform factorization of the linearized subdomain systems in addition, resulting in significant speed-up of the scheme. e) We test the performance of the method for nonlinear systems arising from flow of non-Newtonian fluids.

### 6.3.1 Global mortar formulation

We present a formal definition of mortars as follows:

$$\begin{aligned} p|_{\Gamma_{ij}} &= \sum_k \alpha_{H_k} \varphi_k^{\alpha}(x,y) \\ c|_{\Gamma_{ij}} &= \sum_k \beta_{H_k} \varphi_k^{\beta}(x,y) \end{aligned} \tag{6.8}$$

$$\begin{aligned} M_{H_{ij}}^{\alpha,\beta} &= span(\{\varphi_k^{\alpha,\beta}(x,y) \in L^2(\Gamma) : k = 1,...,dof\ |_{\Gamma_{ij}}^{fl,tr}\}) \\ M_H^{\alpha,\beta} &= \oplus M_{H_{ij}}^{\alpha,\beta} \end{aligned} \tag{6.9}$$

Consider $\Gamma_{ij}$ as the interface shared between subdomains $i$ and $j$. In eq. 6.8, the interface pressures and concentrations are written as linear combinations of mortar basis functions (i.e. $\varphi^{\alpha}$ for pressure and $\varphi^{\beta}$ for concentration). The span of these bases at interface $\Gamma_{ij}$ constitutes the mortar subspace $M_{Hij}$ at that interface (eq. 6.9). The number of mortar unknowns (or degrees of freedom) on $\Gamma_{ij}$ are denoted by $dof|_{\Gamma ij}$ (eq. 6.9). The global mortar space $M_H$ (defined on $\Gamma = \cup\ \Gamma_{ij}$) is given by the direct sum of the mortar

subspaces over all the interfaces (eq. 6.9). $L^2(\Gamma)$ represents the space of square-integrable functions on $\Gamma$. $\alpha_H$ and $\beta_H$ are the Lagrange multipliers for flow and transport, respectively. The superscript $\alpha$ corresponds to flow and $\beta$ to transport. In this work, subdomains are either at the pore or at the continuum scale. Given the flow and transport equations presented in sections 6.2.1 and 6.2.2, along with the requirement that bulk/species fluxes at the shared interface between any two subdomains should be "continuous", the global system for the problem can be formulated.

$$\begin{aligned} 0 &= F_i^{fl}(\overrightarrow{p_h}, \overrightarrow{\alpha_H})|_{\Omega_i}, \quad \forall i = 1,...,n_\Omega \\ 0 &= G_j^{fl}(\overrightarrow{p_h}, \overrightarrow{\alpha_H})|_{\Gamma}, \quad \forall j = 1,...,n_M^{fl} \end{aligned} \tag{6.10}$$

$$\begin{aligned} \frac{\partial \vec{c}_h}{\partial t} &= F_i^{tr}(\overrightarrow{c_h}, \overrightarrow{\beta_H}, t)|_{\Omega_i}, \quad \forall i = 1,...,n_\Omega \\ 0 &= G_j^{tr}(\overrightarrow{c_h}, \overrightarrow{\beta_H}, t)|_{\Gamma}, \qquad \forall j = 1,...,n_M^{tr} \end{aligned} \tag{6.11}$$

Where,

$$G_j^{fl}(\vec{p}_h, \vec{\alpha}_H) = \int_\Gamma \left[\!\left[\vec{n}\cdot\vec{q}\right]\!\right]\varphi_j^\alpha \qquad G_j^{tr}(\vec{c}_h, \overrightarrow{\beta_H}, t) = \int_\Gamma \left[\!\left[\vec{n}\cdot\vec{q}_c\right]\!\right]\varphi_j^\beta \tag{6.12}$$

Using abstract symbolism, eq. 6.10 through 6.12 represent the global system for single-phase flow (eq. 6.10) and solute transport (eq. 6.11). $p_h$ and $c_h$ are the discretized subdomain pressures and concentrations and $\Omega_i$ denotes the $i^{th}$ subdomain ($\Omega = \cup\, \Omega_i$). $n_\Omega$ and $n_M$ are the total number of subdomains and interface unknowns. Superscripts *fl* and *tr* represent flow and transport. $F_i^{fl}$ is the discretized elliptic flow operator and $F_i^{tr}$ the discretized parabolic transport operator for $\Omega_i$, which are functions of the discretized subdomain pressures/concentrations ($p_h$ and $c_h$) and the Lagrange multipliers for

pressure/concentration ($\alpha_H$ and $\beta_H$). Depending on whether the subdomain is pore-scale or continuum-scale, one of eq. 6.1, 6.2, 6.4 (for flow) or 6.3, 6.5 (for transport) is used. $G^{fl}$ and $G^{tr}$ are the interface conditions for the bulk fluid flux and species fluxes, respectively (eq. 6.12). These additional equations guarantee that the flux field is "weakly continuous" from one subdomain to the next so that mass conservation is preserved. More rigorously, the orthogonal projection of the jump-in-flux onto the mortar space must be zero. Sections 6.3.3, 6.3.4 and 6.3.5, concern with efficient numerical schemes for solving this global system in parallel.

### 6.3.2 Interface point partitioning (IPP)

IPP (briefly introduced in chapter 5) is a method used to decompose and group the boundary pores (or grids) of two subdomains, sharing an interface, into bundles. IPP mortars consist of piecewise constant basis functions defined over each bundle. The advantages of this method include: a) Flux will be locally conservative over each bundle; b) there is a simple closed-form equation for the interface condition; c) possible singularity of the interface problem is avoided (since each bundle, by construction, contains at least one point from either side); the singularity issue was first highlighted by Balhoff et al. (2008) as a drawback of using fine Lagrangian mortars; and d) allows for non-iterative and easily parallelizable coupling of the transport system (i.e. the EXPC method). IPP bundles create natural mortar bases which are specific to pore-to-pore and pore-to-continuum interfaces.

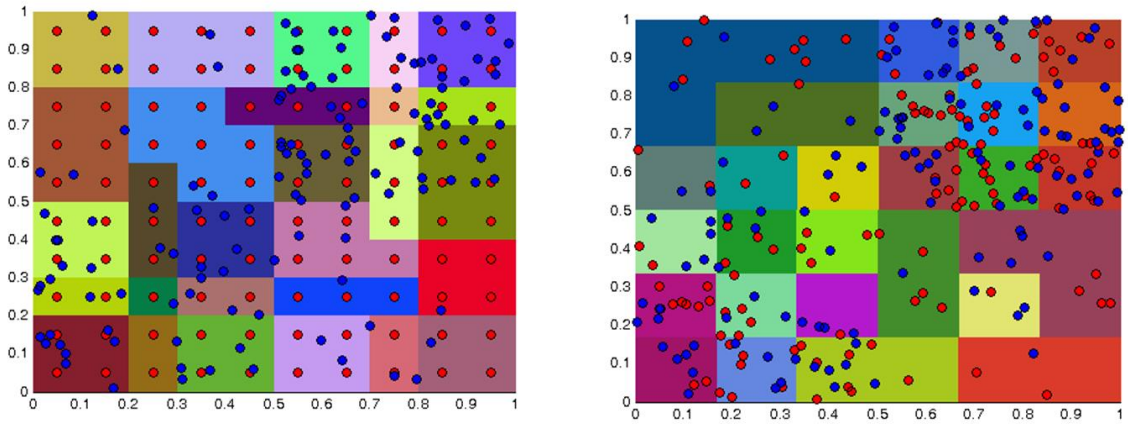

Figure 6.1: Interface Pore Partitioning (IPP) of the interface between (a) a pore- and a continuum-scale, and (b) two pore-scale subdomains. Red dots denote position of the boundary pores/grids on one side of the interface, and blue dots those on the opposite side. Each bundle is colored differently to distinguish it from its neighboring bundles.

The IPP method partitions the interface into bundles of points, which are the positions of the boundary pores (or grids). First, a Cartesian mesh of specified refinement is assumed on the interface (this is what is referred to as an $M \times N$ IPP mesh). Elements that contain points from both sides are grouped and set aside as bundles. Elements that contain points from only one side are merged with the previously formed bundles. The closest bundle is chosen for merger and is determined by using centroids of the points within these elements and the bundles. Centroids of bundles are kept invariant during merger.

With pore-to-continuum interfaces the procedure is slightly different. First, a Cartesian mesh is assumed at the interface. Second, points (boundary grids) only from the continuum side that fall within each mesh element are set aside as a group. Third, the interface area associated with each group is taken to be the union of the interface areas of the continuum grids comprising it. Fourth, groups that contain points from the pore-scale

side are set aside as bundles. The remaining groups are merged with the previously formed bundles using a similar procedure as before. Figure 6.1 shows an example IPP mesh at the interface between two pore-scale subdomains, and a pore-scale and a continuum-scale subdomain.

### 6.3.3 Coupling of flow

The flow equation in this work is a self-adjoint elliptic operator and, therefore, the resulting system will be symmetric and positive-definite. This motivates the type of linear interface solver and factorization method chosen to solve the problem. Consider a domain $\Omega$ decomposed into $\Omega_k$, $k \in [1, n_\Omega]$ subdomains. If the linear (or linearized, if nonlinear) global system is written and the unknowns separated into subdomain and interface parts, we obtain the following system:

$$J_g \delta\vec{x} = \begin{pmatrix} J_{F^{fl}/p} & J_{F^{fl}/\alpha} \\ J_{G^{fl}/p} & J_{G^{fl}/\alpha} \end{pmatrix} \begin{pmatrix} \delta\vec{p} \\ \delta\vec{\alpha} \end{pmatrix} = -\begin{pmatrix} \vec{F}^{fl} \\ \vec{G}^{fl} \end{pmatrix} = -\vec{F}_g \tag{6.13}$$

$$\vec{p} = \begin{pmatrix} \vec{p}_{h,\Omega_1} \\ \vec{p}_{h,\Omega_2} \\ \cdots \end{pmatrix} \quad \vec{\alpha} = \begin{pmatrix} \alpha_{H_1} \\ \alpha_{H_2} \\ \cdots \end{pmatrix} \quad \vec{F}^{fl} = \begin{pmatrix} \vec{F}^{fl}_{\Omega_1} \\ \vec{F}^{fl}_{\Omega_2} \\ \cdots \end{pmatrix} \quad \vec{G}^{fl} = \begin{pmatrix} G_1^{fl} \\ G_2^{fl} \\ \cdots \end{pmatrix} \tag{6.14}$$

In eq. 6.13, $J_g$ is the global Jacobian of the (linear/linearized) problem. The subscript $g$ stands for global. This matrix consists of four parts: $J_{F^{fl}/p}$ and $J_{F^{fl}/\alpha}$ are the partial derivatives of the flow operator with respect to subdomain pressures and Lagrange multipliers, and $J_{G^{fl}/p}$ and $J_{G^{fl}/\alpha}$ are the partial derivatives of the flow interface condition with respect to subdomain pressures and Lagrange multipliers respectively. $\vec{p}$ is the vector of subdomain pressures and $\vec{\alpha}$ is the vector of (flow) Lagrange multipliers. The

Schur complement system of eq. 6.13 can be formed by performing a block Gaussian-Elimination in order to eliminate the subdomains unknowns (i.e. $\vec{p}$). This is under the assumption that $J_{F^{fl}/p}$ is invertible which is true since it is a block-diagonal matrix consisting of invertible blocks (or subdomain Jacobians). The resulting Schur complement system has the following form:

$$
\begin{aligned}
&S\delta\vec{\alpha} = \vec{R} \\
&S = J_{G^{fl}/\alpha} - J_{G^{fl}/p} J_{F^{fl}/p}{}^{-1} J_{F^{fl}/\alpha} \\
&\vec{R} = -(\vec{G}^{fl} - J_{G^{fl}/p} J_{F^{fl}/p}{}^{-1} \vec{F}^{fl})
\end{aligned}
$$

(6.15)

It is easy to see that if the global Jacobian ($J_g$) is symmetric and positive definite then $S$ (eq. 6.15) is also symmetric and positive definite (Saad, 2003). $S$ is referred to as the Schur complement of the global system; solving it yields the interface unknowns which in turn yields the subdomain unknowns. It is important to note that $S$ is not actually formed and the above system is solved using a matrix-free method. Here the Conjugate-Gradient (CG) method is used to solve the Schur complement system in parallel. In addition, the global Jacobian and the residual function are both assembled in parallel offering further computational efficiency. The pseudo code for the GJS algorithm used to solve the flow system is given in figure 6.2. Note that the GJS is a Newton-CG scheme when solving for the flow equation.

*GJS* Algorithm

Initial guess: $\vec{x}_0 = [\vec{p}_0; \vec{\alpha}_0]$

Do k=1…max iteration

{step1}: Compute $\vec{F}_g^{(k)}$ in parallel

{step2}: If $\| \vec{F}_g^{(k)} \|_2 < tol$, break loop; end

{step3}: Assemble $J_g^{(k)}$ in parallel

{step4}: Define function: $Sv^{(k)} = J_{G/\alpha}^{(k)} v - J_{G/p}^{(k)} J_{F/p}^{-1\ (k)} J_{F/\alpha}^{(k)} v$

{step5}: Compute: $\vec{R}^{(k)} = -(\vec{G}^{(k)} - J_{G/p}^{(k)} J_{F/p}^{-1\ (k)} \vec{F}^{(k)})$

{step6}: $\delta\vec{\alpha}^{(k)} = CG - Solver(Sv^{(k)}, \vec{R}^{(k)})$

{step7}: Update interface: $\vec{\alpha}^{(k+1)} = \vec{\alpha}^{(k)} + \delta\vec{\alpha}^{(k)}$

{step8}: Solve for subdomain variables: $\delta\vec{p}^{(k)} = -J_{F/p}^{-1\ (k)} (J_{F/\alpha}^{(k)} \delta\vec{\alpha}^{(k)} + \vec{F}^{(k)})$

{step9}: Update subdomains: $\vec{p}^{(k+1)} = \vec{p}^{(k)} + \delta\vec{p}^{(k)}$

End do

Figure 6.2: Pseudo-code of the algorithm for the GJS method.

In step 4, 5 and 8 of the GJS algorithm, it is very important to be able to solve the $J_{F/p}\vec{w} = \vec{b}$ system efficiently (the superscript *fl* in $F^{fl}$ is dropped because of commonalities with the IMPC method for transport in the next section). As mentioned earlier, $J_{F/p}$ is block-diagonal, so the system is already decoupled with respect to each subdomain. Therefore, each subdomain segment can be solved separately and in parallel. This can be further exploited by noticing the fact that the only item changing between calls is $\vec{b}$. The subdomain components of the $J_{F/p}$ can be decomposed in the first call using Cholesky-Factorization and storing the resultant lower triangular matrices in the workspace of the corresponding processors. Subsequent calls will only require the solution of a lower- and

an upper- triangular system which is much more efficient than the original subdomain solves.

### 6.3.4 Implicit coupling of transport (IMPC)

Once the global flow system (eq. 6.10) is solved using GJS described in section 6.3.3, the global transport system (eq. 6.11) can be solved. IMPC couples the subdomains for transport using an implicit method. The subdomain transport equations 6.3 and 6.5, give rise to an asymmetric global system of equations. There are two contributors to this asymmetry: a) the advection term is discretized using a first-order upwind scheme, and b) in pore networks, pore volumes vary from one to the other. However, a similar algorithm as that presented for flow can be adopted. At every time step the Schur complement of the linearized global transport system is formed as before and the algorithm of figure 6.2 is used to solve it. Since the system is no longer symmetric, the Schur complement cannot be assumed to be symmetric either. Therefore, a Newton-GMRES scheme is utilized instead to solve the global system and the subdomain systems are decomposed using regular LU-Factorization. If the transport system is linear, both the Jacobian and the factorized components can be computed once and reused across time steps saving tremendous overall computation time. The time derivative in eq. 6.11 is discretized using a backward Euler formula and a constant time-stepping scheme is used (more elaborate schemes may similarly be adopted). The global transport system is given by eq. 6.16 and 6.17, and all symbols have analogous meanings as in section 6.3.3.

$$\begin{pmatrix} I - \Delta t\, J_{F^{tr}/c} & -\Delta t\, J_{F^{tr}/\beta} \\ J_{G^{tr}/c} & J_{G^{tr}/\beta} \end{pmatrix} \begin{pmatrix} \delta\vec{c} \\ \delta\vec{\beta} \end{pmatrix} = -\begin{pmatrix} \Delta_t \vec{c} - \Delta t\, \vec{F}^{tr} \\ \vec{G}^{tr} \end{pmatrix} \tag{6.16}$$

$$\vec{c} = \begin{pmatrix} \vec{c}_{h,\Omega_1} \\ \vec{c}_{h,\Omega_2} \\ \cdots \end{pmatrix} \quad \vec{\beta} = \begin{pmatrix} \beta_{H_1} \\ \beta_{H_2} \\ \cdots \end{pmatrix} \quad \vec{F}^{tr} = \begin{pmatrix} \vec{F}^{tr}_{\Omega_1} \\ \vec{F}^{tr}_{\Omega_2} \\ \cdots \end{pmatrix} \quad \vec{G}^{tr} = \begin{pmatrix} G_1^{tr} \\ G_2^{tr} \\ \cdots \end{pmatrix} \tag{6.17}$$

### 6.3.5 Explicit coupling of transport (EXPC)

In contrast to IMPC, the EXPC scheme non-iteratively advances subdomain transports in time without solving an interface problem. Instead a synchronization step is performed with a set frequency between the subdomains. It is here where the idea of IPP bundles becomes most attractive. In chapter 5, we used IPP bundles to explicitly couple advection-dominated transport across an 8×8×1 array of pore-scale models. The requirement for coupling was that the interface flux be locally conservative which was satisfied by using IPP mortars. An average concentration value was computed and projected from the upstream to the downstream side of each bundle. We extend this methodology to incorporate diffusive transport. Despite the extension, we hypothesized this method to be more suitable for moderate to high Peclet regimes which is indeed the case as shown in section 6.4.1. Most regimes in subsurface practical scenarios fall into this range and the extension serves as an important upgrade.

In EXPC, a closed-form balance equation is written over each bundle (eq. 6.18a), and the bundle concentration is back-calculated from rearranging this equation (eq. 6.19). A schematic of a bundle is shown in figure 6.3. Eq. 6.19 is used for each bundle in the synchronization step of EXPC. It reduces to upstream-to-downstream projection of averaged bundle concentrations in the advection-dominated limit (see eq. 5.7). In the diffusion-dominated limit, it reduces to a weighted average of pores/grid concentrations adjacent to the bundle. In principle, the explicitly-calculated bundle concentrations are

the values of the Lagrange multipliers for the piecewise constant basis functions defined over the bundles.

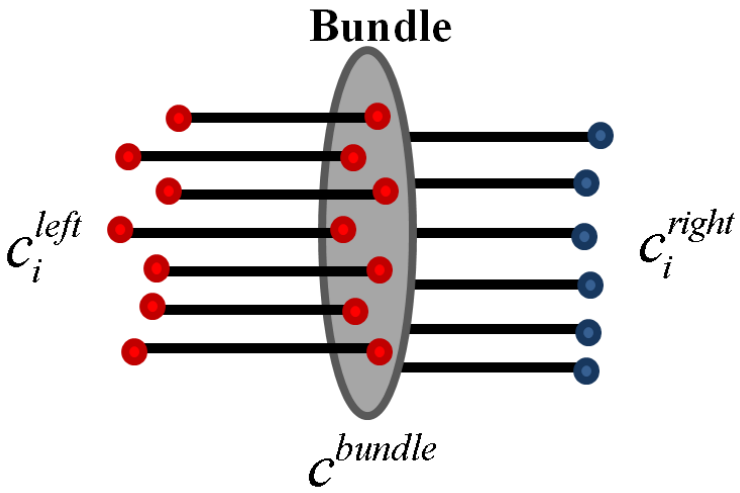


Figure 6.3: Schematic of an IPP bundle connected from both sides to pore-scale subdomains via pore-throats. Concentrations of pores connected through these throats and the concentration of the bundle are annotated.

$$G_k^{fl}(\vec{p},\vec{\alpha}) = \int_{\Gamma \cap bundle} \left[\!\left[\vec{n}\cdot\vec{v}\right]\!\right]\varphi_k = \sum_{i=1}^{N_{left}} q_i^{left} + \sum_{i=1}^{N_{right}} q_i^{right} = 0$$

$$G_k^{tr}(\vec{c},\vec{\beta},t) = \int_{\Gamma \cap bundle} \left[\!\left[\vec{n}\cdot\vec{v}_c\right]\!\right]\varphi_k = \sum_{i=1}^{N_{left}} q_{c_i}^{left} + \sum_{i=1}^{N_{right}} q_{c_i}^{right} = 0 \qquad (6.18a)$$

$$q_{c_i} = q_i c\,|_{upwinded} - Da_i \frac{c_i - c_{bundle}}{l_i} \qquad (6.18b)$$

$$\beta_{bundle} = \frac{\sum_{i=1}^{N_{th}} D_i \frac{a_i c_i}{l_i} - \sum_{i=1}^{N_{th,q<0}} q_i c_i}{\sum_{i=1}^{N_{th}} D_i \frac{a_i}{l_i} + \sum_{i=1}^{N_{th,q>0}} q_i} \qquad (6.19)$$

In eq. 6.18 and 6.19, $c_i$ are the interface pore/grid concentrations and $a_i$, $q_i$ and $l_i$ are the throat/grid cross-sectional areas, flow rates and lengths respectively. $N_{th}$ is the total number of throats/grids associated with the IPP bundle and $N_{th,q<0}$ and $N_{th,q>0}$ are the number of outflowing and inflowing throats/grids with respect to the pores/grids respectively. $D_i$ is the diffusion/dispersion coefficient (depending on whether the subdomain is pore or continuum scale). The pseudo code in figure 6.4 summarizes the steps in EXPC.

*EXPC* Algorithm

{step1}: Solve flow using *IPP* mortars
  Do $I_t$=1:$N_t$
    Do $I_{sub}$=1:$N_\Omega$
{step2}:  Advance subdomain $I_{sub}$ in time
    End do
    Do $I_{bundle}$=1:$N_{bundle}$
{step3}:  Synchronize subdomains sharing bundle $I_{bundle}$ using eq. 6.19
    End do
  End do

Figure 6.4: pseudo-code of the algorithm for the EXPC method.

In the algorithm of figure 6.4, step 2 is an "embarrassingly parallel" task (i.e. no processor communication). The synchronization step (step 3) requires data transfer between parallel workers. Therefore, EXPC is most efficient when synchronization frequency is not too high. When such conditions hold, the advantages of EXPC include: a) parallelism scales almost linearly, b) very fine IPP mesh can be used without affecting computation time (synchronization is cheap), c) subdomains can use independent time stepping schemes, and d) very different models (CTRW vs. PNM) can be coupled

together (because Lagrangian models such as CTRW do not deal with residual vectors/Jacobians). Subdomains can march up to a few fractions of a pore volume injected before being synchronized but the actual frequency depends on the transport regime (Peclet number) as discussed later.

## 6.4 RESULTS AND DISCUSSION

### 6.4.1 Verification and comparison

To verify the coupling approaches a pore-network model of a sphere pack with dimensions $0.2\times0.1\times0.1\text{mm}^3$ is chosen. The resulting network model, extracted using a modified Delaunay tessellation method (Al-Raoush et al., 2003), consists of 8188 pores and 20368 throats. Constant pressure boundary conditions are imposed in the $x$-direction and all other boundaries are sealed. Inlet and outlet concentrations are kept at a constant value of one and zero, respectively. The problem is solved as a whole (referred to the "whole" solution hereafter) and snapshots of concentration fields at the $x = 0.1$mm plane are taken at intermediate times. Pore-volume averaged concentration values of pores nearest to the outlet are computed and recorded through time. The domain is then split into two separate subdomains along the $x = 0.1$mm plane. Flow is solved using GJS followed by solving the transport system using both IMPC and EXPC. This procedure is performed on two domains: a homogeneous ($k_x = 2.31\times10^{-9}$, $k_y = 1.59\times10^{-9}$, $k_z = 1.88\times10^{-9}$ cm$^2$) and a highly heterogeneous (channeled) pore-network ($k_x = 8.78\times10^{-9}$, $k_y = 4.71\times10^{-9}$, $k_z = 5.95\times10^{-9}$ cm$^2$) at three different Peclet numbers: 0.001, 1 and 1000. Transport regime was changed by keeping the pressure gradient in the $x$-direction constant and altering the diffusion coefficient.

Similar to Bruderer et al. (2001) heterogeneity is quantified as the normalized standard deviation of the pore-throat radii ($\sigma_{rth}/\langle r_{th} \rangle$) and is referred to as the "heterogeneity index". The heterogeneous domain was created from the homogeneous network by artificially introducing percolating channels and constrictions (by altering throat conductivities) in the domain. The number of channels and their dilation/contraction factors is specified, and the algorithm seeks for random percolating paths from the inlet to the outlet. The conductivities of the throats comprising the path are multiplied by the dilation/contraction factor. The paths are chosen such that they do not intersect themselves on any pore (but different paths may intersect one another). Such heterogeneity causes channeled flow to occur which results in high concentration gradients. The homogeneous network was subjected to ~10 channels with dilation/contraction factors ranging between 0.001-100 to create the heterogeneous network. The heterogeneity indices of the homogeneous and heterogeneous networks are 0.23 and 2.4, respectively. Probability distribution functions of the pore-throat radii of the two networks are presented in figure 6.5.

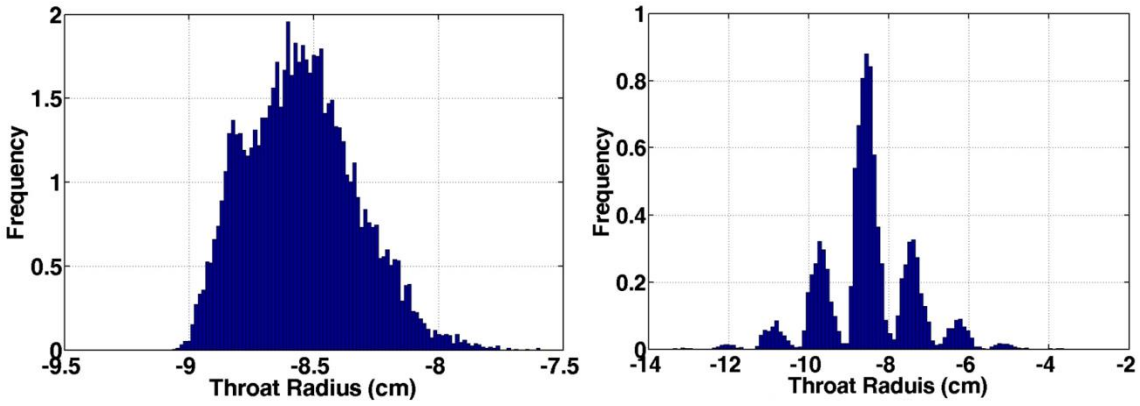


Figure 6.5: Probability distribution functions of the logarithm of the throat radii for the (a) homogeneous and the (b) heterogeneous networks. The *x*-axis is in log scale and has units of cm.

The whole transport system and the subdomain transport systems in the EXPC method were both solved with the `ode23tb` solver in MATLAB which is an implementation of an Implicit Runge-Kutta formula. The relative and absolute tolerances used for these solvers were $10^{-4}$ and $10^{-5}$, respectively. The average dimensionless time steps used in the IMPC method are summarized in tables 6.1 and 6.2. The tolerances for the Newton and the linear solvers in IMPC and GJS were both set to $10^{-10}$. Both EXPC and IMPC were solved in series to obtain the verification results.

Figures 6.6 and 6.7 summarize the concentration-field snapshots at the $x = 0.1$mm plane and the near-outlet concentration plots respectively, at the three transport regimes for the homogeneous and heterogeneous networks. In the interface plots (fig. 6.6) a 10×10 IPP mesh was used whereas in the outlet concentration plots (fig. 6.7) a 2×2 IPP mesh was utilized (further refinement of the interface mesh had small corrective effects on the near-outlet concentration plots). Moreover, tables 6.1 and 6.2 summarize details of the parameters used (EXPC coupling frequency, time of snapshot of interface concentration, IPP mesh size, IMPC time step) to produce figures 6.6 and 6.7 respectively. In addition, figures 6.8a and 6.8b show the interface pressure fields for the heterogeneous network (better results were obtained for homogeneous network but not shown here for brevity). Finally, figures 6.8c to 6.8f show the interface concentration fields for various refinements of the IPP mesh alongside the whole solution for the case of $Pe = 1000$ and homogeneous network (similar results were obtained for other regimes and the heterogeneous network).

Figure 6.7 shows good agreement between the (explicitly and implicitly) coupled and the whole near-outlet concentration plots. Figure 6.6 demonstrates that, at intermediate times, the concentration fields along the $x = 0.1$mm plane from the coupled

solutions converge to the whole solution at higher IPP mesh refinements. The convergence can be better observed from figures 6.8c to 6.8f, in which the IPP refinement is increased from 3×3 to 10×10. It is noteworthy that a 5×5 mesh accurately captures essential features of the concentration field (at least in the case of $Pe = 1000$, homogeneous network). The EXPC and IMPC schemes yield similar results since both methods use the same IPP mesh to perform the coupling. Finally, figure 6.8a and 6.8b demonstrate good agreement between interface pressure fields between the coupled and whole solutions. Therefore, figures 6.6, 6.7, 6.8a-f serve as verification of the GJS, IMPC and EXPC methods and demonstrate that these methods are capable of producing results with acceptable accuracy compared to solving the domain as a whole.

As tables 6.1 and 6.2 suggest, at low Peclet numbers the coupling frequency has to increase rapidly in order for EXPC to produce accurate results. Since EXPC would normally solve the transport system in parallel, high frequencies imply high communication time between processors (in addition to ultimately smaller subdomain time steps). Therefore, it is computationally unattractive to use EXPC for $Pe \ll 1$. For moderate to high Peclet numbers (i.e. $Pe \geq 1$) an average frequency of ~7.7 ($\Delta t_{dimensionless}^{-1}$) yields accurate results for both the homogeneous and heterogeneous domains as figures 6.6 and 6.7 suggest. No such restriction applies to IMPC at low Peclet regimes and it can be used as an alternative where EXPC becomes inefficient. Note that these frequencies are all for the case of a plume moving perpendicular to the interface. Lower frequencies may be sufficient for other orientations.

| Summary of Parameters Used in Interface Concentration Plots | | | | | |
|---|---|---|---|---|---|
| Transport Regime | Network | Snapshot Time (dimensionless) | EXPC Frequency ($\Delta t_{dimensionless}^{-1}$) | IPP mesh | Average IMPC $\Delta t$ |
| Pe = 0.001 | Homogeneous | 5.4 | 193.1 | 10×10 | 3.3e-2 |
| | Heterogeneous | 0.4 | 1086.7 | 10×10 | 2.2e-3 |
| Pe = 1 | Homogeneous | 47.4 | 6.4 | 10×10 | 3.6e-1 |
| | Heterogeneous | 5.6 | 9.1 | 10×10 | 3.4e-2 |
| Pe = 1000 | Homogeneous | 34.6 | 6.4 | 10×10 | 2.8e-1 |
| | Heterogeneous | 6.1 | 9.1 | 10×10 | 3.4e-2 |

Table 6.1: Summary of parameters used to produce the interface concentration plots.

| Summary of Parameters Used in Near-Outlet Concentration Plots | | | | |
|---|---|---|---|---|
| Transport Regime | Network | EXPC Frequency ($\Delta t_{dimensionless}^{-1}$) | IPP mesh | Average IMPC $\Delta t$ |
| Pe = 0.001 | Homogeneous | 64.4 | 2×2 | 3.3e-2 |
| | Heterogeneous | 362.2 | 2×2 | 2.2e-3 |
| Pe = 1 | Homogeneous | 6.4 | 2×2 | 3.6e-1 |
| | Heterogeneous | 9.1 | 2×2 | 3.4e-2 |
| Pe = 1000 | Homogeneous | 6.4 | 2×2 | 2.8e-1 |
| | Heterogeneous | 9.1 | 2×2 | 3.4e-2 |

Table 6.2: Summary of parameters used to produce the near-outlet concentration plots.

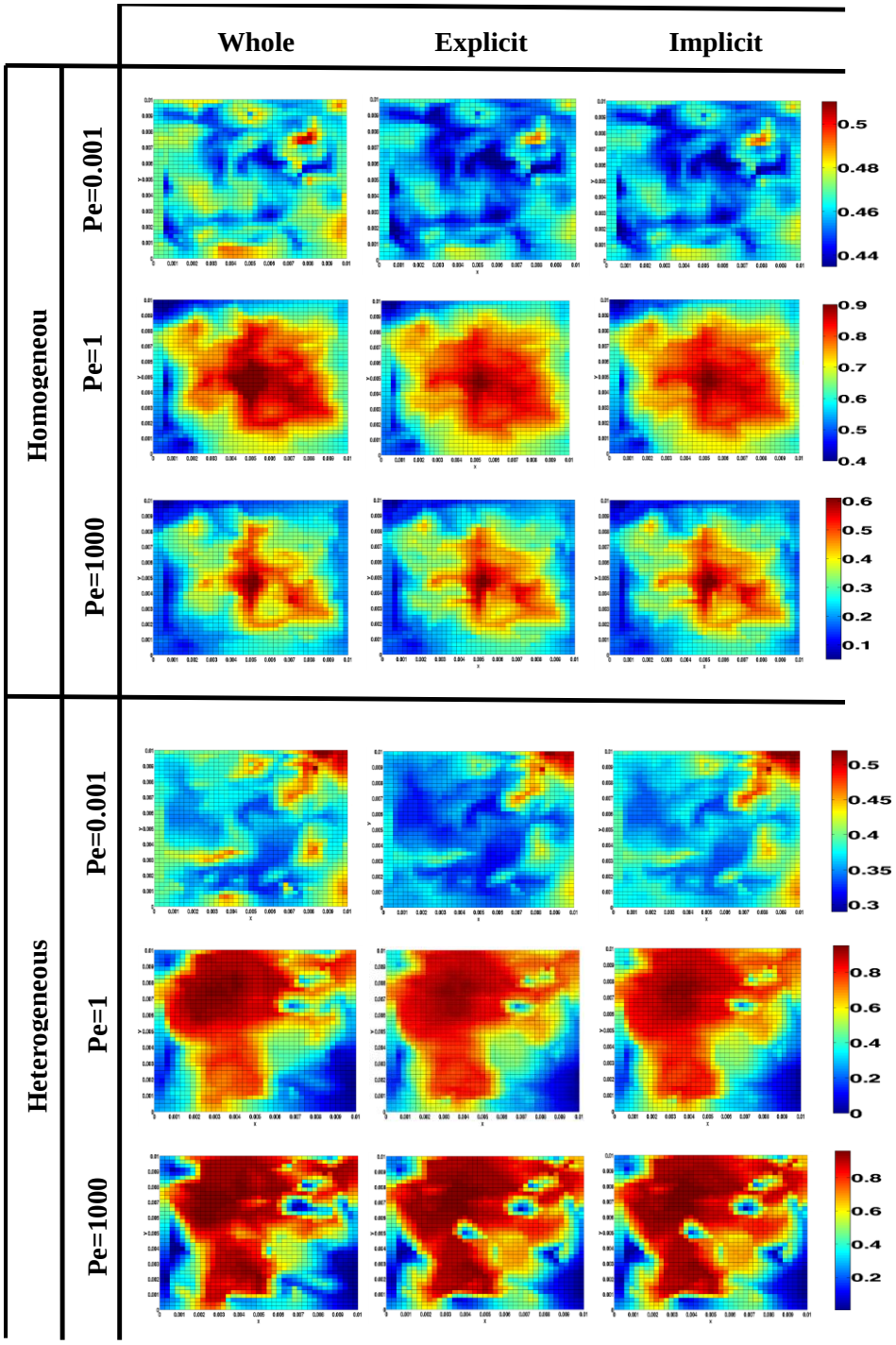


Figure 6.6: Dimensionless concentration fields along the $x$ = 0.1mm plane for the whole, explicit and implicit solutions of the homogeneous and heterogeneous networks. A 10×10 IPP mortar was used for all coupled solutions.

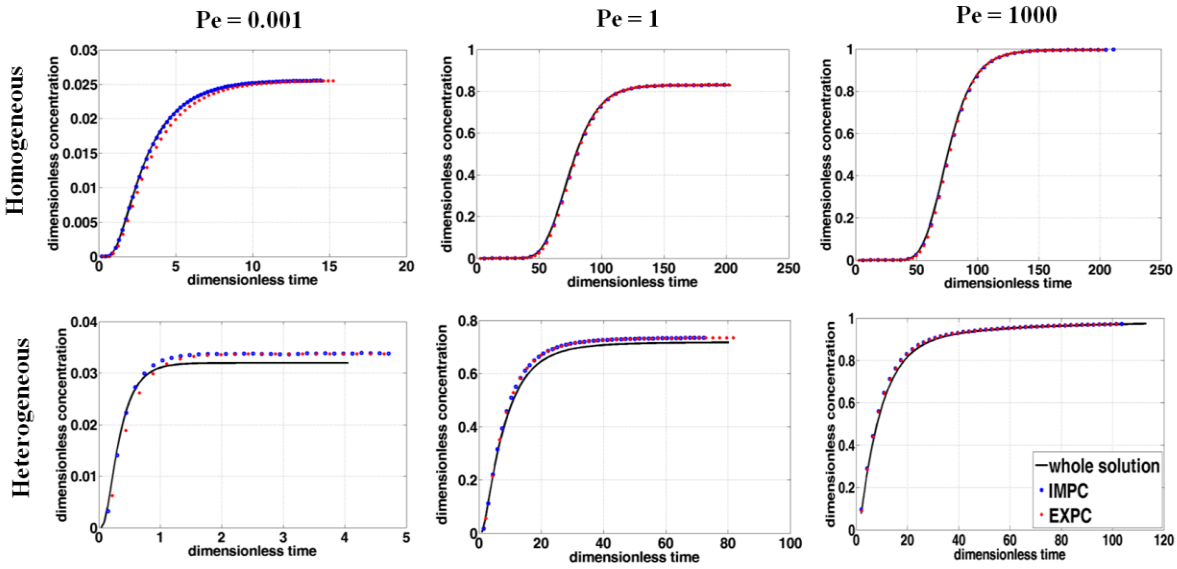


Figure 6.7: Dimensionless near-outlet concentrations of the domain plotted versus dimensionless time for homogeneous and heterogeneous networks at Peclet numbers 0.001, 1 and 1000. The solid line, blue circles and red stars refer to whole, implicit and explicit solutions, respectively.

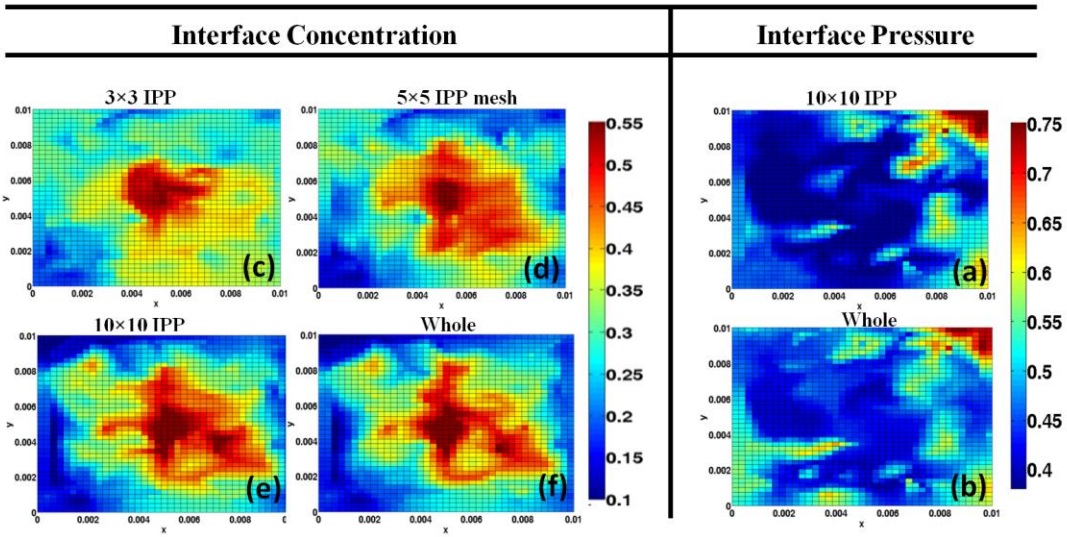


Figure 6.8: (a) and (b) are normalized interface pressure plots of the heterogeneous network obtained from the 10×10 IPP mesh and the whole solution, respectively. (c), (d) and (e) are interface concentration plots for different IPP mesh sizes (3×3, 5×5, 10×10) for the homogeneous network at *Pe* = 1000 obtained with the IMPC method and (f) is the whole solution.

If the EXPC solutions, with the 10×10 IPP mesh and the frequencies denoted in table 6.1, are taken as the baseline, we can decrease the coupling frequency and observe how the error (relative to the whole solution) increases. Figure 6.9 demonstrates how this error increases for each case (transport regime and network type) as we decrease the coupling frequency by an integer multiple of the values listed in table 6.1. The errors were calculated using eq. 6.20, where $c_p$ indicates the pore concentration and $c_{inlet}$ the inlet concentration values. Figure 6.9 shows that errors for all baseline cases (with 10×10 IPP mesh), lie within 1-4% of the whole solutions. The graphs associated with the low Peclet regime have considerably larger slopes compared to moderate and high Peclet regimes. This indicates that for $Pe \ll 1$, coupling frequency not only is high but also is more sensitive (i.e. increases rapidly) to decreasing frequency.

$$\%err = < \frac{\left| c_p - c_p^{whole} \right|}{c_{inlet}} > \times 100 \tag{6.20}$$

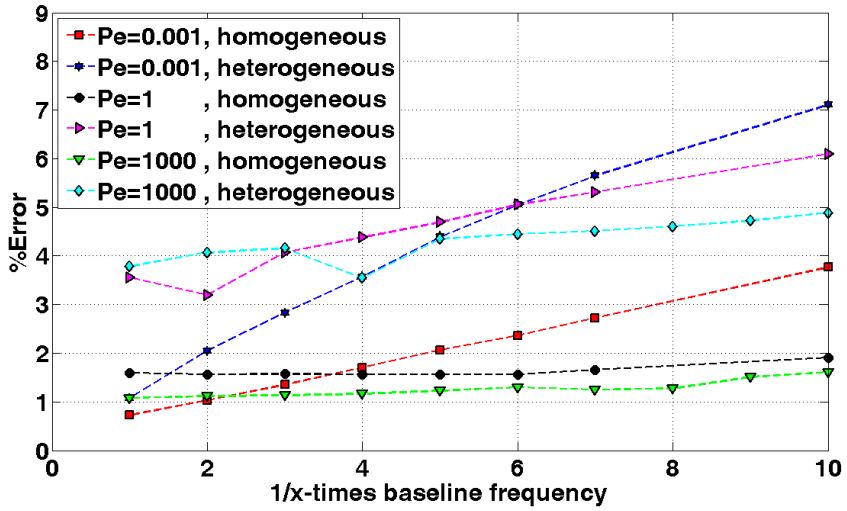


Figure 6.9: Errors (computed via eq. 6.20) versus *x*-fold decrease in EXPC coupling frequency of the baseline cases (listed in table 6.1).

To compare IPP to Lagrangian mortars, pores closest to the $x = 0.1$mm plane in the heterogeneous network were artificially rearranged so as to create two concentrated lines separated by an impermeable region (see fig. 6.10f). Snapshots of interface concentrations were taken at a dimensionless time of ~2.8 and $Pe = 1$. Figure 6.10e shows the whole solution, whereas figures 6.10a to 6.10d show the coupled solutions (using IMPC) via IPP and Lagrangian mortars. Comparing figure 6.10a to 6.10c, we notice that for the same number of degrees of freedom (DOF = 36), the IPP mortar produces a slightly better approximation than bilinears when compared to the whole solution (fig. 6.10e). However, comparing figure 6.10b to 6.10d reveals that the Lagrangian approximation is noticeably poorer than that of IPP for nearly the same number of DOFs (DOF = 74-81) (slightly fewer for IPP). We found that Lagrangian mortars, at times, produced unacceptable results for such heterogeneous pore-scale interfaces; even at high refinements and sometimes with concentration values above one (e.g. fig. 6.10b). However, IPP mortars consistently produced acceptable approximations to the whole solution. The performance of Lagrangian mortars was much better for homogeneous pore-scale interfaces. The interface Jacobian became singular for Lagrangian mortars finer than 4×4 (a problem pointed out by Balhoff et al., 2008) and had to be manually adjusted to avoid the singularity (in fig. 6.10a and 6.10b). For IPP mortars this adjustment was automatic by construction (see fig. 6.10f). We conclude that IPP mortars have noticeable advantages over Lagrangian mortars for pore-to-pore and pore-to-continuum interfaces. Although the clusters and impermeable regions in figure 6.10f were created artificially, such features are typical of real media and are captured with these mortars.

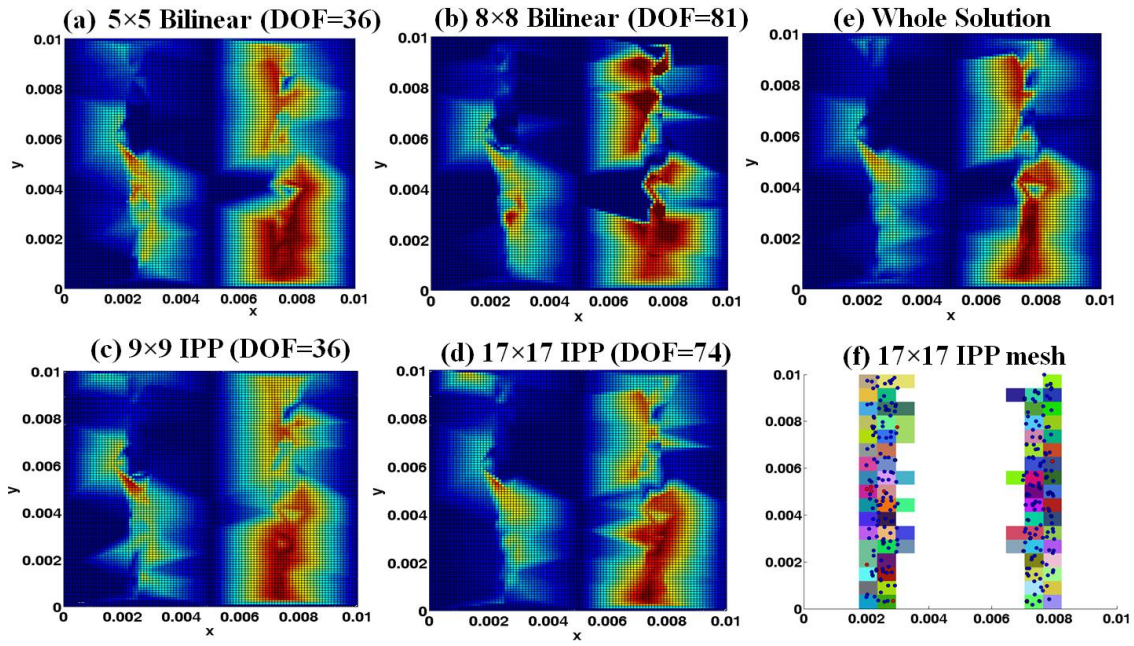


Figure 6.10: Interface concentration fields for network with rearranged pore locations: (a) 5×5 bilinear mortar (DOF = 36), (b) 8×8 bilinear mortar (DOF = 81), (c) 9×9 IPP mortar (DOF = 36), (d) 17×17 IPP mortar (DOF = 74), and (e) whole solution; (f) 17×17 IPP mesh schematic.

The bundle-point-density (defined as the average number of pores within a bundle) for the 3×3, 5×5 and 10×10 IPP meshes in figures 6.6, 6.7 and 6.8c-e are 29, 10 and 3, respectively. The values for the 9×9 and 17×17 IPP meshes in figures 6.10c and 6.10d were 7 and 4, respectively. The error, computed via eq. 6.20, for using a bundle-point-density of 29, in all these figures, was less than 5% (for all regimes, network types and interface-pore distributions). The optimal interface mesh is a delicate balance between computational efficiency and accuracy, and in section 6.4.3.3 a rough criterion for the computational limit is provided (eq. 6.22). This optimal mesh size also depends on the scale and heterogeneity of the plume approaching the interface (coarser mesh might be sufficient for thick versus narrower plumes). Lastly, in all cases studied, the movement

of the plume was perpendicular to the interface. Coarser interface mesh might be sufficient for other orientations. The mortar mesh would ideally be adaptively refined using error indicators based on the jump-in-flux at the interface (Peszynska, 2005). Projections onto a fine mortar mesh can provide such an indicator but this is not pursued in this work.

### 6.4.2 Hybrid modeling

The mortar methods discussed can be easily extended to couple pore and continuum scale subdomains. The interest for doing such mixed-domain modeling comes from: a) the advantage of increasing local modeling accuracy in certain applications (e.g. along fractures or wellbore cement that may act as escape passages for $CO_2$ in carbon sequestration), b) The need for hybrid modeling when continuum assumptions locally break down in critical parts of the domain (Battiato and Tartakovsky, 2011), and c) The need for incorporating effects of the surrounding media on the subdomain for accurate predictions of flow and transport (Sun et al., 2012b). In this section, we present two cases through which we attempt to verify and demonstrate the flexibilities of the hybrid mortar domain decomposition methods.

For the first case, consider a domain consisting of a heterogeneous pore-scale subdomain in between two homogeneous pore-scale subdomains (network properties discussed in section 6.4.1). First, the domain is solved entirely at the pore scale using the coupling methods previously discussed. Transport is coupled using IMPC (same results were obtained using EXPC). Subsequently, both of the homogeneous pore-scale subdomains are replaced with representative continuum subdomains and the problem is resolved (direct upscaling is valid due to perfect mixing at the pore scale and

homogeneity of subdomains). Permeability and porosity of the continuum subdomains are obtained directly from their pore-scale counterparts (Darcy's law used for permeability). Dispersion coefficients were obtained by fitting continuum break-through curves to that of the pore-scale (under flow conditions similar to that experienced by their pore-scale counterparts in the coupled domain). Initial and boundary conditions are similar to those used in section 6.4.1. 5×5 IPP meshes were used at subdomain interfaces in both simulations.

Figure 6.11 shows concentration fields after the injection of ~0.64 pore volumes, before and after substitution of continuum surrogates for the homogeneous pore-scale subdomains. We use pore-volumes-injected as a more appropriate measure of dimensionless time (in the presence of continuum subdomains). In figure 6.11a, the homogeneous subdomains both experience a Peclet number of ~2.5, and the heterogeneous subdomain experiences a value of ~1.25 (since it is more permeable and thus incurs a lower pressure drop). The Peclet number over the entire pore-scale domain is ~2.5. The channeling behavior observed in the concentration field of the heterogeneous subdomain in figure 6.11a is captured by the hybrid simulation as shown in figure 6.11b. Figure 6.12 suggests excellent agreement between the pore-volume-averaged concentration profiles of the two domain types at the location demarcated in figure 6.11a with a dashed line. This serves as verification of the mortar methods as hybrid modeling tools. Although in the scenario studied hybrid modeling might not have been a necessity (due to perfect mixing at the pore scale and the absence of reaction), the methods can be applied to such scenarios without modification. The homogeneity of the lateral subdomains with the assumption of pore-level mixing in the absence of reaction justifies the upscaling and verification of the hybrid method.

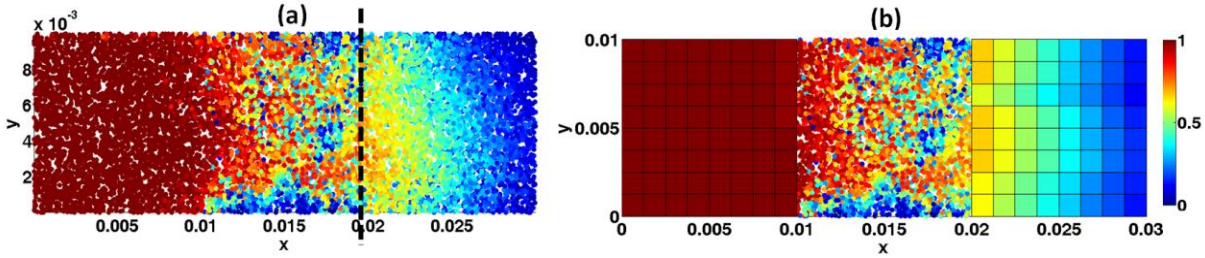


Figure 6.11: Concentration fields after ~0.64 pore-volumes injected in a domain consisting of a heterogeneous pore-scale subdomain in between a) two homogeneous pore-scale subdomains, and b) continuum representations of the two homogeneous pore-scale subdomains. Injection is from left to right. Axes are in cm. The dashed line is where pore-volume-averaged concentration profiles of figure 6.12 were recorded.

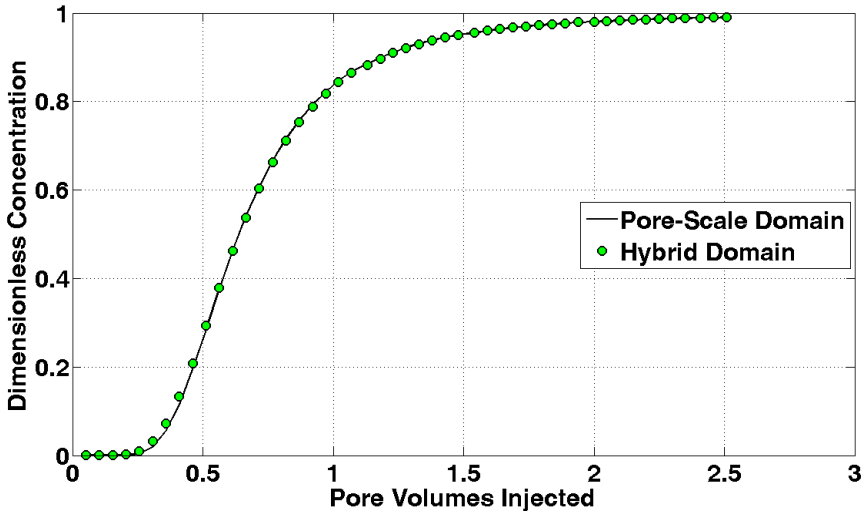


Figure 6.12: Pore-volume-averaged concentration profile versus pore-volumes injected for the pore-scale and hybrid domains depicted in figure 6.11, recorded at the location marked by the dashed line.

For the second case, consider a 2×2 arrangement of pore-scale and continuum subdomains similar to Balhoff et al. (2008) (see figure 6.13). Three of the subdomains (i.e. (1,1), (1,2), (2,2)) are modeled at the continuum and one is modeled at the pore scale

(2,1). The (1,1) and (2,2) subdomains both have 8×8×8 discretizations where the (1,2) subdomain has a 5×5×5 discretization. These discretizations are non-matching where they share an interface. The (2,1) pore-scale model is highly heterogeneous (properties discussed in section 6.4.1). There are four interfaces in the domain: a) two of them are between continuum subdomains (we called them c2c interfaces), and b) the other two are between pore-scale and continuum subdomains (we call them p2c interfaces). The mortars used for c2c interfaces are 3×3 bilinear Lagrangians, and the ones used for p2c interfaces are 5×5 IPPs. Solute is injected into the (1,2) subdomain in the negative *x*-direction and extracted from the (2,1) subdomain also in the negative *x*-direction. Finer continuum discretizations are used adjacent to the pore-scale subdomain to transfer information more accurately between scales. All grids within the continuum subdomains have the same macroscopic properties (permeability, porosity and dispersion coefficient). For convenience, and as a proof of concept, the transverse and longitudinal dispersion coefficients are assumed to be equal, although we realize this in general is not the case. The methods can be used for the case of full tensor dispersion coefficients without modification.

The continuum subdomains are upscaled representations of the homogeneous network described in section 6.4.1. If the domain is modeled entirely at the pore-scale (similar to the previous case) the Peclet numbers calculated for each block are: ~1.1 for (1,1), ~1.6 for (2,1), ~2.4 for (1,2) and ~1.5 for (2,2) with a value of ~1.8 for the domain as a whole. Figure 6.13 shows the pressure and concentration fields for this hybrid domain after ~0.64 pore-volumes injected. It demonstrates how the method allows for seamless and flexible coupling of the pore scale to the continuum scale, additionally incorporating non-matching discretizations of the continuum. This allows for the gradual coarsening of the continuum discretizations away from the pore-scale region.

It is noteworthy that the continuum grids used in the previous two cases are very small for all practical purposes. In theory, the concept of an REV is not violated since all continuum grids were assigned the same macroscopic properties (i.e. no claim was made about understanding heterogeneity at grid level) and the macroscopic equations are valid at the limit. Nevertheless, the cases hold as proof of concept for the validity and flexibility of the mortar methods as hybrid modeling tools. In practice, the pore-scale region might involve wellbore cement (during $CO_2$ escape scenarios) or a propped-up fracture coupled to the surrounding (continuum) matrix. In such cases, the scales of the interfaces shared between the two regions are large enough, and coarser continuum grids adjacent to the pore scale region would be applied.

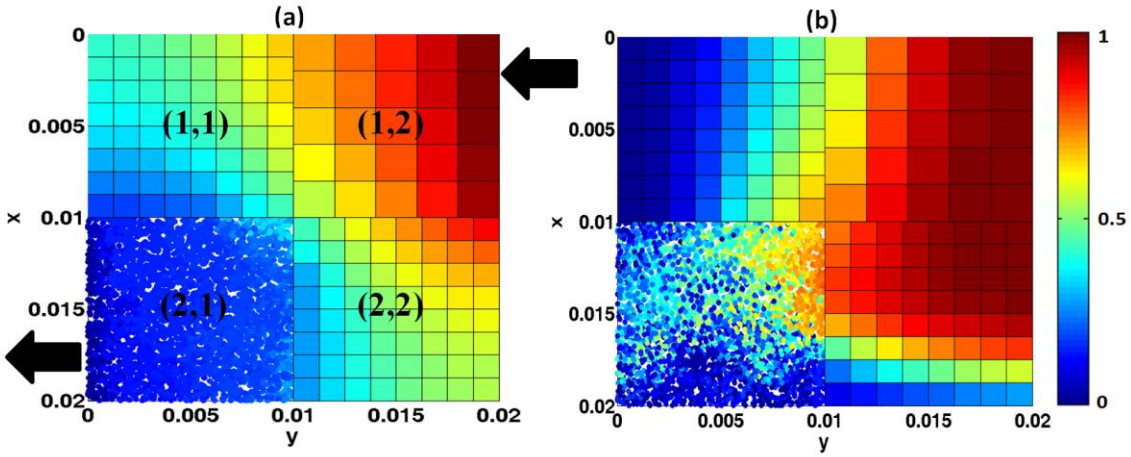


Figure 6.13: a) Pressure and b) concentration fields of the hybrid domain with non-matching continuum grids. Concentration and pressure values are normalized against inlet values. Inlet and outlets are indicated with arrows. Axes are in cm. Snapshot is taken after ~0.64 pore-volumes are injected.

### 6.4.3 Computational study

In this section, the computational aspects of the domain decomposition methods are studied. We compare the computational advantages of using mortars against solving the problem as a whole. We make comparisons between IMPC and EXPC wherever appropriate. The domains studied consist of units (called unit blocks) that have dimensions of $0.4\times0.1\times0.4$ mm$^3$. These units are also used to construct subdomains of larger sizes. We have restricted ourselves, without loss of generality of the results, to a moderate transport regime of $Pe \approx 2$. Boundary and initial conditions are similar to those in section 6.4.1. The time-dependent transport problem is simulated until the injected plume has traveled roughly 30% of the total $x$-dimension. The objective is to make fair comparisons on a time-step-to-time-step basis for transport simulations. We divide the time interval into five segments. The whole and the IMPC solutions are obtained by marching five steps forward in time. A backward Euler scheme is used to discretize the time derivative for both. The EXPC solution is obtained by synchronizing the subdomains five times and marching each subdomain one time step in between two consecutive synchronizations. The relatively few time steps were chosen as a compromise between keeping the overall computational load at a tractable level (considering domain size is variable) and assigning sufficient loads to each processor. Since the comparisons are on a time-step-to-time-step basis, the results are valid for finer time steps as well.

Four studies are conducted: 1) domain size is varied keeping everything else constant, 2) number of subdomains is varied keeping domain size constant, 3) number of interface degrees of freedom is varied keeping number of subdomains and domain size constant, and 4) scalability of a nonlinear flow system is studied by changing domain size. All simulations are run on a dual CPU (hexa-core per CPU) (Intel(R) Xeon(R) CPU,

X5670 @ 2.93GHz) machine. No preconditioners are used for solving the interface problems, which would provide additional computational benefits.

#### *6.4.3.1 Variable domain size*

A domain consisting of one unit block is chosen and its size is consecutively increased by appending more unit blocks in the *y*-direction (fig. 6.14a). The domains are simulated for both flow and transport by solving them as a whole as well as using mortars (GJS for flow, IMPC and EXPC for transport). 2×2 IPP mortars were used between subdomains (i.e. unit blocks). Effects of using finer mortar mesh are studied in section 6.4.3.3. Flow and transport are solved both in parallel and in series to demonstrate advantages of mortars both in the presence and absence of parallelism.

In figure 6.14b, the coupled-in-series solution for flow becomes slightly more attractive than the whole solution for domains larger than 8 unit blocks. An extrapolation of the plots seems to suggest that at larger domain sizes larger advantages would become apparent. It is evident that the parallel schemes in figure 6.14b have obvious benefits over the whole solution, and the wall-clock times increase only slightly with domain size. As for the transport problem, figure 6.14c suggests a very large difference (nearly one order of magnitude) between the whole and the coupled-in-series clock times. Since figure 6.14c is in log scale, figure 6.14d is presented to highlight further benefits obtained from parallelism. The graphs for the parallel IMPC and EXPC schemes remain virtually flat as the problem size (and simultaneously the number of processors) is increased. It is noteworthy that every time step taken by the EXPC scheme is consistently cheaper than an equivalent time step taken by the IMPC scheme (no interface problem is solved in EXPC). However, one must note that at low Peclet regimes higher coupling frequencies

would increase the total number of time steps taken by EXPC as well as the inter-processor communication time (as shown in section 6.4.1) and this could shift the balance in favor of IMPC. Wall-clock times are much smaller for flow compared to transport. The tolerance used in the CG and GMRES solvers, as well as in the Newton iterations of the GJS and the IMPC schemes, was $10^{-10}$. No restart value was used in the GMRES solver.

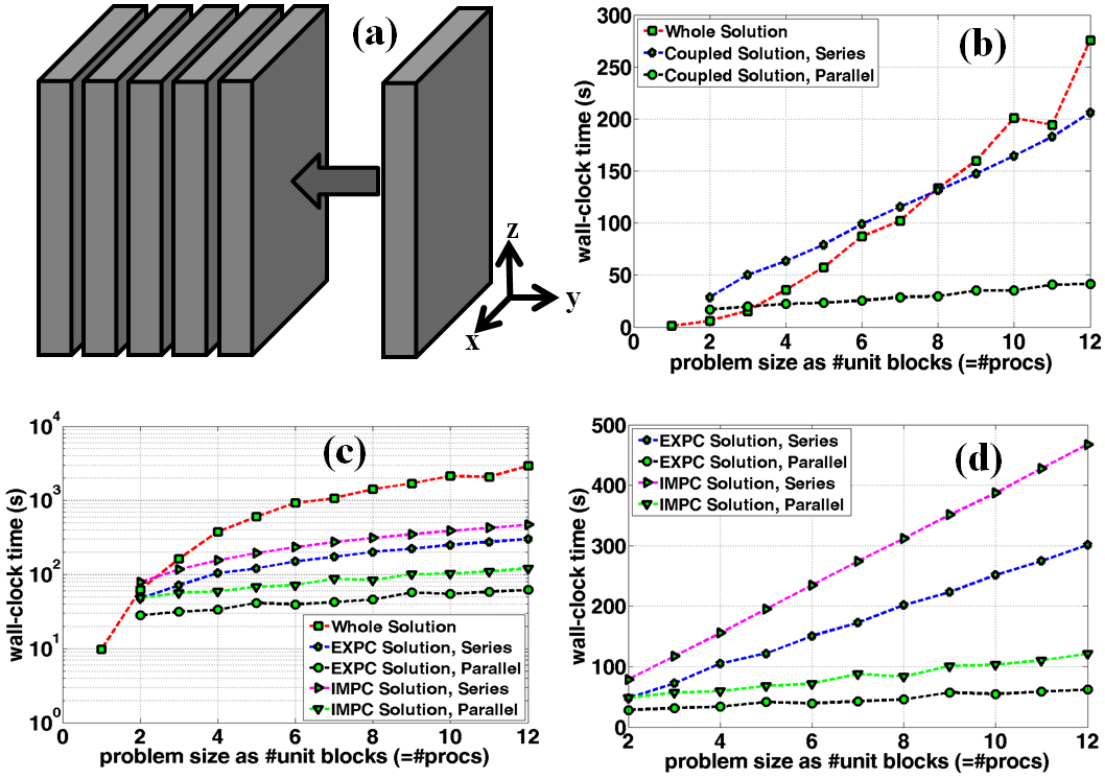


Figure 6.14: (a) Schematic of increasing domain size by appending unit blocks in *y*-direction, (b) wall-clock time vs. problem size (i.e. # of unit blocks) for flow including the whole, coupled-in-series, coupled-in-parallel cases. c) wall-clock time vs. problem size for transport including the whole, coupled-in-series, coupled-in-parallel cases (log scale). d) Same as (c) excluding the whole solution, for a clearer comparison of IMPC and EXPC in series and parallel.

#### *6.4.3.2 Variable decomposition*

A domain size of 12 unit blocks is assembled. The domain is initially solved as a whole for flow and transport. It is then successively split into 2, 3, 4, 6 and 12 equal subdomains along the x-direction with 2×2 IPP mortars placed in between (Effects of finer mortar mesh are studied in section 6.4.3.3). Subdomains consist of 6, 4, 3, 2 and 1 unit blocks each, respectively. The split domain is solved in parallel for flow and transport using mortars with number of processors equaling the number of subdomains. Parallel efficiency is calculated using eq. 6.21 (measuring strong scalability). Figure 6.15a summarizes the efficiencies obtained for each case.

$$parallel\ efficiency = \frac{\Delta t_{series}}{N_{cpu} \times \Delta t_{parallel,Ncpu}} \tag{6.21}$$

Since at least two subdomains are necessary for coupling, $\Delta t_{series}$ is replaced by twice the wall-clock time of the 2-subdomain case (i.e. 2-subdomain case assumes an efficiency of 1). The >1 efficiencies result from merely decomposing the domain, because flow and transport computational loads scale nonlinearly with problem size. Figure 6.15b suggests that the flow problem requires the domain to be split fine enough (>2 subdomains here) for mortars to become advantageous (over the whole solution). However, immediate benefits are noticeable for the transport problem. We conclude that mortars have obvious computational benefits over the single domain solution. Figure 6.15 suggests that efficiencies decline when maximum number of processors is used. We associate this decline to the reduction of per-core resources (e.g. cache space) as the number of parallel workers is increased. Increasing the number of physical processors would circumvent this problem, but due to technical and resource limitations this was not

tested. Similar tolerances were used as in the previous section, and no restart values were applied in the GMRES solves.

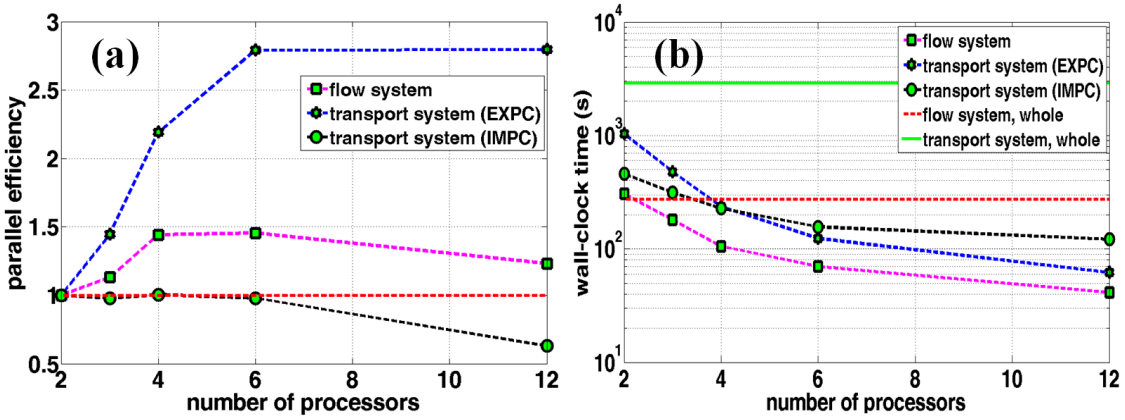


Figure 6.15: (a) Parallel-efficiency (or strong scaling) of flow (GJS) and transport (IMPC and EXPC), (b) wall-clock times of flow and transport versus number of processors. Clock times of the whole solutions are shown as horizontal lines.

#### *6.4.3.3 Variable interface mesh*

A domain size comprised of six unit blocks is considered. The domain is split into three equal subdomains along the *x*-direction (two unit blocks each). The problem is solved for flow and transport in parallel (with three processors). The IPP mesh is changed between simulations and is set to: 2×2, 6×6, 10×10, 15×15, 20×20, 25×25, 30×30, 35×35, and 40×40 (i.e. total number of interface degrees of freedom (DOFs) between 8 and 3200). Wall-clock times of simulations are recorded and shown in figure 6.16. Clock times of the whole solutions are indicated with horizontal lines.

Figure 6.16 shows that, as the interface mesh is refined, the computational limit imposed by the whole solution is eventually surpassed rendering the mortar methods (GJS and IMPC) computationally disadvantageous. This threshold for flow is rather low

in this case (since the problem size is small), but it is much higher for transport. It is noteworthy that EXPC is insensitive to the interface IPP mesh size, and very accurate solutions may be acquired without affecting computational efficiency.

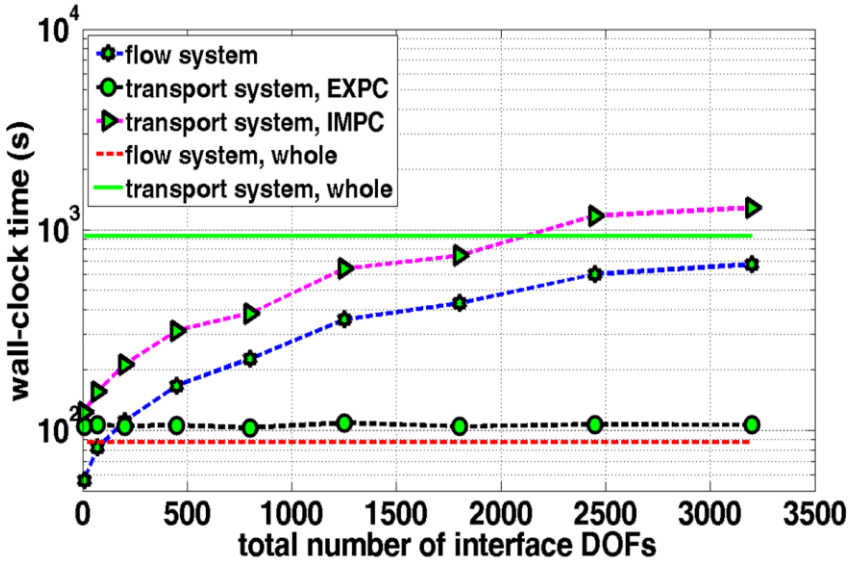


Figure 6.16: Wall-clock times for flow (GJS*)* and transport (IMPC and EXPC) vs. total number of interface DOFs. Clock times of the whole solutions are depicted with horizontal lines.

Figure 6.16 suggests it is helpful to have an a priori estimate of the computational limits beyond which the discussed methods would become unattractive. In general, it is difficult to develop an exact criterion but a rough estimate can be made. In chapter 5, we first presented a criterion for a problem that has a *p*-order scaling of computational load with problem size. This is given by eq. 6.22 with $N_{blk}$ being the number of subdomains and $N_{cpu}$ the number of processors. Originally, $\rho_{dof}$ was denoted as the number of interface unknowns per subdomain. Here, we recognize it as the number of linear interface iterations divided by the number of subdomains. Since an *a priori* knowledge of the

number of linear interface iterations may not be available, any modest guess bounded by the number of interface unknowns would suffice.

$$\frac{\rho_{dof}}{N_{cpu} \times N_{blk}^{(p-2)}} < 1 \tag{6.22}$$

While eq. 6.22 gives a rough estimate of whether mortars provide computational benefits over the whole solution, it does not take into account problem setup (step 3 in the algorithm of figure 6.2) and benefits from subdomain factorizations. It should merely be regarded as a first estimate prior to applying these methods. For the flow problem the criterion is satisfied with the 2×2 IPP mesh only, which is a close estimate considering GJS becomes disadvantageous beyond 6×6 IPP. For transport, the criterion is satisfied for 2×2 and 6×6 IPP, which is a conservative estimate considering that IMPC becomes disadvantageous beyond 30×30 IPP (fig. 6.16). Considering that the graphs for GJS and IMPC in figure 6.16 appear linear on a linear plot, a bundle-point-density of 29 (i.e. DOF = 288 and <5% error) would make mortars ~4 times faster than the whole solution for transport but ~1.5 times slower for flow (although they become faster for larger domains). We conclude that GJS and IMPC are computationally limited by the number of interface DOFs and eq. 6.22 can provide a first estimate of this limit, whereas EXPC is computationally insensitive to the interface mesh. All simulations were run with similar tolerances as in section 6.4.3.1, and the restart value for the GMRES solver was set to 20.

#### *6.4.3.4 Nonlinear flow scalability*

Domain size is augmented similar to section 6.4.3.1 (subdomains consist of one unit block). For each domain size, only the nonlinear flow equation (eq. 6.2) is solved

(transport not considered). The power-law behavior of the fluid (with index $n = 0.5$) renders the problem non-linear. The flow problem is solved in parallel both as a whole domain and as coupled subdomains using GJS with 2×2 IPP mortars (with number of processors and subdomains being equal). Effects of finer mortars were studied in section 6.4.3.3. Figure 6.17a shows wall-clock times of the whole and coupled solutions versus problem size. Despite the slight increase in clock times of GJS, there is a ~6 fold enhancement in the performance of the 12-unit-block domain over the whole solution. The deteriorating performance for higher numbers of parallel workers is ascribed to the reduction of per-core resources (e.g. cache space) as mentioned earlier.

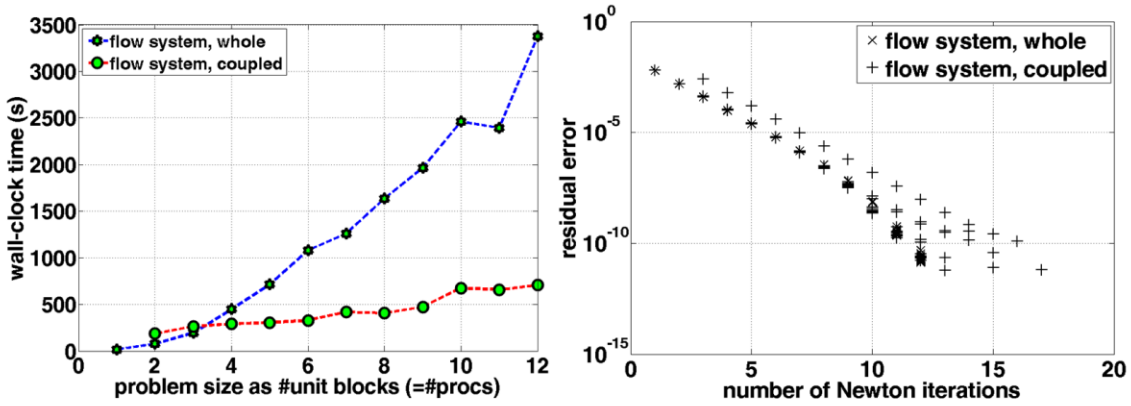


Figure 6.17: (a) Wall-clock time vs. problem size (i.e. # unit blocks) for non-linear flow system solved as a whole (small stars) and as coupled subdomains (big circles). (b) Residual error vs. Newton iterations for whole (cross) and coupled (plus) solutions.

Figure 6.17b demonstrates residual errors (computed as the root mean squares of the residual vectors) versus the number of Newton iterations for both the whole and coupled solutions. Residual errors from all domain sizes (both the whole and coupled solutions) are collapsed onto figure 6.17b (hence the scatter). The plot shows that the rate

of convergence is nearly the same whether the problem is solved as a whole domain or as coupled subdomains. This confirms that (at least for the cases studied) there is no loss in rate of convergence when GJS is applied. Thus, mortars are more efficient even for nonlinear flow problems (as those studied herein) with nearly unaltered rates of convergence.

## 6.5 CONCLUSIONS

The following summarizes our findings:

- Efficient mortar methods were developed for coupling flow and transport across pore- and continuum-scale subdomains (GJS: for flow, and IMPC/EXPC: for transport). The methods were verified under various transport regimes and levels of heterogeneity. The methods were further shown to be valid and flexible hybrid modeling tools. Diffusive transport was included in the coupling scheme, which was neglected in chapter 5.
- EXPC was shown to be more suitable for moderate to high Peclet regimes ($Pe$ >1) while IMPC has no such restriction. On a time-step-to-time step basis EXPC scaled better than IMPC, and is recommended for $Pe$ >1 (it is also more flexible than IMPC).
- IPP mortars were extended to pore-to-continuum interfaces and shown to be more suitable than Lagrangian mortars wherever pore-scale subdomains are involved.
- The methods were shown to be much more efficient than solving the domain as a whole even in series (especially for transport). Favorable (weak and strong) parallel scalabilities were obtained.

- The methods were applied to the non-linear flow of a power-law fluid and were shown to be very efficient with no loss in rate of convergence.

The methods developed remain unaltered in presence of (homogeneous/heterogeneous) reactions, multiple species, and more detailed pore-scale physics. Future work is directed towards extending the methods to multiphase flow and transport, and further enhancement of the IPP mortars (i.e. higher orders).

# Chapter 7: Conclusions and Future Directions

In the following we summarize our findings and discuss their implications. Since specific conclusions germane to the material in each chapter are already contained therein, we refrain from reiterating them here. Instead conclusions are drawn in a rather broad sense, so as to highlight possible directions for future research. A list of such directions is provided under section 7.2.

## 7.1. CONCLUSIONS

An Eulerian network model, referred to as the streamline splitting method (SSM), was developed and shown to accurately capture partial mixing within pores. Predictions were in very good agreement with CFD simulations as well as micromodel experiments, and the model was shown to perform at a very low computational cost, on the order of a few minutes on a desktop machine. The specific algorithm developed to approximate the distribution of streamlines within pores can also be used in Lagrangian models such as particle tracking (PT) without further modification.

Our results suggest that the choice of pore-level mixing assumptions (perfect mixing vs. partial mixing) has a high impact on the magnitude of macroscopic transverse dispersion in *ordered* media. In *disordered* media, the effects seem to be substantially lower. This observation is in agreement with another study regarding two-dimensional disordered fracture networks (Park et al., 2001b). While we have focused on three-dimensional disordered porous media, one may be able to draw a parallel between the two studies. That said, two issues still remain outstanding: a) while mixing assumptions seem to be of low significance in disordered granular media (e.g. sandstones), more research is needed before similar conclusions can be drawn for other types of porous

material. b) Even though average differences in pore-scale concentration fields are small, the effects of mixing assumptions on transverse dispersion coefficients may still be considerable due to possible tailings in the concentration fields.

An Eulerian network model, referred to as the superposing transport method (STM), was developed and shown to accurately capture shear dispersion within throats. Predictions were in good agreement with CFD simulations and experimental data from the literature. The applicability of STM is for *linear* transport problems only. The formulation of the method is relatively simple and provides a much more efficient alternative to Lagrangian methods under certain boundary conditions and domain sizes. The method has the flexibility to perform simulations on networks with either finite (something current particle tracking models have difficulty with) or zero pore volumes. While partial mixing and shear dispersion are separately incorporated into SSM and STM, respectively, we note that there are no restrictions for the two models to be combined into one.

While comparatively efficient than alternative methods for certain boundary conditions and domain sizes, the computational performance of STM needs further improvement. Since current limitations are not inherent to the method, several practical solutions were proposed in chapter 4. The main proposition is to approximate recorded pore concentration profiles using piecewise linear functions, rather than the current piecewise constants. This would potentially reduce computer memory requirements while simultaneously increase modeling accuracy. Considering that applications of STM span several engineering fields (e.g. electrical, chemical, etc.) and that it can be used, without modification, to perform field-scale transport simulations, the proposed improvements are worthy of future pursuit.

A discussion on the origins of supra-linear scaling of longitudinal dispersion vs. Peclet number, conjoined with an analysis of past modeling results from the literature was provided. The general conclusion is that supra-linear dispersion arises whenever the pore-space contains (near-) stagnant regions for diffusion to laterally stretch the solute and produce a minimum in the $D_L/(v_{int}d_p)$ vs. $Pe_d$ graph. These regions are either the ever-present boundary layers near the fluid-solid interface (leading to a $D_L \sim Pe_d \log Pe_d$ scaling; Saffman, 1959) or topological features such as dead-end pores (leading to a $D_L \sim Pe_d^2$ scaling; Koch and Brady, 1985). This interpretation seems to corroborate with all numerical results discussed from the literature (including this work), that exhibit such a supra-linear regime.

It was shown that the predictive capacity of *all* Eulerian network models, including STM, is inherently limited for *ordered* media. The limitation is a result of the fact that particle "memories" are effectively erased upon their arrival at the pores. The consequence is that an erroneous $D_L \sim Pe_d$ scaling prevails at high Peclet numbers, instead of the known $D_L \sim Pe_d^2$ scaling in ordered media (Edwards et al., 1991). Circumventing this problem requires the delicate task of mapping incoming solute particles (at the pores) to appropriate radial positions at the outlet throats. This is currently only possible under a Lagrangian framework.

The combination of the (verified) mortar domain decomposition methods and the reactive transport network model developed in chapter 5 for advection-dominated transport was used to study "emergent" behavior of calcite precipitation in the context of geologic $CO_2$ sequestration. Field observations along the Little Grand Wash fault suggest that pore-filling calcite cement occludes the pore space and potentially leads to observed shifts in preferential flow paths. Such an "emergent" behavior was not predicted in our simulations, although cementation did eventually lead to an occlusion of the pore space.

The disagreement was attributed to either an oversimplification of the problem physics (e.g. single-phase flow, simplified geochemistry, etc.), or unrealistic initial conditions (e.g. distribution of reactive minerals). Even so, the study demonstrated the application of the mortar methods for large and highly heterogeneous pore-scale domains.

The domain decomposition methods were further extended and verified in chapter 6 to include diffusive transport and pore-to-continuum coupling. We showed that they are accurate and computationally more efficient than single-domain simulations (even in series). Satisfactory parallel scalability on a dual CPU (hexa-core per CPU) machine was demonstrated. These methods may be applied to: study problems in which REV sizes are larger than the scale of a single pore network, conveniently characterize network-scale heterogeneities/discontinuities, perform multi-model simulations within the same computational domain, and study emergent behavior at sufficiently large scales. In the context of hybrid modeling, the methods may be used to perform "concurrent" simulations (i.e. when insufficient scale separation exists; Sheibe et al, 2014) of localized pore-scale inclusions in an otherwise continuum domain. In reservoir engineering, the methods are deemed to be most appropriate for near-well applications (as they provide the only point of direct data acquisition from the reservoir, in order to characterize the pore-scale subdomains). By envisioning a pore-scale "skin" around the wellbore one may be able to study/predict wormhole formation during acid stimulation, and/or $CO_2$ leakage through wellbore cement. Other applications include mixing induced mineral precipitation/dissolution scenarios (Tartakovsky et al., 2008a), in which two fluids with different compositions come into contact and undergo reactions over the range of a few pore diameters (that can be represented locally at the pore scale). A purely continuum description for such problems is inadequate for quantitative predictions (Tartakovsky et al., 2008b).

## 7.2 FUTURE DIRECTIONS

The following summarizes a number of possible directions for future research:

- SSM predictions have not been compared to transverse dispersion coefficient data from the literature. Additionally, the impact of pore-level mixing assumptions on this parameter is yet to be quantified.
- The inter-pocket mass transfer term in the formulation of SSM was derived for passive tracer transport. Under reactive transport conditions (mixing induced homogeneous reactions and/or fluid-mineral heterogeneous reactions) this term needs most likely to be modified, to reflect proper local initial/boundary conditions.
- The algorithmic modifications to STM proposed in chapter 4, would be a worthy future research direction. These modifications could substantially alleviate computer memory requirements and potentially reduce computational cost by nearly an order of magnitude.
- Currently no computationally efficient while accurate method for transport modeling on ordered pore networks exists. Eulerian network models are inherently limited in this case, and no simple modifications seem sufficient for overcoming the limitations. For this reason, a Lagrangian framework (e.g. particle tracking) would be an appropriate starting point for the development of the "simplest" modeling approach.
- The IPP mortars developed in chapters 5 and 6 consist of piecewise constant basis functions defined over each bundle. Despite the advantages that piecewise constant bases provide (e.g. simple closed-form equations for synchronizing interface concentrations in EXPC), they possess the disadvantage of causing

numerical artifacts in situations where a concentration front is moving parallel to the subdomain interface. The problem is that solute concentrations may be unrealistically propagated ahead of the front. To overcome this artifact, one can either use a fine interface mesh or adaptively refine it in the vicinity of the concentration front. While this would eliminate the problem, a better solution would be to use higher order mortars. In order to preserve the current advantages of IPP mortars for pore-to-pore and pore-to-continuum interfaces (i.e. local flux continuity and avoiding possible singularity of the interface problem due to empty interface grids), one may add two more degrees of freedom per IPP basis function. This increases their order by one, and results in discontinuous piecewise linear bases allowing them to assume gradients in arbitrary directions.

- The domain decomposition methods presented in chapters 5 and 6 were designed for single-phase flow problems. Extensions to two-phase flow are a necessary and obvious future direction, but a highly non-trivial one. A preliminary study regarding this was performed and determined that the specifics of the domain decomposition method and the interface problem depend, to a large extent, on the specific pore-scale models (e.g. pore network, Lattice Boltzmann, etc.; there are even strong variations within different pore network approaches) involved in the simulation. The coupling of the subdomains is also more complicated compared to its continuum counterpart, because pore-scale behavior of multi-phase flow is dominated by capillarity. This leads to a very discontinuous “on-and-off” type behavior, resulting in frequent singularity of the interface problem.

# Appendices

## APPENDIX A: STREAMLINE SPLITTING ALGORITHM FLOWCHART

Figure A.1 presents the details of the algorithm used for identifying preferred outlets for a given inlet *i* (i.e. member of the $Pr_i$ set) and the kind of access the inlet (i.e. *full*, *partial* or *limited*) is granted to these outlets:

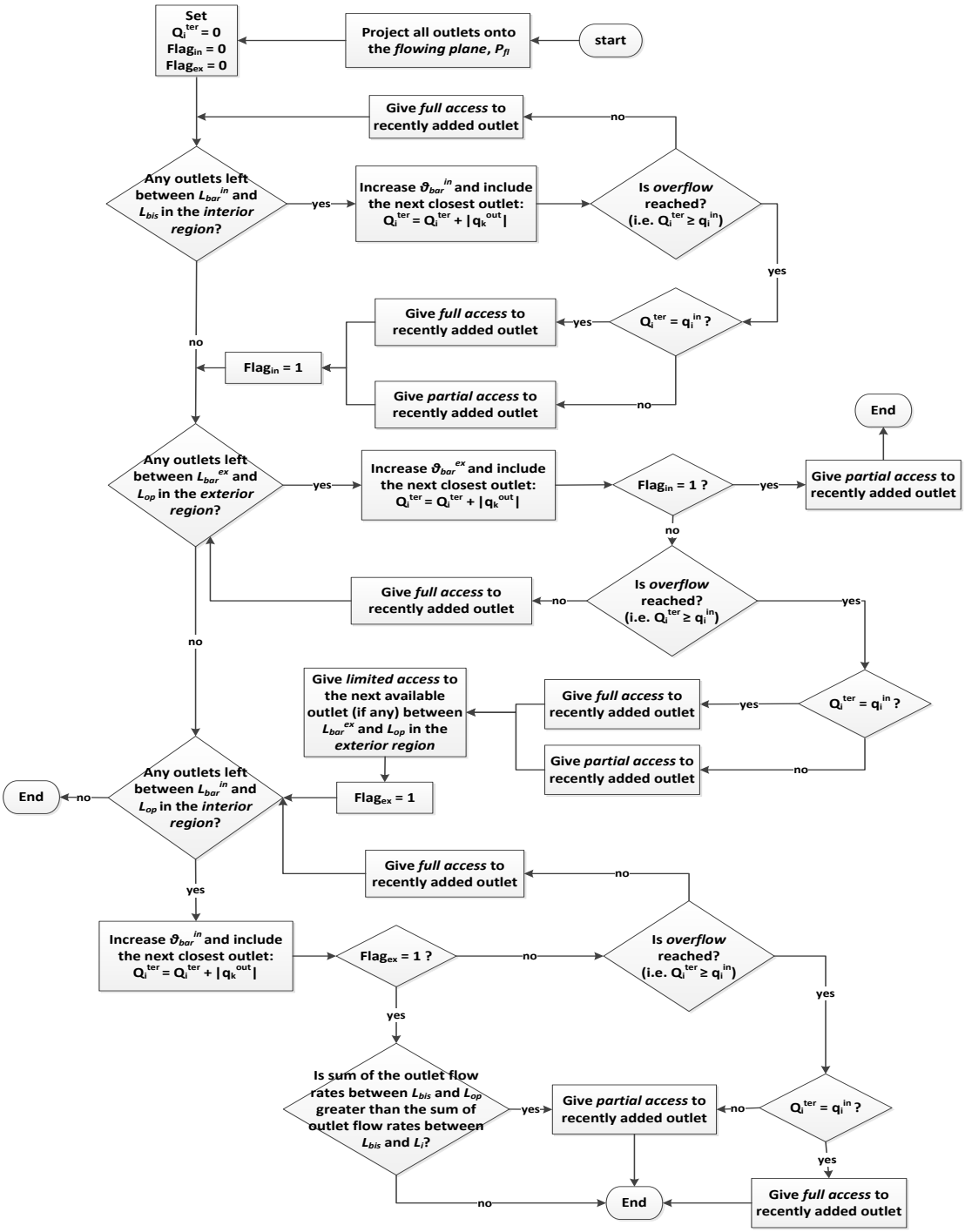


Figure A.1: Flowchart of the algorithm used for determining the preferred outlets of a given inlet *i* (i.e. members of $Pr_i$). Sub- or superscripts *i*, *out*, *in* and *ex* refer to the *inlet*, *outlet*, *interior* and *exterior*. $q_i$ is the flow rate of the given inlet *i*.

## APPENDIX B: EQUIVALENCE OF FLOW RATE-WEIGHTED DISTRIBUTION OF INFLOWING STREAMS AND CHOOSING $\Omega_{Io} = |Q_o|$ AS THE COEFFICIENTS OF THE OBJECTIVE FUNCTION GIVEN BY EQ. 3.5

Consider, for simplicity, a pore with two inlets and two outlets. Let the flow rates of the two inlets be denoted by $q_1$ and $q_2$ and similarly for the two outlets by $q_3$ and $q_4$ (all positive values). Note that since the flow equation (eq. 3.2) is solved, mass balance (i.e. $q_1 + q_2 = q_3 + q_4$) applies. We assume that both inlets have *partial access* to both outlets (no *full* or *limited access*). We begin by writing the restrictions given by equations 3.4b and 3.4c:

$$\begin{cases} x_{13}q_3 + x_{14}q_4 = q_1 \\ x_{23}q_3 + x_{24}q_4 = q_2 \\ x_{13} + x_{23} = 1 \\ x_{14} + x_{24} = 1 \end{cases} \tag{B.1}$$

Since no *full-access* outlets exist the above system cannot be reduced any further. Note that both outlets belong to both $Pr_1$ and $Pr_2$, thus the change of variable given by eq. 3.7 needs to be applied (e.g. $x_{13} = 1 - y_{13}$). Subsequently, we obtain the following system (we make use of $q_1 + q_2 = q_3 + q_4$):

$$\begin{pmatrix} 1 & 0 & 1 & 0 \\ 0 & 1 & 0 & 1 \\ q_3 & q_4 & 0 & 0 \\ 0 & 0 & q_3 & q_4 \end{pmatrix} \begin{pmatrix} y_{13} \\ y_{14} \\ y_{23} \\ y_{24} \end{pmatrix} = \begin{pmatrix} 1 \\ 1 \\ q_2 \\ q_1 \end{pmatrix} \tag{B.2}$$

Converting the above system to reduced-row-echelon form we obtain:

$$\begin{pmatrix} 1 & 0 & 1 & 0 \\ 0 & 1 & 0 & 1 \\ 0 & 0 & q_3 & q_4 \\ 0 & 0 & 0 & 0 \end{pmatrix} \begin{pmatrix} y_{13} \\ y_{14} \\ y_{23} \\ y_{24} \end{pmatrix} = \begin{pmatrix} 1 \\ 1 \\ q_1 \\ 0 \end{pmatrix} \tag{B.3}$$

The following is the general solution of the above system:

$$y_{13} = 1 - \frac{1}{q_3}(q_1 - q_4 t) \qquad y_{14} = 1 - t \qquad y_{23} = \frac{1}{q_3}(q_1 - q_4 t) \qquad y_{24} = t \tag{B.4}$$

Forming the objective function (given by eq. 3.5) with $\omega_{io} = |q_o|$ we have:

$$F(t) := q_3 y_{13}^2 + q_3 y_{23}^2 + q_4 y_{14}^2 + q_4 y_{24}^2 \tag{B.5}$$

Substituting eq. B.4 into eq. B.5 and taking the derivative with respect to $t$ and equating the resulting expression to zero, we obtain the following value for $t$ that minimizes the objective function:

$$t_{cr} = \frac{q_1}{q_3 + q_4} = \frac{q_1}{q_1 + q_2} \tag{B.6}$$

Finally, by substituting eq. B.6 into eq. B.4 and transforming back to $x_{io}$ we get:

$$x_{13} = \frac{q_1}{q_1 + q_2} \qquad x_{14} = \frac{q_1}{q_1 + q_2} \qquad x_{23} = \frac{q_2}{q_1 + q_2} \qquad x_{24} = \frac{q_2}{q_1 + q_2} \tag{B.7}$$

This is precisely the result one would get using "stream-tube routing" (i.e. eq. 3.11) or a flow rate-weighted distribution of the inflowing rates $q_1$ and $q_2$ among the outlets. The proof for two inlets and any number of outlets is identical to the proof given here, but this simple case was chosen for clarity. For more than two inlets the above procedure remains the same, however the objective function could easily become multivariate and therefore a general mathematical proof becomes cumbersome and was

thus not attempted. Instead, the claim was numerically verified for a large number of cases with more than two inlets.

## APPENDIX C: COUNTER EXAMPLES FOR A PREVIOUSLY PROPOSED STREAMLINE SPLITTING METHOD

The rules proposed by Jha et al. (2011) were a step forward in capturing reversibility of advection within pores. However, they were limited to pores with less than or equal to four neighbors. More importantly they neglect throat *orientations*. In their method, throats are displaced away from the pore center by a fixed amount (to remove overlap), and a mapping is established based only on *distances* between the inlets and outlets. Since throat orientations determine relative positions of *opposing streams* with respect to any given inlet, neglecting them renders any method invalid (ref. section 3.2.3.1). Figure C.1 consists of simple counter examples to the rules of Jha et al. (2011) for two-inlet-two-outlet configurations. We have followed their convention in labeling the throats and configurations. Figure C.1 demonstrates concentration fields of a dummy tracer in the absence of diffusion at steady state. Boundary conditions for each throat are depicted in the figure (units are not necessary in the calculation of $x_{io}$ for reasons mentioned in section 3.3.1). Table C.1 summarizes predictions made using their method and the streamline splitting algorithm of section 3.2.3.1 vs. COMSOL simulations. Table C.1 shows that their method incurs large errors, whereas the streamline splitting predictions are very accurate.

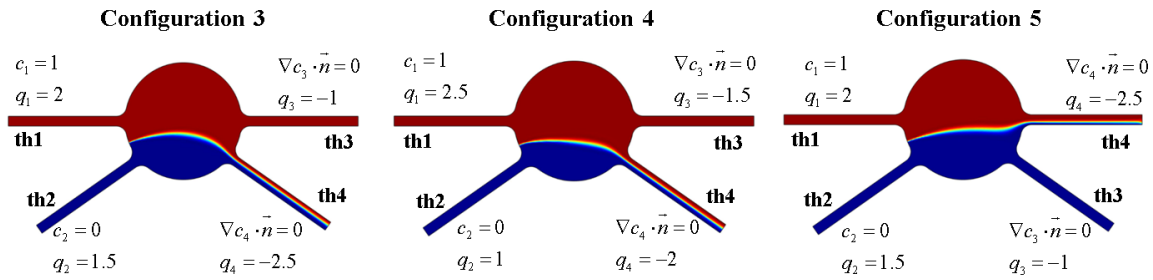


Figure C.1: Counter examples for the streamline splitting rules proposed by Jha et al. (2011). Their conventions for labeling throats/configurations are followed. Boundary conditions are annotated.

| | **COMSOL Simulations** | | ***Jha et al.* (2011) method** | | **Streamline Splitting** | |
|---|---|---|---|---|---|---|
| | $x_{13}$ | $x_{14}$ | $x_{13}$ | $x_{14}$ | $x_{13}$ | $x_{14}$ |
| **Configuration 3** | 0.99 | 0.39 | 0.00 | 0.8 | 1.00 | 0.4 |
| **Configuration 4** | 0.99 | 0.49 | 0.33 | 1.00 | 1.00 | 0.5 |
| **Configuration 5** | 0.00 | 0.79 | 1.00 | 0.4 | 0.00 | 0.8 |

Table C.1: Comparison of the predictions made using the method proposed by Jha et al. (2011) and the streamline splitting method proposed in this work against COMSOL simulations.

## APPENDIX D: INTER-POCKET MASS TRANSFER TERM

### D.1 Derivation

Assume a pore that contains two pockets sharing an interface. If we idealize the shape of the pore and the containing pockets as cuboids (as shown in figure D.1) the species mass transfer term can be quantitatively approximated. Consider that at time $t_0$ the pockets have initial concentration values of $c_1$ and $c_2$ creating a discontinuity at the interface (fig. D.1). The heat equation with homogeneous Neumann boundary conditions (given by eq. D.1), describes the inter-diffusion of two bounded bodies. The Neumann boundary conditions represent the impenetrability of the pore walls and $H(x)$ represents the Heaviside step function.

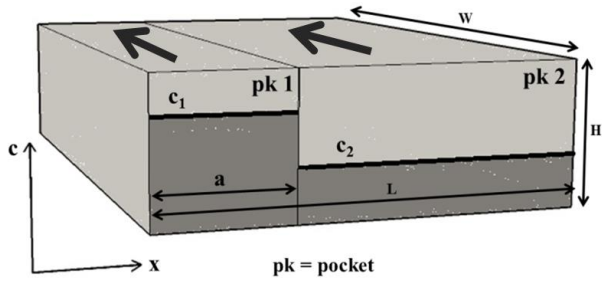


Figure D.1: An idealized cuboid pore containing two pockets with a concentration discontinuity at the interface at time $t_0$, which diffuses slowly with time. Thick arrows denote flow direction.

$$
\begin{aligned}
&c_t = D_m c_{xx} \qquad 0 < x < L, \quad t > 0 \\
&u_x(0,t) = u_x(\mathrm{L},t) = 0 \\
&u(0,t) = c_1 H(x) + (\mathrm{c}_2 - c_1) H(x-a)
\end{aligned}
\tag{D.1}
$$

Eq. D.1 can be solved by the method of separation of variables to obtain the concentration field given by eq. D.2:

$$c(x,t) = \frac{1}{2}A_0 + \sum_{n=1}^{\infty} A_n e^{-(\frac{n\pi}{L})^2 Dt} \cos(\frac{n\pi x}{L})$$

$$A_n = \frac{2}{L}\int_o^L u(0,\mathrm{t})\cos(\frac{n\pi x}{L})dx = \frac{2}{n\pi}(\mathrm{c}_1 - c_2)\sin(\frac{n\pi a}{L}) \qquad \text{(D.2)}$$

The solution can then be differentiated and multiplied by $D_m$ to obtain the instantaneous flux at $x = a$. Integrating this flux on t ϵ [0, T] and over the interfacial area yields the cumulative mass transfer in this time interval (eq. D.3):

$$\Delta \mathrm{N(T)}|_{x=a} = \int_0^T HW(-D_m c_x|_{x=a})\,\mathrm{dt} = [-HW\sum_{n=1}^{\infty}\frac{2L}{(n\pi)^2}\sin^2(\frac{n\pi a}{L})(e^{-(\frac{n\pi}{L})^2 DT} - 1)](\mathrm{c}_1 - c_2) \qquad \text{(D.3)}$$

The average mass transfer rate can, thus, be defined by eq. D.4:

$$\Psi_{21}(c_2, c_1) = -\frac{\Delta N(T)|_{x=a}}{T} \qquad \text{(D.4)}$$

In eq. D.3 and D.4, dimensions of the idealized pockets (i.e. *L*, *W*, *H* and *a*) are required. If an *a priori* knowledge of these parameters is known from the network and flow geometry (as is the case in section 3.3.2), then they can be used in the computations. Otherwise, one can use the approximations given by eq. D.5, where $V_1$ and $V_2$ are the pocket volumes (obtained from eq. 3.13) and $V_p$ is the pore volume. Note that a pore may contain more than two pockets, in which case each will be exchanging mass with the rest of the pockets in the pore. Thus the same methodology can be used by considering the pockets pairwise.

$$\gamma = (V_p)^{1/3} \qquad W = H = \gamma \qquad L = \frac{V_1 + V_2}{\gamma^2} \qquad a = \frac{V_1}{\gamma^2} \qquad \text{(D.5)}$$

*T* is the *transport time scale* and is very important in calculating $\Psi_{21}$.The smaller *T* is, the larger the inter-pocket mass transfer rate will be. At high Peclet numbers it is

reasonable to assume that, at the pore level, advection (fast) and diffusion (slow) are mathematically decoupled. Therefore, one can envision advection and diffusion taking place sequentially over the course of the time required for the pore fluid to be fully recycled. This is the fluid residence time in the pore and is denoted by $t_a$ in eq. D.6. Therefore, after each advection step the pocket concentrations would become completely uniform, and the diffuse interface between the pockets would be re-sharpened. This, then, justifies solving a Riemann problem for the diffusion step, as is done to obtain $\Delta N$ in eq. D.3.

At low Peclet numbers, a similar mathematical decoupling of advection and diffusion holds. However, the argument for solving a Riemann problem in the diffusion step is not as rigorous. Nevertheless, we intend to use the same equation (i.e. eq. D.3-D.4) here as well. To that end, we define $t_d$ (in eq. D.6) as the diffusion time scale, which is the time required for a Brownian particle, starting from the inter-pocket interface, to traverse the shortest of the two lateral dimensions of the pockets. This is when the presence of the pore boundaries is felt by the particles. The value for $T$ can then be taken as $\alpha t_d$. The need for $\alpha$ (<1) comes from the fact that $T = t_d$ produces the right trend with respect to Peclet number but a slight under-prediction of the inter-pocket mass transfer rate (when compared to CFD simulations; ref. appendix D.2).

$$t_a = \frac{V_p}{|Q_p|} \qquad\qquad t_d = \frac{[\min(a, L-a)]^2}{2D_m} \tag{D.6}$$

We refer to the ratio of $t_d$ over $t_a$ as $r$, which *quantifies the pore-level competition between advection and diffusion*. Note that $t_a$ is the fluid residence time, and thus is defined based on the longitudinal length scale of the pore, and $t_d$ is based on the lateral length scale of the pore. Therefore, $r$ embeds characteristics of both the transport regime

(i.e. Peclet number) and pore geometry (i.e. pore aspect-ratio). We denote the range for the validity of $T = t_a$ as $r \geq X$ (where $X$ must be a value larger than one), and the range for the validity of $T = \alpha t_d$ as $r \leq Y$ (where $Y$ must be a value less than one). The physical interpretation for $X$ is based on considering how far a Brownian particle would travel in the lateral dimension from the time it enters the pore till the time it exits it. The interpretation for $Y$ follows from considering the fact that the time at which the presence of the lateral pore-boundaries is felt by a Brownian particle must be much smaller than the residence time of the particle within the pore at the onset of diffusion-dominated regime. For moderate Peclet numbers (i.e. $X > r > Y$) a continuous interpolation is performed to obtain the appropriate values for $T$. Figure D.2 summarizes the selection of the transport time scale, $T$, for different transport regimes. The interpolation consists of the plane going through vectors $b_1$ and $b_2$ given by eq. D.7 (and shown in figure D.2).

$$\vec{n} = \vec{b}_1 \times \vec{b}_2 \qquad \vec{b}_1 = (1, Y, \alpha Y) \qquad \vec{b}_2 = (1, X, 1) \tag{D.7}$$

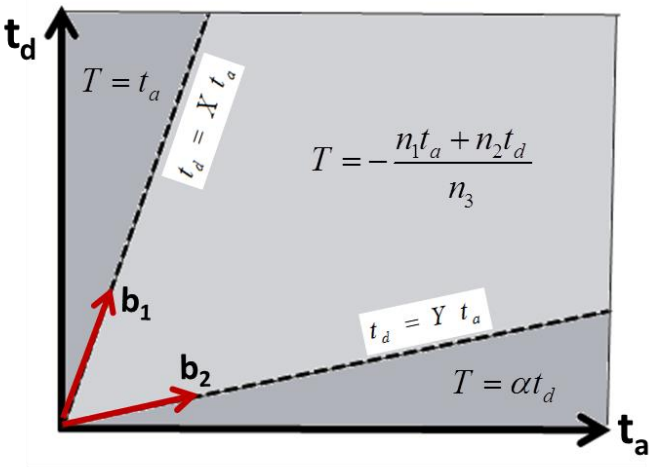


Figure D.2: Map for choosing the transport time scale, $T$ in eq. D.3-D.4, based on values of the advection and diffusion time scales (i.e. $t_a$ and $t_d$).

**D.2: Determining *X*, *Y*, and *α* from direct simulations**

The exact values for *X*, *Y* and *α* were determined through direct COMSOL simulations on three pore geometries with very different pore aspect-ratios (= $L_{p1}/L_{p2}$); shown in figure D.3. Pore aspect-ratios were equal to 1, 2 and 4 for geometries shown in D3a, D3b and D3c. Subsequently, SSM simulations were run for these pores as well. Inlet #1 and #2 boundary conditions consisted of (constant) one- and zero- concentration values, respectively. Concentration gradients at both outlets were set to zero. The steady-state outlet concentrations were then recorded while altering Peclet number (i.e. fluid velocity). Figure D.4 shows the SSM and directly simulated outlet concentration values plotted against *r* for all three geometries. The SSM simulations correspond to employing: $X = 6$, $Y = 0.1$ and $\alpha = 0.5$. Note that these parameters provide good estimates of outlet concentration values for all three geometries. *X* was determined by plotting SSM predictions, using $T = t_a$ in eq. D.3-D.4 for all transport regimes, against direct simulations and determining the point at which the two plots were within 5% of each other relative to the maximum concentration value (i.e. one). *Y* was obtained by simply determining the point at which the difference between the two outlet concentrations, obtained from the direct simulations, was within 5% of the maximum concentration value. Once *X* and *Y* were determined, *α* (<1) was altered in such a way that SSM and the direct simulation predictions for *Y* agreed. Note that for all three pore aspect-ratios, the graphs collapse onto one another when plotted against *r* (indicating proper scaling). This is because *r* is a dimensionless combination of Peclet number and pore aspect-ratio. Note that the only two necessary metrics here are the lateral and longitudinal dimensions of the pore, thus the *X*, *Y* and *α* found herein could be applied to other geometries as well with reasonable accuracy. It is noteworthy, however, that the value for *Y* depended slightly on

pore aspect-ratio and varied between 0.1-0.3; however, a value of 0.1 was deemed as appropriate since it appeared to produce good results for all three pore geometries.

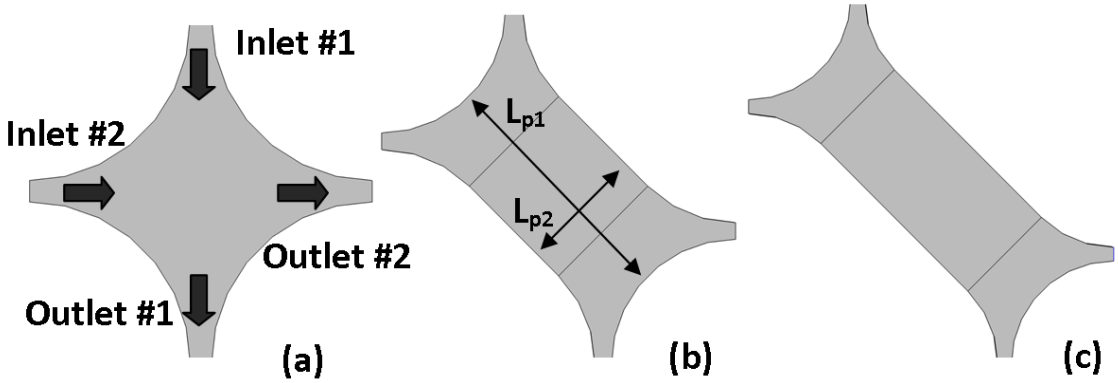


Figure D.3: Three pore-geometries, (a), (b) and (c), with aspect ratios equal to 1, 2 and 4, respectively. Flow direction is annotated.

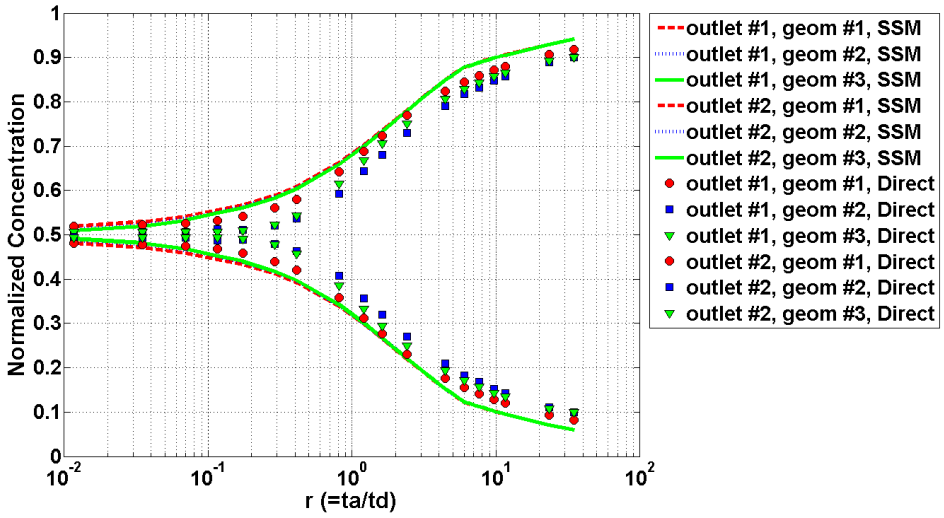


Figure D.4: SSM and directly-simulated steady-state outlet concentration values versus *r* for the pore geometries shown in figure D.3.

## APPENDIX E: EFFECT OF TRANSVERSE ANGLE ($\zeta$) ON SPLITTING OF STREAMLINES

The dependence of streamline splitting on transverse angle ($\zeta$) was determined through numerous CFD simulations. Herein, we summarize some of these results and justify the proposed inequality constraint given by eq. 3.9 and 3.10. CFD simulations were performed on two-inlet-two-outlet pore geometries with inlet and outlet flow rates all equal in magnitude (the choice is justified later). We use case V in figure 3.4 as a visual guide for describing these simulations. In a manner similar to that described in section 3.3.1, $x_{23}$ and $x_{24}$ were measured from CFD. The positions of outlets 3 and 4 were systematically varied to sweep a range of transverse angles from 0 to $90^o$. Note that for any given value of $\zeta$, the positions of the outlets are still free to vary by changing the angle between them. Therefore, not just the transverse angle but also the angle between the two outlets was varied. $x_{23}$ and $x_{24}$ were then obtained using the SSM algorithm with the inequality constraint given by eq. 3.9 and 3.10.

Figure E.1 provides a comparison between CFD and the SSM algorithm. Note the clear correlation between the transverse angle and the "stolen" portion of the inflowing streams. In the absence of such "stealing" (e.g. in 2D), $x_{23}$ and $x_{24}$ would be 0 and 1, respectively (which is why inlet/outlet flow rates were chosen to be equal in magnitude). The scatter in the CFD data hints at a small dependence on the angle between the two outlets. Note that $x_{23}$ and $x_{24}$ do not quite asymptote at 1 and 0, respectively. We suspect this to be due to geometric aspects regarding the shape and size of the entrance region of the outlet throats (and possibly the distance between them). For the sake of simplicity and the difficulty in characterizing these less important factors, such weak dependencies are ignored. In this regard, the SSM predictions (with the inequality constraint of eq. 3.9 and 3.10) in figure E.1 are regarded satisfactory.

We conclude by making two further remarks: 1) the SSM algorithm with eq. 3.9 and 3.10 was further tested on a few pore geometries with more than two outlets and non-equal flow rates, and equally satisfactory results were obtained. 2) The CFD data were also plotted against the angle between the *projected* outlets onto the *flowing plane*. This resulted in a poorer correlation in the data (with double the scatter).

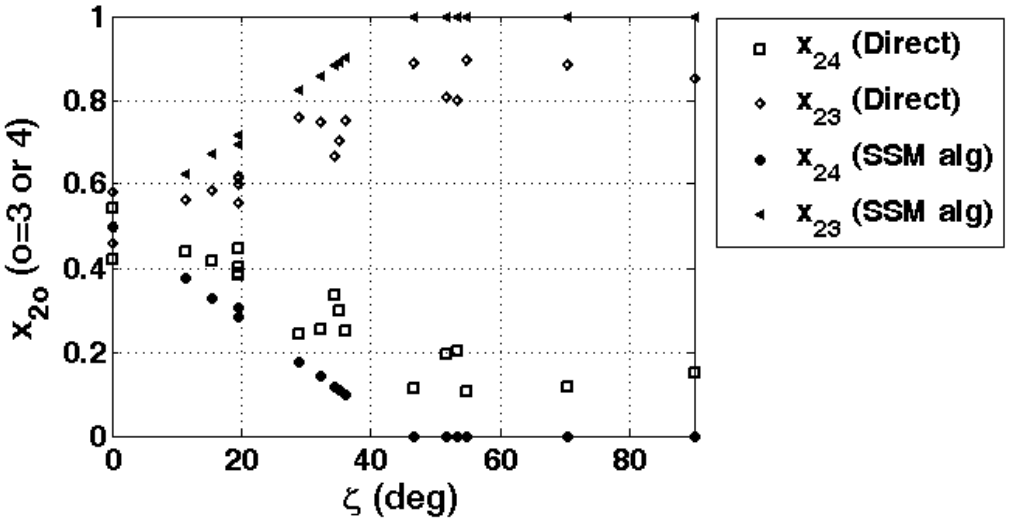


Figure E.1: Plot of $x_{23}$ and $x_{24}$ (using case V in fig. 3.4 as a visual guide) vs. transverse angle ($\zeta$), obtained from CFD simulations and the SSM algorithm (with the inequality constraint given by eq. 3.9 and 3.10).

## APPENDIX F: APPLICABILITY OF TAYLOR-ARIS DISPERSION COEFFICIENT IN PORE NETWORKS

The validity of the Taylor-Aris theory for cylindrical ducts has been rigorously delineated in a classic paper by Ananthakrishnan et al. (1965) and can be expressed by eq. F.1:

$$(\frac{tD_m}{V_0}) > \mathrm{T}_{\min} \qquad \text{(F.1)}$$

$t$, $D_m$, and $V_0$ represent time, molecular diffusion coefficient and maximum centerline velocity within the cylindrical capillary, respectively. If $t$ is taken to be the mean tube residence time (= $L/u$; $u$ is mean fluid velocity), eq. F.1 can be rearranged to obtain eq. F.2; $Pe_R$ (= $V_0R/D_m$) and $\kappa$ (= $L/R$) represent Peclet number and tube aspect ratio, respectively. For $Pe_R$ >100, $T_{min}$ = 0.8 and, thus, the aspect ratio of the throat must be $\geq$ 40. In this work, $\kappa \in$ [1-10] (compare to $\kappa \in$ [2-40] in Sorbie and Clifford, 1991; $\kappa$ = 5 in Saffman, 1959).

$$2\frac{\kappa}{Pe_R} > \mathrm{T}_{\min} \qquad \text{(F.2)}$$

For $Pe_R$ <100, $T_{min}$ is a rapidly increasing function of 1/$Pe_R$. This means that even for small values of $Pe_R$, large aspect ratios are required (e.g. for $Pe_R$ = 1, $T_{min}$ >20 hence $\kappa$ >10; see Table 1 of Ananthakrishnan et al. 1965). Gill and Ananthakrishnan (1966) additionally found that for $Pe_R$ <100, $T_{min}$ is dependent upon the choice of the inlet boundary condition, and that dirichelet type inlet conditions (i.e. the most relevant type in a pore network) require longer times to asymptote (compared to Danckwert's- or doubly-infinite type); the shortest being that of a slug stimulus (Nunge and Gill, 1969; Gill and Ananthakrishnan, 1967).

## APPENDIX G: FORMULATION OF SEMI-EMPIRICAL SOLUTE FLOW RATES

### G.1 Exact asymptotic analysis of solute inflow

We are interested in deriving the asymptotic behavior of the rate of solute inflow, $q_{cd}^{FI}$ and $q_{cd}^{FO}$, in a cylindrical duct at the limit of early times (i.e. as $\tau \rightarrow 0$). This is then used to formulate the functional form of the semi-empirical expressions for $q_{cd}^{FI}$ and $q_{cd}^{FO}$ in eq. 4.6c-d. Consider the following 1D transport problem on a semi-infinite domain (variable definitions are the same as in section 4.2.1.1):

$$\frac{\partial c}{\partial t} = D_m \frac{\partial^2 c}{\partial x^2} - v\frac{\partial c}{\partial x}$$
$$c(t=0) = 0 \qquad c(x=0) = 1 \qquad \frac{\partial c}{\partial x}(x \rightarrow \infty) = 0 \tag{G.1}$$

The solution to eq. G.1 is given by eq. G.2 (Van Genuchten and Alves, 1982):

$$c(x,t) = \frac{1}{2} erfc\left(\frac{x - vt}{2\sqrt{D_m t}}\right) + \frac{1}{2}\exp\left(\frac{vx}{D_m}\right) erf\left(\frac{x + vt}{2\sqrt{D_m t}}\right) \tag{G.2}$$

The reason why eq. G.1 and G.2 are relevant, is because at very early times radial gradients do not exist (which come about later by advection) and the solute has not had enough time to sense the outflow boundary (hence the semi-infinite assumption). Using eq. G.2 we can compute the flux of solute inflow (i.e. $q_c^{flx}$) given by eq. G.3:

$$q_c^{flx}|_{x=0} = (vc - D_m \frac{\partial c}{\partial x})|_{x=0} = v + \sqrt{\frac{D_m}{\pi t}}\, \mathrm{e}^{-\left(\frac{vt}{2\sqrt{D_m t}}\right)^2} - \frac{v}{2} erfc\left(\frac{vt}{2\sqrt{D_m t}}\right) \tag{G.3}$$

Integrating eq. G.3 across the duct cross-section (see eq. 4.4) and noting that $v = V_0(1-(r/R)^2)$, we obtain eq. G.4:

$$q_c^I = (2\pi R^2)\left\{\frac{1}{2}\left(\frac{D_m}{V_0 t}\right) erf\,(B) - \frac{V_0}{2}\left(\frac{1}{2} erfc(B) + \frac{1}{(2B)^2} erf\,(B) - \frac{1}{2B\sqrt{\pi}}\exp(-B^2)\right)\right\} + \frac{\pi R^2 V_0}{2}$$

$$B = \frac{V_0}{2}\sqrt{\frac{t}{D_m}}$$

(G.4)

The integration was accompanied by making use of the error function integration tables given by Ng and Geller (1969). We remark that eq. G.4 can be used for both forward and backward transport by setting the sign of $V_0$ to positive or negative, respectively. Taking the limit of eq. G.4 as $t \rightarrow 0$ and after a series of tedious manipulations we obtain eq. G.5a. Additionally non-dimensionalizing eq. G.5a yields eq. G.5b.

$$\lim_{t\to 0} q_c^I = R^2\sqrt{\frac{\pi D_m}{t}} \qquad \text{(G.5a)}$$

$$\lim_{\tau\to 0} q_{cd}^I = \frac{1}{2\sqrt{\pi Pe_L \tau}} \qquad \text{(G.5b)}$$

Eq. G.5a and G.5b hold for both forward and backward transport, but eq. G.5b is only correct in magnitude (not sign) for backward transport. In deriving eq. G.5, we made use of eq. G.6, which is easily verified by expressing all components involved in the limit by their Taylor expansion:

$$\lim_{B\to 0}\frac{1}{B^2} erf\,(B) = \frac{2}{B\sqrt{\pi}} \qquad \lim_{B\to 0}\frac{1}{B} e^{-B^2} = \frac{1}{B} \qquad \text{(G.6)}$$

Compare eq. G.5 to the proposed expressions for $q_{cd}^{FI}$ and $q_{cd}^{BI}$ (i.e. eq. 4.6c-d). At late times the outflow boundary is sensed by the solute and $q_{cd}^I$ approaches its steady state value. This is the additive term $C^F$ and $C^B$ on the RHS of eq. 4.6c-d. Furthermore, the area under the $(q_{cd}^{FI} - C^F)(\tau)$ and $(q_{cd}^{BI} - C^B)(\tau)$ curves must be finite, as discussed in section 4.2.1.1. The exponential in the numerator of the first term in the RHS of eq. 4.6c-d

ensures this. A simple check confirms that eq. 4.6c-d meets both early-time and late-time asymptotes.

**G.2 Steady state solute flow rate**

At very low Peclet numbers, the steady state concentration field associated with eq. 4.1 tends to a linear variation along the tube axis. The steady state solute flow rate (i.e. $q_{c,ss}$) can, thus, be approximated by eq. G.7 (for forward/backward transport); where $V_0$ is taken to be a positive number for convenience:

$$q_{c,ss}^{F} = \pi R^2 (D_m \frac{c^F|_{x=0} - c^F|_{x=L}}{L} + \frac{V_0}{2} c^F|_{x=0})$$
$$q_{c,ss}^{B} = \pi R^2 (D_m \frac{c^B|_{x=0} - c^B|_{x=L}}{L} - \frac{V_0}{2} c^B|_{x=0}) \qquad \text{(G.7)}$$

Applying the corresponding boundary conditions for forward/backward transport in eq. G.7 followed by non-dimensionalizing the resulting expressions yields eq. G.8:

$$C^F = \frac{q_{c,ss}^F}{2\pi R^2 V_0} = \frac{1}{2Pe_L} + \frac{1}{4} \qquad C^B = \frac{q_{c,ss}^B}{2\pi R^2 V_0} = \frac{1}{2Pe_L} \qquad \text{(G.8)}$$

On the other hand, at high Peclet numbers diffusion vanishes and $C^F \rightarrow 1/4$ and $C^B \rightarrow 0$. Therefore, the functional form of the dimensionless steady state solute flow rate (i.e. eq. 4.7b) was formulated such that it satisfies these limits (readily verified by inspection). We note that the fitting constants in eq. 4.7b may still be improved by fitting it to steady state results of a mass conservative CFD method (accuracy of eq. 4.7b starts to fade for $Pe_L > 10$ even though associated errors maybe negligible as $C^F \simeq 1/4$ and $C^B \simeq 0$ hold for all practical purposes).

## G.3 Cumulative solute flow expressions

In STM, expressions for *cumulative* solute throughput (as opposed flow rates) within a given time interval, through each throat, are required to compute the $\delta Q_c$ quantities in eq. 4.12. Even though one could numerically integrate the rate expressions given by eq. 4.6, analytical expressions are highly preferred (for accuracy and computational reasons); these are given by eq. G.9.

$$\int_{\tau_1}^{\tau_2} q_{cd}^{FO} d\tilde{\tau} = C^F \left[ \frac{1}{2} \left\{ e^{-\frac{b^F}{\varsigma a^F}} \left( e^{\frac{\Upsilon^F}{\varsigma a^F}} erf(\Upsilon^F) - e^{\frac{1}{(2\varsigma a^F)^2}} erf(\Upsilon^F - \frac{1}{2\varsigma a^F}) \right) + \tau \right\} e^{-Pe_R d} + U(\tau - 1)\left( \tau + \frac{1}{\tau} \right)(1 - e^{-Pe_R d}) \right]_{\tau_1}^{\tau_2} \quad \text{(G.9a)}$$

$$\int_{\tau_1}^{\tau_2} q_{cd}^{BO} d\tilde{\tau} = \frac{C^B}{2} \left[ e^{-\frac{b^B}{\varsigma a^B}} \left( e^{\frac{\Upsilon^B}{\varsigma a^B}} erf(\Upsilon^B) - e^{\frac{1}{(2\varsigma a^B)^2}} erf(\Upsilon^B - \frac{1}{2\varsigma a^B}) \right) + \tau \right]_{\tau_1}^{\tau_2} \quad \text{(G.9b)}$$

$$\int_{\tau_1}^{\tau_2} q_{cd}^{FI} d\tilde{\tau} = \left[ A^F \sqrt{\frac{\pi\varepsilon}{Pe_L D}} erf\left( \sqrt{\frac{D\tau}{\varepsilon}} \right) + C^F \tau \right]_{\tau_1}^{\tau_2} \quad \text{(G.9c)}$$

$$\int_{\tau_1}^{\tau_2} q_{cd}^{BI} d\tilde{\tau} = \left[ A^B \sqrt{\frac{\pi\varepsilon}{Pe_L D}} erf\left( \sqrt{\frac{D\tau}{\varepsilon}} \right) + C^B \tau \right]_{\tau_1}^{\tau_2} \quad \text{(G.9d)}$$

Where,

$$\Upsilon^F = a^F \log(\tau) + b^F \qquad \Upsilon^B = a^B \log(\tau) + b^B \qquad \varsigma = \log(e) \qquad \varepsilon = 0.95 \quad \text{(G.10)}$$

The derivation of these integrals is rather tedious but straightforward, and therefore omitted. Integration of eq. G.9a-b was accompanied by making use of the error function integration tables given by Ng and Geller (1969). The relationship between the lower incomplete gamma function and the error function (i.e. eq. G.11) was used in deriving eq. G.9c-d.

$$\Gamma^L(\frac{1}{2}, x) = \sqrt{\pi} erf(\sqrt{x}) \tag{G.11}$$

**G.4 Constraining solute flow rates and boundary correction**

As discussed in section 4.2.1.1, $q_{cd}^{FO}$ and $q_{cd}^{BO}$ had to be recorded a distance of $(1-\varepsilon)L$ ($\varepsilon = 0.95$) away from the actual outflow boundary (i.e. the *BB'* transect line shown in figure 4.1a-b) to avoid numerical errors from the CFD simulations that were in violation of global mass conservation. These rate expressions were then corrected for the actual outflow boundary following the steps outlined below (we drop superscripts *F* and *B* as the following applies to both forward and backward transport). These steps additionally render the rate expressions in eq. 4.6 mass conservative, by constraining some of their parameters.

i) Eq. 4.5b must hold for the portion of the duct between *AA'* and *BB'* (denoted by the subscript *p*) as long as the time variable is non-dimensionalized with respect to the distance between them; denoted by $\tau_p = \tau/\varepsilon$. Thus, we can compute $WI_p$ from eq. G.12 and the correlations given in eq. 4.8 for $WO_p$ and $\overline{C}_{ss,p}$.

$$\underbrace{\int_0^\infty (q_{cd}^I - C) d\tilde{\tau}_p}_{WI_p} + \underbrace{\int_0^\infty (C - q_{cd,p}^O) d\tilde{\tau}_p}_{WO_p} = \frac{\overline{C}_{ss,p}}{2} \tag{G.12}$$

ii) Evaluating the first integral in eq. G.12 analytically (with the change of variable $\tau = \varepsilon\tau_p$ and using eq. G.9) we additionally obtain eq. G.13 for $WI_p$. *A* is then calculated from eq. G.13 and the $WI_p$ value from the previous step (i.e. eq. 4.9a).

$$WI_p = \frac{A}{\sqrt{\varepsilon Pe_L D}}\Gamma(0.5) \tag{G.13}$$

iii) Reapplying eq. 4.5b to the full length of the duct (denoted by the subscript *f*) (the associated time variable, $\tau$, non-dimensionalized with respect the duct length) we write eq. G.14. Since $WI_f = \varepsilon WI_p$ (verified from $\tau = \varepsilon\tau_p$), $WO_f$ is calculated from eq. G.14 and the correlations given in eq. 4.8 for $\overline{c}_{ss,f}$.

$$\underbrace{\int_0^\infty (q_{cd}^I - C)d\tilde{\tau}}_{WI_f} + \underbrace{\int_0^\infty (C - q_{cd,f}^O)d\tilde{\tau}}_{WO_f} = \frac{\overline{c}_{ss,f}}{2} \tag{G.14}$$

iv) We assume that parameters *a* and *d*, in eq. 4.6a and 4.6b for $q_{cd}^{FO}$ and $q_{cd}^{BO}$, remain unaltered in going from *BB'* to the actual outflow boundary (*C* and *D* are known to remain unchanged, because they are associated with steady state and solute inflow, respectively). This is a good assumption because (1- $\varepsilon$)*L* constitutes a very small portion of the total residence time and duct length. By evaluating the second integral in eq. G.14 analytically for $WO_f$ (using eq. G.9) and equating it to the value obtained in step (iii), *b* can be back-calculated; which is the expression given in eq. 4.9.

All above steps are already implemented in eq. 4.6-10. The *max* operator in eq. 4.10 is a precautionary measure to avoid assigning small negative numbers to $WI_p$ at high Peclet numbers (although their effects are negligible since $WI_p \to 0$ as $Pe_R \to \infty$). Figure G.1 shows that the CFD data for $c_{ss,p}^F$, $c_{ss,f}^F - \varepsilon c_{ss,p}^F$, $c_{ss,f}^B - \varepsilon c_{ss,p}^B$, $WO_p^F$, and $WO_p^B$ correlate very well with $Pe_L$ (solid lines represent correlations given by eq. 4.8). In figure G.1, all aspect ratios (i.e. $\kappa$) are collapsed onto the same plot (some dots consist of the superposition of multiple points with different $\kappa$). The solid line for $c_{ss,f}^F$ in figure G.1d is

back-calculated from all other quantities. The plots for $c_{ss,p}^{F}$, $c_{ss,f}^{F}$-$\varepsilon c_{ss,p}^{F}$, $c_{ss,f}^{B}$-$\varepsilon c_{ss,p}^{B}$, and $c_{ss,f}^{F}$ correspond to $Pe_R \leq 200$. We develop analytical approximations for these quantities below when $Pe_R > 200$; which we find to be more accurate than the CFD results. The reason $c_{ss,f}^{F}$-$\varepsilon c_{ss,p}^{F}$ and $c_{ss,f}^{B}$-$\varepsilon c_{ss,p}^{B}$ were chosen for correlating the data (instead of e.g. $c_{ss,f}^{F}$ and $c_{ss,f}^{B}$), was to satisfy an additional constraint given by eq. G.15. Eq. G.15 essentially states that if $q_{cd,p}^{O}$ and $q_{cd,f}^{O}$ (i.e. dimensionless outflow rates) are drawn on the same plot (i.e. same time axis), the shaded area shown in figure 4.1c is bigger for the full duct compared to the portion between *AA'* and *BB'* (fig. 4.1a-b).

$$\int_0^\infty (C - q_{cd,f}^{O}) d\tilde{\tau}_p = \frac{WO_f}{\varepsilon} \geq WO_p = \int_0^\infty (C - q_{cd,p}^{O}) d\tilde{\tau}_p \qquad \text{(G.15)}$$

From eq. G.12 and G.14 and noting that $WI_f = \varepsilon WI_p$, eq. G.15 can be expressed as follows:

$$\overline{c}_{ss,f} - \varepsilon \overline{c}_{ss,p} \geq 0 \qquad \text{(G.16)}$$

When $Pe_R > 200$, a boundary layer clearly forms towards the outlet at steady state. Since the thickness of this boundary layer seems nearly uniform from CFD simulations, we approximate forward transport by eq. G.17 with the origin of the $x$ coordinate placed at the outlet and directed against the flow direction (backward transport follows similarly):

$$-\frac{V_0}{2}\frac{\partial c}{\partial x} = D_m \frac{\partial^2 c}{\partial x^2} \qquad c(x=0) = 0 \qquad c(x \to \infty) = 1 \qquad \text{(G.17)}$$

Eq. G.17 has a simple solution. Taking the boundary layer thickness, $\delta$, to be the distance from the outlet to the point where $c = 0.99$, we compute the average concentration within the boundary layer, $c_{BL} = 0.785$, and take the concentration in the rest of the duct to be equal to 1 (i.e. $c_{ss,p}^{F} = 1$) . The average steady state concentration

over the full length of the duct is, therefore, given by eq. G.18. Rearranging eq. G.18 and substituting the value for $c_{BL}$ yields eq. 4.8f. These steps can be similarly repeated for backward transport. Lastly, we note that the theoretical constants $\Pi_i$ in table 4.1 can be easily determined from geometric considerations and the fact that $c_{ss,f}^{F} \rightarrow 0.5$ as $Pe_R \rightarrow 0$ and $c_{ss,f}^{F} \rightarrow 1$ as $Pe_R \rightarrow \infty$ .

$$\bar{c}_{ss,f}^{F} = 1 \times (1 - \frac{\delta}{L}) + c_{BL} \times \frac{\delta}{L} \qquad \delta = \frac{2R\ln(100)}{Pe_R} \tag{G.18}$$

Figures G.2 and G.3 depict some of the parameters appearing in the semi-empirical rate expressions (i.e. eq. 4.6). In figure G.2, $a^F$, $C^F$, and $d$ are directly correlated via eq. 4.7a-c, whereas $b^F$ is back-calculated using eq. 4.9b (i.e. the steps outline above). It can be seen that $b^F$ follows the CFD data quite closely. Directly correlating $b^F$ with the data was quite challenging because of its complicated shape (which led to mismatches between the back-calculated $WO_p$ and the data and was, therefore, abandoned). It is interesting to note the "humps" and "slumps" in $a^F$ and $b^F$ respectively. A parallel between these and the macroscopic "slump" in figure 4.10b is drawn in section 4.3.3.2. In figure G.3, the parameter $D$ is directly correlated via eq. 4.7c, while $A^F$ and $b^B$ are back-calculated from eq. 4.9 (i.e. the steps outlined above). Although it appears from figure G.3a that $A^F$ does not follow CFD data very well, these data are not considered to be the most accurate. This is because the CFD data for $q_{cd}^{I}$ do not satisfy the early-time asymptotic behavior of appendix G.1 at high Peclet regimes (see fig. 4.2b). We suspect this to be due to the need for finer mesh (than the highest setting in COMSOL©) near the inlet at high Peclet numbers. From this perspective, the mass balance constraints provide a certain level of confidence in the back-calculated quantities for this parameter.

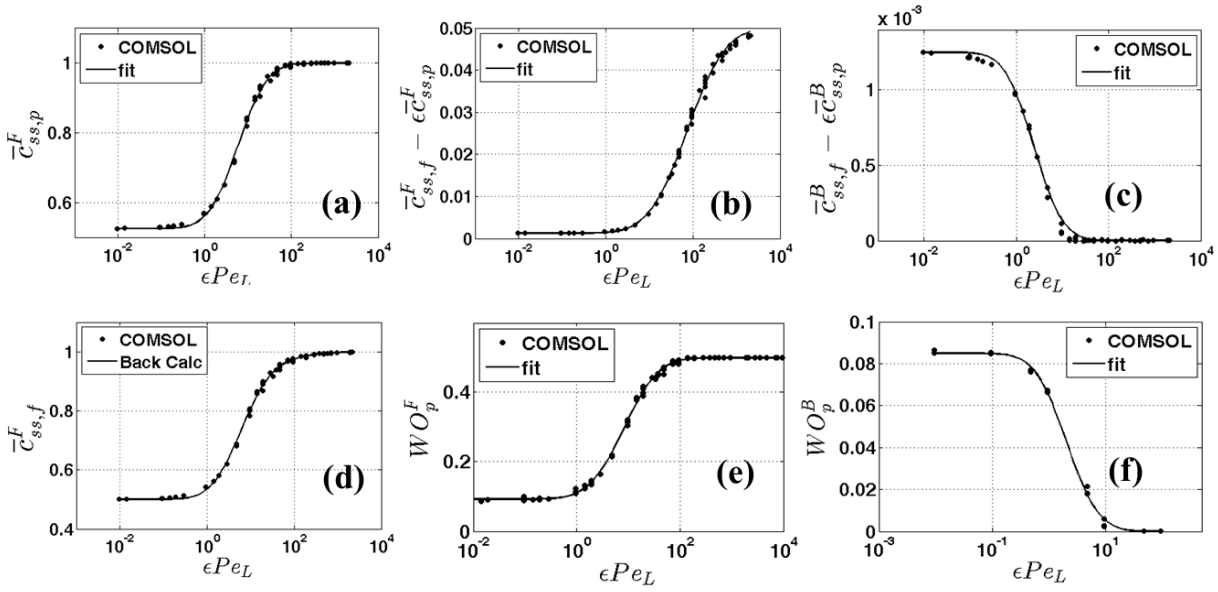


Figure G.1: (a) $c_{ss,p}{}^F$, (b) ($c_{ss,f}{}^F - \varepsilon c_{ss,p}{}^F$ ), (c) ($c_{ss,f}{}^B - \varepsilon c_{ss,p}{}^B$ ), (d) $c_{ss,f}{}^F$, (e) $WO_p{}^F$, and (f) $WO_p{}^B$ vs. Peclet number. Dots include CFD data for all aspect ratios examined. (a), (b), (c) and (d) correspond to $Pe_R \leq 200$.

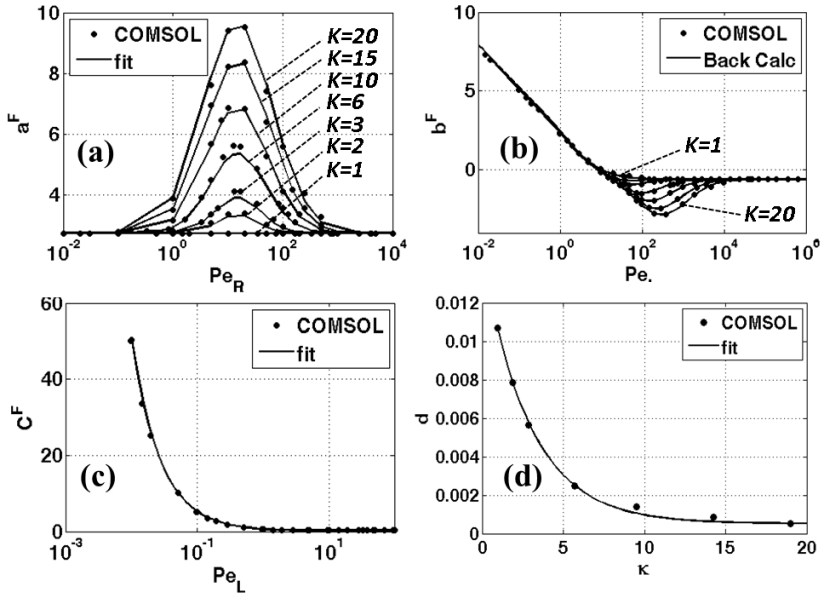


Figure G.2: Parameters (a) $a^F$, (b) $b^F$, (c) $C^F$ vs. Peclet number, and (d) $d$ vs. aspect ratio (in eq. 4.6). Dots represent CFD simulations. The solid lines in (a), (b), and (c) represent eq. 4.7 (the global fit). In (b) only the plots for $\kappa = 1$ and $\kappa = 20$ are annotated, while the rest lie monotonically in between. The solid line in (b) for $b^F$ is back-calculated from 4.9b.

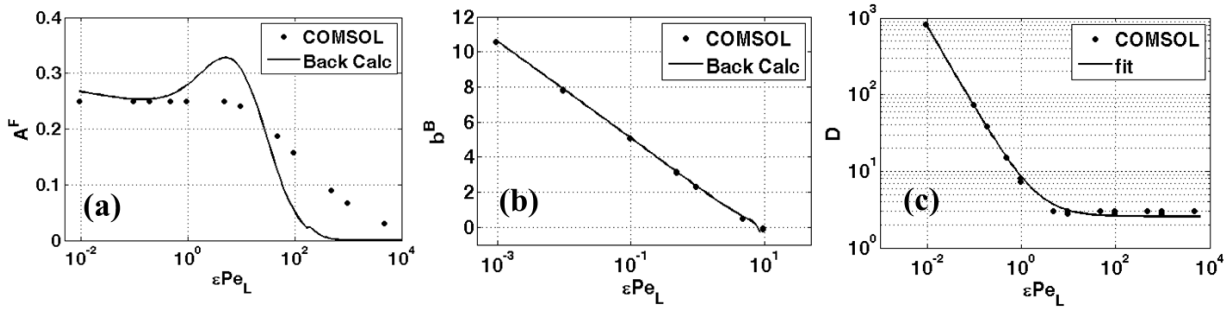


Figure G.3: Parameters (a) $A^F$ ($\kappa = 1$), (b) $b^B$, and (c) $D$ (in eq. 4.6) vs. Peclet number. Dots represent CFD simulations. The solid lines in (a) and (b) for $A^F$ and $b^B$ are back-calculated from eq. 4.9. The solid line in (c) represents eq. 4.7c (the global fit) for $D$.

## APPENDIX H: PLUG-FLOW SOLUTE FLOW RATES

Consider the 1D transport problem for a semi-infinite cylindrical domain described by eq. G.1, with its solution given by eq. G.2. Assuming a plug-flow velocity profile of magnitude $v$, the (dimensional) solute flow rates at the inlet and a distance $L$ away from the inlet can be computed and are given by eq. H.1. All other variable definitions are the same as in section 4.2.1.1.

$$q_c^{FI} = (\pi R^2)\left( vc - D_m \frac{\partial c}{\partial x} \right)|_{x=0} = \frac{(\pi R^2)}{2}\left[ verfc\left( \frac{-vt}{2\sqrt{D_m t}} \right) + 2\sqrt{\frac{D_m}{\pi t}}\, \mathrm{e}^{-\left(\frac{vt}{2\sqrt{D_m t}}\right)^2} \right] \tag{H.1a}$$

$$\begin{aligned} q_c^{FO} &= (\pi R^2)\left( vc - D_m \frac{\partial c}{\partial x} \right)|_{x=L} \\ &= \frac{(\pi R^2)}{2}\left[ verfc\left( \frac{L - vt}{2\sqrt{D_m t}} \right) + \sqrt{\frac{D_m}{\pi t}} e^{\left(\frac{vL}{D_m}\right)} e^{-\left(\frac{L+vt}{2\sqrt{D_m t}}\right)^2} + \sqrt{\frac{D_m}{\pi t}} e^{-\left(\frac{L-vt}{2\sqrt{D_m t}}\right)^2} \right] \end{aligned} \tag{H.1b}$$

Using eq. H.1a and H.1b in STM, implies that solute exiting one throat into a pore will not diffusion back into another inlet of the same pore. In other words, while counter-current diffusion within a single throat *is* accounted for, it is ignored in the transitions from one inlet throat to the next in an interconnected pore network. Note that, in applying eq. H.1, terms corresponding to *BO* and *BI* are set to zero in STM (i.e. eq. 4.12). This situation is only valid at sufficiently high Peclet numbers. The transport problem in eq. H.2 is considered to derive an appropriate criterion.

$$\frac{V_0}{2}\frac{\partial c}{\partial x} = D_m \frac{\partial^2 c}{\partial x^2} \qquad c(x=0) = 0 \qquad c(x=L) = 1 \tag{H.2}$$

The steady-state solute flow rate corresponding to eq. H.2 is eq. H.3:

$$q_{cd,ss} = \frac{q_{c,ss}}{v} = \frac{1}{1 - e^{Pe_L}} \qquad Pe_L = \frac{vL}{D_m} \tag{H.3}$$

$$Pe_L > \ln\left(1 + tol^{-1}\right) \tag{H.4}$$

A criterion is now obtained by requiring $q_{cd,ss}$ to be smaller than a set tolerance, *tol*, which yields eq. H.4. For *tol* = 1e-5, $Pe_L$ >10 appears to be a practical condition for when to safely ignore backward transport in a pore network (and thus using eq. H.1 in STM). This criterion can also be used for parabolic velocity profiles (to ignore backward transport), since $C^B$ rapidly tends to zero in this range according to eq. 4.7b.

## APPENDIX I: ASSIGNING PORE VOLUMES TO THROATS

Networks extracted via the modified Delaunay tessellation algorithm used (Al-Raoush et al., 2003) assign all the void volume (within the tetrahedra) to the pores. In the STM simulations of section 4.3.3.1, we assume pores are volumeless and throats contain all the void volume. Here, we describe a procedure whereby pore volumes are assigned to their neighboring throats in geometrically representative manner (honoring as much of the available information as possible). We note that an alternative procedure was described by Thompson (1996), although the following seems to be a bit simpler.

Consider pore $p_i$ connected to $N_{pi}^t$ throats. Let $V_{pi}$ and $rc_{pi}$ denote pore volume and the radius of the largest inscribed sphere within the pore, respectively. The distance between $p_i$ and $p_j$ is indicated by $d_{ij}$. Let $t_{ij}$ represent the throat connecting $p_i$ to $p_j$, and $V_{tij}$, $G_{tij}$, $rc_{tij}$ represent its volume, hydraulic conductivity, and radius of the largest inscribed sphere at the narrowest constriction, respectively. Denote the fraction of $V_{pi}$ assigned to $t_{ij}$ by $V_{pi}^{tij}$. As a first approximation to $V_{pi}^{tij}$, we compute $V_{pi}^{tij,*}$ by assuming that the void space between the centers of $p_i$ to $t_{ij}$ is shaped as a truncated cone with height $d_{ij}/2$ and base radii $rc_{pi}$ and $rc_{tij}$. Eq. I.1 yields the volume of this truncated cone. These volumes are then used as weights to distribute $V_{pi}$ among $t_{ij}$ $\forall j$ via eq. I.2. Note that each throat receives contributions from both pores connected to it.

$$V_{p_i}^{t_{ij},*} = \frac{\pi d_{ij}}{6}\left(rc_{p_i}{}^2 + rc_{t_{ij}}{}^2 + rc_{t_{ij}} rc_{p_i}\right) \tag{I.1}$$

$$V_{p_i}^{t_{ij}} = V_{p_i} \frac{V_{p_i}^{t_{ij},*}}{\sum_{j=1}^{N_{p_i}^t} V_{p_i}^{t_{ij},*}} \tag{I.2}$$

Throat hydraulic conductivities, $G_{tij}$, are accurately computed using the procedure described in Thompson (1996). Using this additional information, lengths ($L_{tij}$) and radii

($R_{tij}$) of the cylindrically approximated throats can be computed from eq. I.3 (i.e. two equations with two unknowns). Since the semi-empirical rate expressions given by eq. 4.6 are strictly valid for $\kappa(=L_{tij}/R_{tij}) \geq 1$, throats with $\kappa < 1$ (in section4.3.3.1) are set to $\kappa = 1$ (while keeping $V_{tij}$ constant).

$$V_{p_i}^{t_{ij}} = \pi R_{t_{ij}}^2 L_{t_{ij}} \qquad G_{t_{ij}} = \frac{\pi R_{t_{tij}}^4}{8 L_{t_{ij}}} \tag{I.3}$$

## APPENDIX J: PRECIPITATION REACTIONS

The coupled ODEs that describe the reaction part of the operator-split in chapter 5 are:

$$\begin{aligned} V_{p,i}\frac{dc_{HCO_3^-,i}}{dt} &= V_{p,i}\left(k_1 - k_2\left(c_{HCO^-_3,i} - c^{eq}{}_{HCO_3^-,i}\right)\right) \\ V_{p,i}\frac{dc_{CaCO_3,i}}{dt} &= \frac{V_{p,i}k_2}{2}\left(c_{HCO^-_3,i} - c^{eq}{}_{HCO_3^-,i}\right) \end{aligned} \tag{J.1}$$

The ODEs are amenable to an analytical solution:

$$\left.\begin{aligned} c_{HCO_3}(t) &= \frac{\left(2\rho_{CaCO_3} + c^{eq}_{HCO_3^-}\right)}{2} - \frac{A}{2\sqrt{k_2}}\frac{C_0\exp\left(\frac{\sqrt{k_2}A}{2\rho_{CaCO_3}}t\right)+1}{C_0\exp\left(\frac{\sqrt{k_2}A}{2\rho_{CaCO_3}}t\right)-1} \\ V_p(t) &= V_{p,0}\exp\left[\frac{k_2}{2\rho_{CaCO_3}}\left(c^{eq}_{HCO_3^-} - \frac{\left(2\rho_{CaCO_3} + c^{eq}_{HCO_3^-}\right)}{2} - \frac{A}{2\sqrt{k_2}}\right)t + \ln\left(\frac{C_0\exp\left(\frac{\sqrt{k_2}A}{2\rho_{CaCO_3}}t\right)-1}{C_0-1}\right)\right] \end{aligned}\right\} A^2 > 0$$

$$\left.\begin{aligned} c_{HCO_3}(t) &= \frac{\left(2\rho_{CaCO_3} + c^{eq}_{HCO_3^-}\right)}{2} - \frac{A}{2\sqrt{k_2}}\tan\left(-\frac{\sqrt{k_2}A^*}{4\rho_{CaCO_3}}t + C_0^*\right) \\ V_p(t) &= V_{p0}\exp\left[\frac{k_2}{2\rho_{CaCO_3}}\left(c^{eq}_{HCO_3^-} - \frac{\left(2\rho_{CaCO_3} + c^{eq}_{HCO_3^-}\right)}{2}\right)t + \ln\left(\frac{\sec(C_0^*)}{\sec\left(\frac{\sqrt{k_2}A^*}{4\rho_{CaCO_3}}t - C_0^*\right)}\right)\right] \end{aligned}\right\} A^2 < 0$$

(J.2)

Where,

$$A = \left(4k_2\rho_{CaCO_3}^2 + (-8k_1 - 4c_{HCO_3^-}^{eq}k_2)\rho_{CaCO_3} + c_{HCO_3^-}^{eq\ 2}k_2\right)^{1/2}$$

$$A^* = \left(-4k_2\rho_{CaCO_3}^2 + (4c_{HCO_3^-}^{eq}k_2 + 8k_1)\rho_{CaCO_3} - c_{HCO_3^-}^{eq\ 2}k_2\right)^{1/2}$$

$$C_0 = \frac{A + \sqrt{k_2}(2\rho_{CaCO_3} + c_{HCO_3^-}^{eq} - 2c_{HCO_3^-,0})}{\sqrt{k_2}(2\rho_{CaCO_3} + c_{HCO_3^-}^{eq} - 2c_{HCO_3^-,0}) - A} \qquad \text{(J.3)}$$

$$C_0^* = \arctan\left(\frac{\sqrt{k_2}(2\rho_{CaCO_3} + c_{HCO_3^-}^{eq} - 2c_{HCO_3^-,0})}{A^*}\right)$$

Here, $c_{HCO3-}$ is the concentration of bicarbonate species and $V_p$ is the pore volume, $\rho_{CaCO3}$ is the density of calcite. $A$, $A^*$, $C_0$, and $C_0^*$ are defined constants. The change in volume of the pore is proportional to amount of Calcite produced during the time step:

$$\frac{dV_{p,i}}{dt} = -\frac{1}{\rho_{CaCO_3}}\frac{d(V_p c_{CaCO_3})}{dt} \qquad \text{(J.4)}$$

Eq. J.4 was used in combination with eq. J.1 to derive eq. J.2-3. The concentration of the generated calcite changes according to:

$$c_{CaCO_3}(t) = \frac{V_{p0}}{V_p(t)}(\rho_{CaCO_3} + c_{CaCO_3,0}) - \rho_{CaCO_3} \qquad \text{(J.5)}$$

## APPENDIX K: GENERALIZED SEMI-ANALYTICAL SOLUTION FOR PASSIVE/REACTIVE SOLUTE TRANSPORT IN CYLINDRICAL DUCTS[4]

A semi-analytical solution for the transient advection-diffusion-reaction problem within finite and semi-infinite ducts is derived. The solution allows for general radial- and time-dependent inlet/outlet conditions, complex boundary conditions on the duct wall including adsorption and decay, and arbitrary velocity profiles of the transporting fluid. The only numerical step of the solution is the inverse Laplace transform in the time variable. Therefore, the approach also produces fully analytical steady-state solutions. The solution is verified against computational fluid dynamics (CFD) simulations under various boundary conditions and velocity profiles (Newtonian and power-law), and in all cases good agreement is obtained. Although theoretically applicable to all regimes, the solution is computationally difficult at very high Peclet numbers and very early times due to numerical instabilities as a result of finite precision arithmetic of computers. A convergence analysis is conducted to delineate the boundaries of this limit for two important cases.

The solution was derived using a new approach for solving two-dimensional partial differential equations (PDEs) with non-constant coefficients which parallels the Frobenius and power series methods for solving ordinary differential equations (ODEs). The approach reduces the original PDE to a single infinite-order ODE with constant coefficients. The approach is suspected to provide solutions to a large class of PDEs of this type. The solution may find applications in a number of engineering and/or

[4] The material in this appendix was published under the following reference, which was completed under the supervision of Matthew Balhoff.

Mehmani, Yashar, and Matthew T. Balhoff. "Generalized semi-analytical solution of advection–diffusion–reaction in finite and semi-infinite cylindrical ducts." International Journal of Heat and Mass Transfer 78 (2014): 1155-1165.

biomedical fields, it can be used to verify numerical simulators, and serve as a simple and easy-to-implement alternative where access to numerical simulators is not available.

## K.1 Introduction

The problem of heat and mass transfer within cylindrical tubes has been examined for over a century since Graetz considered a simplified version of the problem in 1882 (Graetz, 1882, 1885). His work and those that have followed since consider the steady-state, fully developed temperature profile of a fluid flowing in a constant-wall-temperature duct. The problem has relevance in the design and analysis of heat exchangers. Graetz had originally considered the steady-state problem ignoring axial conduction (or diffusion). An analytical solution including this term was recently developed by Lahjomri and Oubarra (1999). Their method employs an approach similar to the method of separation of variables, with the difference that the Eigen-functions do not form an orthogonal set. The elegance of their approach is that despite the non-orthogonally of the Eigen-bases the "Fourier-coefficients" are explicitly recovered. The solution has been further extended to scenarios with added physics, such as viscous dissipation and slip flow (e.g. Barron et al., 1997; Jeong and Jeong, 2006) using very similar approaches.

The problem of solute dispersion within cylindrical ducts appears to be first considered by Taylor (1953), who showed that the late-time dispersal of solutes follows Fickian behavior. Aris (1956) later extended Taylor's theory by including axial diffusion into his analysis (originally ignored by Taylor). The dispersion problem was later extensively studied by various investigators, both with the aim of extending Taylors theory and delineating its limits e.g. Ananthakrishnan et al. (1965), Gill and

Sankarasubramanian (1970). The majority of the work on dispersion concerns itself with the cross-sectional average of the concentration. However, there are scenarios (e.g. ascertaining the local Sherwood number along the duct wall) where knowledge of the local concentration field becomes important. The solution of the unsteady-state transport equation for the local concentration field has been attempted by a handful of investigators. Lighthill (1966) derived a simple and elegant analytical solution applicable to early times when the stretching solute has not had enough time to sense the walls of the duct. The applicability of his solution becomes important at large Peclet numbers. Chun (1970) and Hunt (1977) both used perturbation analysis to obtain solutions limited to very low ($Pe < 0.1$) and very high Peclet numbers, respectively. Tseng and Besant (1972) derived an exact solution for the solute transport equation in an infinite tube with impulse and step-change initial conditions. The solution involved an expansion with respect to zero-order Bessel functions (of first kind) in the radial component which transformed the differential equation into a matrix form. In the process, Eigenvalues and Eigenvectors of the corresponding matrix had to be computed and, overall, the solution was rather numerically involved.

Perhaps the most comprehensive solution and analysis done so far was by Yu in a series of papers (1976, 1979, and 1981). His approach was to similarly expand the solution in terms of zero-order Bessel functions (of first kind) in the radial component. This converted the original differential equation into an infinite system of coupled second order differential equations in infinite unknowns. However, for an infinite tube Yu was able to use the Fourier and the Laplace transforms to obtain solutions for impulse and step change initial conditions. The resulting solution was numerically involved and required quite a bit of computational effort. Shankar and Lenhoff (1989) remedied this problem by replacing the Fourier transform step of Yu by a Fourier expansion. However,

they had to ignore the axial diffusion term in the process. That said Yu showed his approach could reproduce the Taylor limit, provided ample comparison with almost all previous models developed in the literature, and showed his solution was equivalent to that of Tseng and Besant (1972). Although his analysis showing the equivalence of his approach to that of Gill and Sankarasubramanian (1970) was later disputed by Gill and Sankarasubramanian (1980) and shown to be incorrect.

All the literature mentioned above, provide solutions for the case of an infinite tube with no boundary conditions imposed in the axial direction (other than decay conditions at infinity). In fact, the author is unaware of any work that provides analytical treatments of finite length pipes with prescribed axial inlet/outlet conditions. This is understandable since analysis of the problem becomes even more difficult for finite length ducts and previous approaches, for the most part, become inapplicable. Furthermore, previous work is limited to very specific and rather simple boundary conditions imposed on the duct wall. The goal of the current work is to present a new semi-analytical solution that has the flexibility to be applied to a vast majority of heat/mass transfer problems in cylindrical ducts (as well as Cartesian slits). It is applicable to both finite and semi-infinite tubes and allows for general boundary conditions at the duct wall, inlet and outlet. The solution is semi-analytical because it involves a numerical Laplace inverse transform step in the time variable (which is numerically simple). For steady-state scenarios our approach produces fully-analytical solutions due to the absence of the Laplace transform step. The solution approach appears to be applicable to a wide class of partial differential equations (PDEs) (in both Cartesian and cylindrical coordinates) with variable coefficients, and parallels (and seems to extend) the Frobenius and power series methods for solving ordinary differential equations (ODEs).

## K.2 Problem statement

The transport of a dilute solute species under laminar flow of a single-phase Newtonian fluid within a cylindrical duct and subject to first-order decay is described by eq. K.1. We assume negligible entrance effects and assume fully developed flow starting from the pipe inlet, which is a good assumption for sufficiently long pipes and sufficiently small Reynolds numbers (exact quantification of the entrance length can be found in Durst et al., 2005). Additional assumptions include isothermal flow and a concentration-independent molecular diffusion coefficient. If the species is allowed to adsorb onto the walls of the duct and undergo an independent decay process, eq. K.2 is additionally needed to describe the rate of change of the adsorbed solute. Note that the form of eq. K.1 remains unchanged in the description of heat transfer under similar assumptions, in which case concentration needs to be replaced by temperature. In this case, eq. K.2, however, requires an additional diffusion term arising from the conduction of heat along the duct wall. This term will not be included in the analysis of here (since the focus is primarily on solute transport) and requires further analytic treatment. The solution approach presented in section K.3 is not limited to parabolic fluid velocity profiles (as it appears in eq. K.1). However, to keep the analysis simple we demonstrate the approach for a Newtonian fluid. An example of a non-Newtonian (power-law) fluid is discussed in section K.4.4.

$$\frac{\partial \tilde{c}}{\partial t} + V_0\left(1-\left(\frac{r}{R}\right)^2\right)\frac{\partial \tilde{c}}{\partial x} = D_m\left(\frac{1}{r}\frac{\partial}{\partial r}\left(r\frac{\partial \tilde{c}}{\partial r}\right)+\frac{\partial^2 \tilde{c}}{\partial x^2}\right)-\omega\tilde{c} \qquad \text{(K.1)}$$

$$\delta\frac{\partial \tilde{\phi}}{\partial t} = -D_m\frac{\partial \tilde{c}}{\partial r}\Big|_{r=R} - \gamma\phi\delta \qquad \text{(K.2)}$$

In eq. K.1 and K.2, $\tilde{c}$ is the concentration within the fluid bulk, $\tilde{\phi}$ is the concentration of the adsorbed solute onto the duct wall, $V_0$ is the maximum centerline fluid velocity, $D_m$ is the molecular diffusion coefficient, $\omega$ is the rate of decay within the fluid bulk, $\delta$ is the pipe wall thickness, $\gamma$ the rate of decay of the adsorbed solute, and $R$ is the duct radius. Equations K.1 and K.2 are subject to the following initial and general boundary conditions:

$$\tilde{c}(t=0,x,r)=0 \qquad \tilde{\phi}(t=0,x)=0 \tag{K.3a}$$

$$\frac{\partial \tilde{c}}{\partial r}|_{r=0}=0 \tag{K.3b}$$

$$-D_m \frac{\partial \tilde{c}}{\partial r}|_{r=R}=h(\tilde{c}|_{r=R}-\tilde{\phi}) \qquad \text{(special cases: } \frac{\partial \tilde{c}}{\partial r}|_{r=R}=0 \text{ and } \tilde{c}|_{r=R}=0\text{)} \tag{K.3c}$$

$$\tilde{a}_1 \frac{\partial \tilde{c}}{\partial x}|_{x=0}+\tilde{a}_2 \tilde{c}|_{x=0}=f(t) \tag{K.3d}$$

$$\begin{cases} \tilde{b}_1 \dfrac{\partial \tilde{c}}{\partial x}|_{x=L}+\tilde{b}_2 \tilde{c}|_{x=L}=g(t) & if\ x\in[0,L] \\ \tilde{c}, \dfrac{\partial \tilde{c}}{\partial x}\to 0 \quad as \quad x\to\infty & if\ x\in[0,\infty) \end{cases} \tag{K.3e}$$

Eq. K.3b expresses the axial symmetry of the concentration profile across the duct cross-section. Eq. K.3c relates the rate of mass transfer at the duct wall to the concentration difference between the fluid bulk and the adsorbed solute ($h$ is the mass transfer coefficient). To allow analytic treatment, this boundary condition assumes linear first-order adsorption rates. Two special cases of this boundary condition are also given within parentheses in eq. K.3c. Eq. K.3c is responsible for the coupling of eq. K.1 and K.2. Eq. K.3d and K.3e describe general boundary conditions imposed at the inlet and outlet of a finite pipe. $a_1$, $a_2$, $\tilde{b}_1$ and $\tilde{b}_2$ can be, in their most general form, functions of $r$ (the radial coordinate) (typically related to physical attributes of the system) without

setting any limitations on the analysis provided in section K.3. For convenience, they are assumed to be constant parameters throughout this appendix unless stated otherwise. A discussion pertaining to cases where these parameters are dependent on *r* is provided at the end of section K.3. For similar reasons, $f$ and $g$ are assumed to be arbitrary functions of time alone, whereas they can generally depend on *r* as well. For a semi-infinite pipe the outlet condition is replaced by the limiting condition given in eq. K.3e. In order to reduce the number of free parameters and present our final results in a more useful format, eq. K.1-3 are non-dimensionalized with the following choice of non-dimensional variables.

$$\xi = \frac{r}{R} \qquad \lambda = \frac{x}{L} \qquad \tau = \frac{tV_0}{L} \qquad c = \frac{\tilde{c}}{\tilde{c}_0} \qquad \phi = \frac{\tilde{\phi}}{\tilde{c}_0} \qquad \kappa = \left(\frac{L}{R}\right)^2 \qquad Z = \frac{D_m L}{V_0 R \delta}$$

$$Pe = \frac{V_0 L}{D_m} \qquad Sh = \frac{Rh}{D_m} \qquad Da_I = \frac{L\omega}{V_0} \qquad Da_{II} = \frac{\gamma L}{V_0} \tag{K.4}$$

The characteristic concentration $\tilde{c}_0$ is typically chosen as the maximum concentration value attainable within the system. In the results presented in section K.4, it is chosen as the (constant) inlet concentration value. The resulting dimensionless differential equations are eq. K.5 and K.6:

$$\frac{\partial c}{\partial \tau} + (1-\xi^2)\frac{\partial c}{\partial \lambda} = \frac{\kappa}{Pe}\frac{1}{\xi}\frac{\partial}{\partial \xi}\left(\xi \frac{\partial c}{\partial \xi}\right) + \frac{1}{Pe}\frac{\partial^2 c}{\partial \lambda^2} - Da_I c \tag{K.5}$$

$$\frac{\partial \phi}{\partial \tau} = -Z\frac{\partial c}{\partial \xi}\Big|_{\xi=1} - Da_{II}\phi \tag{K.6}$$

Subject to the following dimensionless initial and boundary conditions:

$$c(\tau = 0, \lambda, \xi) = 0 \qquad \phi(\tau = 0, \lambda) = 0 \tag{K.7a}$$

$$\frac{\partial c}{\partial \xi}|_{\xi=0}=0 \tag{K.7b}$$

$$\frac{\partial c}{\partial \xi}|_{\xi=1}=-Sh(c|_{\xi=1}-\phi) \qquad \text{(special cases: } \frac{\partial c}{\partial \xi}|_{\xi=1}=0 \text{ and } c|_{\xi=1}=0\text{)} \tag{K.7c}$$

$$a_1\frac{\partial c}{\partial \lambda}|_{\lambda=0}+a_2 c|_{\lambda=0}=f(\tau) \tag{K.7d}$$

$$\begin{cases} b_1\dfrac{\partial c}{\partial \lambda}|_{\lambda=1}+b_2 c|_{\lambda=1}=g(\tau) & \text{if } \lambda\in[0,1] \\ c,\dfrac{\partial c}{\partial \lambda}\to 0 \quad as \quad \lambda\to\infty & \text{if } \lambda\in[0,\infty) \end{cases} \tag{K.7e}$$

In eq. K.5-7, *Sh* is the Sherwood (or Nusselt in heat transfer) number (mass transfer over diffusion), *Pe* is the Peclet number (advection over diffusion), and $\kappa$ is the aspect ratio of the finite duct. $Da_I$ and $Da_{II}$ denote Damköhler numbers (reaction over advection) associated with the fluid bulk and the pipe wall respectively. It should be noted that for semi-infinite ducts *L* is replaced by *R* in all the equations above (eq. K.4-7) without any impact on the following mathematical analysis. Other parameters arising within eq. K.5-7 are defined in eq. K.7f. The functions *f* and *g* are simply obtained by transforming the time variable *t* into $\tau$ within $f$ and $g$.

$$a_1=\frac{a_1\tilde{c}_0}{L} \qquad a_2=a_2\tilde{c}_0 \qquad b_1=\frac{\tilde{b}_1\tilde{c}_0}{L} \qquad b_2=\tilde{b}_2\tilde{c}_0 \tag{K.7f}$$

**K.3 Problem solution**

As the first step the Laplace transforms of *c* and $\phi$ is taken with respect to the time variable (i.e. $\tau$). The Laplace transform is defined as:

$$\hat{c}(T,\lambda,\xi)=\int_0^\infty c(\tau,\lambda,\xi)e^{-T\tau}d\tau \qquad \phi(T,\lambda)=\int_0^\infty \phi(\tau,\lambda)e^{-T\tau}d\tau \tag{K.8}$$

Thus eq. K.5, K.6 and K.7 respectively become:

$$(T + Da_I)\hat{c} + (1-\xi^2)\frac{\partial \hat{c}}{\partial \lambda} = \frac{\kappa}{Pe}\frac{1}{\xi}\frac{\partial}{\partial \xi}(\xi \frac{\partial \hat{c}}{\partial \xi}) + \frac{1}{Pe}\frac{\partial^2 \hat{c}}{\partial \lambda^2} \tag{K.9}$$

$$\phi = -\frac{Z}{(Da_{II} + T)}\frac{\partial \hat{c}}{\partial \xi}|_{\xi=1} \tag{K.10}$$

$$\frac{\partial \hat{c}}{\partial \xi}|_{\xi=0} = 0 \tag{K.11a}$$

$$\phi = \frac{1}{Sh}\frac{\partial \hat{c}}{\partial \xi}|_{\xi=1} + \hat{c}|_{\xi=1} \tag{K.11b}$$

$$a_1 \frac{\partial \hat{c}}{\partial \lambda}|_{\lambda=0} + a_2 \hat{c}|_{\lambda=0} = F(T) \tag{K.11c}$$

$$\begin{cases} b_1 \dfrac{\partial \hat{c}}{\partial \lambda}|_{\lambda=1} + b_2 \hat{c}|_{\lambda=1} = G(T) & if\ \lambda \in [0,1] \\ \hat{c}, \dfrac{\partial \hat{c}}{\partial \lambda} \to 0 \quad as \quad \lambda \to \infty & if\ \lambda \in [0,\infty) \end{cases} \tag{K.11d}$$

Combining eq. K.10 and K.11b we obtain:

$$(\frac{1}{Sh} + \frac{Z}{Da_{II} + T})\frac{\partial \hat{c}}{\partial \xi}|_{\xi=1} + \hat{c}|_{\xi=1} = 0 \tag{K.12}$$

Thus we readily observe that by taking the Laplace transform we have decoupled eq. K.5 from K.6. Now, we *formally* introduce eq. K.13 as the solution to eq. K.9 subject to eq. K.11a, K.12, K.11c and K.11d. Note that the solution approach that follows bears similarities to the Frobenius method for solving ODEs with variable coefficients. Therefore, the following solution approach may be regarded as an extension to the Frobenius method (or power series method in Cartesian problems) for solving PDEs with

variable coefficients, and is expected to be applicable to a large class of PDEs in two-variables. To the author's knowledge, this is the first time such an extension is proposed (further discussion is provided at the end of this section).

$$\hat{c} = \sum_{n=0}^{\infty} A_n(\lambda)\xi^n \tag{K.13}$$

Substituting eq. K.13 into eq. K.9 and grouping terms of the same $\xi$-power we obtain:

$$\begin{aligned}
&A_0(\lambda) \neq 0 \\
&A_2(\lambda) = \frac{(T + Da_I)A_0 + A_0' - (1/Pe)A_0''}{(4\kappa / Pe)} \\
&A_{2m}(\lambda) = \frac{(T + Da_I)A_{2m-2} + A_{2m-2}' - A_{2m-4}' - (1/Pe)A_{2m-2}''}{(2m)^2(\kappa / Pe)} \\
&A_{2m-1}(\lambda) = 0 \qquad\qquad \forall m \geq 1
\end{aligned} \tag{K.14}$$

The derivatives appearing in eq. K.14 are with respect to the variable $\lambda$. Using eq. K.14 all $A_{2m}$ terms can be written as a linear combination of $A_0$ and its derivatives (i.e. eq. K.15):

$$A_{2m}(\lambda) = \sum_{j=0}^{2m} \alpha_{2m,j} A_0^{(j)} \tag{K.15}$$

The $\alpha_{2m,j}$ coefficients are readily computed recursively from eq. K.14 (note that $\alpha_{0,0} = 1$). On the other hand, inserting eq. K.13 into eq. K.12 and eq. K.11a respectively yields:

$$A_0(\lambda) + \sum_{n=1}^{\infty} [1 + (\frac{1}{Sh} + \frac{Z}{T + Da_{II}})n] A_n(\lambda) = 0 \tag{K.16}$$

$$A_1(\lambda) = 0 \tag{K.17}$$

Eq. K.17 is consistent with eq. K.14 obtained from the differential equation K.9. Note that the two special cases of boundary conditions at the duct wall (pointed out in eq. K.7c) yield the following equations instead of eq. K.16:

$$\sum_{n=1}^{\infty} nA_n(\lambda) = 0 \tag{K.18}$$

$$\sum_{n=0}^{\infty} A_n(\lambda) = 0 \tag{K.19}$$

Since all $A_n$ terms in eq. K.16, K.18 and K.19 can be written in terms of $A_0$ and its derivatives, they can be considered as "*transcendental equations"* in the form of infinite-order ordinary differential equations with respect to the single unknown function $A_0(\lambda)$. For computational purposes these equations need to be truncated to a finite number of terms; say $N_R$ (an even integer in this case). Therefore, truncating eq. K.16 (similarly eq. K.18 and K.19) and substituting eq. K.15 for all $A_n$ terms with $n \geq 2$, we obtain the following:

$$\sum_{k=0}^{N_R} c_k A_0^{(k)} = 0 \tag{K.20a}$$

$$c_k = \sum_{m=\left\lfloor \frac{k+1}{2} \right\rfloor}^{N_R/2} \left( 1 + \left( \frac{1}{Sh} + \frac{Z}{T + Da_{II}} \right) (2m) \right) \alpha_{2m,k} \tag{K.20b}$$

$$c_k = \sum_{m=\left\lfloor \frac{k+1}{2} \right\rfloor}^{N_R/2} (2m)\alpha_{2m,k} \tag{K.20c}$$

$$c_k = \sum_{m=\left\lfloor \frac{k+1}{2} \right\rfloor}^{N_R/2} \alpha_{2m,k} \tag{K.20d}$$

Eq. K.20a is a linear, homogeneous, finite-order ordinary differential equation with constant coefficients. The $c_k$ coefficients given by eq. K.20b, K.20c and K.20d

correspond to eq. K.16, K.18 and K.19 respectively. Note that these coefficients may assume different forms depending on the specific problem at hand, but can be easily derived (e.g. non-Newtonian fluids when odd $A_n$ terms are non-zero). In general, these coefficients are complex because the Laplace variable $T$ may be complex. However, the numerical Laplace inversion algorithm used in this work (Stehfest, 1970; explained later in this section) requires function evaluations for which the Laplace variable $T$ is real. In this case, the $c_k$ coefficients in eq. K.20a can also be expected to be real (because all other parameters involved are real) and we proceed further on this basis. We should note, however, that this by no means prevents one from using inverse algorithms that require function evaluations for complex values of $T$. The difference would be in the possible absence of conjugate roots in the characteristic polynomial (i.e. eq. K.21) discussed next.

Eq. K.20a has very simple bases for its solution, which can be constructed from the roots of its characteristic polynomial given by eq. K.21.

$$\sum_{k=0}^{N_R} c_k s^k = 0 \tag{K.21}$$

The roots of this polynomial are easily obtained via computing the Eigenvalues of its companion matrix using a computer. Here, this is readily accomplished by calling the "roots" command in MATLAB. Note that this step is no more difficult than computing the roots of transcendental equations involving Bessel functions (for obtaining the Eigenvalues) in the approaches used by previous authors (e.g. Tseng and Besant, 1972). Depending on whether a given root is real or complex, eq. K.22 denotes its corresponding basis $b_i$.

$$b_i(\lambda) = \begin{cases} e^{r_i \lambda} & r_i \in \mathbb{R} \\ e^{v_i \lambda} \sin(u_i \lambda) \ \ \& \ \ e^{v_i \lambda} \cos(u_i \lambda) & v_i \pm u_i i \in \mathbb{C} \end{cases} \tag{K.22}$$

One may perhaps wish to also consider the possibility of repeated roots. However, the occurrence of repeated roots was never observed during numerous calculations conducted herein. This renders the analysis and its implementation into computer code much simpler. The general solution of eq. K.20a can now be constructed by linearly combining the bases $b_i$ given by eq. K.23.

$$A_0(\lambda) = \sum_{i=1}^{N_R} \beta_i b_i(\lambda) \tag{K.23}$$

In order to obtain the unknown $\beta_i$ coefficients, we substitute eq. K.13 into eq. K.11c and K.11d (and group similar $\xi$-powers) from which we get eq. K.24 for the inlet:

$$\begin{cases} a_1 A_0'(0) + a_2 A_0(0) = F(T) \\ a_1 A_n'(0) + a_2 A_n(0) = 0 \qquad \forall n \geq 1 \end{cases} \tag{K.24}$$

And eq. K.25 for the outlet of a finite duct:

$$\begin{cases} b_1 A_0'(1) + b_2 A_0(1) = G(T) \\ b_1 A_n'(1) + b_2 A_n(1) = 0 \qquad \forall n \geq 1 \end{cases} \tag{K.25}$$

Substituting eq. K.15 for all $A_n$ terms in eq. K.24 and K.25, we obtain an infinite set of equations describing the boundary conditions of $A_0$ at $\lambda = 0$ and 1 for a finite-length duct. Choosing from this system an equal number of boundary conditions at $\lambda = 0$ as at $\lambda = 1$, one can compute the $\beta_i$ coefficients in eq. K.23. This is done by solving a relatively small (depending on the order of truncation, $N_R$) system of equations with respect to the unknowns $\beta_i$. The treatment is even simpler for semi-infinite ducts. Namely, by

substituting eq. K.13 into the limiting boundary condition of eq. K.11d at infinity, we obtain:

$$A_0^{(n)}(\lambda) \to 0 \quad as \quad \lambda \to \infty \qquad \forall n \geq 0 \tag{K.26}$$

Eq. K.26 dictates that bases, $b_i$, in which the power of the exponential function is a positive number multiplied by $\lambda$ (i.e. $e^{r_i\lambda}$ or $e^{v_i\lambda}$ where $r_i$, $v_i > 0$), have a corresponding $\beta_i$ coefficient that is zero. This reduces the number of the unknown $\beta_i$ coefficients to be calculated. A sufficient number of boundary conditions for $A_0$ at $\lambda = 0$ is then chosen (from eq. K.24) to determine the rest of the $\beta_i$ coefficients (by again solving a relatively small system of equations). Since in the process of determining the $\beta_i$ coefficients it becomes necessary to accurately calculate the derivatives of the bases (i.e. $b_i$), eq. K.27-30 provide simple (and easy-to-implement) means of determining the $k^{th}$-derivative of these bases.

$$(e^{r_i\lambda})^{(k)} = r_i^n e^{r_i\lambda} \tag{K.27}$$

$$(\sin(u_i\lambda))^{(k)} = \begin{cases} (-1)^{k/2} u_i^k \sin(u_i\lambda) & k = 2l, \quad \forall l \geq 0 \\ (-1)^{(k-1)/2} u_i^k \cos(u_i\lambda) & k = 2l-1, \quad \forall l \geq 1 \end{cases} \tag{K.28}$$

$$(\cos(u_i\lambda))^{(k)} = \begin{cases} (-1)^{k/2} u_i^k \cos(u_i\lambda) & k = 2l, \quad \forall l \geq 0 \\ (-1)^{(k+1)/2} u_i^k \sin(u_i\lambda) & k = 2l-1, \quad \forall l \geq 1 \end{cases} \tag{K.29}$$

$$\begin{aligned} (e^{v_i\lambda}\sin(u_i\lambda))^{(k)} &= \sum_{j=0}^{k} \binom{k}{j} (e^{v_i\lambda})^{(k-j)} (\sin(u_i\lambda))^{(j)} \\ (e^{v_i\lambda}\cos(u_i\lambda))^{(k)} &= \sum_{j=0}^{k} \binom{k}{j} (e^{v_i\lambda})^{(k-j)} (\cos(u_i\lambda))^{(j)} \end{aligned} \tag{K.30}$$

Once the $\beta_i$ coefficients are calculated $A_0$ is automatically obtained from eq. K.23. Subsequently all $A_n$ terms can be obtained from eq. K.15. Substituting the $A_n$ terms into eq. K.13 and eq. K.31 yields the analytical solution to the coupled differential equations K.5 and K.6 subject to the initial/boundary conditions of eq. K.7 in the Laplace time domain. Moreover, the cross-sectional average concentration in the Laplace time domain can be calculated from eq. K.32.

$$\phi = -\frac{Z}{(Da_{II} + T)} \sum_{n=1}^{\infty} nA_n(\lambda) \tag{K.31}$$

$$c_m = 2\sum_{n=0}^{\infty} \frac{A_n(\lambda)}{n+2} \tag{K.32}$$

Finally, we need to transform the analytical solution (eq. K.13, K.31, K.32) from the Laplace domain back into the real time domain. Since the Laplace variable $T$ has been absorbed into the formulation and into the roots of the characteristic polynomial given by eq. K.21, we need to perform the Laplace inversion numerically. In this work, we have used the well-known Stehfest (1970) method to perform the inversion. The method is given here by eq. K.33 for convenience. In eq. K.33, $Y(T)$ is the Laplace transform of $y(t)$, and $N_L$ is an even integer. We used this method due to its simplicity and thus ease in implementation. Many other Laplace inversion algorithms exist in the literature for which the reader is referred to Cheng (1994) and Duffy (2004). Note that one could either numerically invert the whole solution (i.e. eq. K.13, K.31 and K.32) at once, or only invert $A_0$ and use derivative theorems to invert the rest of the $A_n$ terms (the former was performed herein). The Laplace inversion is the only numerical step in the solution of the system given by eq. K.5-7. This is the reason why we refer to it as a semi-analytical solution. It is noteworthy that the steady-state solution of the system given by eq. K.5-7

does not require the Laplace transform and our analysis yields a fully-analytical solution to the problem. This is relevant for steady-state Graetz problems in finite or semi-infinite pipes.

$$y(t) \simeq \frac{\ln 2}{t} \sum_{n=1}^{N_L} h_n Y\left(\frac{n \ln 2}{t}\right)$$
$$h_n = (-1)^{n+N/2} \sum_{k=(n+1)/2}^{\min(n, N_L/2)} \frac{k^{N/2}(2k)!}{(N/2-k)!\,k!\,(k-1)!\,(n-k)!\,(2k-n)!} \tag{K.33}$$

We conclude this section with a few remarks. As mentioned earlier, the form of the solution given by eq. K.13 was inspired by the Frobenius method for solving ODEs with variable coefficients and regular singular points. In fact, if one were to draw a parallel and form the "indicial equation" for eq. K.9, by insisting $A_0(\lambda) \neq 0$ one would obtain a double root of zero for this equation. This together with considering axial symmetry of the concentration field (via eq. K.11a) results in the proposed form of the solution (i.e. eq. K.13). Therefore, one can imagine how this way of viewing cylindrical problems (among others) both with axial and radial dependence allows for solving a vast number of problems by simply following the proposed steps. This in effect reduces the original variable coefficient partial differential equation into an infinite order ordinary differential equation with constant coefficients. The method allows for the examination of finite pipes (which does not appear to have been pursued by previous investigators) as well as semi-infinite pipes. One might be tempted to take the analogy with the Frobenius method to the extreme and apply it to annular flow geometries. However, non-trivial extensions of the current analysis are required which is outside the scope of this work. Interestingly enough, the method can also be applied for 2D Cartesian problems (e.g. flow through finite/semi-infinite slits) following the same steps outlined above. In this

case, eq. K.13 would be expanded with respect to the transverse y-coordinate (instead of the radial coordinate) and the resulting analysis would be similar to the power series method in solving ODEs (due to an absence of singularities).

Finally, the formulation of physically meaningful and correct inlet and outlet conditions is a non-trivial task and has been the subject of extensive study (e.g. Liou and Wang, 1990). Among the different choices of inlet/outlet conditions, typically a generalized Dankwerts type boundary condition may be used (taking into account the velocity profile of the fluid within the pipe). This consists of Neumann boundary conditions at the outlet and an inlet condition of the form given by eq. K.34 (after non-dimensionalizing and taking the Laplace transform with respect to the time variable). In eq. K.34, *W(T)* represents the Laplace transform of an arbitrary function of time *w(τ)*.

$$-\frac{1}{Pe}\frac{\partial \hat{c}}{\partial \lambda}\Big|_{\lambda=0^+} + (1-\xi^2)\hat{c}\Big|_{\lambda=0^+} = (1-\xi^2)W(T) \qquad \text{(K.34)}$$

By comparison of eq. K.34 with eq. K.11c, it is clear that $a_2$ and $F$ are functions of $\xi$. After substituting eq. K.13 into eq. K.34 and grouping similar $\xi$-power terms we get eq. K.35 as the inlet condition for eq. K.20a (instead of eq. K.24). The analysis then proceeds unaltered from this point forward. Therefore, complex radially dependent inlet/outlet conditions such as eq. K.34 can be naturally accommodated into the proposed solution approach. The verification results and examples provided in section K.4, however, focus on relatively simple inlet/outlet conditions.

$$\begin{cases} -\dfrac{1}{Pe}A_0'(0) + A_0(0) = W(T) \\ -\dfrac{1}{Pe}A_2'(0) + A_2(0) - A_0(0) = -W(T) \\ -\dfrac{1}{Pe}A_{2m}'(0) + A_{2m}(0) - A_{2m-2}(0) = 0 \qquad \forall m \geq 2 \end{cases} \tag{K.35}$$

**K.4 Results and discussion**

We consider several special cases and present results obtained from the semi-analytical solution (developed in the previous section). The results are then compared to Computational Fluid Dynamics (CFD) simulations performed in COMSOL©, which utilizes the Finite Element method (FEM) to solve eq. K.5. In the following, the number of terms used in the series expansion given by eq. K.13 was taken in the range $N_R$ = 50-74 and the number of terms used in the numerical inverse Laplace transform (i.e. eq. K.33) was taken in the range $N_L$ = 12-16 (where $N_L$ is an even integer). The number of elements used in the COMSOL© simulations was 32774 for the semi-infinite ducts, and 12891 for the finite ducts. In both the semi-analytical solution and the COMSOL© simulations, $N_R$, $N_L$ and number of FEM mesh refinements were increased until negligible changes in the results were recorded. In some of the following cases, small but noticeable differences between the two solutions are observed (especially at larger Peclet numbers). We ascribe this to the incomplete convergence of the series given by eq. K.13. Complete convergence could not be achieved for these cases, because inclusion of higher order terms in the series (i.e. eq. K.13) resulted in numerical instabilities as a result of finite precision arithmetic of computers. For the same reason, the following results could not be pursued to very high Peclet numbers (and are presented for $Pe \leq 40$ for semi-infinite ducts and $Pe \leq 18$ for finite ducts). This is discussed in further detail in section K.4.6,

where we present a convergence analysis for two of the presented cases in order to delineate the applicability limit of the solution.

### *K.4.1 Zero concentration gradient at the wall, semi-infinite duct*

A semi-infinite duct with initial conditions given by eq. K.7a and boundary conditions given by eq. K.36 was considered (with no adsorption and no decay within the fluid bulk):

$$c|_{\lambda=0}=1 \qquad c|_{\lambda\to\infty}\to 0 \qquad \frac{\partial c}{\partial \xi}|_{\xi=0,1}=0 \tag{K.36}$$

To simulate a semi-infinite duct in COMSOL©, a tube of length $L = 10R$ was considered and the simulations were stopped before the outlet boundary was sensed by the evolving concentration field. Figure K.1 compares snapshots of radial and axial concentration profiles (at various radial and axial transects) obtained from the semi-analytical solution (shown as solid lines) to those obtained from COMSOL© simulations (shown as circles) at three different Peclet numbers: $Pe = 0.5$, 15 and 40. As can be seen, there is very good agreement between the two and the boundary conditions are clearly satisfied. Figures K.1a and K.1b correspond to $Pe = 0.5$ and $\tau = 1$, fig. K.1c and K.1d correspond to $Pe = 15$ and $\tau = 2.25$, and fig. K.1e and K.1f correspond to $Pe = 40$ and $\tau = 6.3$.

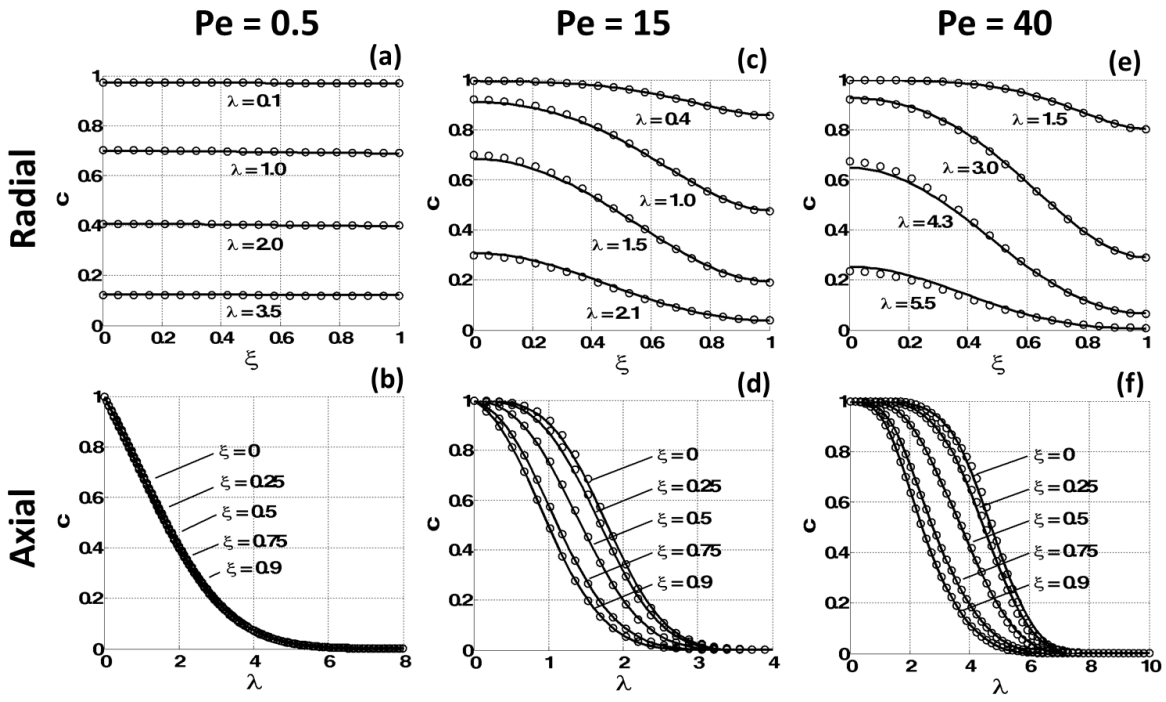


Figure K.1: Radial and axial concentration profiles obtained from the semi-analytical solution (solid line) and COMSOL© (circles) at three different Peclet numbers for a semi-infinite tube with zero concentration gradient at the duct wall. (a), (b) correspond to $\tau = 1$and $Pe = 0.5$, (c), (d) correspond to $\tau = 2.25$ and $Pe = 15$, and (e), (f) correspond to $\tau = 6.3$ and $Pe = 40$.

### *K.4.2 Zero concentration at the wall, semi-infinite duct*

The boundary conditions for this case are given by eq. K.37 (with no adsorption and no decay within the fluid bulk).

$$c|_{\lambda=0}=1 \qquad c|_{\lambda\to\infty}\to 0 \qquad \frac{\partial c}{\partial \xi}|_{\xi=0}=0 \qquad c|_{\xi=1}=0 \tag{K.37}$$

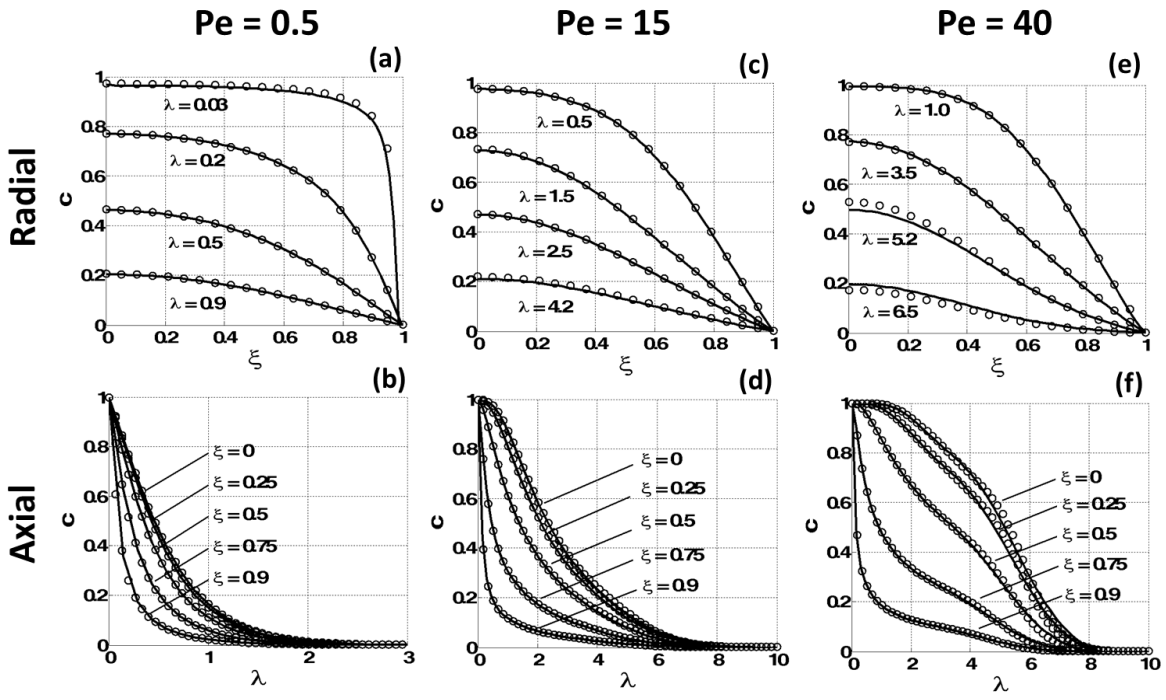


Figure K.2: Radial and axial concentration profiles obtained from the semi-analytical solution (solid line) and COMSOL© (circles) at three different Peclet numbers for a semi-infinite tube with zero concentration at the duct wall. (a), (b) correspond to $\tau = 0.25$ and $Pe = 0.5$, (c), (d) correspond to $\tau = 7.5$ and $Pe = 15$, and (e), (f) correspond to $\tau = 7.4$ and $Pe = 40$.

Figure K.2 compares the semi-analytical solution to the numerical solution of COMSOL© at three different Peclet numbers: $Pe = 0.5$, 15 and 40. Once again very good agreement between COMSOL© and the semi-analytical solution is observed, which clearly satisfy the boundary conditions imposed. As in the previous section, a tube length of $L = 10R$ was considered to simulate semi-infinite ducts in COMSOL©. Figures K.2a and K.2b correspond to $Pe = 0.5$ and $\tau = 0.25$, fig. K.2c and K.2d correspond to $Pe = 15$ and $\tau = 7.5$, and fig. K.2e and K.2f correspond to $Pe = 40$ and $\tau = 7.4$. Note that in this case the concentration field eventually reaches steady state (due to solute outflux at the

duct wall), for which the analysis of section K.3 provides a fully analytical steady-state solution.

### *K.4.3 Zero concentration gradient at the wall and outlet, finite duct*

The boundary conditions for this case are given by eq. K.38 (with no adsorption and no decay within the fluid bulk).

$$c|_{\lambda=0}=1 \qquad \frac{\partial c}{\partial \lambda}|_{\lambda=1}=0 \qquad \frac{\partial c}{\partial \xi}|_{\xi=0,1}=0 \tag{K.38}$$

Figure K.3 compares the semi-analytical solution to the numerical solution of COMSOL© at three different Peclet numbers: $Pe$ = 0.5, 10 and 18. Since the ducts are finite in length, $\kappa$ = 16 is chosen ($\kappa$ defines the aspect ratio of the pipe). Once again very good agreement between COMSOL© and the semi-analytical solution is observed, which satisfy the boundary conditions imposed. The satisfaction of the outlet conditions in figure K.3.f may not appear to be very clear. It was verified that this is due to a combination of using finite number of plotting points close to the outlet (in both the CFD and semi-analytical solutions), normalization of the axial coordinate by its length, and suppression of outlet effects due to the slight increase in Peclet number. Figures K.3a and K.3b correspond to $Pe$ = 0.5 and $\tau$ = 0.32, fig. K.3c and K.3d correspond to $Pe$ = 10 and $\tau$ = 1.2, and fig. K.3e and K.3f correspond to $Pe$ = 18 and $\tau$ = 1.92. The outlet condition in eq. K.38 is commonly prescribed for finite length domains and is known as the Danckwerts (1953) exit condition.

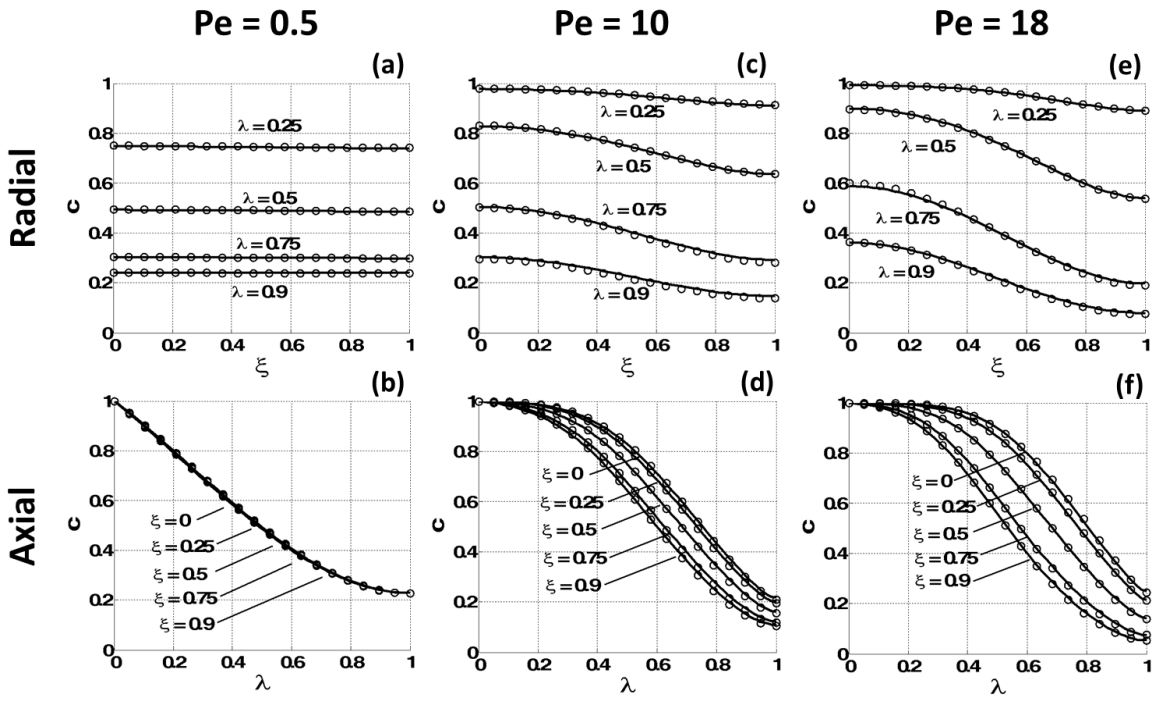


Figure K.3: Radial and axial concentration profiles obtained from the semi-analytical solution (solid line) and COMSOL© (circles) at three different Peclet numbers for a finite tube ($\kappa = 16$) with zero concentration gradient at the duct wall and outlet. (a), (b) correspond to $\tau = 0.32$ and $Pe = 0.5$, (c), (d) correspond to $\tau = 1.2$ and $Pe = 10$, and (e), (f) correspond to $\tau = 1.92$ and $Pe = 18$.

### *K.4.4 Zero concentration gradient at the wall and zero concentration at the outlet, finite duct*

The boundary conditions for this case are given by eq. K.39 (with no adsorption and no decay within the fluid bulk).

$$c|_{\lambda=0}=1 \qquad c|_{\lambda=1}=0 \qquad \frac{\partial c}{\partial \xi}|_{\xi=0,1}=0 \tag{K.39}$$

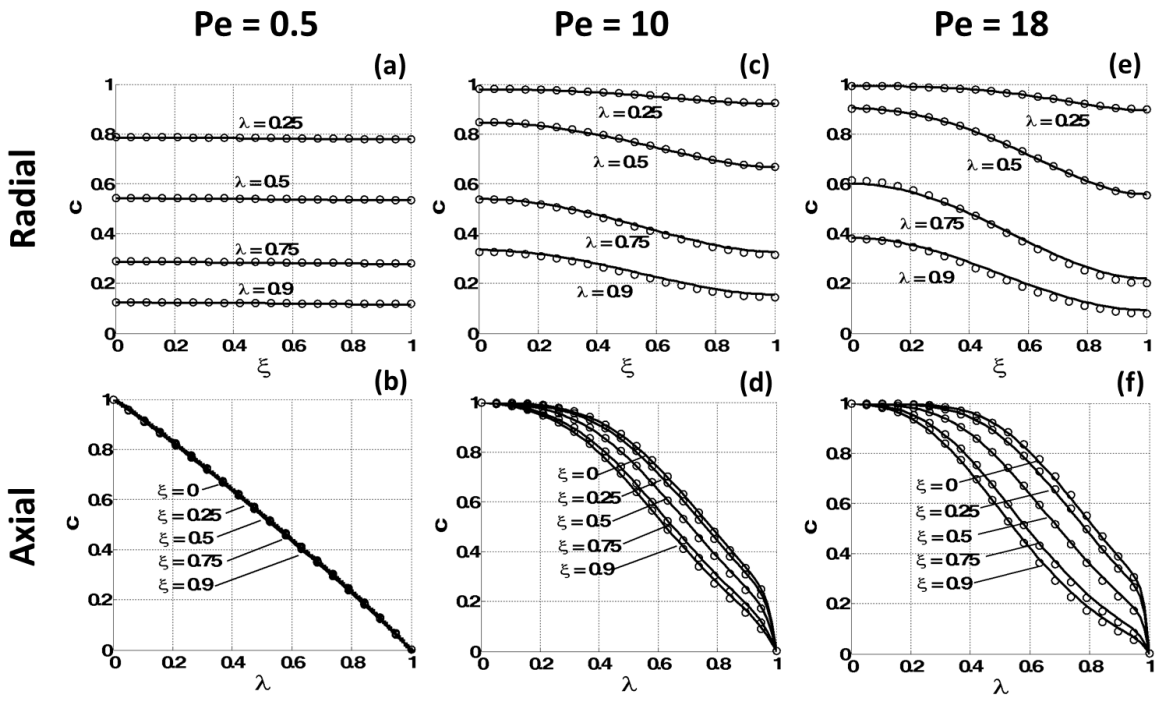


Figure K.4: Radial and axial concentration profiles obtained from the semi-analytical solution (solid line) and COMSOL© (circles) at three different Peclet numbers for a finite tube ($\kappa = 16$) with zero concentration gradient at the duct wall and zero concentration at the outlet. (a), (b) correspond to $\tau = 0.44$ and $Pe = 0.5$, (c), (d) correspond to $\tau = 1.25$ and $Pe = 10$, and (e), (f) correspond to $\tau = 1.21$ and $Pe = 18$.

Figure K.4 compares the semi-analytical solution to the numerical solution of COMSOL© at three different Peclet numbers: $Pe = 0.5$, 10 and 18. Since the ducts are finite in length, $\kappa = 16$ is chosen. Once again very good agreement between COMSOL© and the semi-analytical solution is observed, which clearly satisfy the boundary conditions imposed. Figures K.4a and K.4b correspond to $Pe = 0.5$ and $\tau = 0.44$, fig. K.4c and K.4d correspond to $Pe = 10$ and $\tau = 1.25$, and fig. K.4e and K.4f correspond to $Pe = 18$ and $\tau = 1.21$. In figure K.4, notice the formation of a thin boundary layer at the outlet of the duct. Numerical methods typically require substantial refinement in such

regions to avoid numerical errors, whereas the semi-analytical solution can produce accurate measures of the boundary layer thickness.

### *K.4.4 Zero concentration gradient at the wall, semi-infinite duct, power-law fluid*

The analysis of section K.3 can also be applied to fluids with non-parabolic velocity profiles. This extends further the generality of the solution approach developed to almost arbitrary velocity profiles. As long as the velocity profile is analytic (i.e. has a Taylor expansion) around $r = 0$ the analysis remains unchanged (although one may wish to use a truncated version of the Taylor expansion for simplicity). This will naturally result in a different recursive relation for the $A_n$ terms than eq. K.14 (with the odd terms possibly non-zero). If the velocity profile is not analytic around $r = 0$, one can simply fit a low order polynomial to the velocity profile as an approximation (which would loosely be equivalent to the truncated version of its Taylor expansion around a different point).

Here we choose to examine a power-law fluid with a power-law index of $n = 1/3$ which results in the velocity profile $V(\xi) = V_0(1-\xi^4)$. Following the steps of the analysis presented in section K.3, the recursive relation given by eq. K.40 is obtained for the $A_n$ terms:

$$
\begin{aligned}
&A_0(\lambda) \neq 0 \\
&A_2(\lambda) = \frac{(T + Da_I)A_0 + A_0' - (1/Pe)A_0''}{(4\kappa / Pe)} \\
&A_4(\lambda) = \frac{(T + Da_I)A_2 + A_2' - (1/Pe)A_2''}{(16\kappa / Pe)} \\
&A_{2m}(\lambda) = \frac{(T + Da_I)A_{2m-2} + A_{2m-2}' - A_{2m-6}' - (1/Pe)A_{2m-2}''}{(2m)^2(\kappa / Pe)} \\
&A_{2m-1}(\lambda) = 0 \qquad \forall m \geq 1
\end{aligned}
\qquad \text{(K.40)}
$$

Figures K.5a and K.5b compare radial and axial concentration profiles obtained from the semi-analytical solution to those obtained from direct CFD simulations in COMSOL©. Initial and boundary conditions are similar to those in section K.4.1 (with no adsorption and no decay within the fluid bulk). These results correspond to $Pe = 20$ and $\tau = 5.57$. A power-law index of $n = 1/3$ implies shear thinning behavior of the fluid, and thus a relatively flat velocity profile (also higher overall flow rate) compared to the Newtonian counterpart. For the same Peclet number this results in the transport of solute further downstream from the inlet compared to the Newtonian fluid. This is also partly because radial diffusion does not retard the advancing concentration front as much for the power-law fluid, due to low radial concentration gradients (except only near the walls) imposed by the velocity profile. This is clearly seen in figure K.5c for a Newtonian fluid under the same conditions (i.e. maximum fluid velocity, molecular diffusion coefficient and pipe dimensions).

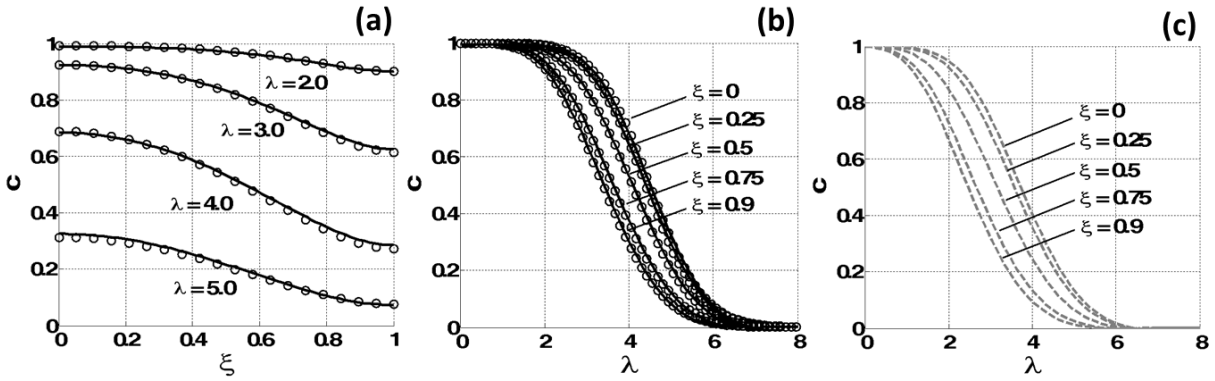


Figure K.5: (a) radial and (b) axial concentration profiles obtained from the semi-analytical solution (solid line) and COMSOL© (circles) for a semi-infinite tube and a power-law fluid with a power-law index of $n = 1/3$, at $Pe = 20$ and $\tau = 5.57$. (c) axial profile of Newtonian fluid under the same conditions.

### *K.4.5 Adsorption and decay at the wall, semi-infinite duct*

The boundary conditions for this case are given by eq. K.41 (with no decay within the fluid bulk).

$$c|_{\lambda=0}=1 \qquad c|_{\lambda\to\infty}\to 0 \qquad \frac{\partial c}{\partial \xi}|_{\xi=0}=0 \qquad \frac{\partial c}{\partial \xi}|_{\xi=1}=-Sh(c|_{\xi=1}-\phi) \qquad \text{(K.41)}$$

Figures K.6a and K.6b show radial and axial concentration profiles of the bulk fluid at various transects, and figure K.6c shows the deposition profile along the duct wall. These results correspond to $Pe$ = 20, $Sh$ = $10^6$, $Da_{II}$ = 500, $Z$ = 50, and $\tau$ = 20, and note that they reflect the boundary condition imposed. Unfortunately these results could not be verified with COMSOL© due to the additional coupled equation K.6 (which appears to be not supported by the software). Nevertheless, given the verifications performed in the previous sections, we assume that these results bear similar levels of accuracy as the ones already presented.

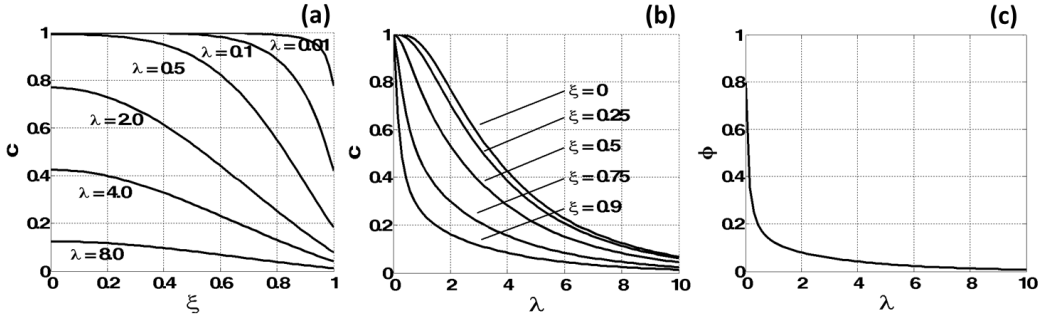


Figure K.6: (a) radial and (b) axial fluid bulk concentration profiles obtained from the semi-analytical solution at $\tau$ = 20 for a semi-infinite tube with adsorption of solute at the duct wall where $Pe$ = 20, $Sh$ = $10^6$, $Da_{II}$ = 500, $Z$ = 50. (c) shows the concentration of the adsorbed solute onto the duct wall at this time.

### *K.4.6 Convergence analysis*

The rate of convergence of the series given by eq. K.13 depends upon the magnitude of the dimensionless parameters that comprise it (e.g. *Pe*). Here, for brevity, we focus on two of the more important cases already discussed, namely the semi-infinite duct of section K.4.1 and the finite duct of section K.4.3. In both cases, the parameters appearing in the $A_n$ terms of eq. K.13 consist of $T$ and $Pe$, and additionally $\kappa$ for the finite duct case. As $Pe$ and $T$ increase the rate of convergence of the series in eq. K.13 decreases, requiring more terms for its convergence (i.e. $N_R$ needs to increase). However, as $N_R$ increases beyond a certain limit the series becomes numerically unstable. The instability is a result of the order of magnitude differences arising within the internal numerics of the solution (mainly due to the recurrence relation given by eq. K.14) which leads to the compounding of round-off errors (due to finite precision arithmetic of computers). One instance where this occurs is in the computation of the $\beta_i$ coefficients in eq. K.23. As $N_R$ increases it becomes progressively more difficult to obtain accurate values for the $\beta_i$ coefficients, because the system of equations formed by the inlet/outlet conditions, given by eq. K.24 (and eq. K.25 for finite ducts), becomes increasingly more ill-conditioned. This poses a computational limit on the largest Peclet number (i.e. $Pe$) and smallest time (i.e. $\tau$) for which we can obtain a meaningfully accurate solution. This should not be very surprising as similar observations of slow convergence rates for early times and high Peclet numbers were made in previously proposed solutions (e.g. Yu, 1976).

The convergence of the series in eq. K.13 was studied at various values of $Pe$, $T$ and $\kappa$ for the two cases mentioned. Specifically, for any fixed $Pe$ (and $\kappa$ for the finite duct case) the largest value of $T$ (the Laplace time variable) for which eq. K.13 converges (without instabilities) within a relative error of $10^{-4}$ was determined. Convergence was

considered at four points with $\lambda$ = 0.001, 0.01, 0.1, 1 and $\xi$ = 1 (where it appeared to be the slowest). These maximum $T$ values were then plotted against $Pe$ and a power law function was fitted through the data. Eq. K.42 is the inequality that has to be satisfied in order for the series in eq. K.13 to converge within a relative error of $10^{-4}$. This inequality, in turn, sets a lower limit for the time variable $\tau$, as they are related via eq. 43 if the Stehfest inversion algorithm (i.e. eq. K.33) is used. Combining eq. K.42 and K.43 we obtain eq. K.44 which delineates the smallest time (i.e. $\tau$; as a function of $Pe$ and $N_L$) for which the semi-analytical solution can be applied without incurring numerical instabilities. There also exists a maximum $Pe$ beyond which the series in eq. K.13 becomes numerically unstable regardless of the value of $T$. The $p$ and $q$ fitting parameters as well as the maximum $Pe$ are summarized in table K.1 for both the semi-infinite and finite duct cases considered. If a different Laplace inversion method is used, only eq. K.42 would be of value in deriving an inequality for $\tau$ similar to eq. K.44. Eq. K.42 and K.44 should be regarded as approximate as the behavior close to the limit may not be very accurate. At early times (where eq. K.44 is not satisfied), one may find the solution proposed by Lighthill (1966) complementary to the current solution, since neither the outlet nor the wall boundaries are likely to have been felt by the transporting solute.

$$T < pPe^{q} \tag{K.42}$$

$$T = \frac{N_L \ln 2}{t} \tag{K.43}$$

$$\tau > \frac{N_L \ln 2}{pPe^{q}} \tag{K.44}$$

| | Infinite duct | | | Finite duct | | |
|---|---|---|---|---|---|---|
| Aspect ratio | **p** | **q** | **max Pe** | **p** | **q** | **max Pe** |
| $\kappa = 1$ | 196 | -0.67 | ~60 | 268 | -0.89 | ~20 |
| $\kappa = 4$ | - | - | - | 999 | -0.88 | ~40 |
| $\kappa = 16$ | - | - | - | 4507 | -1.0 | ~80 |

Table K.1: summary of exponent parameters in eq. K.42 and maximum Peclet numbers applicable for the infinite and finite duct cases considered in section K.4.6.

We conclude section K.4 with the following comment: among all the previous literature reviewed, we believe the only method that may have the potential to be applied to finite length ducts is that of Yu's (1976). To that end, the Fourier expansion (instead of the transform) of their infinite system of differential equations (in infinite unknowns) has to be taken, which makes the incorporation of general inlet/outlet conditions such as eq. K.7d and K.7e very difficult, if not unfeasible. The generality and ease-in-implementation of the current analysis makes it much simpler and thus more favorable to that of Yu's (1976), specifically because instead of dealing with an infinite array of differential equations one only deals with one (i.e. eq. K.20a). That said the current analysis has the aforementioned computational limit due to finite precision arithmetic of computers, making it inapplicable to very high Peclet numbers and very early times. For infinite ducts Yu's analysis does not have this issue (although increasingly more terms in their expansion is also required), which seems to be due to the orthogonality of the radial basis chosen (i.e. zero order Bessel functions of first kind, instead of polynomials chosen herein; see eq. K.13). Therefore, in order to bridge the gap to higher Peclet numbers, one either has to remove the computational limit of the current semi-analytical solution (through some sort of scaling of the linear system constructed from the inlet/outlet conditions given by eq. K.24-25, or perturbation analysis of eq. K.20a) or investigate the

possibility of extending Yu's work to finite-length ducts, both of which appear to be areas worth exploring further in the future.

## K.5 Applications

The problem of solute transport within cylinders is ubiquitous in many engineering and biomedical applications. Therefore the solution approach presented in section K.3 may find interest in a number of different fields, a few of which are mentioned in the following.

In nuclear science, high-temperature reactors of fission products are cooled using gaseous Helium. Small leaks of these products into the coolant are transported along cylindrical ducts, which then deposit onto the duct wall and undergo radioactive decay. An accurate estimate of these deposits would allow determining maintenance requirements to minimize any possible health hazards to the operators (Durkee, 1984). Durkee and Lee (1984) provide a solution for the estimation of the deposition profile, but the solution is limited due to the mathematical simplification made (i.e. eq. K.45 in their work). Specifically, their approach does not properly solve the transient problem at hand, but simply pre-multiplies the steady-state solution by a moving Heaviside function.

In the chemical and petroleum industry, internal pipeline corrosion is one example where our semi-analytical solution might be utilized. The presence of corrosive constituents such as hydrogen sulfide ($H_2S$), carbon dioxide ($CO_2$) and salts within the fluid could cause corrosion of the transporting pipeline. Under appropriate boundary conditions at the pipe wall and neglecting the slight change in pipe diameter due to corrosion, one may calculate the rate of consumption of these solutes at the wall and thus obtain an estimate of axial corrosion profiles. The solution may also find use in the field

of microfluidic design and experimentation (see Toepke and Beebe, 2006), where duct diameters are sufficiently small for Peclet numbers to fall within the computational limit of the solution (see section K.4.6).

In biomedical/biochemical sciences, intravenous delivery of drugs and bioactive agents into medium/slow flowing blood vessels such as arterioles and capillaries is a scenario in which the axial adsorption or accumulation of concentration near the endothelial cells may pose to be of important interest. Tangelder et al. (1986) studied velocity profiles within mesenteric arterioles of rabbits. A simple calculation shows that the Peclet regime within these arterioles is well within the range of the computational limit of our analysis (see section K.4.6). Furthermore, they show that the velocity profile within these arterioles is non-parabolic. In fact, the power-law velocity profile considered in section K.4.4 serves as a close approximation. Rugonyi (2008) developed a simplified model for estimating near-wall axial concentration profiles following drug release into blood vessels. Figure K.6c resembles qualitatively the profiles obtained by Rugonyi (2008) (although wall conditions and Peclet regimes differ). Note that the delivery of a finite amount of drug can be modeled by simply changing the inlet boundary condition given by eq. K.7d to eq. K.45. In eq. K.45, $\Pi$ is the rectangular function, $c_0$ is the amplitude of the pulse injected and $\varepsilon$ determines the duration of the injection period (i.e. $\tau = 0$ to $1/\varepsilon$).

$$c|_{\lambda=0} = c_0 \Pi(\varepsilon\tau - 0.5) \qquad \text{(K.45)}$$

## K.6 Conclusions

We derive a semi-analytical solution to the transient advection-diffusion-reaction equation in finite and semi-infinite ducts. The solution is applicable for general radial- and time-dependent inlet/outlet conditions, complex boundary conditions on the duct wall including adsorption and decay, and arbitrary velocity profiles of the transporting fluid. This is the first time (to the best of our knowledge) such a solution is proposed for finite length ducts. The only numerical step of the solution is the inverse Laplace transform in the time variable. The approach also produces fully analytical steady-state solutions due to the absence of the Laplace transform step. The solution was verified against computational fluid dynamics (CFD) simulations for various boundary conditions and velocity profiles (Newtonian and power-law), and in all cases good agreement was obtained. In some cases, small but noticeable differences between the CFD and semi-analytical solutions were observed (especially at larger Peclet numbers) which were ascribed to the incomplete convergence of the series given by eq. K.13. In these cases, addition of higher order terms resulted in numerical instabilities. These instabilities are a result of the order of magnitude differences arising within the internal numerics of the solution which leads to the compounding of round-off errors (due to finite precision arithmetic of computers). Therefore, although theoretically applicable to all regimes, the solution is computationally difficult at very high Peclet numbers and very early times. A convergence analysis was conducted to delineate the boundaries of this limit for two important cases: (a) a semi-infinite duct with Neumann wall conditions, and (b) a finite duct with Neumann wall and outlet conditions. For these cases, the minimum time and maximum Peclet number for which reliable results, devoid of said instabilities, could be obtained from the semi-analytical solution can be determined from eq. K.44 and table K.1. At early times (where eq. K.44 is not satisfied), one may find the solution proposed

by Lighthill (1966) complementary to the current solution, since neither the outlet nor the wall boundaries are likely to have been felt by the transporting solute.

The derivation of the solution involved using a new approach for solving two-dimensional partial differential equations (PDEs) with non-constant coefficients, which was inspired by the Frobenius (and power series) method for solving ordinary differential equations (ODEs). The approach converts the original variable coefficient PDE to a single infinite-order ODE with constant coefficients. Although applied here to problems in cylindrical coordinates, the method is applicable to Cartesian problems (e.g. flow through slits) as well. Thus, the method is suspected to provide solutions for a large class of PDEs of this type. The current solution may find applications in a number of engineering and/or biomedical fields, it can be used to verify numerical simulators and serve as a simple and easy-to-implement alternative where access to numerical simulators is not available.

# Bibliography


Acharya, R. C., M. I. J. Van Dijke, A. Leijnse, S. E. A. T. M. Van der Zee, and K. S. Sorbie. "Upscaling of tracer transport including convection and Brownian motion using a 3D network model." *Developments in Water Science* 55 (2004): 115-125.

Acharya, R. C., S. E. A. T. M. Van der Zee, and A. Leijnse. "Transport modeling of nonlinearly adsorbing solutes in physically heterogeneous pore networks." *Water resources research* 41, no. 2 (2005).

Acharya, R. C., M. I. J. Van Dijke, K. S. Sorbie, S. E. A. T. M. Van der Zee, and A. Leijnse. "Quantification of longitudinal dispersion by upscaling Brownian motion of tracer displacement in a 3D pore-scale network model." *Advances in water resources* 30, no. 2 (2007a): 199-213.

Acharya, R. C., S. E. A. T. M. Van der Zee, and A. Leijnse. "Approaches for modeling longitudinal dispersion in pore-networks." *Advances in water resources* 30, no. 2 (2007b): 261-272.

Al-Gharbi, Mohammed S., and Martin J. Blunt. "Dynamic network modeling of two-phase drainage in porous media." *Physical Review E* 71, no. 1 (2005): 016308.

Algive, Lionnel, Samir Bekri, and Olga Vizika-kavvadias. "Reactive pore network modeling dedicated to the determination of the petrophysical property changes while injecting $CO_2$." In *SPE Annual Technical conference and Exhibition*. Society of Petroleum Engineers, (2009).

Algive, Lionnel, Samir Bekri, and Olga Vizika. "Pore-network modeling dedicated to the determination of the petrophysical-property changes in the presence of reactive fluid." *SPE Journal* 15, no. 03 (2010): 618-633.

Algive, Lionnel, Samir Békri, Fadi H. Nader, Olivier Lerat, and Olga Vizika. "Impact of diagenetic alterations on the petrophysical and multiphase flow properties of carbonate rocks using a reactive pore network modeling approach." *Oil & Gas Science and Technology–Revue d'IFP Energies nouvelles* 67, no. 1 (2012): 147-160.

Al-Raoush, Riyadh, Karsten Thompson, and Clinton S. Willson. "Comparison of network generation techniques for unconsolidated porous media." *Soil Science Society of America Journal* 67, no. 6 (2003): 1687-1700.

Alvarado, Vladimir, Howard Ted Davis, and L. E. Scriven. "Effects of pore-level reaction on dispersion in porous media." *Chemical engineering science* 52, no. 17 (1997): 2865-2881.

Ananthakrishnan, V., W. N. Gill, and Allen J. Barduhn. "Laminar dispersion in capillaries: Part I. Mathematical analysis." *AIChE Journal* 11, no. 6 (1965): 1063-1072.

Anderson, John David, “Computational fluid dynamics.” Vol. 206. New York: McGraw-Hill, (1995).

Arbogast, Todd, Lawrence C. Cowsar, Mary F. Wheeler, and Ivan Yotov. "Mixed finite element methods on nonmatching multiblock grids." *SIAM Journal on Numerical Analysis* 37, no. 4 (2000): 1295-1315.

Arbogast, Todd, Gergina Pencheva, Mary F. Wheeler, and Ivan Yotov. "A multiscale mortar mixed finite element method." *Multiscale Modeling & Simulation* 6, no. 1 (2007): 319-346.

Aris, Rutherford. "On the dispersion of a solute in a fluid flowing through a tube." *Proceedings of the Royal Society of London. Series A. Mathematical and Physical Sciences* 235, no. 1200 (1956): 67-77.

Aris, Rutherford, and Neal R. Amundson. "Some remarks on longitudinal mixing or diffusion in fixed beds." *AIChE Journal* 3, no. 2 (1957): 280-282.

Balhoff, Matthew. "Modeling the flow of non-Newtonian fluids in packed beds at the pore scale." PhD dissertation., Louisiana State University, (2005).

Balhoff, Matthew T., Karsten E. Thompson, and Martin Hjortsø. "Coupling pore-scale networks to continuum-scale models of porous media." *Computers & Geosciences* 33, no. 3 (2007): 393-410.

Balhoff, Matthew T., Sunil G. Thomas, and Mary F. Wheeler. "Mortar coupling and upscaling of pore-scale models." *Computational Geosciences* 12, no. 1 (2008): 15-27.

Balhoff, Matthew T., and Mary F. Wheeler. "A predictive pore-scale model for non-Darcy flow in porous media." *SPE Journal* 14, no. 04 (2009): 579-587.

Balhoff, Matthew, Daniel Sanchez-Rivera, Alan Kwok, Yashar Mehmani, and Maša Prodanović. "Numerical algorithms for network modeling of yield stress and other non-Newtonian fluids in porous media." *Transport in porous media* 93, no. 3 (2012): 363-379.

Bakke, Stig, and Pål-Eric Øren. "3-D pore-scale modelling of sandstones and flow simulations in the pore networks." *SPE JOURNAL-RICHARDSON*- 2 (1997): 136-149.

Barron, Randall F., Xianming Wang, Timothy A. Ameel, and Robert O. Warrington. "The Graetz problem extended to slip-flow." *International Journal of Heat and Mass Transfer* 40, no. 8 (1997): 1817-1823.

Battiato, Ilenia, Daniel M. Tartakovsky, Alexandre M. Tartakovsky, and T. Scheibe. "On breakdown of macroscopic models of mixing-controlled heterogeneous reactions in porous media." *Advances in water resources* 32, no. 11 (2009): 1664-1673.

Battiato, I., and D. M. Tartakovsky. "Applicability regimes for macroscopic models of reactive transport in porous media." *Journal of contaminant hydrology* 120 (2011): 18-26.

Battiato, Ilenia, Daniel M. Tartakovsky, Alexandre M. Tartakovsky, and Timothy D. Scheibe. "Hybrid models of reactive transport in porous and fractured media." *Advances in Water Resources* 34, no. 9 (2011): 1140-1150.

Beckingham, L. E., C. A. Peters, W. Um, K. W. Jones, and W. B. Lindquist. "2D and 3D imaging resolution trade-offs in quantifying pore throats for prediction of permeability." *Advances in Water Resources* 62 (2013): 1-12.

Berkowitz, Brian, and Robert P. Ewing. "Percolation theory and network modeling applications in soil physics." *Surveys in Geophysics* 19, no. 1 (1998): 23-72.

Berkowitz, Brian, Curt Naumann, and Leslie Smith. "Mass transfer at fracture intersections: An evaluation of mixing models." *Water resources research* 30, no. 6 (1994): 1765-1773.

Bernardi, Christine. "A new nonconforming approach to domain decomposition: the mortar element method." *Nonliner Partial Differential Equations and Their Applications* (1994).

Bijeljic, Branko, Ann H. Muggeridge, and Martin J. Blunt. "Pore-scale modeling of longitudinal dispersion." *Water Resources Research* 40, no. 11 (2004).

Bijeljic, Branko, and Martin Julian Blunt. "A Physically-Based Description of Dispersion in Porous Media." In *SPE Annual Technical Conference and Exhibition*. Society of Petroleum Engineers, (2006).

Bijeljic, Branko, and Martin J. Blunt. "Pore-scale modeling of transverse dispersion in porous media." *Water Resources Research* 43, no. 12 (2007).

Blunt, Martin J. "Flow in porous media—pore-network models and multiphase flow." *Current opinion in colloid & interface science* 6, no. 3 (2001): 197-207.

Bons, Paul Dirk, Boudewijn Philip van Milligen, and Philipp Blum. "A general unified expression for solute and heat dispersion in homogeneous porous media." *Water Resources Research* 49, no. 10 (2013): 6166-6178.

Boso, Francesca, and Ilenia Battiato. "Homogenizability conditions for multicomponent reactive transport." *Advances in Water Resources* 62 (2013): 254-265.

Brenner, Howard. "The diffusion model of longitudinal mixing in beds of finite length. Numerical values." *Chemical Engineering Science* 17, no. 4 (1962): 229-243.

Bruderer, Céline, and Yves Bernabé. "Network modeling of dispersion: Transition from Taylor dispersion in homogeneous networks to mechanical dispersion in very heterogeneous ones." *Water resources research* 37, no. 4 (2001): 897-908.

Bryant, Steven, and Martin Blunt. "Prediction of relative permeability in simple porous media." *Physical Review A* 46, no. 4 (1992): 2004.

Bryant, Steven L., David W. Mellor, and Christopher A. Cade. "Physically representative network models of transport in porous media." *AIChE Journal* 39, no. 3 (1993a): 387-396.

Bryant, Steven, Christopher Cade, and David Mellor. "Permeability prediction from geologic models." *AAPG Bulletin* 77, no. 8 (1993b): 1338-1350.

Bryntesson, L. Mattias. "Pore network modelling of the behaviour of a solute in chromatography media: transient and steady-state diffusion properties." *Journal of Chromatography A* 945, no. 1 (2002): 103-115.

Burnside, N. M., B. Dockrill, Z. K. Shipton, and R. M. Ellam. "Dating and Constraining Leakage Rates from a Natural Analogue for CO2 Storage–The Little Grand Wash and Salt Wash Fault." In *Fault and Top Seals: from Pore to Basin Scale*. (2009).

Celia, Michael A., Paul C. Reeves, and Lin A. Ferrand. "Recent advances in pore scale models for multiphase flow in porous media." *Reviews of Geophysics* 33, no. S2 (1995): 1049-1057.

Chen, Shiyi, and Gary D. Doolen. "Lattice Boltzmann method for fluid flows." *Annual review of fluid mechanics* 30, no. 1 (1998): 329-364.

Cheng, Alexander HD, Paston Sidauruk, and Younane Abousleiman. "Approximate inversion of the Laplace transform." *Mathematica Journal* 4, no. 2 (1994): 76-82.

Chomsurin, Cheema, and Charles J. Werth. "Analysis of pore-scale nonaqueous phase liquid dissolution in etched silicon pore networks." *Water resources research* 39, no. 9 (2003).

Chu, Jay, Björn Engquist, Maša Prodanovic, and Richard Tsai. "A multiscale method coupling network and continuum models in porous media I: Steady-state single phase flow." *Multiscale Modeling & Simulation* 10, no. 2 (2012): 515-549.

Chu, Jay, Björn Engquist, Maša Prodanović, and Richard Tsai. "A multiscale method coupling network and continuum models in porous media II—Single-and two-phase flows." In *Advances in Applied Mathematics, Modeling, and Computational Science*, pp. 161-185. Springer US, (2013).

Chun, D. H. "Distribution of concentration in flow through a circular pipe." *International Journal of Heat and Mass Transfer* 13, no. 4 (1970): 717-723.

Coelho, D., J-F. Thovert, and P. M. Adler. "Geometrical and transport properties of random packings of spheres and aspherical particles." *Physical Review E* 55, no. 2 (1997): 1959.

Danckwerts, P. V. "Continuous flow systems: distribution of residence times." *Chemical Engineering Science* 2, no. 1 (1953): 1-13.

De Arcangelis, Lucilla, Joel Koplik, Sidney Redner, and David Wilkinson. "Hydrodynamic dispersion in network models of porous media." *Physical review letters* 57, no. 8 (1986): 996.

Delgado, J. M. P. Q. "A critical review of dispersion in packed beds." *Heat and mass transfer* 42, no. 4 (2006): 279-310.

Dockrill, Ben, and Zoe K. Shipton. "Structural controls on leakage from a natural $CO_2$ geologic storage site: Central Utah, USA." *Journal of Structural Geology* 32, no. 11 (2010): 1768-1782.

Dong, Hu, and Martin J. Blunt. "Pore-network extraction from micro-computerized-tomography images." *Physical review E* 80, no. 3 (2009): 036307.

Duffy, Dean G., "Transform methods for solving partial differential equations." CRC press, (2004).

Durkee Jr, J. W., and C. E. Lee. "An analytic benchmark solution to the linear, time-dependent isothermal laminar flow fission-product plateout problem." *Annals of Nuclear Energy* 11, no. 7 (1984): 337-345.

Durst, F., S. Ray, B. Ünsal, and O. A. Bayoumi. "The development lengths of laminar pipe and channel flows." *Journal of fluids engineering* 127, no. 6 (2005): 1154-1160.

Edwards, D. A., M. Shapiro, H. Brenner, and M. Shapira. "Dispersion of inert solutes in spatially periodic, two-dimensional model porous media." *Transport in Porous Media* 6, no. 4 (1991): 337-358.

Eichhubl, Peter, and James R. Boles. "Rates of fluid flow in fault systems; evidence for episodic rapid fluid flow in the Miocene Monterey Formation, coastal California." *American Journal of Science* 300, no. 7 (2000): 571-600.

Fatt, Irving. "The network model of porous media I. Capillary pressure characteristics." (1956a).

Fatt, I. "The network model of porous media. 2. Dynamic properties of a single size tube network." *TRANSACTIONS OF THE AMERICAN INSTITUTE OF MINING AND METALLURGICAL ENGINEERS* 207, no. 7 (1956b): 160-163.

Fatt, I. "The network model of porous media III. Dynamic properties of networks with tube radius distribution." *Trans. AIME* 207 (1956c): 164-181.

Finney, John Leslie. "Random packings and the structure of the liquid state." University of London (United Kingdom), PhD dissertation, (1968).

Fischer, Ulrich, and Michael A. Celia. "Prediction of relative and absolute permeabilities for gas and water from soil water retention curves using a pore-scale network model." *Water Resources Research* 35, no. 4 (1999): 1089-1100.

Fredd, Christopher N., and H. Scott Fogler. "Influence of transport and reaction on wormhole formation in porous media." *AIChE journal* 44, no. 9 (1998): 1933-1949.

Furrer, Hansjörg. "Über die Konvergenz zentrierter und normierter Summen von Zufallsvariablen und ihre Auswirkungen auf die Risikomessung." (2012).

Fried, J. J., and M. A. Combarnous. "Dispersion in porous media." *Adv. Hydrosci* 7, no. 169 (1971).

Gani, M. Royhan, and J. P. Bhattacharya. "Bed-scale facies architecture of an ancient delta lobe deposit of the wall creek member, Central Wyoming, USA." In *Proceedings of the AAPG Annual Convention & Exhibition, Salt Lake City, UT*, pp. 11-14. (2003).

Ganis, B., M. Juntunen, G. Pencheva, M. F. Wheeler, and I. Yotov. "A Global Jacobian Method for Simultaneous Solution of Mortar and Subdomain Variables in Nonlinear Porous Media Flow." (2012): ICES Report 12-46, The Institute for Computational Engineering and Sciences, The University of Texas at Austin.

Gill, William N., and V. Ananthakrishnan. "Laminar dispersion in capillaries: Part II. Effect of inlet boundary conditions and turner type of system capacitance." *AIChE Journal* 12, no. 5 (1966): 906-915.

Gill, William N., and V. Ananthakrishnan. "Laminar dispersion in capillaries: Part IV. The slug stimulus." *AIChE Journal* 13, no. 4 (1967): 801-807.

Gill, W. N., and R. Sankarasubramanian. "Exact analysis of unsteady convective diffusion." *Proceedings of the Royal Society of London. A. Mathematical and Physical Sciences* 316, no. 1526 (1970): 341-350.

Gill, W. N., and R. Sankarasubramanian, Discussion: "On laminar dispersion for flow through round tubes", *J. Appl. Mech.* 47 (4) (1980) 975-976, http://dx.doi.org/10.1115/1.3153832 (J.S. Yu, ASME J. Appl. Mech. 46 (1979) 750-756).

Graetz, von L. "Über die wärmeleitungsfähigkeit von flüssigkeiten." *Annalen der Physik* 254, no. 1 (1882): 79-94.

Graetz, von L. "Über die wärmeleitungsfähigkeit von flüssigkeiten." *Annalen der Physik* 261, no. 7 (1885): 337-357.

Hoefner, M. L., and H. Scott Fogler. "Pore evolution and channel formation during flow and reaction in porous media." *AIChE Journal* 34, no. 1 (1988): 45-54.

Hunt, Bruce. "Diffusion in laminar pipe flow." *International Journal of Heat and Mass Transfer* 20, no. 4 (1977): 393-401.

Jeong, Ho-Eyoul, and Jae-Tack Jeong. "Extended Graetz problem including streamwise conduction and viscous dissipation in microchannel." *International Journal of Heat and Mass Transfer* 49, no. 13 (2006): 2151-2157.

Jha, R. K. "Pore level investigation of dispersivity." *MS Thesis*, The University of Texas at Austin, (May, 2005).

Jha, Raman K., Steven Bryant, and Larry W. Lake. "Effect of diffusion on dispersion." *SPE Journal* 16, no. 01 (2011): 65-77.

Jodrey, W. S., and E. M. Tory. "Computer simulation of close random packing of equal spheres." *Physical review A* 32, no. 4 (1985): 2347.

Joekar-Niasar, Vahid. "The Immiscibles, Capillarity effects in porous media, pore-network modeling.", (2010).

Joekar-Niasar, V., S. Majid Hassanizadeh, and H. K. Dahle. "Non-equilibrium effects in capillarity and interfacial area in two-phase flow: dynamic pore-network modelling." *Journal of Fluid Mechanics* 655 (2010): 38-71.

Jourak, Amir, J. Gunnar I. Hellström, T. Staffan Lundström, and Vilnis Frishfelds. "Numerical derivation of dispersion coefficients for flow through three-dimensional randomly packed beds of monodisperse spheres." *AIChE Journal* 60, no. 2 (2014): 749-761.

Kandhai, Drona, D. Hlushkou, Alfons G. Hoekstra, Peter MA Sloot, H. Van As, and U. Tallarek. "Influence of stagnant zones on transient and asymptotic dispersion in macroscopically homogeneous porous media." *Physical review letters* 88, no. 23 (2002): 234501.

Kechagia, Persefoni E., Ioannis N. Tsimpanogiannis, Yanis C. Yortsos, and Peter C. Lichtner. "On the upscaling of reaction-transport processes in porous media with fast or finite kinetics." *Chemical engineering science* 57, no. 13 (2002): 2565-2577.

Khrapitchev, A. A., and P. T. Callaghan. "Reversible and irreversible dispersion in a porous medium." *Physics of Fluids (1994-present)* 15, no. 9 (2003): 2649-2660.

Kim, D., C. A. Peters, and W. B. Lindquist. "Upscaling geochemical reaction rates accompanying acidic CO2-saturated brine flow in sandstone aquifers." *Water Resources Research* 47, no. 1 (2011).

Kim, D., and W. B. Lindquist. "Dependence of pore-to-core up-scaled reaction rate on flow rate in porous media." *Transport in porous media* 94, no. 2 (2012): 555-569.

Koch, Donald L., and John F. Brady. "Dispersion in fixed beds." *Journal of Fluid Mechanics* 154 (1985): 399-427.

Köhne, J. Maximilian, Steffen Schlüter, and Hans-Jörg Vogel. "Predicting solute transport in structured soil using pore network models." *Vadose Zone Journal* 10, no. 3 (2011): 1082-1096.

Koplik, J., and T. J. Lasseter. "Two-phase flow in random network models of porous media." *Society of Petroleum Engineers Journal* 25, no. 1 (1985): 89-100.

Koplik, J., S. Redner, and D. Wilkinson. "Transport and dispersion in random networks with percolation disorder." *Physical Review A* 37, no. 7 (1988): 2619.

Korenaga, Takashi, Fenghua Shen, and Teruo Takahashi. "An experimental study of the dispersion in laminar tube flow." *AIChE journal* 35, no. 8 (1989): 1395-1398.

Lahjomri, J., and A. Oubarra. "Analytical solution of the Graetz problem with axial conduction." *Journal of heat transfer* 121, no. 4 (1999): 1078-1083.

Li, Li, Catherine A. Peters, and Michael A. Celia. "Upscaling geochemical reaction rates using pore-scale network modeling." *Advances in water resources* 29, no. 9 (2006): 1351-1370.

Li, Li, Catherine A. Peters, and Michael A. Celia. "Applicability of averaged concentrations in determining geochemical reaction rates in heterogeneous porous media." *American Journal of Science* 307, no. 10 (2007a): 1146-1166.

Li, L., C. A. Peters, and M. A. Celia. "Effects of mineral spatial distribution on reaction rates in porous media." *Water resources research* 43, no. 1 (2007b).

Li, Shuai, Amir Raoof, and Ruud Schotting. "Solute dispersion under electric and pressure driven flows; pore scale processes." *Journal of Hydrology* 517 (2014): 1107-1113.

Lighthill, M. J. "Initial development of diffusion in Poiseuille flow." *IMA Journal of Applied Mathematics* 2, no. 1 (1966): 97-108.

Lindquist, W. Brent, Sang-Moon Lee, David A. Coker, Keith W. Jones, and Per Spanne. "Medial axis analysis of void structure in three-dimensional tomographic images of porous media." *Journal of Geophysical Research: Solid Earth (1978–2012)* 101, no. B4 (1996): 8297-8310.

Lindquist, W. B., and A. Venkatarangan. "Investigating 3D geometry of porous media from high resolution images." *Physics and Chemistry of the Earth, Part A: Solid Earth and Geodesy* 24, no. 7 (1999): 593-599.

Liou, Ching-Tien, and Feng-Sheng Wang. "Solutions to the extended Graetz problem for a power-model fluid with viscous dissipation and different entrance boundary conditions." *Numerical heat transfer* 17, no. 1 (1990): 91-108.

Lopez, Xavier, Per H. Valvatne, and Martin J. Blunt. "Predictive network modeling of single-phase non-Newtonian flow in porous media." *Journal of colloid and interface science* 264, no. 1 (2003): 256-265.

Lu, Chuan, and Yannis C. Yortsos. "Dynamics of forward filtration combustion at the pore-network level." *AIChE journal* 51, no. 4 (2005): 1279-1296.

Maier, Robert S., Daniel M. Kroll, Robert S. Bernard, Stacy E. Howington, John F. Peters, and H. Ted Davis. "Pore-scale simulation of dispersion." *Physics of Fluids (1994-present)* 12, no. 8 (2000): 2065-2079.

Maier, Robert S., Daniel M. Kroll, Robert S. Bernard, Stacy E. Howington, John F. Peters, and H. Ted Davis. "Hydrodynamic dispersion in confined packed beds." *Physics of Fluids (1994-present)* 15, no. 12 (2003): 3795-3815.

Martins, António A., Paulo E. Laranjeira, Carlos Henrique Braga, and Teresa M. Mata. "MODELING OF TRANSPORT PHENOMENA IN POROUS MEDIA USING NETWORK MODELS.", *Progress in Porous Media Research*, (2009).

Mohanty, K. K., H. T. Davis, and L. E. Scriven. "Physics of oil entrapment in water-wet rock." *SPE Reservoir Engineering* 2, no. 01 (1987): 113-128.

Molins, Sergi, David Trebotich, Carl I. Steefel, and Chaopeng Shen. "An investigation of the effect of pore scale flow on average geochemical reaction rates using direct numerical simulation." *Water Resources Research* 48, no. 3 (2012).

Monaghan, Joe J. "Smoothed particle hydrodynamics." *Annual review of astronomy and astrophysics* 30 (1992): 543-574.

Moore, Joseph, Michael Adams, Richard Allis, Susan Lutz, and Steven Rauzi. "Mineralogical and geochemical consequences of the long-term presence of $CO_2$ in natural reservoirs: An example from the Springerville–St. Johns Field, Arizona, and New Mexico, USA." *Chemical Geology* 217, no. 3 (2005): 365-385.

Moroni, Monica, and John H. Cushman. "Three-dimensional particle tracking velocimetry studies of the transition from pore dispersion to Fickian Dispersion for homogeneous porous media." *Water Resources Research* 37, no. 4 (2001): 873-884.

Mostaghimi, Peyman, Branko Bijeljic, and Martin Julian Blunt. "Simulation of flow and dispersion on pore-space images." In *SPE Annual Technical Conference and Exhibition, Italy. doi*, vol. 10. (2012).

Nauman, E. Bruce, "Chemical reactor design, optimization, and scaleup." John Wiley & Sons, (2008).

Ng, Edward W., and Murray Geller. "A table of integrals of the error functions." *Journal of Research of the National Bureau of Standards B* 73 (1969): 1-20.

Nigam, K. D. P., and Alok K. Saxena. "Residence time distribution in straight and curved tubes." *Encyclopedia of fluid mechanics* 1 (1986): 675-762.

Nitsche, Johannes M., Hou-Chien Chang, Paul A. Weber, and Bruce J. Nicholson. "A Transient Diffusion Model Yields Unitary Gap Junctional Permeabilities from

Images of Cell-to-Cell Fluorescent Dye Transfer Between Xenopus Oocytes." *Biophysical journal* 86, no. 4 (2004): 2058-2077.

Nogues, Juan P., Jeffrey P. Fitts, Michael A. Celia, and Catherine A. Peters. "Permeability evolution due to dissolution and precipitation of carbonates using reactive transport modeling in pore networks." *Water Resources Research* 49, no. 9 (2013): 6006-6021.

Nunge, Richard J., and William N. Gill. "Mechanisms affecting dispersion and miscible displacement." *Industrial & Engineering Chemistry* 61, no. 9 (1969): 33-49.

Oostrom, M., Y. Mehmani, P. Romero-Gomez, Y. Tang, H. Liu, H. Yoon, Q. Kang et al. "Pore-scale and continuum simulations of solute transport micromodel benchmark experiments." *Computational Geosciences* (2014): 1-23.

Øren, Pål-Eric, and Stig Bakke. "Process based reconstruction of sandstones and prediction of transport properties." *Transport in Porous Media* 46, no. 2-3 (2002): 311-343.

Pearce, J., I. Czernichowski-Lauriol, S. Lombardi, S. Brune, A. Nador, J. Baker, H. Pauwels, G. Hatziyannis, S. Beaubien, and E. Faber. "A review of natural $CO_2$ accumulations in Europe as analogues for geological sequestration." *Geological Society, London, Special Publications* 233, no. 1 (2004): 29-41.

Perkins, T. K., and O. C. Johnston. "A review of diffusion and dispersion in porous media." *Society of Petroleum Engineers Journal* 3, no. 01 (1963): 70-84.

Peszyńska, Małgorzata, Mary F. Wheeler, and Ivan Yotov. "Mortar upscaling for multiphase flow in porous media." *Computational Geosciences* 6, no. 1 (2002): 73-100.

Peszynska, Malgorzata. "Mortar adaptivity in mixed methods for flow in porous media." *Int. J. Numer. Anal. Model* 2, no. 3 (2005): 241-282.

Ovaysi, Saeed, and Mohammad Piri. "Pore-scale modeling of dispersion in disordered porous media." *Journal of contaminant hydrology* 124, no. 1 (2011): 68-81.

Park, Young-Jin, and Kang-Kun Lee. "Analytical solutions for solute transfer characteristics at continuous fracture junctions." *Water resources research* 35, no. 5 (1999): 1531-1537.

Park, Young-Jin, Kang-Kun Lee, and Brian Berkowitz. "Effects of junction transfer characteristics on transport in fracture networks." *Water Resources Research* 37, no. 4 (2001a): 909-923.

Park, Young-Jin, Jean-Raynald Dreuzy, Kang-Kun Lee, and Brian Berkowitz. "Transport and intersection mixing in random fracture networks with power law length distributions." *Water Resources Research* 37, no. 10 (2001b): 2493-2501.

Parker, J. C., and M. Th Genuchten. "Flux-averaged and volume-averaged concentrations in continuum approaches to solute transport." *Water Resources Research* 20, no. 7 (1984): 866-872.

Pegoraro, Paula R., Mariana Marangoni, and Jorge AW Gut. "Residence Time Distribution Models Derived from Non-Ideal Laminar Velocity Profiles in Tubes." *Chemical Engineering & Technology* 35, no. 9 (2012): 1593-1603.

Petersen, Robert Thomas. "Pore-scale modeling of the impact of surrounding flow behavior on multiphase flow properties.", Master's Thesis, (2009).

Pfannkuch, Hans-Olaf. "Contribution à l'étude des déplacements de fluides miscibles dans un milieu poreux." Revue de l'Institut français du pétrole et Annales des combustibles liquides, (1963).

Picard, Guillemette, and Kurt Frey. "Method for modeling transport of particles in realistic porous networks: Application to the computation of NMR flow propagators." *Physical Review e* 75, no. 6 (2007): 066311.

Piri, Mohammad, and Martin J. Blunt. "Three-dimensional mixed-wet random pore-scale network modeling of two-and three-phase flow in porous media. I. Model description." *Physical Review E* 71, no. 2 (2005): 026301.

Prat, Marc. "Recent advances in pore-scale models for drying of porous media." *Chemical engineering journal* 86, no. 1 (2002): 153-164.

Prodanović, M., W. B. Lindquist, and R. S. Seright. "Porous structure and fluid partitioning in polyethylene cores from 3D X-ray microtomographic imaging." *Journal of Colloid and Interface Science* 298, no. 1 (2006): 282-297.

Raoof, A., H. M. Nick, S. M. Hassanizadeh, and C. J. Spiers. "PoreFlow: A complex pore-network model for simulation of reactive transport in variably saturated porous media." *Computers & Geosciences* 61 (2013): 160-174.

Rhodes, Matthew E., and Martin J. Blunt. "An exact particle tracking algorithm for advective-dispersive transport in networks with complete mixing at nodes." *Water resources research* 42, no. 4 (2006).

Rhodes, Matthew, Branko Bijeljic, and Martin J. Blunt. "A rigorous pore-to-field-scale simulation method for single-phase flow based on continuous-time random walks." *SPE Journal* 14, no. 01 (2009): 88-94.

Rugonyi, Sandra. "Effect of blood flow on near-the-wall mass transport of drugs and other bioactive agents: A simple formula to estimate boundary layer concentrations." *Journal of biomechanical engineering* 130, no. 2 (2008): 021010.

Saad, Yousef, "Iterative methods for sparse linear systems.", Siam, (2003).

Saffman, P. G. "A theory of dispersion in a porous medium." *Journal of Fluid Mechanics* 6, no. 03 (1959): 321-349.

Sahimi, Muhammad, Barry D. Hughes, L. E. Scriven, and H. Ted Davis. "Dispersion in flow through porous media—I. One-phase flow." *Chemical engineering science* 41, no. 8 (1986): 2103-2122.

Sahimi, Muhammad, "Flow and transport in porous media and fractured rock: from classical methods to modern approaches.", John Wiley & Sons, (2012).

Scheibe, Timothy D., Alexandre M. Tartakovsky, Daniel M. Tartakovsky, George D. Redden, and Paul Meakin. "Hybrid numerical methods for multiscale simulations of subsurface biogeochemical processes." In *Journal of Physics: Conference Series*, vol. 78, no. 1, p. 012063. IOP Publishing, (2007).

Seymour, Joseph D., and Paul T. Callaghan. "Generalized approach to NMR analysis of flow and dispersion in porous media." *AIChE Journal* 43, no. 8 (1997): 2096-2111.

Shankar, A., and A. M. Lenhoff. "Dispersion in laminar flow in short tubes." *AIChE journal* 35, no. 12 (1989): 2048-2052.

Sheppard, A. P., R. M. Sok, H. Averdunk, V. B. Robins, and A. Ghous. "Analysis of rock microstructure using high-resolution X-ray tomography." In *Proceedings of the International Symposium of the Society of Core Analysts*. (2006).

Shipton, Zoe K., James P. Evans, D. Kirschner, Peter T. Kolesar, Anthony P. Williams, and Jason Heath. "Analysis of CO2 leakage through 'low-permeability' faults from natural reservoirs in the Colorado Plateau, east-central Utah." *Geological Society, London, Special Publications* 233, no. 1 (2004): 43-58.

Silin, Dmitriy, and Tad Patzek. "Pore space morphology analysis using maximal inscribed spheres." *Physica A: Statistical Mechanics and its Applications* 371, no. 2 (2006): 336-360.

Sorbie, K. S., and P. J. Clifford. "The inclusion of molecular diffusion effects in the network modelling of hydrodynamic dispersion in porous media." *Chemical engineering science* 46, no. 10 (1991): 2525-2542.

Stehfest, Harald. "Algorithm 368: Numerical inversion of Laplace transforms [D5]." *Communications of the ACM* 13, no. 1 (1970): 47-49.

Stöhr, Michael. "Analysis of flow and transport in refractive index matched porous media." (2003).

Suchomel, Brian J., Benito M. Chen, and Myron B. Allen. "Macroscale properties of porous media from a network model of biofilm processes." *Transport in porous media* 31, no. 1 (1998a): 39-66.

Suchomel, Brian J., Benito M. Chen, and Myron B. Allen III. "Network model of flow, transport and biofilm effects in porous media." *Transport in Porous Media* 30, no. 1 (1998b): 1-23.

Sun, Tie, Yashar Mehmani, Jaideep Bhagmane, and Matthew Thomas Balhoff. "Pore to continuum upscaling of permeability in heterogeneous porous media using mortars." *International Journal of Oil, Gas and Coal Technology* 5, no. 2 (2012a): 249-266.

Sun, Tie, Yashar Mehmani, and Matthew T. Balhoff. "Hybrid multiscale modeling through direct substitution of pore-scale models into near-well reservoir simulators." *Energy & Fuels* 26, no. 9 (2012b): 5828-5836.

Tangelder, Geert Jan, Dick W. Slaaf, A. M. Muijtjens, Theo Arts, M. G. Oude Egbrink, and Robert S. Reneman. "Velocity profiles of blood platelets and red blood cells flowing in arterioles of the rabbit mesentery." *Circulation Research* 59, no. 5 (1986): 505-514.

Tartakovsky, Alexandre M., Daniel M. Tartakovsky, Timothy D. Scheibe, and Paul Meakin. "Hybrid simulations of reaction-diffusion systems in porous media." *SIAM Journal on Scientific Computing* 30, no. 6 (2008a): 2799-2816.

Tartakovsky, Alexandre M., G. Redden, Peter C. Lichtner, Timothy D. Scheibe, and Paul Meakin. "Mixing-induced precipitation: Experimental study and multiscale numerical analysis." *Water Resources Research* 44, no. 6 (2008b).

Taylor, Geoffrey. "Dispersion of soluble matter in solvent flowing slowly through a tube." *Proceedings of the Royal Society of London. Series A. Mathematical and Physical Sciences* 219, no. 1137 (1953): 186-203.

Thane, Cynthia Gabrielle, “Geometry and topology of model sediments and their influence on sediment properties.”, Master’s Thesis, (2006).

Thauvin, F., and K. K. Mohanty. "Network modeling of non-Darcy flow through porous media." *Transport in Porous Media* 31, no. 1 (1998): 19-37.

Thompson, Karsten E., Clinton S. Willson, Christopher D. White, Stephanie Nyman, Janok P. Bhattacharya, and Allen H. Reed, “Application of a new grain-based reconstruction algorithm to microtomography images for quantitative characterization and flow modeling.”, No. NRL/JA/7430-07-13. NAVAL RESEARCH LAB STENNIS SPACE CENTER MS MARINE GEOACOUSTICS DIV, (2008).

Thovert, J. F., J. Salles, and P. M. Adler. "Computerized characterization of the geometry of real porous media: their discretization, analysis and interpretation." *Journal of microscopy* 170, no. 1 (1993): 65-79.

Toepke, Michael W., and David J. Beebe. "PDMS absorption of small molecules and consequences in microfluidic applications." *Lab Chip* 6, no. 12 (2006): 1484-1486.

Tseng, C. M., and R. W. Besant. "Transient heat and mass transfer in fully developed laminar tube flows." *International Journal of Heat and Mass Transfer* 15, no. 2 (1972): 203-215.

Van Genuchten, M. Th, and W. J. Alves, "Analytical solutions of the one-dimensional convective-dispersive solute transport equation.", No. 157268. United States Department of Agriculture, Economic Research Service, (1982).

van Milligen, B. Ph, and Paul D. Bons. "Analytical model for tracer dispersion in porous media." *Physical Review E* 85, no. 1 (2012): 011306.

van Milligen, B. Ph, and P. D. Bons. "Simplified numerical model for clarifying scaling behavior in the intermediate dispersion regime in homogeneous porous media." *Computer Physics Communications* (2014).

Varloteaux, Clément, Samir Békri, and Pierre M. Adler. "Pore network modelling to determine the transport properties in presence of a reactive fluid: From pore to reservoir scale." *Advances in Water Resources* 53 (2013): 87-100.

Wheeler, Mary F., Todd Arbogast, Steven Bryant, Joe Eaton, Q. Lu, Malgorzata Peszynska, and Ivan Yotov. "A parallel multiblock/multidomain approach for reservoir simulation." In *Proceedings of the 15th Reservoir Simulation Symposium*, no. 51884, pp. 51-61. (1999).

Wildenschild, Dorthe, and Adrian P. Sheppard. "X-ray imaging and analysis techniques for quantifying pore-scale structure and processes in subsurface porous medium systems." *Advances in Water Resources* 51 (2013): 217-246.

Willingham, Thomas W., Charles J. Werth, and Albert J. Valocchi. "Evaluation of the effects of porous media structure on mixing-controlled reactions using pore-scale modeling and micromodel experiments." *Environmental science & technology* 42, no. 9 (2008): 3185-3193.

Wood, Brian D. "Inertial effects in dispersion in porous media." *Water resources research* 43, no. 12 (2007).

Wörner, Martin. "Approximate residence time distribution of fully develop laminar flow in a straight rectangular channel." *Chemical Engineering Science* 65, no. 11 (2010): 3499-3507.

Yang, Xiaofan, Timothy D. Scheibe, Marshall C. Richmond, William A. Perkins, Sarah J. Vogt, Sarah L. Codd, Joseph D. Seymour, and Matthew I. McKinley. "Direct numerical simulation of pore-scale flow in a bead pack: Comparison with magnetic resonance imaging observations." *Advances in Water Resources* 54 (2013): 228-241.

Yortsos, Y. C., and M. Sharma. "Application of percolation theory to noncatalytic gas-solid reactions." *AIChE journal* 32, no. 1 (1986): 46-55.

Yu, J. S. "An approximate analysis of laminar dispersion in circular tubes." *Journal of Applied Mechanics* 43, no. 4 (1976): 537-542.

Yu, J. S. "On laminar dispersion for flow through round tubes." *Journal of Applied Mechanics* 46, no. 4 (1979): 750-756.

Yu, J. S. "Dispersion in laminar flow through tubes by simultaneous diffusion and convection." *Journal of Applied Mechanics* 48, no. 2 (1981): 217-223.

Zaretskiy, Yan, Sebastian Geiger, Ken Sorbie, and Malte Förster. "Efficient flow and transport simulations in reconstructed 3D pore geometries." *Advances in Water Resources* 33, no. 12 (2010): 1508-1516.